# Reconfigurable Cryogenic Microwave Devices Using Low Temperature Superconducting rf-SQUIDs

by

Navjot Kaur Khaira

A thesis
presented to the University of Waterloo
in fulfillment of the
thesis requirement for the degree of
Doctor of Philosophy
in
Electrical and Computer Engineering

Waterloo, Ontario, Canada, 2022

© Navjot Kaur Khaira 2022

## Examining Committee Membership

The following served on the Examining Committee for this thesis. The decision of the Examining Committee is by majority vote.

External Examiner:
**Luca Pierantoni**
*Professor*
Electrical Engineering
Università Politecnica delle Marche, Ancona, Italy

Supervisor:
**Raafat R. Mansour**
*Professor*
Department of Electrical and Computer Engineering
University of Waterloo, Waterloo, ON N2L 3G1, Canada

Internal Member(s):
**Omar M. Ramahi**
*Professor*
Department of Electrical and Computer Engineering
University of Waterloo, Waterloo, ON N2L 3G1, Canada

**Guo-Xing Miao**
*Associate Professor*
Department of Electrical and Computer Engineering
University of Waterloo, Waterloo, ON N2L 3G1, Canada

Internal-External Member:
**Eihab Abdel-Rahman**
*Professor*
Department of System Design Engineering
University of Waterloo, Waterloo, ON N2L 3G1, Canada

## Author's Declaration

I hereby declare that I am the sole author of this thesis. This is a true copy of the thesis, including any required final revisions, as accepted by my examiners.

I understand that my thesis may be made electronically available to the public.

## Abstract

In the physical implementation of modern superconducting quantum computing systems, microwaves play a significant role in the control and measurement of qubits. The advances towards the use of microwaves in the quantum signal processing regime have inspired research on a suite of superconducting radio frequency (RF) components such as phase shifters, beam splitters, circulators, isolators, Josephson parametric amplifiers, and kinetic inductance travelling wave amplifiers. Although many room-temperature microwave components are commercially available, but there is a need to develop cryogenic microwave components, considering the challenges involved in the successful delivery of room-temperature generated microwave signals to the qubit chip. For the furtherance of large-scale quantum systems, tremendous efforts are being made to integrate the microwave photon generation, modulation, and routing in the cryogenic conditions adjacent to the qubits. This has created an urgent demand for various superconducting RF components.

In order to tune the phase of on-chip coherent microwave sources in cryogenic environment, a compact, low-loss, fast-tunable, wideband phase shifter is needed. Superconducting phase shifters are also employed in the chip-to-chip quantum network communication with microwave photons and have recently found applications in the future secure communication using far-field microwave quantum technologies. This thesis reports the development of radio frequency superconducting quantum interference devices (rf-SQUIDs) based analog phase shifters for such quantum applications. Each rf-SQUID is a superconducting loop shunted by a Josephson junction (JJ) and a long array of rf-SQUIDs is coupled with a low temperature superconductor (LTS) niobium (Nb) microwave transmission line (TL). The inductance of rf-SQUIDs is dependent on the flux threading the loop, which can be precisely controlled by applying a dc current or RF power or a combination of the two. Since the variable inductance of an array of rf-SQUIDs is tightly coupled to the TL, they change the inductance of the TL leading to a phase shift. The issue with this design is that the phase shift is achieved at the expense of changing characteristic impedance of the TL. In order to address this issue, a

phase shifter using a reflective-type topology is developed. It utilizes a superconducting hybrid coupler monolithically integrated with two tunable reflective loads. An array of rf-SQUIDs is used to achieve inductive tuning in the reflective loads, resulting in a broadband true time delay phase shift. The inductance tuning using rf-SQUIDs is also employed to demonstrate a tunable superconducting microwave resonator, which offers ultra-wide tuning range of 1.24 GHz at the fundamental resonance at 5.6 GHz. Superconducting tunable resonators have vast potential applications in microwave tunable filters, tunable couplers, tunable parametric amplifiers, SQUID multiplexers, and astrophysical detectors.

This thesis reports first ever implementation of a power dependent cryogenic power limiter based on rf-SQUIDS. The objective is to develop a LTS power limiter, which can provide protection against power levels above $-15$ dBm and can be monolithically integrated with other components on the superconducting chip. The output power increases linearly with the input power up to $-15$ dBm, and as the input power level increases beyond $-15$ dBm, the device offers an increasing attenuation to limit the output RF power to $-15$ dBm. Apart from the quantum measurement systems, cryogenic power limiters find applications in digital RF receivers. Such digital receivers are rapid single flux quantum (RSFQ) based, which cannot handle high power levels. When controlled by using dc current, this power limiter topology can be used as an analog variable attenuator as demonstrated in this thesis. Design and simulations of a cryogenic magnetless circulator based on the principle of spatiotemporal modulation angular-momentum (STM- AM) are also presented in this thesis. Microwave circulators have found a prominent role in the qubit readout circuitry and are used in conjunction with Josephson parametric amplifiers. The scheme is based on the parametric modulation of three identical, strongly and symmetrically coupled resonators.

The devices are realized using MIT Lincoln Laboratory SFQ5ee eight-layer niobium-based process, which provides a solid technology platform for building superconducting circuits.

## Acknowledgements

I would like to extend my deepest gratitude to my supervisor Dr. Raafat R. Mansour. He is an excellent example of a successful engineer and professor. It has been an honour to be his student. During my MASc and PhD journey, he gave me the opportunity to work on challenging new topics in the microwave field, making this a huge learning experience for me. I am indebted to him for his generous contributions of time, ideas, resources and encouragement to make my research experience productive and stimulating. His positive and enthusiastic attitude towards research kept me motivated. Every time I gave a presentation at a conference, he was always so happy and proud of me. He stands by and protects his students like no one else. Apart from research, I have learnt a lot of life skills from him, especially the value of patience.

I have no words to express my gratitude to my best friend, my husband Dr. Tejinder Singh for his eternal love and unflinching support throughout my journey. We are not only life-partners but also lab-partners. He is a genius at engineering and computer skills, who has genuine interest in learning new things every day. He makes everything seem so effortless and I always look up to him. I consider myself extremely lucky to have met him. He has stood by my side during all the successes and failures of my life. I wouldn't have made it this far without him.

I would like to thank Prof. Omar Ramahi, Prof. Eihab Abdel Rahman and Prof. Guo-Xing Miao who served as my PhD committee members. I would also like to thank Prof. Luca Pierantoni for serving as the external examiner and providing his valuable feedback. I also want to acknowledge my colleagues in the CIRFE group including Johnny (Huayong) Jia, Edward Jin and Armin Smajevic for their support during those long hours of cryogenic chip testing. I would like to thank our lab manager Dr. Luis Enrique Gutierrez for maintaining the lab equipment and providing the necessary inventory/-supplies. Special thanks to our ex-lab manager Bill Jolley, whose professional experience has been a great help at several times.

Aside from my academic colleagues, I want to address my parents for all their love and encouragement: my father who raised me with a love of science and supported me

in all my pursuits, and my mother whose spirituality and positive outlook towards life has been the guiding compass for me. Her voice always puts me at ease whenever I am stressed in my life. My sister has been my best friend all my life and I love her dearly and thank her for all her emotional support. I will not miss a chance to thank my younger brother for bringing all the fun and laughter into my life. I am grateful to my mother-in-law and father-in-law for being so kind and loving.

I would like to thank my Lord Almightly for providing me the wisdom and strength during all the low times of my life and blessing me with such amazing and loving people in my life. He has given me the intelligence and will-power to learn and explore the wonders that He has created, for nothing is possible without His will.

Last but not the least, I appreciate the financial support from the provincial government of Ontario for awarding me the Ontario Graduate Scholarship (OGS) two times and the University of Waterloo for the Engineering Excellence Doctoral Fellowship for the entire duration of my doctoral studies. I also appreciate financial support from the University of Waterloo in the form of President's Graduate Scholarship, Faculty of Engineering Awards (four times) and Waterloo Institute for Nanotechnology (WIN) for selecting me twice as a Nanofellowship recipient. I would also like to thank all the members of IEEE Microwave Theory and Techniques Society (MTT-S), who are my academic and professional family.

## Dedication

*To my loving husband Dr. Tejinder Singh*
*and my parents.*

# Table of Contents

**Examining Committee Membership** ii

**Author's Declaration** iii

**Abstract** iv

**Acknowledgements** vi

**Dedication** viii

**List of Figures** xiii

**List of Tables** xxiv

**List of Abbreviations** xxv

**1 Introduction** 1

1.1 Motivation . . . . . 1

1.2 Research Objectives . . . . . 4

1.3 Thesis Outline . . . . . 6

**2 Background Information** 7

2.1 Brief History of Superconductivity . . . . . 7

2.2 Power Limiters . . . 8
2.2.1 High Temperature Superconductor Based Microwave Limiters . . . 8
2.2.2 Semiconductor Limiters using PIN/Schottky Diodes . . . 12
2.2.3 RF-MEMS Based Power Limiters . . . 19
2.2.4 Vanadium Dioxide Based Power Limiters . . . 22
2.2.5 Frequency Selective Power Limiters . . . 24
2.3 Microwave Circulators . . . 27

**3 rf-SQUIDs and Cryogenic Microwave Phase Shifter 35**
3.1 Introduction to Josephson Junctions and rf-SQUIDs . . . 35
3.1.1 Flux Quantization in a Superconducting Loop . . . 35
3.1.2 Josephson Junctions . . . 36
3.1.3 rf-SQUIDs . . . 37
3.2 rf-SQUIDs Coupled Microstrip TL . . . 39
3.3 Simulations for Mutual Inductance and Coupling Coefficient . . . 46
3.4 Multi-layer Superconducting Fabrication Process . . . 51
3.4.1 MIT Lincoln Laboratory (MIT-LL) SFQ5ee Process . . . 51
3.5 Cryogenic Test Setup for RF Measurements . . . 53
3.5.1 Device Testing at Cryogenic Temperatures . . . 53
3.6 LTS Phase Shifter Using rf-SQUIDs . . . 54

**4 Superconducting Microwave Resonator and Reflective Type Phase Shifter 61**
4.1 Superconducting Tunable Microwave Resonator . . . 61
4.1.1 Design and Operation Principle of the Tunable Resonator . . . 63
4.1.2 MIM Capacitor . . . 66
4.1.3 Experimental Measurements of Superconducting Resonator . . . 66
4.2 LTS Wideband Quadrature Hybrid Couplers . . . 72
4.2.1 Design of CPW Based Hybrid Coupler . . . 74

4.2.2 Simulations and Experimental measurement . . . . . 76
4.3 Reflective Type Phase Shifter . . . . . 79
4.3.1 RTPS Design and Operation Principle . . . . . 80
4.3.2 Tunable Reflective Load . . . . . 83
4.3.3 Measurement Results . . . . . 87
4.3.4 Maximizing the Phase Shift . . . . . 92

**5 Power Dependent Microwave Power Limiter and Variable Attenuator 93**
5.1 Superconducting Microwave Power Limiter Using rf-SQUIDs . . . . . 93
5.1.1 RF Power Dependent Phase Shift in DJI Transmission line . . . . . 94
5.1.2 Power Limiter Design and Operation Principle . . . . . 96
5.1.3 Measurement Results of Power Limiter . . . . . 99
5.2 Variable Attenuator . . . . . 103
5.2.1 Phase Shifter Using rf-SQUIDs . . . . . 108

**6 Magnetless Superconducting Circulator 113**
6.1 LTS Microwave Magnetless Circulator . . . . . 113
6.2 Operation Principle . . . . . 114
6.3 Simulations . . . . . 116
6.4 Circulator Design . . . . . 119
6.5 Fabrication and Future Improvement . . . . . 122

**7 Conclusion 124**

**Thesis List of Publications/Contributions 126**

**References 128**

**Appendices 139**

**A Complete Chip Layouts** **140**

**Glossary** **146**

# List of Figures

1.1 A typical measurement and control setup for a superconducting quantum computing chip sitting at the base plate of a dilution refrigerator at ∼10 mK. The state of the superconducting qubits is probed by injecting a set of strongly attenuated microwave tones ($< -120$ dBm) that are subsequently amplified and delivered back to room temperature. The qubit induces a state-dependent phase shift of the probe tone that is measured via homodyne detection at room temperature. The weak output signal from qubit is amplified using superconducting parametric amplifiers, such as a Josephson parametric amplifier (JPA), operating at 10 mK and semiconductor HEMT amplifiers operating at 4 K. RF circulators are used to protect the quantum circuit from reflections and noise. Separate input lines are used for qubit control microwave pulses [2]. . . . . 2

1.2 (**a**) Power limiter used to protect low noise amplifiers (LNAs) and other sensitive receiver electronics, (**b**) Power characteristics of a limiter showing the output power is limited after the input power crosses the threshold value . . . . . 4

2.1 (**a**) Comparison of power limiting behavior for CW and 5 µs pulsed microwave signals at 3 GHz at 76 K. In the pulsed case, Pout corresponds to the peak power. The solid line shows Pout = Pin, (**b**) Frequency dependence of the attenuation constant in the superconducting ($T$ =70 K) and normal states ($T$ =95 K). [16] . . . . . 9

2.2 (**a**) Frequency dependence of the characteristic impedance of the transmission line limiter in the superconducting and normal states, (**b**) Incident and transmitted signal magnitudes for a power limiter at 76 K for a 100 ns wide pulse. [16] . . . . . 10

2.3 (**a**) Schematic diagram of the power limiting device: (1) substrate; (2) grounded base; (3) strip conductors of side resonators with compensated coupling; (4) strip conductors of the central composite resonator; (5) film conductor of HTS element, (**b**) Amplitude-frequency characteristics of the device in cases when the HTS element occurs in the (1,3) superconducting and (2,4) normal state. (1,2) are the results of numerical simulation while (3,4) is experimental data. [18] . . . . . 10

2.4 (**a**) Design of the microstrip reflective power limiter with (1) dielectric substrate; (2) copper external resonator; (3) copper parts of the internal resonator; (4) HTS element; (5) $NdGaO_3$ substrate; also a photograph of the device's experimental realization is shown, (**b**) Frequency response of the power limiter in the open state (solid line), the closed state (dashed line) and in the absence of internal resonator and HTS element (dotted line). [19] . . . . . 11

2.5 (**a**) Current density in a CPW with a 10 μm wide center strip and a 5 μm gap. The HTS film is 150 nm thick, the ground planes are 100 μm wide, and the input power is 0 dBm, (**b**) Temperature rise and upper power threshold in two different samples made of a sapphire substrate and a quartz substrate. [20] . . . . . 13

2.6 Different popular configurations for PIN diode limiter. [23] . . . . . 13

2.7 (**a**) A single stage limiter using PIN diode, (**b**) Output power vs Input power for a single-stage limiter.[23] . . . . . 14

2.8 (**a**) Power transfer function for a Single-stage limiter, (**b**) Two-stage limiter using PIN diodes.[23] . . . . . 15

2.9 (**a**) A microwave two-stage limiter circuit composed of two coupled $\lambda/4$ microstrip resonators loaded by anti-parallel pairs of Schottky diodes, (**b**) Simulated and measured characteristics of output power versus input power of the microwave limiter at center frequency of 2.87 GHz. [24] . 16

2.10 (**a**) Schematic of a two-stage limiter design using 6 PIN diodes , (**b**) Measured limiting provided by two-stage limiter circuit. [25] . . . . . 17

2.11 (**a**) Schematic of a two-stage limiter design using 8 PIN diodes , (**b**) Measured limiting characteristics of the circuit. [25] . . . . . 17

2.12 (**a**) Circuit for the simulation of stacked antiparallel configuration, (**b**) Image of the fabricated limiter. [26] . . . . . 18

2.13 (**a**) Input power versus output power at 30 MHz, (**b**) Input power versus output power at 300 MHz. [26] . . . . . 18

2.14 Cross section of a shunt capacitive RF MEMS switch displaying the self-actuation phenomenon used for power limiting. [28] . . . . . 19

2.15 (**a**) SEM picture of a RF-MEMS based power limiter developed using single shunt switch, (**b**) Computed and measured input/output power characteristics of the limiter at 10.24 GHz. [28] . . . . . 20

2.16 (**a**) SEM picture of an array of RF MEMS shunt switches used as a power limiter, (**b**) Computed and measured input/output power characteristics of the limiter at 10.24 GHz. [28] . . . . . 21

2.17 (**a**) SEM picture of the fabricated thermally actuated switch, (**b**) Power level at which switch actuates vs applied dc actuation voltage. [31] . . . . 21

2.18 (**a**) Power limiter design consisting of a CPW transmission line with $VO_2$ film patterned in the gaps between the signal line and the ground planes, (**b**) Transmitted vs incident CW microwave power at 10 GHz for a 100 μm-length $VO_2$-based CPW transmission line at different operating temperatures. [32] . . . . . 23

2.19 (**a**) Image of the microwave power limiter based on two dividers using two identical distributed $VO_2$ films and Ni-doped carbon patterns, (**b**) Measurements of the transmitted power versus the incident power at 10 GHz for different DC bias voltages. [33] . . . . . 23

2.20 A spectrum (left) with various above-threshold (1,4,5) and below-threshold (2,3) measured signals. When this spectrum is passed through a frequency selective limiter (FSL), it's response changes to provide selective attenuation of above-threshold signals (middle). Below threshold signals of interest are unaffected (right).[37] . . . . . 25

2.21 (**a**) Design of the thin film YIG limiter, (**b**) Measured power limiting at different frequencies. [34] . . . . . 26

2.22 (**a**) Geometry of magnetostatic wave frequency selective limiter utilizing surface wave propagation for low loss and low threshold, (**b**) Power limiting for three YIG films with different ScGa doping. [35] . . . . . 27

2.23 (**a**)Frequency selective limiter device, (**b**)Measured RF input and output power at L-band, (**c**) Measured output power as a function of frequency. [37] . . . . . 27

2.24 (**a**) Image of the fabricated power limiter using one hybrid coupler, two MEMS switches and two bandpass filters, (**b**) Power characteristics of the limiter. [38] . . . . . 28

2.25 Circuit implementation of the non-reciprocal coupled-resonator loop at radio frequencies (**a**) A single resonant circuit of the proposed device comprising of an L-C tank with modulated capacitance. Capacitance modulation is achieved with varactor diodes, (**b**) A loop formed by three identical resonators coupled through three identical capacitances, (**c**) Photograph of the fabricated prototype. [45] . . . . . 29

2.26 (**a**) Measured transmission from port 1 to ports 2 and 3 without modulation ($V_m = 0V$). The power is equally split to the output ports, (**b**) Measured scattering parameters when $V_m = 0.6V$. Incident power to ports 1, 2 and 3 is transmitted to ports 2, 3 and 1, respectively, (**c**) Simulated response of the loop for the case when $V_m = 0.6V$. [45] . . . . . 30

2.27 The single-ended topologies of STM-AM circulators (**a**) Bandpass/wye, (**b**) bandstop/wye, (**c**) bandstop/delta, and (**d**) bandpass/delta.[2] . . . 30

2.28 (**a**) Schematic of the magnet-less circulator. Photograph of the fabricated prototype is shown in the inset, (**b**) Simulated S-parameters without modulation (dashed lines) and with modulation (solid lines). [46] . . . . . 31

2.29 (**a**) Schematic of the voltage-mode differential STM circulator and photograph of the fabricated prototype, (**b**) Measured S-parameters. [47] . . . . 31

2.30 (**a**) Implementation of the switched capacitors in a modified wye topology where the inductors are transformed into a delta connection, (**b**) Photograph of the chip layout and the packaged chip mounted on a PCB. [48] 32

2.31 (**a**) FBAR chip showing the schematic of connection and the designed PCB of the circulator. Three FBARs are monolithically integrated on one chip, (**b**) Measured insertion loss (IL) from TX to ANT and from ANT to RX and measured isolation (IX) from TX to RX. [49] . . . . . 33

3.1 Left: The schematic of a Josephson junction, a thin layer of insulator sandwiched between two superconductors, Right: First time experimental verification of the Josephson effect. Current-voltage characteristics for a Sn-$SnO_x$-Pb tunnel structure at ∼1.5 K, (a) for a field of $6 \times 10^{-7}$ T, and (b) for a field of $4 \times 10^{-5}$ T [53]. . . . . 36

3.2 (**a**) One-junction rf-SQUID, (**b**) Two-junction dc-SQUID. . . . . 38

3.3 rf-SQUID consisting of a superconducting loop of inductance, $L$, interrupted by a single Josephson junction. . . . 38
3.4 (a) Cross-section view, (b) 3D view of a microstrip transmission line coupled to an array of SQUIDs . . . 40
3.5 3D view of the microstrip TL magnetically coupled to an array of rf-SQUIDs. 41
3.6 (**a**) Equivalent circuit of a TL unit cell containing a rf-SQUID, (**b**) 3D view of rf-SQUIDs placed between the top conductor and ground plane of TL. . 41
3.7 (a) The lumped element model of a distributed Josephson inductance (DJI) transmission line, (b) Small signal RF equivalent circuit of the DJI . 42
3.8 Microstrip TL unit-cell in Sonnet EM . . . 46
3.9 3D model of an rf-SQUID in Sonnet EM . . . 47
3.10 (**a**) rf-SQUID and TL model in Ansys Maxwell 3D, (**b**) Cross-section view of the model. . . . 48
3.11 Simulation model of rf-SQUID coupling a microstrip TL in Ansys Maxwell 3D . . . 48
3.12 Magnetic flux density in rf-SQUID using Ansys Maxwell 3D . . . 49
3.13 (**a**) Dynamic inductance, $L_{dyn}$ and transmission line inductance, $L$ of a unit-cell, (**b**) Calculated relative phase shift at 11.6 GHz as a function of dc current ranging from 0 mA to 8 mA . . . 51
3.14 (**a**) Dynamic inductance, $L_{dyn}$ of a transmission line cell as a function of RF power ranging from $-30$ dBm to 10 dBm, (**b**) Calculated relative phase shift for the RF power range $-30$ dBm to 10 dBm . . . 53
3.15 Cross section of the MIT-LL 10 kA/cm$^2$ SFQ5ee process. . . . 54
3.16 Scanning electron microscope (SEM) of the wafer cross section highlighting the MIT-LL SFQ5ee process node. Various Nb metal layers (M0-M7), vias (I0-I6), josephson junction (JJ), resistor layers (r5 and mΩ), and a high-kinetic inductance layer are indicated [61]. . . . 54
3.17 (**a**) rf-SQUIDs placed under the microstrip TL using two additional Nb layers, (**b**) rf-SQUIDs placed on both sides of the microstrip TL on the same Nb layer. . . . 55
3.18 Cryogenic test setup at CIRFE showing the Lakeshore probe station, PNA and PSU. The enlarged image highlights the chips loaded in the cryo chamber. . . . 55

3.19 (a) Schematic of the phase shifter comprising of an array of rf-SQUIDS coupled to the superconducting transmission line (TL), (b) 3D rendered image showing rf-SQUIDs distributed underneath the superconducting TL. 56

3.20 Optical micrograph of the fabricated phase shifter. The signal is given at the RF input, which connects to a meandered microstrip line coupled with rf-SQUIDs and a phase shift is observed in the signal at the RF output. . . 57

3.21 Measured relative phase shift and $S$-parameters of the phase shifter with control current of $I_{\text{min}} = 0\,\text{mA}$ and $I_{\text{max}} = 36\,\text{mA}$ over (a) 9.5 GHz to 10.5 GHz, (b) 21.75 GHz to 22.75 GHz, (c) insertion loss and return loss for the frequency range 0 GHz to 26.5 GHz. . . . . 58

3.22 Measurement results of the phase shifter for a control current ranging from 0 mA to 36 mA. The phase shift, insertion loss and return loss for three different frequencies in the $X$-band and $K$-band are shown. . . . . 59

4.1 Optical micrograph of the LTS resonator highlighting the MIM capacitor and the microstrip TL inductor connected in shunt with the central microstrip connecting two RF ports. The control line runs parallel to the rf-SQUIDs array and terminates in a DC pad on each end. The inset highlights the rf-SQUID loop placed between the microstrip inductor (carrying the RF signal) and the dc control line. . . . . 62

4.2 (a) 3D view of the proposed LTS resonator layout comprising a single RF port, a MIM capacitor, a microstrip TL inductor and an array of rf-SQUIDs, (b) Optical micrograph of the fabricated device. . . . . 65

4.3 Simulated $S_{11}$ of the resonator using ADS circuit simulation and Sonnet EM simulation showing a close match. . . . . 67

4.4 (a) Measured $S_{11}$ of the resonator for a control current sweep from 0 mA to 2 mA. (b) Resonance frequency shift as a function of control current. . . 68

4.5 (a) Measured $S_{11}$ of the resonator for different values of RF power ranging from $-30\,\text{dBm}$ to 0 dBm. (b) Resonance frequency shift as a function of input RF power. . . . . 69

4.6 (a) Measured $S_{11}$ of the resonator for different values of RF power ranging from $-30\,\text{dBm}$ to 0 dBm. (b) Resonance frequency shift as a function of input RF power. . . . . 70

4.7 (a) Schematic of the quadrature hybrid coupler displaying all the four RF ports: Input, Through, Coupled and Isolated. (b) The design of CPW-based hybrid coupler using two tandem coupled lines and interconnections between signal lines and ground planes. . . . . 72

4.8 (a) Optical micrograph of the fabricated hybrid coupler. The length has been trimmed to include the ends and the center part of the design, (b) an enlarged image of the monolithically integrated 50 Ω micro resistor termination, (c) an enlarged image of the coupled lines crossover in the tandem design highlighting the dimensional parameters. . . . . 73

4.9 3D rendered image of the meandered hybrid coupler design-C with a compact footprint of 0.45 mm × 0.31 mm. The enlarged section shows the crossovers connecting the coupled lines and the ground planes. . . . . 74

4.10 Size comparison of the hybrid couplers design-A, design-B, and design-C. The design-C has 64% smaller footprint compared to design-B while operating at the similar wideband frequency range. . . . . 75

4.11 Left: Optical micrograph of a single port integrated 50 Ω termination used for verification, right: The simulated and measured response of the termination from dc to 50 GHz. . . . . 76

4.12 Simulation and measurement of the hybrid coupler design-A with the desired coupling performance observed over the 26 GHz to 44 GHz frequency range. . . . . 77

4.13 Simulated and measured S-parameters of the hybrid coupler design-B showing excellent coupling for the frequency range 8 GHz to 18 GHz. The simulation results are represented by dotted lines, and the solid lines demonstrate the measured response of the device. . . . . 77

4.14 S-parameters simulation of the compact hybrid coupler design-C showing the 3 dB coupled response between 8 GHz and 18 GHz. . . . . 78

4.15 Schematic of the proposed reflection-type phase shifter (RTPS) consisting of a quadrature hybrid coupler terminated with two identical reflective loads. The input RF signal is split equally by the hybrid coupler, reflected off of the two reflective loads, and the phase shifted signal is obtained at the RF output. $\Gamma$ is the reflection coefficient and $X_L$ is the tunable reactance of each reflective load. . . . . 80

4.16 Layout of the proposed LTS based reflective-type phase shifter (RTPS) showing the monolithic integration of a hybrid coupler section with two identical reflective loads. An array of rf-SQUIDs is used to provide tunable inductance in each reflective load. Dimensional parameters of each rf-SQUID are highlighted along with the $Nb/AlO_x/Nb$ JJ used in each SQUID loop. . . . . 81

4.17 Fabricated micrograph of the standalone reflective load used in the proposed RTPS. . . . . 83

4.18 (a) Circuit model of a single rf-SQUID coupled to microstrip line section, (b) 3D realization of the circuit model. . . . . 85

4.19 The lumped element equivalent circuit of the reflective load and the simulated load impedance range and phase shift range. . . . . 86

4.20 (a) Measured S-parameters of the analog phase shifter from 8 GHz to 18 GHz for the control current range 0 mA to 3 mA, and (b) Measured relative phase shift of the device in the *X*- and *Ku*- Band. . . . . 88

4.21 Measured relative phase shift for control current values 0 mA to 3 mA (a) in the frequency range 8 GHz to 12 GHz, and (b) in the frequency range 12 GHz to 18 GHz. . . . . 88

4.22 Simulated phase shift prediction with the change in control current from 0 mA to 3 mA and the measured phase shift from the fabricated device (a) at the centre frequency 10 GHz in the *X*- band, (b) at the centre frequency 15 GHz in the Ku- band, (c) measured insertion loss at 10 GHz and 15 GHz with the control current, (d) measured return loss with the control current at 10 GHz and 15 GHz. . . . . 89

4.23 The lumped element equivalent circuit of the reflective load and the improved load impedance range and phase shift range. . . . . 91

5.1 Measured S-parameters and relative phase shift of the microstrip line coupled with rf-SQUIDs over the RF power sweep from $-30$ dBm to 10 dBm. 95

5.2 Calculated phase shift prediction with the change in RF power and the measured phase shift from the fabricated device. . . . . 96

5.3 Schematic of the proposed power limiter consisting of two quadrature hybrid couplers and two microstrip TLs. One of the microstrip TL is coupled to an array of rf-SQUIDs and provides a variable phase $\theta_2$, while the other microstrip TL offers a fixed phase angle $\theta_1$. The output powers $P_1$ and $P_2$ are a function of the phase difference $\Delta\theta$ between the two microstrip TLs. 97

5.4 Optical micrograph of the developed power limiter showing the monolithic integration of two quadrature hybrid coupler sections with two meandered microstrip TLs. The JJs underneath the top microstrip TL and the 50 Ω load termination are highlighted. . . . . 98

5.5 Layout of the meandered microstrip TLs used in the power limiter. The top microstrip is coupled to rf-SQUIDs. The two microstrip lines share a common ground plane. . . . . 98

5.6 The chips loaded inside the cryogenic chamber of Lakeshore probe station for testing. The chamber has two RF GSG probes, two dc probes and the chip holder is loaded on the 4 K temperature stage. . . . . 100

5.7 Measured insertion loss and return loss response of the power limiter over the frequency range 9 GHz to 11 GHz with the input RF power level sweeping from −30 dBm to 10 dBm. . . . . 101

5.8 (a) Measured insertion loss and return loss of the power limiter for the input RF power range of −30 dBm to 10 dBm, (b) Measured output RF power as the input RF power is increased from −30 dBm to 10 dBm. . . . . 102

5.9 Two tone intermodulation response of the power limiter at different input RF power levels ranging from −30 dBm to 5 dBm. . . . . 103

5.10 Design layout of a superconducting microwave variable attenuator consisting of two microstrip TLs disposed between two hybrid couplers. One of the microstrip TL is loaded with 230 rf-SQUIDs. The unused hybrid coupler's ports are terminated with 50 Ω micro-resistors. . . . . 105

5.11 Layout of the folded microstrip TLs used in the variable attenuator. The top microstrip is coupled to an array of rf-SQUIDs. The top an bottom microstrip line share a common ground plane. . . . . 105

5.12 The chips loaded inside the cryogenic chamber of Lakeshore probe station for testing. The chamber has two RF GSG probes, two dc probes and the chip holder is loaded on the 4 K temperature stage. . . . . 106

5.13 Measured S parameters of the variable attenuator showing the insertion loss $S_{21}$ and return loss $S_{11}$ for the control current sweep from 0 mA to 4.5 mA. . . . 107

5.14 Optical micrograph of the fabricated phase shifter consisting of an array of rf-SQUIDs placed along a meandered microstrip TL connecting the two RF ports. The control current is provided to a separate microstrip running parallel to the rf-SQUIDs. The enlarged section highlights the rf-SQUID loop placed between the RF signal carrying microstrip line and the dc current line. . . . 109

5.15 Measured S-parameters of the phase shifter from 1 GHz to 20 GHz with a dc current sweep from 0 mA to 4.5 mA. The relative phase shift ($\angle S_{21}$), insertion loss ($|S_{21}|$), return loss ($|S_{11}|$) in the *X*-band and *Ku*-band are highlighted. . . . 110

5.16 Optical micrograph of the phase shifter design similar to Fig. 5.14 with the rf-SQUIDs removed. Two parallel running microstrip lines can be seen in the highlighted section. . . . 111

5.17 Measured S-parameters of the phase shifter from 1 GHz to 20 GHz with a dc current sweep from 0 mA to 4.5 mA. No change in signal phase ($\angle S_{21}$), insertion loss ($|S_{21}|$), return loss ($|S_{11}|$) is observed. . . . 112

6.1 (**a**) rf SQUID is used as a tunable inductor, (**b**) Three port circulator showing the direction of signal circulation, (**c**) The proposed schematic of a superconducting circulator based on synthetic rotation. Three rf SQUIDs are modulated by RF signal 120° out of phase from each other. The phase progression between the three modulating signals establishes the direction of circulation, (**d**) The SQUIDs act as tunable inductors and modulate the coupling coefficient between the three resonators with resonance frequencies $\omega_1(t), \omega_2(t), \omega_3(t)$ . . . 115

6.2 Surface plots of S-parameters versus the normalized modulation frequency and normalized modulation amplitude (**a**) Isolation, (**b**) Insertion Loss, (**c**) Return Loss. . . . 117

6.3 3D plots of S-parameters versus the normalized modulation frequency and normalized modulation amplitude (**a**) Isolation, (**b**) Insertion Loss, (**c**) Return Loss, (**d**) Simulated S-parameters showing non-reciprocal operation. . . . 118

6.4 The resonator design steps: (1) a MIM capacitor and microstrip inductor, the Sonnet EM simulation for the resonator, (2) rf-SQUIDs coupled to the inductor, (3) modulation signal routed alongside the rf-SQUIDs. . . . . 119

6.5 Sonnet EM model of a meandered microstrip line, simulated phase of 120° at 1.63 GHz. . . . . 120

6.6 Sonnet EM model of a meandered microstrip line, simulated phase of 240° at 1.63 GHz. . . . . 120

6.7 2D layout of the superconducting magnetless circulator consisting of three resonators and the meandered delay lines. . . . . 121

6.8 3D layout image of the superconducting magnetless circulator consisting of three resonators and the meandered delay lines. . . . . 122

6.9 Optical micrograph of the LTS magnetless circulator. The enlarged sections show a single resonator and rf-SQUID. The overall chip footprint is 0.88 mm $\times$ 1.08 mm. . . . . 123

A.1 5mm x 5mm chip layout submitted to MIT-LL. . . . . 141

A.2 5mm x 5mm chip layout submitted to MIT-LL. . . . . 142

A.3 5mm x 5mm chip layout submitted to MIT-LL. . . . . 143

A.4 5mm x 5mm chip layout submitted to MIT-LL. . . . . 144

A.5 5mm x 5mm chip layout submitted to MIT-LL. . . . . 145

# List of Tables


3.1 Simulated results for $L, L_s, M$ and $k$ using Sonnet EM . . . . . 48

3.2 Simulated results for $L, L_s, M$ and $k$ using Ansys Maxwell 3D . . . . . 49

3.3 Analysis of the dynamic inductance and phase shift as a function of current using the given and simulated parameters . . . . . 50

3.4 Analysis of the dynamic inductance and phase shift as a function of RF power. . . . . 52

4.1 Design specifications of Superconducting Resonator . . . . . 64

4.2 Comparison of the proposed superconducting resonator with state-of-the-art . . . . . 71

4.3 Various parameters on device geometry . . . . . 74

4.4 Design specifications of Superconducting Resonator . . . . . 82

4.5 Comparison of the proposed phase shifter with state-of-the-art . . . . . 90

5.1 Design specifications of LTS Power Limiter . . . . . 99

# List of Abbreviations

| | |
|---|---|
| Au | Gold |
| CCD | Charge Coupled Device |
| CIRFE | Centre for Integrated RF Engineering |
| CMOS | Complementary Metal Oxide Semiconductor |
| CPW | Co-Planar Waveguide |
| CW | Continuous Wave RF Power |
| DC | Direct Current |
| DUT | Device Under Test |
| FIB | Focussed Ion Beam |
| FOM | Figure of Merit |
| GSG | Ground-Signal-Ground |
| HEMT | High Electron Mobility Transistor |
| LHe | Liquid Helium |
| LN | Liquid Nitrogen |
| LNA | Low Noise Amplifier |
| MEMS | Microelectromechanical Systems |
| MIM | Metal Insulator Metal |
| MMIC | Monolithic Microwave Integrated Circuit |
| mmWave | Millimeter Wave Frequencies |
| Nb | Niobium |

| | |
|---|---|
| PA | Power Amplifier |
| PNA | Performance Network Analyzer |
| RF | Radio Frequency |
| RF-MEMS | RF Microelectromechanical Systems |
| SEM | Scanning Electron Microscope |
| Si | Silicon |
| $SiO_2$ | Silicon Dioxide |
| SMU | Source Measure Unit |
| TL | Transmission Line |
| VNA | Vector Network Analyzer |

# Chapter 1

# Introduction

## 1.1 Motivation

Apart from COVID-19 related research, quantum computing hardware has become the most heavily invested scientific field in the pandemic era. Tech giants like IBM, Google, Amazon, Intel, Microsoft, and many others are trying to make their own quantum machines while governments across the globe are funding major national research initiatives focused on quantum information. The synergy between microwave engineering and quantum systems is long-standing but is now more evident than ever. Quantum information processing systems rely on microwave technologies for the precise control and readout of quantum states and have stimulated the development of microwave devices in new operating regimes. In today's state of the art technology, each qubit is driven by microwave signals that are generated using room-temperature electronics and carried to individual qubit [1]. The RF chains used for qubit control and detection of the readout signals contain various microwave components such as attenuators, filters, circulators and amplifiers as shown in Fig. 1.1(a). As the number of qubits is increased, the number of coaxial cables running into the cryostat increases exponentially. In order to resolve this issue, the microwave signal generation, shaping, routing, and control needs to be done at the cryogenic temperatures closer to the quantum processor.

The idea of developing on-chip coherent microwave sources in the cryogenic stage is being recently explored [3]. Tuning the phase of such microwave source requires low-loss, fast tunable, wide-band phase shifter. Although many room-temperature phase shifters are available in the literature using CMOS, SiGe, Phase change material

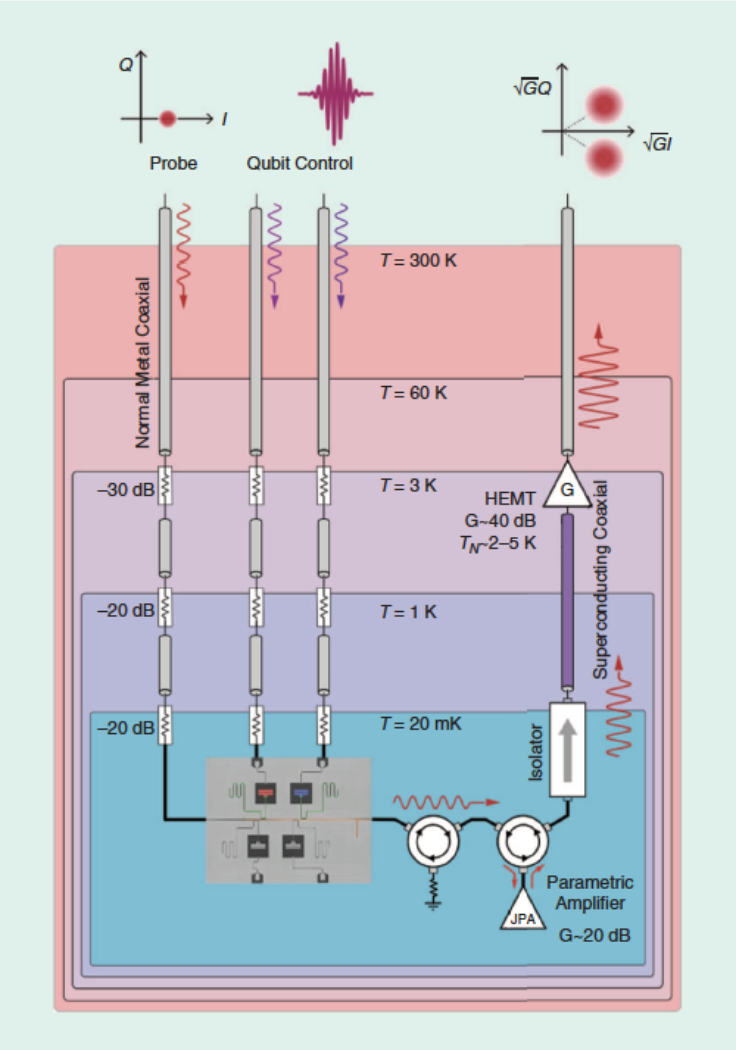



**Figure 1.1:** A typical measurement and control setup for a superconducting quantum computing chip sitting at the base plate of a dilution refrigerator at ∼10 mK. The state of the superconducting qubits is probed by injecting a set of strongly attenuated microwave tones ($< -120$ dBm) that are subsequently amplified and delivered back to room temperature. The qubit induces a state-dependent phase shift of the probe tone that is measured via homodyne detection at room temperature. The weak output signal from qubit is amplified using superconducting parametric amplifiers, such as a Josephson parametric amplifier (JPA), operating at 10 mK and semiconductor HEMT amplifiers operating at 4 K. RF circulators are used to protect the quantum circuit from reflections and noise. Separate input lines are used for qubit control microwave pulses [2].

(PCM) and MEMS technologies [4–7], their performance degrades significantly when operated at cryogenic temperatures. The superconducting phase shifters are thus an appealing candidate with greater reason.

Although the signals required to drive qubits or to read them out are small (e.g. a peak power of $-66$ dBm), the power applied at the room-temperature input is orders of magnitude higher. The quantum state of a qubit is typically read out by probing the linear resonators with weak RF signals (i.e., $< -120$ dBm, 4 GHz to 12 GHz) and measuring an associated state-dependent phase shift [1, 2]. To be compatible with many different types of superconducting quantum devices, there is a need for new topologies for cryogenic microwave components.

Apart from the quantum measurement hardware, a popular application of the power limiters is in the cryogenic RF receivers. Due to the increased wireless signal traffic, there is a demand to develop improved methods to receive the signal-of-interest while simultaneously protecting the sensitive receiver components like low-noise amplifiers (LNAs) and analog-to-digital converters (ADCs) from transient bursts of microwave power. Microwave power limiters provide this capability to communication systems [8]. RF receiver architectures use low-temperature superconductor (LTS) Josephson junction (JJ) based ADC to digitize the RF signal directly from the antenna without the need of a down-conversion circuit [9, 10]. Such ADCs are based on rapid single flux quantum (RSFQ) technology; hence, they are at high risk of getting damaged by any signals with power levels over $-15$ dBm. An ideal limiter has no attenuation when the input power level is low, but as the signal crosses the threshold level, power limiter offers an attenuation that increases with increasing power in order to maintain constant output power as shown in Fig. 1.2. The switching time for such LTS power limiter is expected to be on the order of microseconds or less. The currently available semiconductor diode-based limiters have two major drawbacks: First, the threshold power level is high, and cannot be reduced below a certain level. Second, there is a maximum limit on the input power beyond which the limiter cannot provide the desired attenuation, and the output power starts increasing proportionally with the input power. Magnetostatic surface wave (MSW) frequency selective limiters have significantly low threshold power levels (<-25 dBm), but magnetostatic waves are long wavelength spin waves that exist only over a limited frequency range (400 MHz to 4 GHz). Our objective is to develop a LTS power limiter which can provide protection against power levels below $-15$ dBm, is capable of operating over a wide frequency range, and can be monolithically integrated with other components on the superconducting chip.

The superconducting technology has the potential to realize reconfigurable microwave

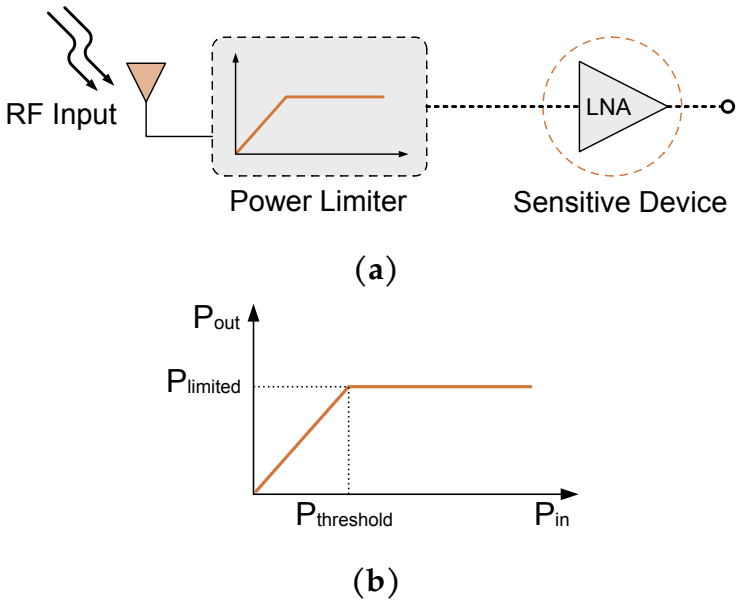



**Figure 1.2:** (**a**) Power limiter used to protect low noise amplifiers (LNAs) and other sensitive receiver electronics, (**b**) Power characteristics of a limiter showing the output power is limited after the input power crosses the threshold value

.

devices with unprecedented performance [11, 12]. The quantum hardware applications have pushed the boundaries of microwave technology and demand innovations in the superconducting microwave hardware. The goal of this doctoral research aligns with the demand and explores the cryogenic microwave components like phase shifters, tunable resonators, variable attenuator, and magnetless circulator.

## 1.2 Research Objectives

**Objective 1: Development of rf-SQUIDs based Superconducting Phase Shifter.**

rf-SQUIDs are capable of detecting magnetic flux with incredible precision and are popular for their applications in magnetometer. The primary objective of this

research is to investigate the behavior of a microwave transmission line loaded by an array of rf-SQUIDs. The inductance of rf-SQUIDs changes with the magnetic flux resulting from the dc current or the RF power on the transmission line. The goal is to simulate the model of one rf-SQUID coupled to a transmission line section and study the change in inductance analytically. The dynamic inductance of the transmission line is altered as the rf-SQUID inductance changes, leading to a change in the wave velocity. The output signal phase shift achieved with the dc current, or RF power provided on the transmission line is investigated.

**Objective 2: Development of Superconducting Tunable Resonator.**

Superconducting microwave resonators reported in the literature primarily benefit from the current-dependence/magnetic-field dependence of nonlinear kinetic inductance in a superconducting transmission line and are capable of providing very limited resonance frequency tunability. The objective is to develop superconducting resonator with tunability range surpassing the current state-of-the-art. Using rf-SQUIDs to achieve the inductance change in the resonator is studied in detail. The possibility of using a separate dc control line to provide the flux to the rf-SQUIDs instead of providing dc current on the RF signal line is investigated.

**Objective 3: Development of Cryogenic Hybrid Couplers and Reflective Type Phase Shifter.**

The goal is to explore other topologies and develop a design of the phase shifter improving on the drawbacks noted in the phase shifter in objective 1. Reflective-type phase shifter topology requires a hybrid coupler and two tunable reflective loads. Hence, the task is divided in two sub-tasks: i) investigation of hybrid coupler configurations that can provide a wideband coupling response, ii) realization of the tunable reflective loads that can provide the maximum phase shift.

**Objective 4: Integration and Demonstration of Power Dependent Power Limiter.**

To date, the research on superconducting limiters utilizes the switching of high temperature superconductor transmission line from low-loss superconducting state to the high-loss normal state when the microwave currents in the device exceed the critical value at high RF power levels. The objective here is to implement a novel topology to achieve the RF power dependent power limiting operation at very low RF power levels using Nb-based low temperature superconductor (LTS) circuits.

**Objective 5: Investigation of Cryogenic Magnetless Circulator.**

The final objective is to investigate possible techniques to build a magnetless circulator. The goal is to find a possible way to implement the principle of spatiotemporal modulation angular-momentum using rf-SQUIDs as flux tunable inductors.

## 1.3 Thesis Outline

This chapter discusses the introduction, motivation and the research objectives followed by Chapter 2 that includes the background information about various superconducting and room-temperature power limiters. It also briefly explores the literature on magnetless microwave circulators. Chapter 3 provides the detail on the simulations, theoretical analysis and design of rf-SQUIDs and the developed superconducting phase shifter. Chapter 3 also provides the detail of the Nb-based multilayer fabrication process and the test setup used for device RF measurements at cryogenic temperatures. Superconducting microwave resonator design and experimental measurements are reported in Chapter 4. It also includes the design and measurements of cryogenic hybrid couplers and the reflective-type phase shifter. Chapter 5 reports the principle, design and experimental testing of power dependent power limiter. The variable attenuator design and response is also included. Chapter 6 includes the future work and provides insights into the proposed design for magnetless cryogenic circulator. A summary of the work is given in Chapter 7. The thesis concludes by listing the references and the list of publications generated from this research. The complete 5 mm $\times$ 5 mm chip layouts submitted for fabrication are highlighted in Appendix A.

# Chapter 2

# Background Information

## 2.1 Brief History of Superconductivity

The phenomenon of zero resistance at low cryogenic temperatures was discovered in 1911 by Prof. H. K. Onnes in the Netherlands in the course of studying the low temperature properties of metals [13]. To his surprise, the electrical resistance of mercury vanished after cooling it in a bath of liquid Helium. This effect was found for a variety of pure metals, alloys and ceramics with different critical temperatures $T_c$. Below, these temperatures, the superconducting state is reached. In 1933, another important property of superconductors was discovered experimentally by W. Meissner and R. Ochsenfeld; they found that superconductors have the tendency to exclude magnetic field. A certain class of superconductors, called Type I, can almost completely exclude magnetic field and, therefore, have almost perfect diamagnetic properties. Guided by the zero resistance and diamagnetism, a theory was developed by F. London and H. London. Even today, the London theory is used extensively in applied superconductor electronics where magnetic fields are weak. This theory assumed a function $\Psi(r)$ representing the superconducting electron fluid that can be thought of as a single giant quantum mechanical wave function that extends throughout the superconductor. It also revealed that magnetic flux is quantized inside superconducting loops. It was later shown that the quantum of magnetic field has the value $\Phi_0 = \mathrm{h}/2\mathrm{e}$, where e is the electron charge and h is Planck's constant.

The concept of electron pairing was introduced in 1956 by L. N. Cooper. Superconducting state was a state of pairing of electrons of equal and opposite momentum and spin, and are known as Cooper pairs. In 1957, J. Bardeen, J. R.

Schrieffer, and L. N. Cooper (BCS) published a microscopic theory of superconductors based on the concept of electron pairing in momentum space. It had been 46 years between the original experimental demonstration of superconductivity and a first-principles theory. With this new understanding, B. Josephson developed a theory for quantum mechanical tunneling between superconductors, in which electron pairs can pass through a thin insulator from one superconductor to the other, even with zero applied voltage. This effect was later experimentally verified by Phil Anderson and John Rowell at the Bell labs. The so-called Josephson effects, combined with low electromagnetic loss, underlie today's electronic applications.

## 2.2 Power Limiters

### 2.2.1 High Temperature Superconductor Based Microwave Limiters

High temperature superconductor (HTS) materials can undergo a transition from the superconducting state to the non-superconducting state when the current density exceeds a critical level. This current-density dependence of superconductor material properties has been exploited to develop power limiters based on HTS materials. The short switching times of one nanosecond or less ensure that very little energy is transmitted through the limiter prior to switching, and so guarantees a high degree of protection to downstream electronics from high-power transient signals. This characteristic makes HTS technology a viable candidate compared to conventional limiting technologies, such as diodes.

The basic idea used in the superconducting power limiters developed few years after the discovery of HTS $Y_1Ba_2Cu_3O_{7-x}$ (YBCO) was to reversibly drive a meandered thin film superconducting transmission line from the low-loss superconducting state to the high-loss normal state by exceeding the critical current density of the superconductor.

In 1999, M. Lindmayer et. al. studied the current limiting properties of HTS YBCO-films on sapphire substrates [14, 15], but typically for DC and low-frequency applications. Sapphire substrates were used for their high thermal conductivity and low microwave loss. They used a mender shaped YBCO thin films of 300 nm thickness deposited on 2-inch and 4-inch sapphire substrates by thermal co-evaporation. The basic idea of the resistive fault current limiter was to use the fault current itself to drive the superconductor into the resistive state. The tests were performed on the films using 30 µs dc pulses and 50 Hz dc pulses for 50 ms, hence they exploited the resistive

switching property of superconductor to develop fault current limiters at much lower frequencies.

In 2003, J. C. Booth et. al. reported a microwave power limiter using a self-attenuating HTS transmission line [16, 17]. It is based on reversibly driving a coplanar waveguide (CPW) transmission line from the low-loss superconducting state to the high-loss normal state when the microwave currents. This transition takes place when the microwave currents within the device exceed a critical value. The 50 Ω CPW transmission line section made from high-$T_c$ superconductor YBCO offers extremely low conductor loss (<0.1 dB attenuation at 40 GHz) and high bandwidth (>40 GHz) in the superconducting state (signal-pass state), but significantly attenuates the microwave signal in the resistive normal state (signal block state). This power limiter demonstrates a reversible limiting operation for continuous wave (CW) signals up to 10 W at 3 GHz, and for 100 µs transient signals up to 100 W as shown in Fig. 2.1. The switching time for this power limiter are demonstrated to be on the order of nanoseconds as shown in Fig. 2.2.

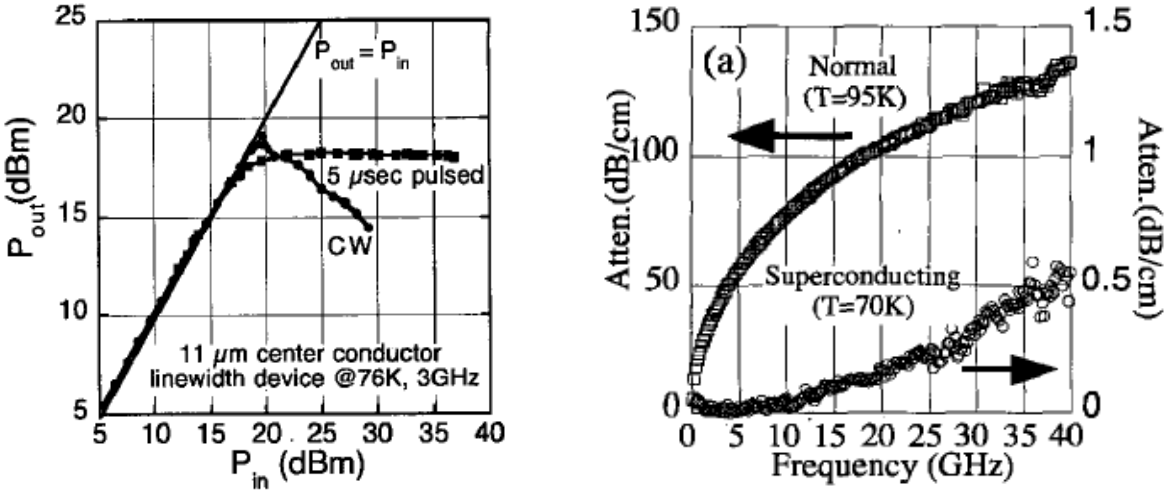
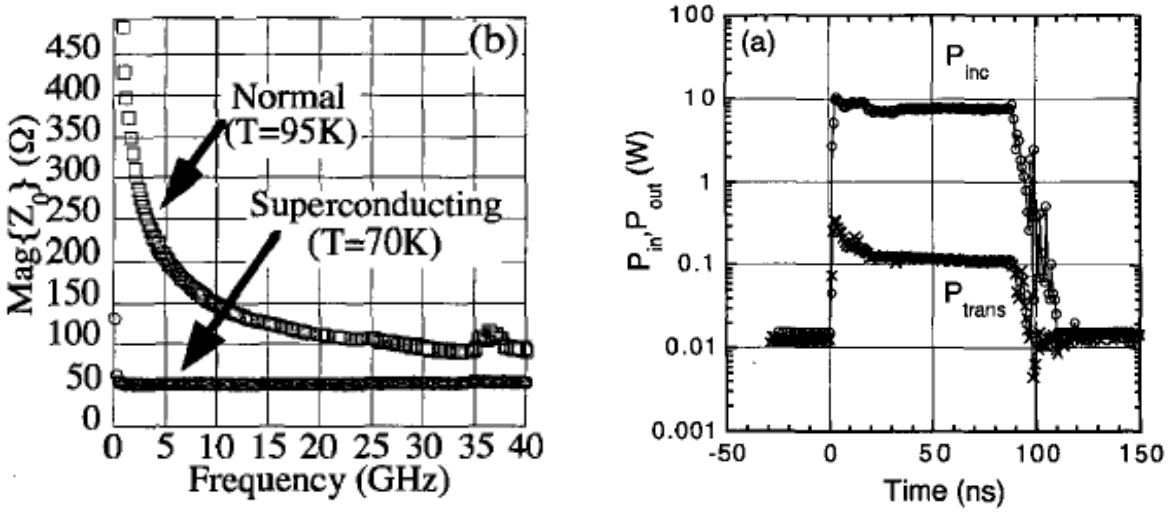


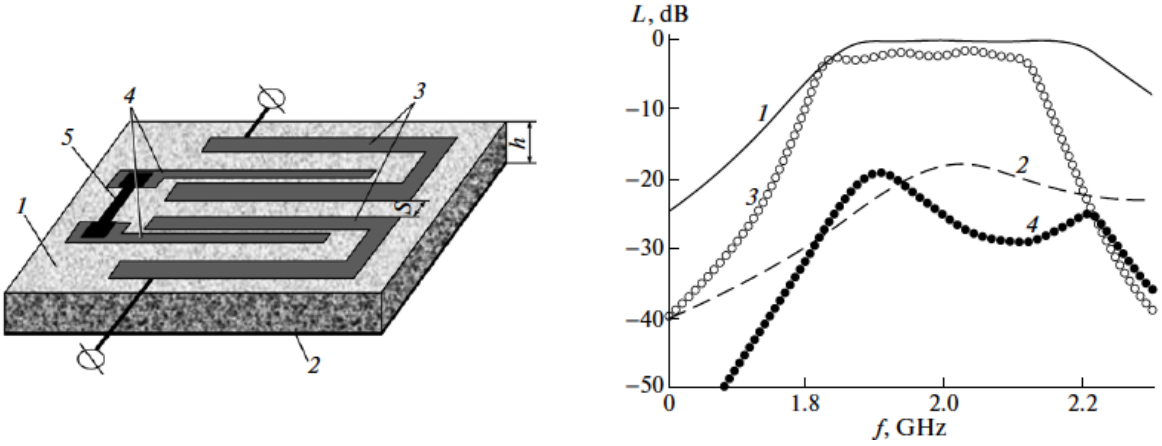

**Figure 2.1:** (**a**) Comparison of power limiting behavior for CW and 5 µs pulsed microwave signals at 3 GHz at 76 K. In the pulsed case, Pout corresponds to the peak power. The solid line shows Pout = Pin, (**b**) Frequency dependence of the attenuation constant in the superconducting ($T$ =70 K) and normal states ($T$ =95 K). [16]

B. A. Belyaev et. al. reported a receiver protecting device based on a HTS microstrip structure [18]. The device as shown in Fig. 2.3(a) represents essentially a three-unit



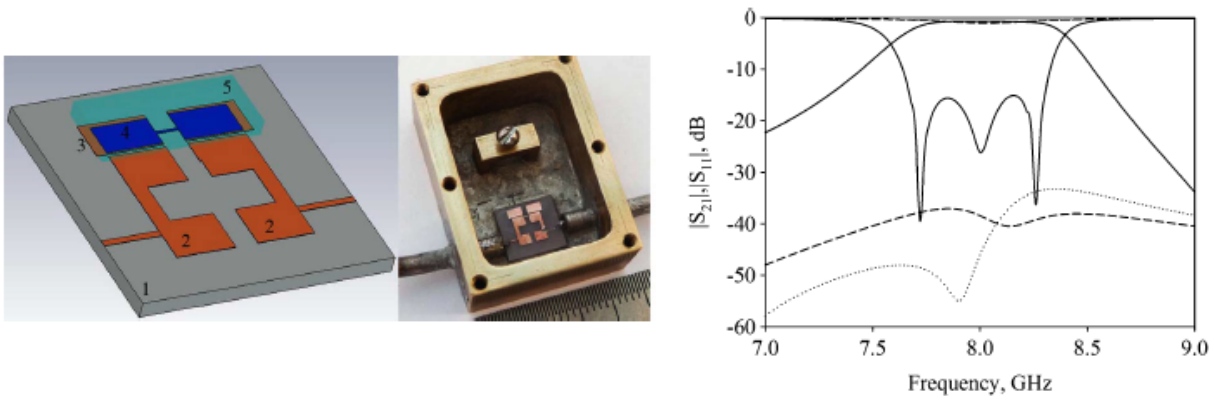

(a) (b)

**Figure 2.2:** (**a**) Frequency dependence of the characteristic impedance of the transmission line limiter in the superconducting and normal states, (**b**) Incident and transmitted signal magnitudes for a power limiter at 76 K for a 100 ns wide pulse. [16]




(a) (b)

**Figure 2.3:** (**a**) Schematic diagram of the power limiting device: (1) substrate; (2) grounded base; (3) strip conductors of side resonators with compensated coupling; (4) strip conductors of the central composite resonator; (5) film conductor of HTS element, (**b**) Amplitude-frequency characteristics of the device in cases when the HTS element occurs in the (1,3) superconducting and (2,4) normal state. (1,2) are the results of numerical simulation while (3,4) is experimental data. [18]




(**a**) (**b**)

**Figure 2.4:** (**a**) Design of the microstrip reflective power limiter with (1) dielectric substrate; (2) copper external resonator; (3) copper parts of the internal resonator; (4) HTS element; (5) $NdGaO_3$ substrate; also a photograph of the device's experimental realization is shown, (**b**) Frequency response of the power limiter in the open state (solid line), the closed state (dashed line) and in the absence of internal resonator and HTS element (dotted line). [19]

microstrip filter. Conductors of the identical input and output hairpin shaped resonators are made of a normal metal, copper. The central composite resonator also has a hairpin shape and is made of copper, but with a cut in the central part that is shunted by an HTS film element made of YBCO on a $NdGaO_3$ substrate. In the event of low-power input signals, the HTS element is in the superconducting state and the central resonator couples the outer pair of non-interacting microstrip resonators in the working frequency band. Under the action of an electromagnetic pulse with the power above a certain threshold, the HTS film element passes from the superconducting to normal state, the $Q$-factor of the inner resonator falls, thus breaking the coupling between outer resonators. This results in the power limitation at the device output due to a strong signal reflection from the input as shown in Fig. 2.3(b).

Another similar design of a power limiter consisting of three resonators with a small HTS element in the central resonator as shown in Fig. 2.4(a) is reported in [19]. The operating frequency of the device is 8 GHz with 8.5% fractional bandwidth. This device remains operable up to 40 W of input power, providing 38 dB limitation.

The spatial distribution of the temperature rise across an HTS transmission line when the current density crosses a critical level is simulated by E. Rocas et. al. using both electromagnetic and thermal modeling [20]. An iterative technique was used that combines the Weeks-Sheen method [21, 22] to calculate the current-density

distribution with a finite-element method to calculate temperature rise at each point of the transmission line. When the critical current density is exceeded, cooper pair breaking begins to occur, and the material starts losing its superconducting properties. This implies higher losses, and therefore higher dissipation, which produce a temperature rise, which in turn increases the fraction of carriers in the normal state. These transient effects end when electrothermal equilibrium is reached. This current-density dependence of superconductor material properties has been exploited to develop power limiters based on HTS materials [16–18, 20].

Both electromagnetic and thermal simulations are coupled and solved concurrently by an iterative convergence algorithm, where the dissipated power is used as input to the thermal-domain simulation, and the obtained temperature rise is used to change the material properties in the electromagnetic domain simulation. Fig. 2.5(a) shows the current density distribution obtained for the cross section of a CPW transmission line. The electro-thermal model developed is used to compare the performance of a CPW power limiter on two different substrates, sapphire and quartz, to demonstrate the impact of the thermal properties on the limiter performance. If the reference temperature is fixed at 83 K, a temperature increment of 7 K implies reaching the critical temperature of 90 K. Hence, the 7 K temperature increment sets the upper power threshold for fast-switching behavior between the limiting and the superconducting state. Fig. 2.5(b) shows the power threshold for achieving the switching behavior; the upper threshold is around 35 dBm for the sapphire sample and 22 dBm for the quartz sample.

### 2.2.2 Semiconductor Limiters using PIN/Schottky Diodes

A number of different PIN diode limiter circuit configurations are commonly used for power limiting purposes [23]. As shown in Fig. 2.6, they are broadly categorized as normal, anti-parallel, stacking and negative bias configuration based on the way the PIN/Schottky diodes are arranged in the circuit to achieve the desired functionality.

A simple, passive receiver-protection limiter comprises a PIN diode and an RF choke inductor connected in shunt with the main signal path[23]. In most limiter circuits, the input and output of the circuit include DC blocking capacitors as shown in Fig. 2.7(a). The single-stage limiter can typically reduce the amplitude of a large input signal by 20 dB to 30 dB. The PIN-limiter diode functions as an incident- power-controlled variable resistor. Without a large input signal, the impedance of the limiter diode is at its maximum, resulting in insertion loss of typically less than 0.5 dB. The choke serves

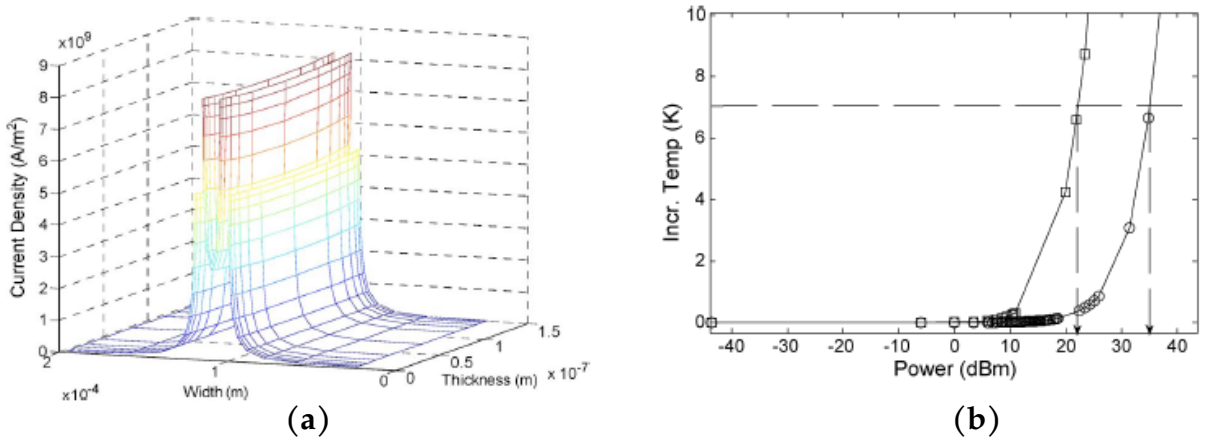



**Figure 2.5:** (**a**) Current density in a CPW with a 10 µm wide center strip and a 5 µm gap. The HTS film is 150 nm thick, the ground planes are 100 µm wide, and the input power is 0 dBm, (**b**) Temperature rise and upper power threshold in two different samples made of a sapphire substrate and a quartz substrate. [20]

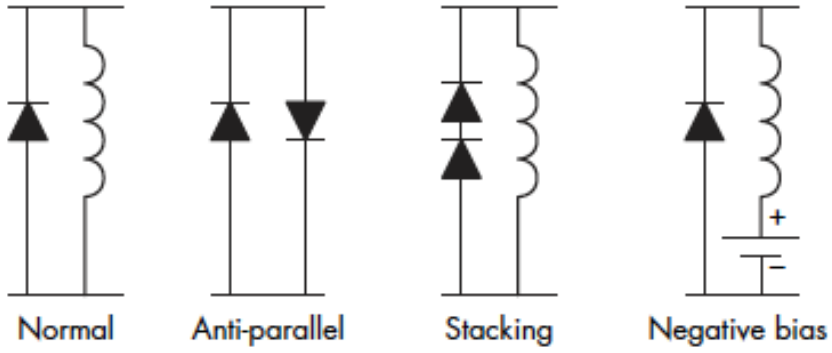



**Figure 2.6:** Different popular configurations for PIN diode limiter. [23]

as the DC return in the diode's RF detector role. In the absence of a signal, the choke also discharges the charge stored in the diode and the DC blocking capacitors. Any large input signal temporarily forces the impedance of the diode to a much lower value, producing an impedance mismatch that reflects most of the input signal power back toward its source. Above the threshold, the transfer function of the limiter shows an increasing insertion loss as signal amplitude increases until the diode is forced to its minimum impedance as shown in Fig. 2.7(b).

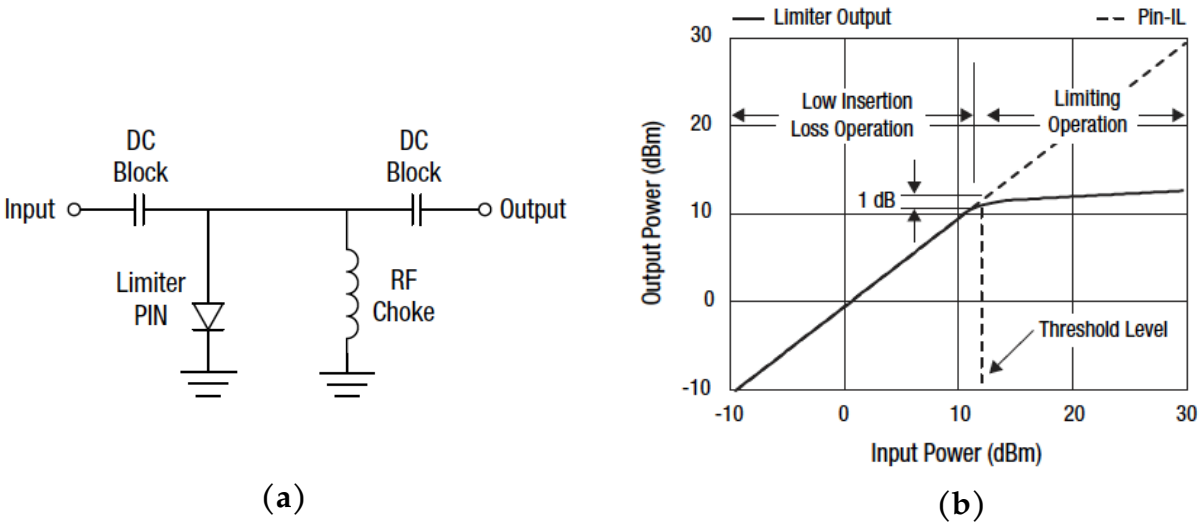



**Figure 2.7:** (**a**) A single stage limiter using PIN diode, (**b**) Output power vs Input power for a single-stage limiter.[23]

A high RF signal level forces the series resistance of the limiter PIN to its minimum value. If the input-signal amplitude increases further, the output power from the limiter also increases on a decibel-for-decibel basis, because the finite, nonzero minimum impedance of the diode remains fixed and reaches a saturation resistance value. Consequently, the reflection loss caused by the impedance mismatch also remains constant. The transfer function for a single stage limiter is shown in Fig. 2.8 a). For a practical limiter, the RF currents in the limiter diode operating in its saturated mode can approach or exceed the value that damages the diode, so avoid operating with input signal levels that force the diode into hard saturation. When the large input signal is no longer present, the impedance of the diode reverts from a very low value to its maximum value after a brief delay elapses. The sensitivity of the receiver is temporarily degraded during this interval, since any signals that might arrive during this interval would be attenuated by the mismatch loss of the diode's very low

impedance.

This limiter circuit can be extended to multistage by using multiple cascaded diodes separated by one-quarter wavelength, $\lambda/4$ as shown in Fig. 2.8 b). The limiter diode at the input, often called "coarse limiter", has a thicker I layer. The limiter PIN diode at the output, referred to as "clean-up stage", is the diode with thinner I layer, selected so that the threshold level of the circuit is low enough to protect the remainder of the receiver components.

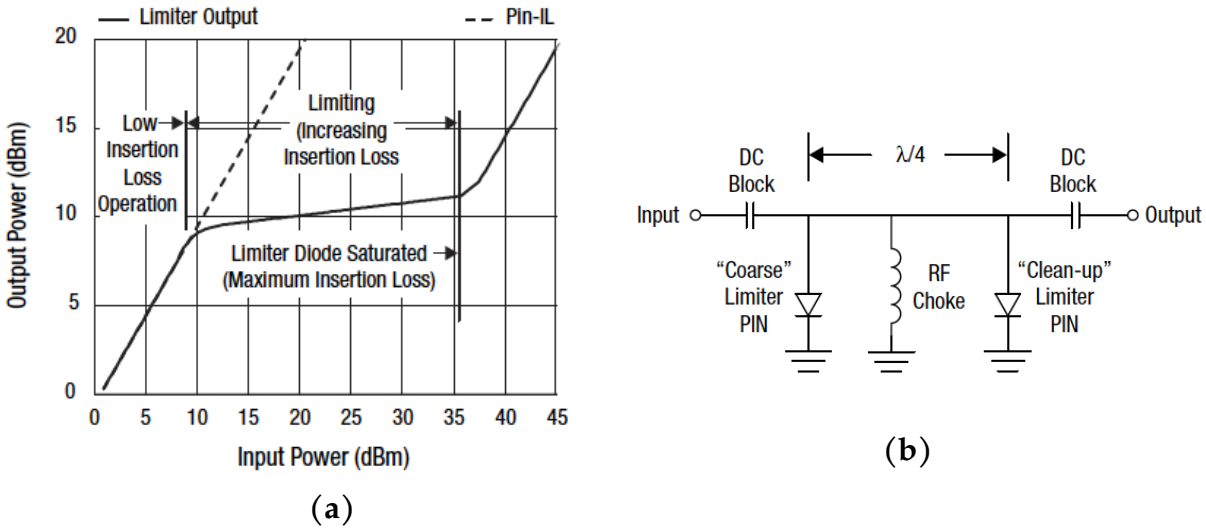



**Figure 2.8:** (**a**) Power transfer function for a Single-stage limiter, (**b**) Two-stage limiter using PIN diodes.[23]

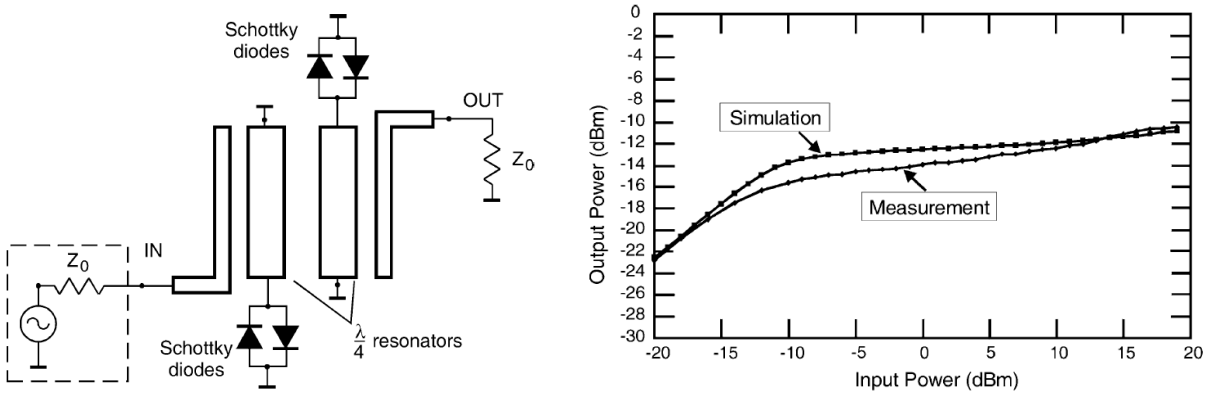
Another popular diode limiter configuration is the anti-parallel configuration. Since the even-order distortion generated by each diode will have opposite polarities, self-cancellation will occur to the extent that the diodes are matched. Using the anti-parallel configuration has an added bonus that it does not need a choke for the DC return. Coupled resonant circuits containing nonlinear elements can be used as microwave power limiters [24]. A nonlinear conductance placed inside the resonant circuit results in an amplitude-dependence of the resonator equivalent conductance and the coupling factor between the resonator and an external circuit. Hence, the transmission of the resonance circuit depends on the input signal power. The appropriate design and optimization allow to combine this effect with the nonlinear conductance large-signal characteristic, which allows to obtain limitation of power transmitted through the set of coupled resonators. The coupling of the resonator and

the external circuits transforms the input signal amplitude applied to the nonlinear element. The nonlinear element used here is an anti-parallel pair of Schottky diodes as shown in Fig. 2.9.

A third diode limiter configuration, the stacked configuration, reduces the overall capacitance because the two diodes are connected in series. Hence, the stacking has also been successfully used to reduce distortion in attenuator and limiter circuits [25].

Vertical GaAs PIN diodes have been available in MMIC circuits since their introduction in 1987. They have been used in building attenuator circuits, single-stage and multiple-stage limiter circuits (Fig. 2.10 a) [27]. A practical single-stage limiter can hardly realize constant output power; hence, multistage limiters are usually used to reduce the flat leakage power if needed. If the peak power-handling requirement is extreme, a stacked diodes may be used to achieve the desired bandwidth. Fig. 2.10 a) shows a schematic of a limiter with 6 PIN diodes, and its measured power limiting is shown in Fig. 2.10 b). Fig. 2.11 a) shows a schematic of the limiter with 8 PIN diodes and its limiting performance is shown in Fig. 2.11 b).

An implementation of the stacked antiparallel configuration is presented by S. Deng et.al. [26] as shown in Fig. 2.12. The circuit consists of two PIN diodes and two zener diodes with the cathodes of the PIN diode and zener diode connected. The configuration can be approximately equivalent to the reverse-biased anti-parallel




(a) (b)

**Figure 2.9:** (**a**) A microwave two-stage limiter circuit composed of two coupled $\lambda/4$ microstrip resonators loaded by anti-parallel pairs of Schottky diodes, (**b**) Simulated and measured characteristics of output power versus input power of the microwave limiter at center frequency of 2.87 GHz. [24]

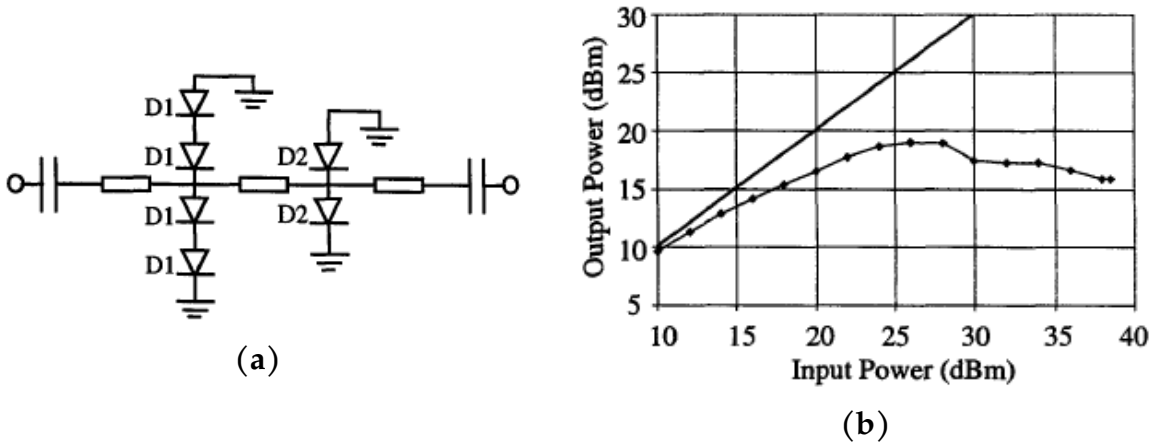



**Figure 2.10:** (**a**) Schematic of a two-stage limiter design using 6 PIN diodes , (**b**) Measured limiting provided by two-stage limiter circuit. [25]

circuit, where the reverse-biased voltage equals to the zener voltage of the stacked zener diode. By varying the zener voltage which can be more easily fabricated, limiters for protecting ADCs with any threshold can be realized theoretically and exhibit excellent second harmonic cancellation because of anti-parallel configuration as shown in Fig. 2.13.

Reverse-bias techniques have been shown to reduce distortion in PIN diode switches and the mechanism is attributed to the negative bias preventing RF rectification.

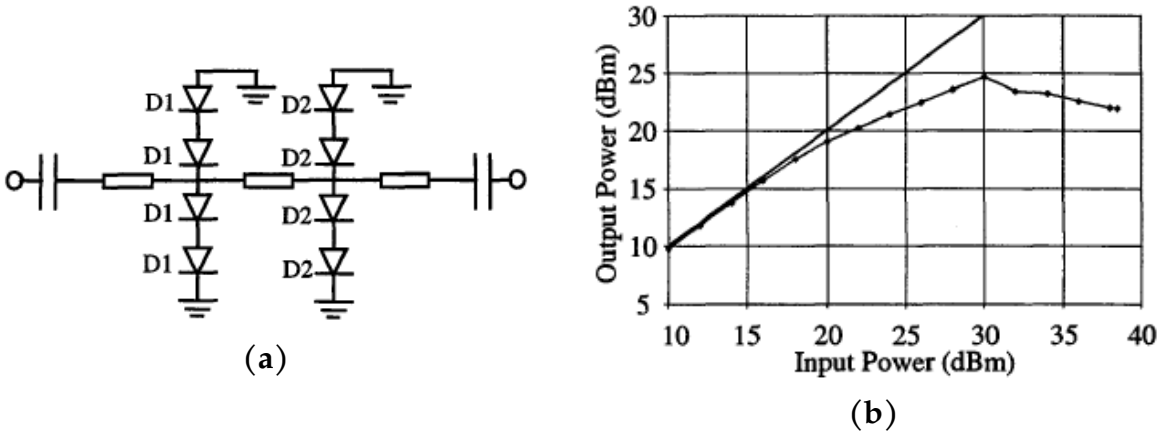
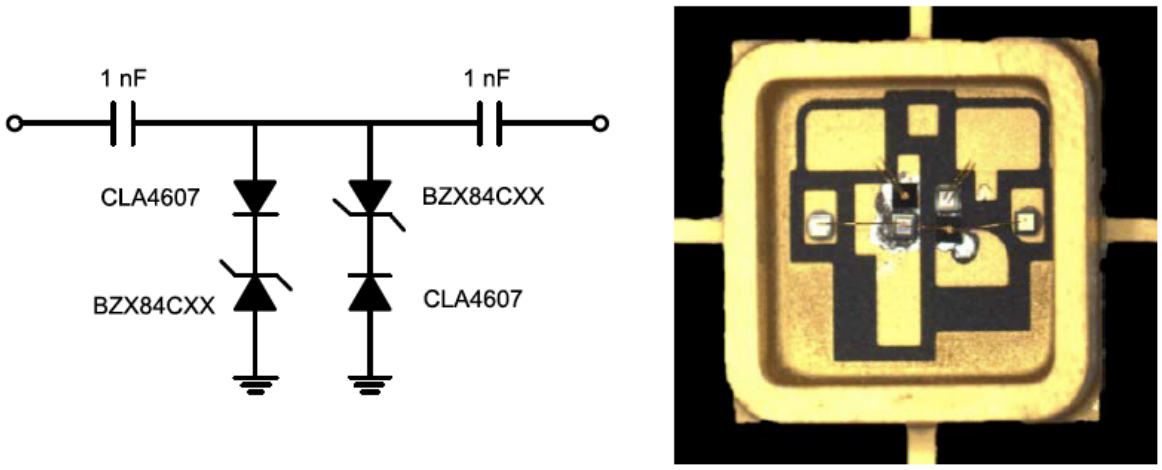



**Figure 2.11:** (**a**) Schematic of a two-stage limiter design using 8 PIN diodes , (**b**) Measured limiting characteristics of the circuit. [25]

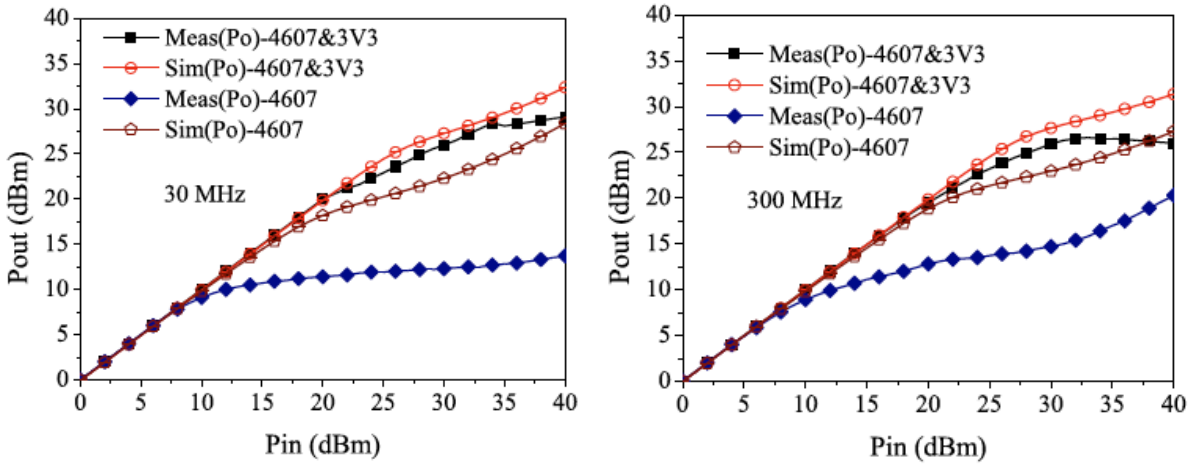



(a) (b)

**Figure 2.12:** (**a**) Circuit for the simulation of stacked antiparallel configuration, (**b**) Image of the fabricated limiter. [26]

Reverse-bias techniques also widen the diode's depletion zone. It is conceivable that the reduced junction capacitance is partly responsible for the improvement in linearity.

Limiters based on diodes are less compact and their current consumption can be tens




(a) (b)

**Figure 2.13:** (**a**) Input power versus output power at 30 MHz, (**b**) Input power versus output power at 300 MHz. [26]

of milliamperes (mA) with significant insertion loss.

### 2.2.3 RF-MEMS Based Power Limiters

The concept of RF-MEMS based limiter has been studied by some research groups considering the well-known self-actuation of RF-MEMS in the case of shunt switches [28, 29]. The advantages of using MEMS switches for power limiter applications include linearity, low power consumption, high isolation and very low insertion loss. J. R. Reid et al. provide an analytical calculation of microwave actuation for shunt capacitive MEMS switches [30]. They studied that the RF actuation of the switch depends not only on the effective RMS voltage of the microwave signal, but also on the heating of the switch due to dissipated microwave power. Hence, the thermal heating of the bridge in the shunt type capacitive MEMS switch further lowers the pull-in voltage of the switch. Fig. 2.14 shows the concept of self-actuation in RF-MEMS [28, 30].

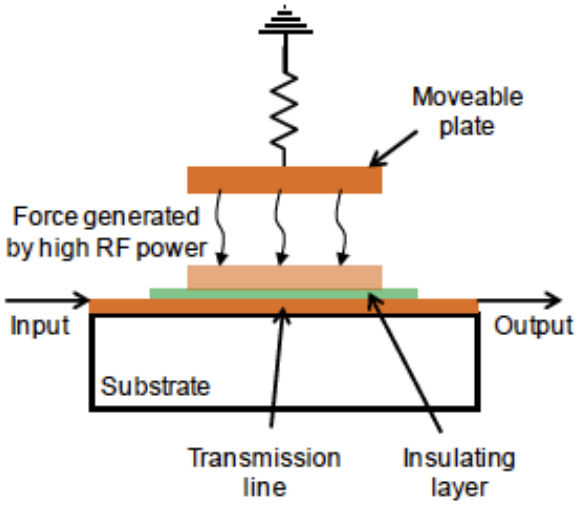



**Figure 2.14:** Cross section of a shunt capacitive RF MEMS switch displaying the self-actuation phenomenon used for power limiting. [28]

J. Gauvin et al. have developed a 10.24 GHz microwave power limiter with adjustable threshold power and high dynamic limiting range using RF self-actuation phenomenon in MEMS switches [28]. A MEMS power limiter using a single shunt RF-MEMS capacitive switch is shown in Fig. 2.15(a). It consists of a 0.8 µm thick

electroplated gold plate suspended 0.3 μm above an insulating layer of aluminum nitride (AlN) patterned on the signal line of CPW. The device offers a dynamic range of 3.4 dBm to 28.1 dBm threshold power with an insertion loss of 0.2 dB.

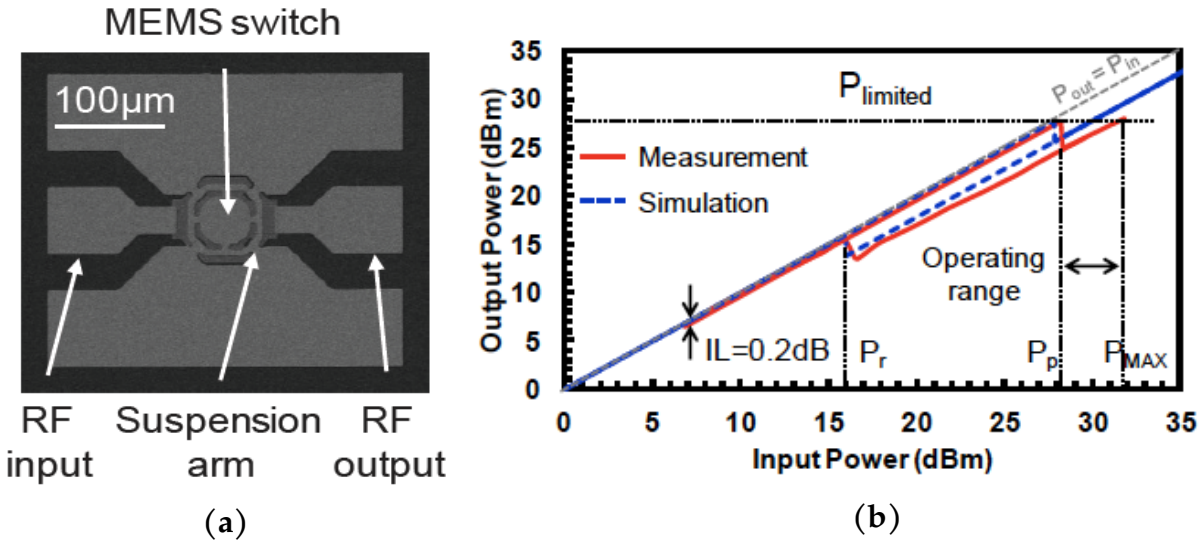
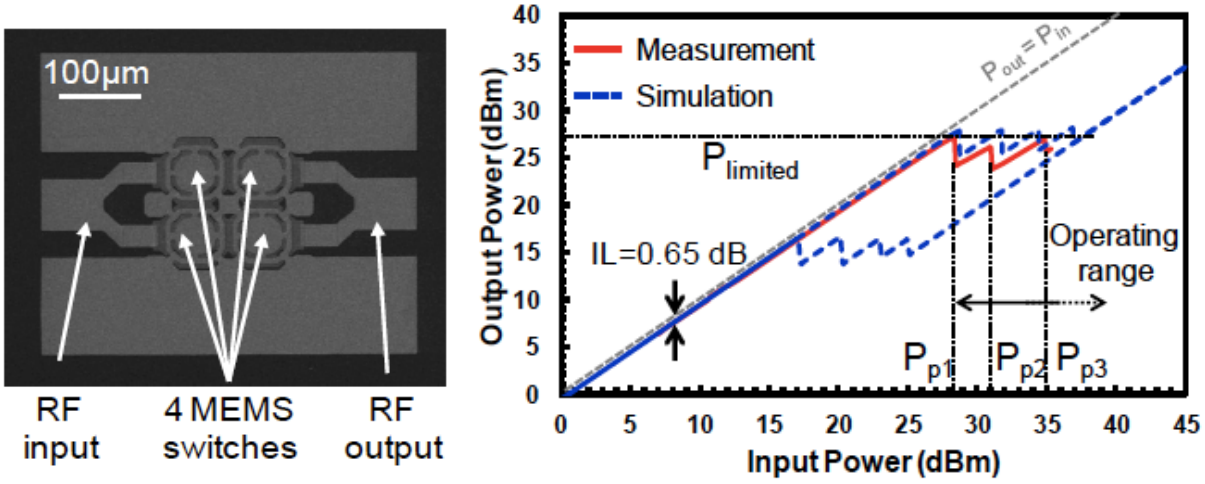



**Figure 2.15:** (**a**) SEM picture of a RF-MEMS based power limiter developed using single shunt switch, (**b**) Computed and measured input/output power characteristics of the limiter at 10.24 GHz. [28]

To increase the operating range, another design of a MEMS power limiter using an array of four MEMS switches is shown in Fig. 2.16(a). The first MEMS actuates at input power 28.2 dBm, attenuating the output power by 3 dB. The output power then starts increasing until the second MEMS actuates at an input power of 31.1 dBm. This phenomenon repeats as shown in Fig. 2.15(b) and the device offers a 27.5 dBm limited output power and a dynamic range of more than 8 dB.

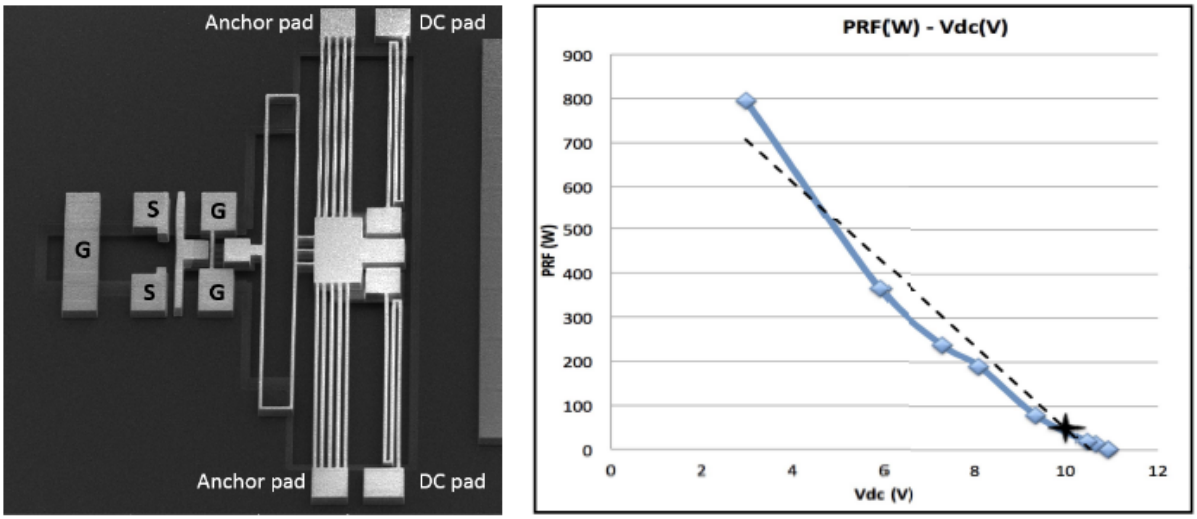
Biasing the MEMS switches allows further decreasing the threshold power. Providing a DC bias of 5.2 V to the MEMS switches lowers the threshold power of the limiter to 14.1 dBm with a dynamic range better than 13 dB, while limiting the output power at 13.8 dBm. Providing a DC bias voltage reduces the gap between the suspended metal bridge and the signal line, which in turn reduces the RF power level at which the switch self-actuates. The only disadvantage of providing the DC bias is the increase in insertion loss of the switch from 0.65 dB to 1 dB.

Not only the capacitive shunt switches, but thermally actuated lateral RF MEMS switches have also been investigated for power limiter applications [31]. Thermally




(a) (b)

**Figure 2.16:** (**a**) SEM picture of an array of RF MEMS shunt switches used as a power limiter, (**b**) Computed and measured input/output power characteristics of the limiter at 10.24 GHz. [28]




(a) (b)

**Figure 2.17:** (**a**) SEM picture of the fabricated thermally actuated switch, (**b**) Power level at which switch actuates vs applied dc actuation voltage. [31]

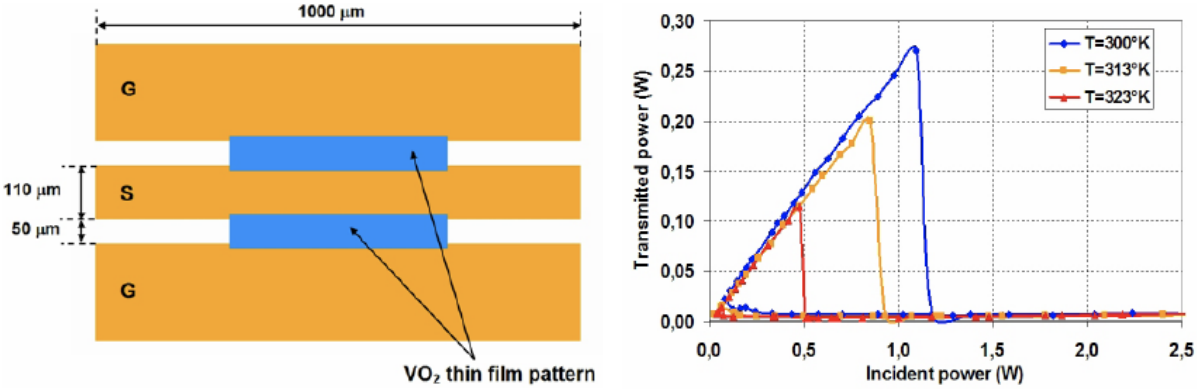
actuated MEMS switches offer improved device sensitivity when used in power limiter applications in comparison with the electrostatically actuated MEMS switches. Fig. 2.17(a) shows a SEM picture of the thermally actuated MEMS switch.

The level of power at which the switch actuates can be varied by controlling the applied dc actuation voltage as shown in Fig. 2.17(b). A DC voltage of 11 V is enough for chevron to push forward the contact plate such that it forms a contact with the signal line and turns the switch-ON. However, to operate the switch in the power limiting region, a voltage less than 11 V is applied such that the contact plate moves sufficiently close to the signal line but does not form the contact. When a high RF power is applied to the signal line, the switch self-actuates. For example, for 10 V applied to the chevron, a RF power of 35 W (45.4 dBm) is sufficient for switch to self-actuate.

### 2.2.4 Vanadium Dioxide Based Power Limiters

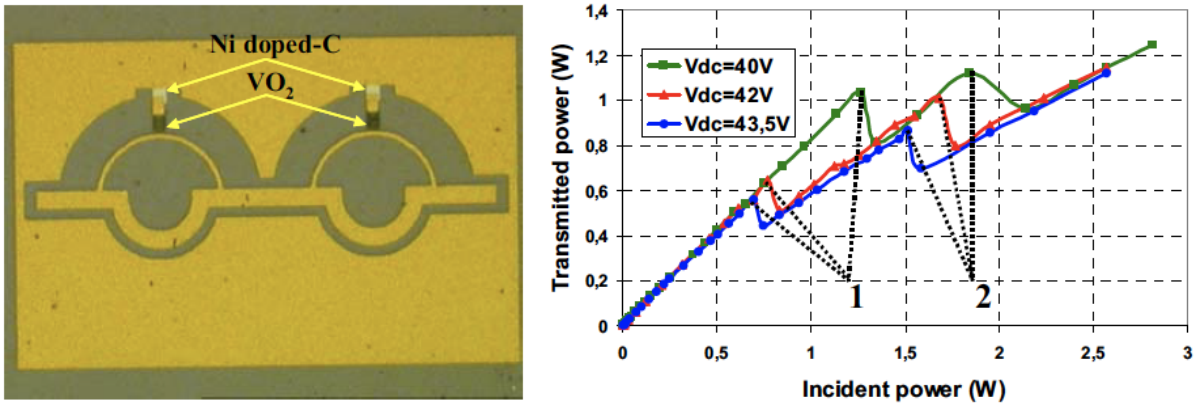
Another approach used to develop microwave power limiting devices is based on reversible semiconductor-to-metal transition of vanadium dioxide thin films integrated on CPW transmission lines [32]. $VO_2$ thin films are patterned on the CPW line such that they fill the gap between the signal line and the ground lines as shown in Fig. 2.18(a). At low microwave power levels and room temperature, the $VO_2$ is in its semi-conducting state with a high resistivity and allows the signal to pass through the line with almost no attenuation ($<$0.7 dB from 100 MHz to 40 GHz). When the incoming RF power level exceeds a threshold value, the $VO_2$ layer undergoes a phase transition to its low-resistive metallic state and the RF signal is shunted to the ground and highly attenuated. $VO_2$ layers are capable of sustaining CW RF power levels as high as 10W, hence can be used for protection against very high RF power levels. The device threshold power can be further lowered by providing an external temperature because lower input RF power is then needed to reach the transition temperature of $VO_2$ as shown in Fig. 2.18(b).

Hence, the device functions as a self-resetting fuse, passing the incoming RF power up to a threshold value and once the value is reached it completely blocks the signal and no power is transmitted to the output. However, another design of a CPW $VO_2$ based power limiter has been reported which allows a relatively constant level of transmitted power even after the transition point [33]. The design involves using two power-dividers and combiners in series configuration with the CPW as show in Fig. 2.19(a). The 50 Ω central linear transmission line is divided into two loops, one thinner 100 Ω branch and another 50 Ω branch. The impedance difference of the two




(a) (b)

**Figure 2.18:** (**a**) Power limiter design consisting of a CPW transmission line with $VO_2$ film patterned in the gaps between the signal line and the ground planes, (**b**) Transmitted vs incident CW microwave power at 10 GHz for a 100 µm-length $VO_2$-based CPW transmission line at different operating temperatures. [32]




(a) (b)

**Figure 2.19:** (**a**) Image of the microwave power limiter based on two dividers using two identical distributed $VO_2$ films and Ni-doped carbon patterns, (**b**) Measurements of the transmitted power versus the incident power at 10 GHz for different DC bias voltages. [33]

branches makes the incident power to be divided in each loop with 1/3 of input power transferring through the 100 Ω branch and the remaining 2/3 of the power passing through the 50 Ω loop. The 100 Ω part of each loop is connected to the ground plane using a $VO_2$ in series with a Ni-doped carbon patterns for insuring the limiting function of the device. When the $VO_2$ is in the semiconducting state, the RF signal is transmitted with small attenuation through the two loops. However, when the RF signal increases beyond the threshold level and the $VO_2$ transitions to the metallic state, 1/3 of the input power is attenuated for each loop as shown in Fig. 2.19(b). Additionally, the trip point of the power limiter can be adjusted by applying a dc bias voltage between the signal line and ground plane.

### 2.2.5 Frequency Selective Power Limiters

Frequency selective limiters (FSL) are non-linear devices that attenuate large radio frequency signals while simultaneously allowing small signals at different frequencies to pass with little change as shown in Fig. 2.20 [34–36]. Frequency selective limiting is a unique feature of ferrite devices and arises from the nonlinear interaction of the spin precession at the signal frequencies, $\omega$, with spin waves at half of the signal, $\omega/2$.

In 1983, S. N. Stitzer reported frequency selective microwave power limiting in thin yttrium-iron-garnet (YIG) films [34]. It is based on the phenomenon that when an RF magnetic field is applied to a ferromagnetic insulator immersed in a static magnetic field, it causes the magnetic dipoles in the crystal to precess at the applied radio frequency [36]. At low levels of the applied RF, the precession angle is proportional to the RF field strength, and the only loss mechanism is the linear damping of the precession angle. At sufficiently high levels of the RF field (above threshold), the precession angle saturates, the coupling becomes nonlinear, and part of the power is coupled through half-frequency spin waves to the crystal lattice, where it is dissipated as heat. However, since the spinwave manifold excited by the strong signal has a relatively narrow bandwidth, low level signals which may be present simultaneously with the strong signal are unaffected by it if they are separated in frequency by more than a few times the spinwave linewidth. The design of such power limiters incorporates a microstrip line coupled continuously to a thin epitaxial YIG film grown on a gadolinium-gallium-garnet (GGG) substrate as shown in Fig. 2.21(a). Measured power limiting data of the YIG power limiter is shown in Fig. 2.21(b) for three different operating frequencies.

Such stripline frequency selective limiters, fabricated using thick YIG films are suitable

for broadband, microwave applications in UHF through S-band (400 MHz to 4 GHz). However, the threshold power levels almost 100 times lower than the stripline designs can be achieved by using scandium-gallium-yttrium-iron-garnet (ScGaYIG) films. A magnetostatic wave limiter with threshold power level $< -20$ dBm, operating in the 400 MHz to 800 MHz has been reported [35]. As shown in Fig. 2.22(a), a YIG film, supported by a GGG substrate is place over microstrip transducers defined on a dielectric substrate. The operating frequency is determined by the magnetic bias field applied parallel to the transducers. Impedance matching circuits are required at the input and output ports to ensure minimum insertion loss. Doping YIG films with scandium and gallium impact the threshold power and power limiting as shown in Fig. 2.22(b).

Reflective-type frequency selective limiters built on single-crystal undoped yttrium iron garnet have also been reported[37]. These are akin to surface acoustic wave devices in that they transduce the energy from the electromagnetic domain into surface waves that have much shorter wavelength than their electromagnetic counterparts. However, in this case, these are magnetostatic surface waves (MSW), and as a result above a critical power level previously referred to as power threshold the energy can no longer be coupled to MSW and is reflected back towards the source. Fig. 2.23 below shows the limiting behavior of the MSW-based device over several frequencies from 998 MHz to 1083 MHz.

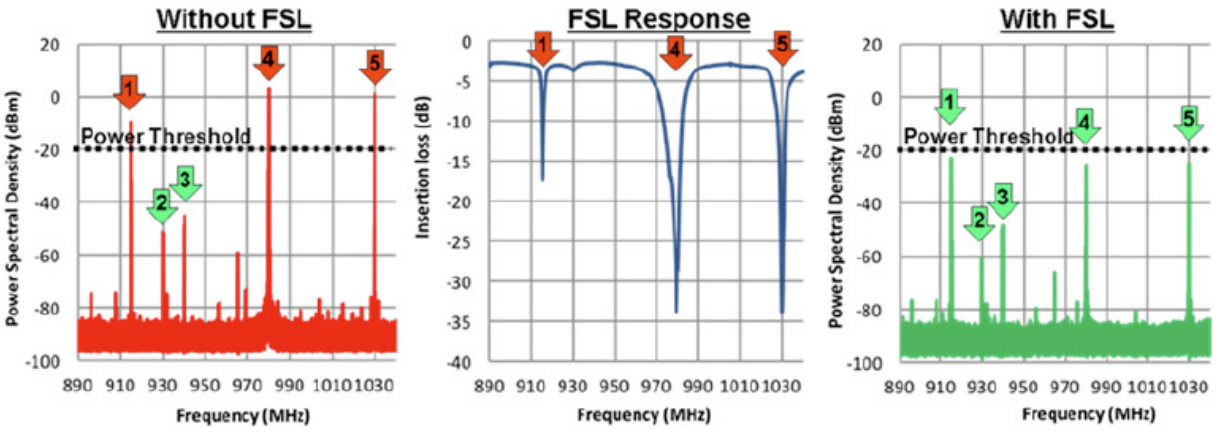
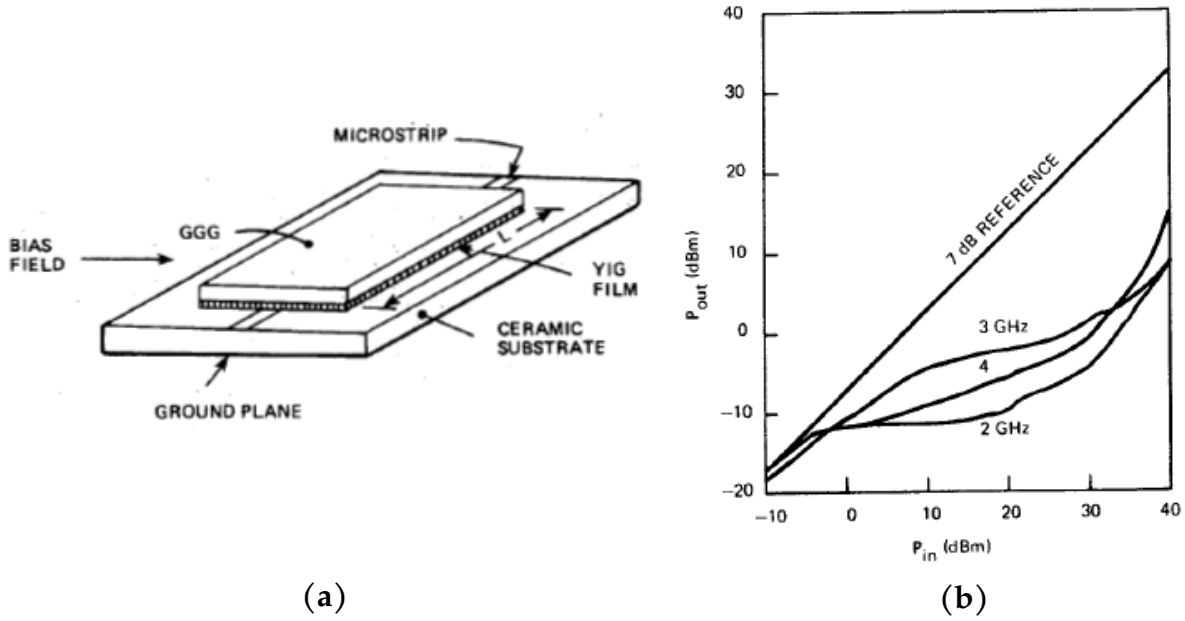



**Figure 2.20:** A spectrum (left) with various above-threshold (1,4,5) and below-threshold (2,3) measured signals. When this spectrum is passed through a frequency selective limiter (FSL), it's response changes to provide selective attenuation of above-threshold signals (middle). Below threshold signals of interest are unaffected (right).[37]

The MSW frequency selective limiters have significantly low threshold power levels ($< -25$ dBm), but magnetostatic waves are long wavelength spin waves that exist only over a limited frequency range (400 MHz to 4 GHz).

Another approach to develop frequency dependent power limiters involves integrating RF MEMS switches with bandpass filters to form a power limiter where the output RF power is limited to specific levels based on the frequency band [38]. The limiter attenuates the high-power signal only within the bandwidth of the integrated filter. As shown in Fig. 2.24(a), the circuit consists of a 90° hybrid coupler at 2.6 GHz with 10 % bandwidth which is coupled to bandpass filters with a center frequency of 2.62 GHz through two Radant RF MEMS SPST switches. The output ports of the bandpass filters are terminated in 50 Ω loads. The dc bias voltage to the MEMS switch is reduced below its actuation voltage (∼76 V) and the input RF power is increased gradually from 0.01 W to 15 W. As the input power level to the limiter circuit reached 12.58 W, a drop in the limiter output power by 8 dB is attained as shown in Fig. 2.24(b).




(a) (b)

**Figure 2.21:** (**a**) Design of the thin film YIG limiter, (**b**) Measured power limiting at different frequencies. [34]

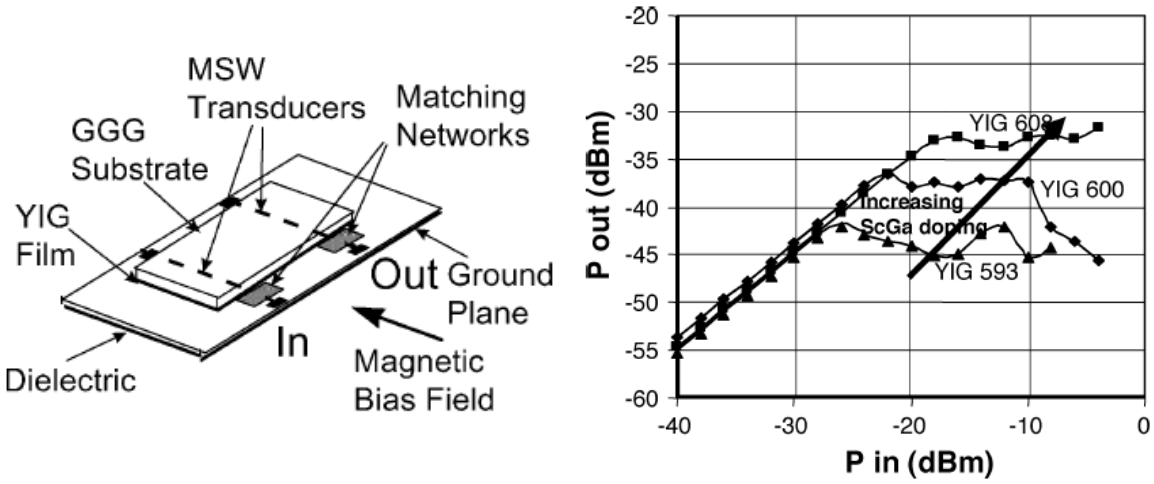



**Figure 2.22:** (**a**) Geometry of magnetostatic wave frequency selective limiter utilizing surface wave propagation for low loss and low threshold, (**b**) Power limiting for three YIG films with different ScGa doping. [35]

## 2.3 Microwave Circulators

For decades, circulators have been built almost exclusively through the magnetic biasing of ferrites [39–41]. These magnetic devices can achieve excellent performance

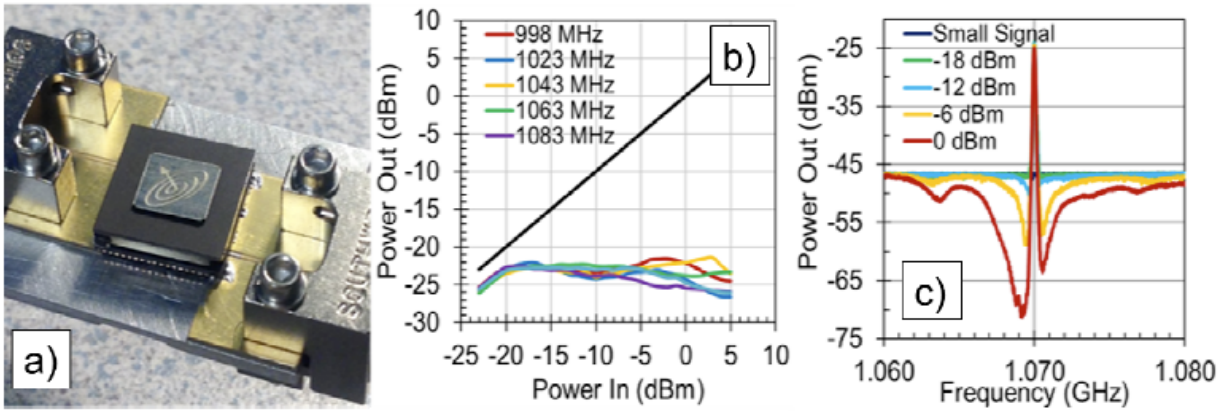
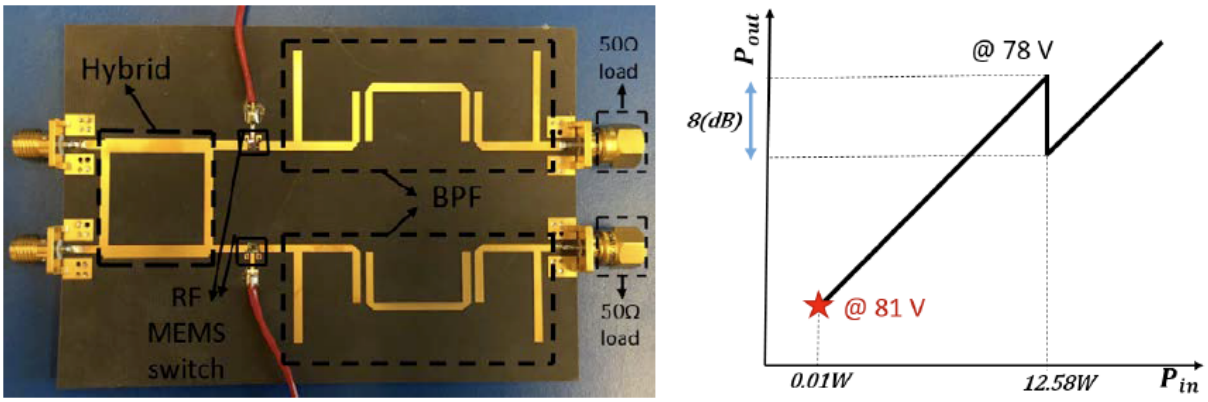



**Figure 2.23:** (**a**)Frequency selective limiter device, (**b**)Measured RF input and output power at L-band, (**c**) Measured output power as a function of frequency. [37]




(a) (b)

**Figure 2.24:** (**a**) Image of the fabricated power limiter using one hybrid coupler, two MEMS switches and two bandpass filters, (**b**) Power characteristics of the limiter. [38]

in terms of isolation, power handling, bandwidth of operation and insertion loss, yet they typically result in bulky, nonintegrable, and expensive devices that may not be suited for various commercial systems or quantum measurement circuits. To overcome these problems, magnet-free implementations of circulators based on active solid-state devices or nonlinear materials with geometric asymmetries have been pursued [42–44]. Despite significant research efforts over many years, these alternative solutions continued to suffer from a fundamentally poor noise figure (NF), nonlinearities and limited power handling. Hence, there is an urgent need of a fully passive magnet-free material that can operate on par, or even outperform magnetic approaches.

Recently, however, it was shown that parametric circuits can overcome these limitations. Soon after the concept of spatiotemporal modulation angular-momentum (STM-AM) was introduced [45], advances in this area have led to the development of circulators that can support metrics of performance comparable to traditional magnetic-biased ferrite devices, while at the same time offering distinct advantages in terms of reduced size, weight, and cost due to the elimination of magnetic bias. In this section, we will discuss the recent developments of STM-AM based circulators.

In [45], Andrea Alu et. al. reported the concept of magnetic-free non-reciprocity and isolation. The scheme is based on the parametric modulation of three identical, strongly and symmetrically coupled resonators as shown in Fig. 2.25(b). The resonant frequencies of the individual tanks are modulated by external signals with the same amplitude and a relative phase difference of 120°, imparting an effective electronic

angular momentum to the system. Individual LC tanks consist of capacitance C equally distributed on both sides of the inductance L as shown in Fig. 2.25(a) and the resonance frequency modulation is achieved by means of capacitance modulation using varactor diodes. The diodes are biased by two signals, a static signal $V_{dc}$, which provides the required reverse bias and controls the static capacitance, and a RF signal $v_m(t)$ providing the time modulation. Fig. 2.25(c) shows a photograph of the fabricated prototype.

Without modulation, the signal is equally split at the two output ports and the system is fully reciprocal as show in Fig. 2.26(a). When the modulation signal is switched on, the symmetry is broken, and power is unequally split. For $V_m = 0.6V$, as can be seen in Fig. 2.26(b), at the resonance frequency of 170 MHz, power incident at ports 1, 2 and 3 is routed to ports 2, 3 and 1, respectively, demonstrating the circulator operation. For comparison, Fig. 2.26(c) shows the S-parameters obtained using full-wave and circuit simulations, which show agreement with the measurement results.

Apart from this arrangement of the LC-tanks, three series or parallel LC tanks can be connected in a loop or to a central node [2], resulting in four single-ended topologies shown in Fig. 2.27. In the absence of any kind of modulation, the tanks resonate at the natural oscillation frequency given by :

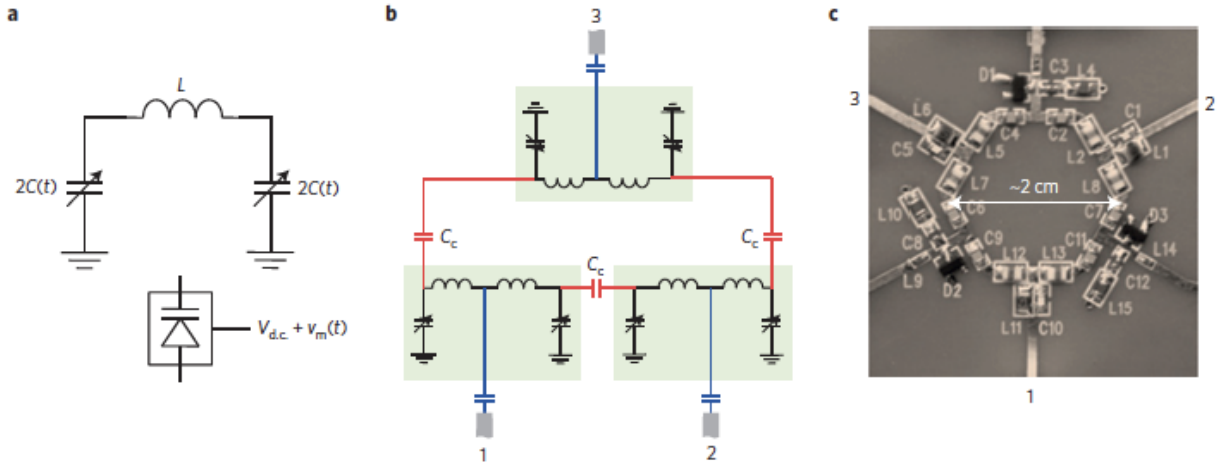



**Figure 2.25:** Circuit implementation of the non-reciprocal coupled-resonator loop at radio frequencies (**a**) A single resonant circuit of the proposed device comprising of an L-C tank with modulated capacitance. Capacitance modulation is achieved with varactor diodes, (**b**) A loop formed by three identical resonators coupled through three identical capacitances, (**c**) Photograph of the fabricated prototype. [45]

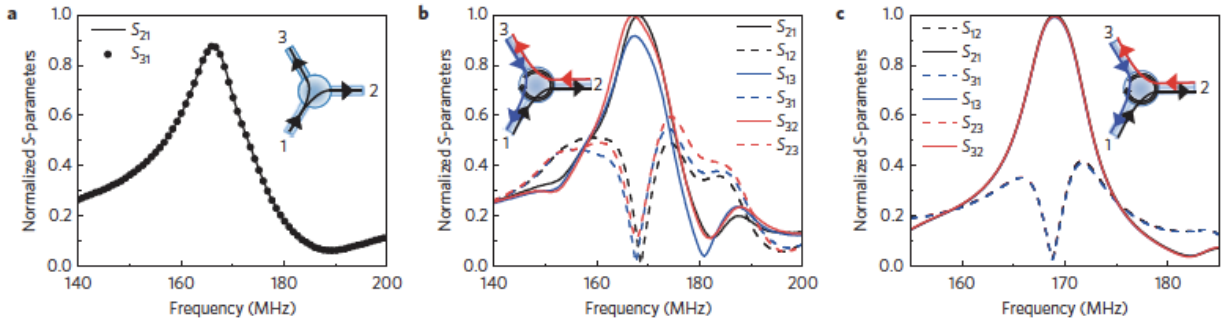



**Figure 2.26:** (**a**) Measured transmission from port 1 to ports 2 and 3 without modulation ($V_m = 0V$). The power is equally split to the output ports, (**b**) Measured scattering parameters when $V_m = 0.6V$. Incident power to ports 1, 2 and 3 is transmitted to ports 2, 3 and 1, respectively, (**c**) Simulated response of the loop for the case when $V_m = 0.6V$. [45]

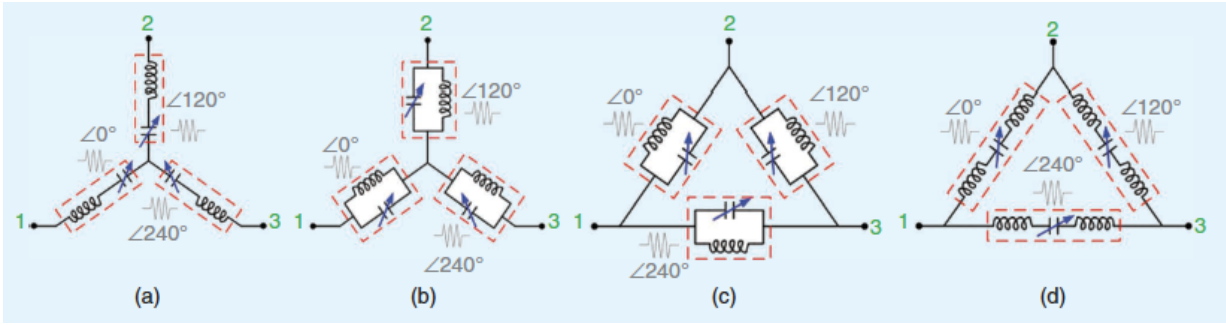



**Figure 2.27:** The single-ended topologies of STM-AM circulators (**a**) Bandpass/wye, (**b**) bandstop/wye, (**c**) bandstop/delta, and (**d**) bandpass/delta.[2]

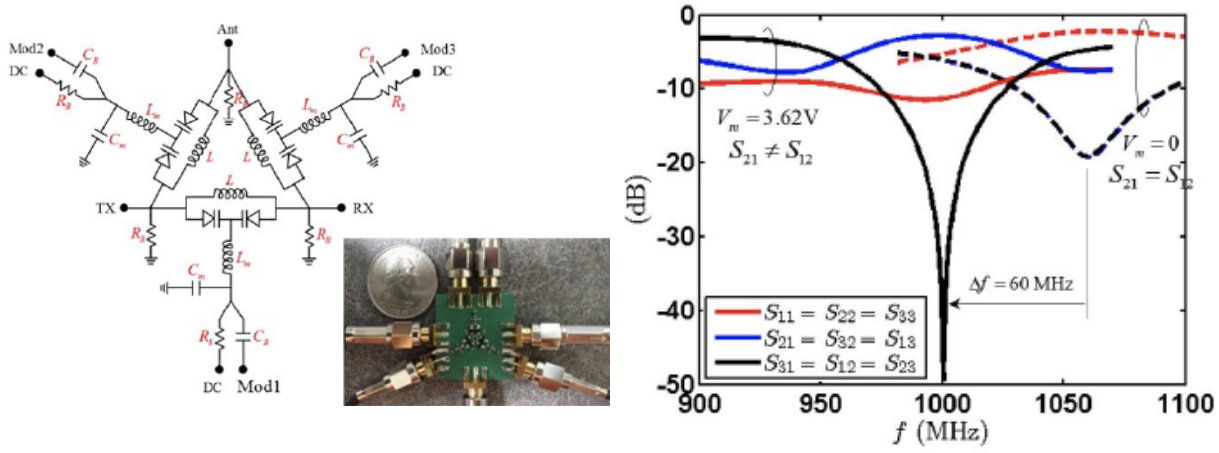
$$f_0 = \frac{1}{2\pi\sqrt{L_0 C_0}}$$

The instantaneous oscillation frequencies of the tanks are spatio-temporally modulated as:

$$f_n = f_0 + \Delta f cos(2\pi f_m t + (n-1)2\pi/3)$$

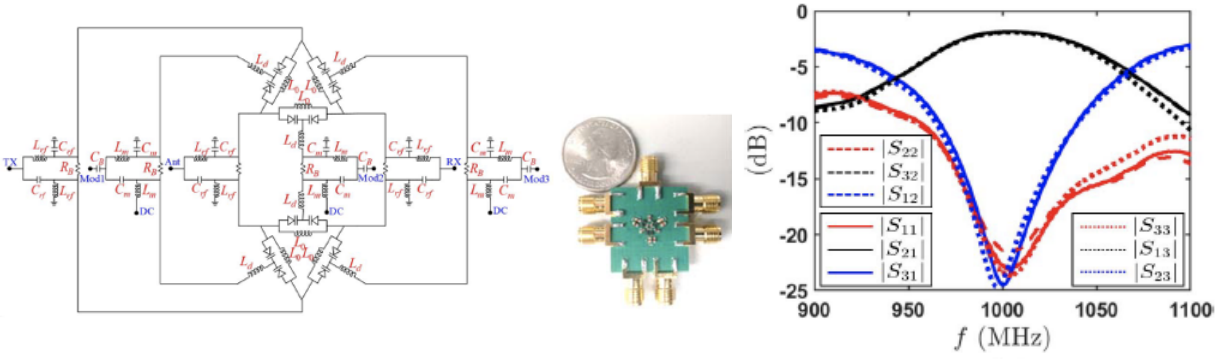
where $\Delta f$ is the modulation depth and $f_m = \omega_m/2\pi$ is the modulation frequency. This modulation scheme generates an effective angular-momentum bias in the clockwise direction. Such biases impart a macroscopic sense of precession to the degenerate modes of opposite handedness, which results into nonreciprocity and isolation.

The bandstop/delta topology displayed in Fig. 2.27(c) was built and tested in [46]. This circuit can also be reconfigured for operation at different channels over a frequency range of 60 MHz by simply changing the dc bias of the varactors. Fig. 2.28(a) shows the complete schematic of the circulator and Fig. 2.28(b) shows the simulated




(a) (b)

**Figure 2.28:** (**a**) Schematic of the magnet-less circulator. Photograph of the fabricated prototype is shown in the inset, (**b**) Simulated S-parameters without modulation (dashed lines) and with modulation (solid lines). [46]




(a) (b)

**Figure 2.29:** (**a**) Schematic of the voltage-mode differential STM circulator and photograph of the fabricated prototype, (**b**) Measured S-parameters. [47]

S-parameters with and without modulation. Without modulation ($V_m = 0$), the circuit is, clearly, reciprocal with the same transfer function seen between the input port (e.g., port 1), and any of the output ports (i.e., $S21 = S31$) and behaves as a bandstop filter. When spatiotemporal modulation is applied with $V_m = 3.62V$, the S-parameters become nonreciprocal. The measured insertion loss, return loss, and isolation at the center frequency of 1 GHz were 3.3 , 10.8 , and 55 dB, respectively, and the measured bandwidth was 2.4 %.

As seen above, single-ended STM-AM circulators can achieve good performance in terms of several metrics, particularly in terms of power handling and noise figure. Nevertheless, these circuits suffer from large Intermodulation products (IMPs) in close proximity to the desired bandwidth resulting from parametric mixing induced by the temporal modulation and from the inevitable nonlinearities associated with its circuit components. This problem was overcome in [47] by combining two single-ended circuits in a differential voltage or current-mode architecture and by maintaining a constant 180° phase difference among their modulation signals, i.e.,

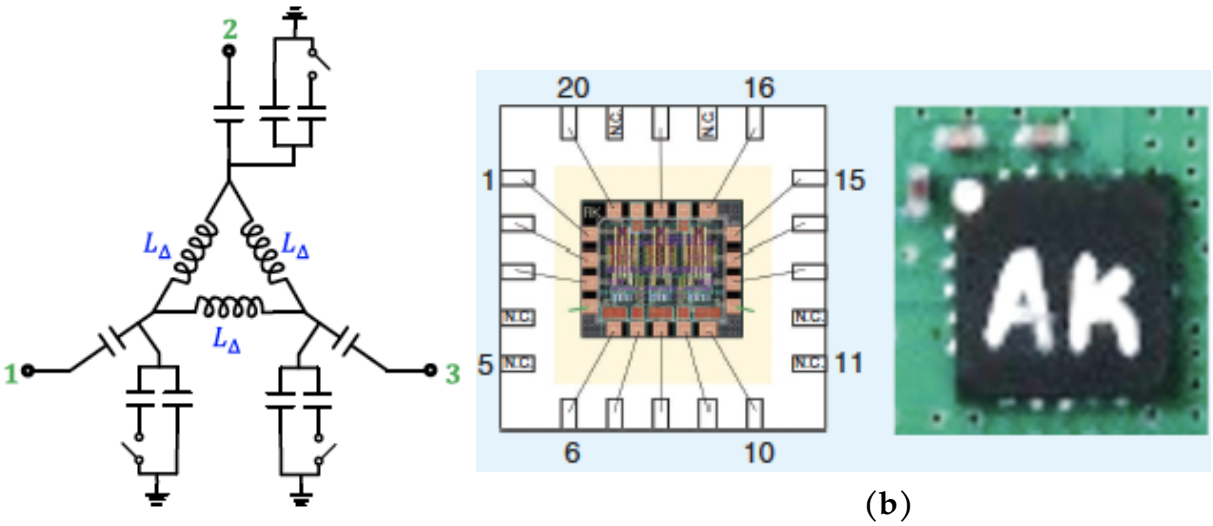
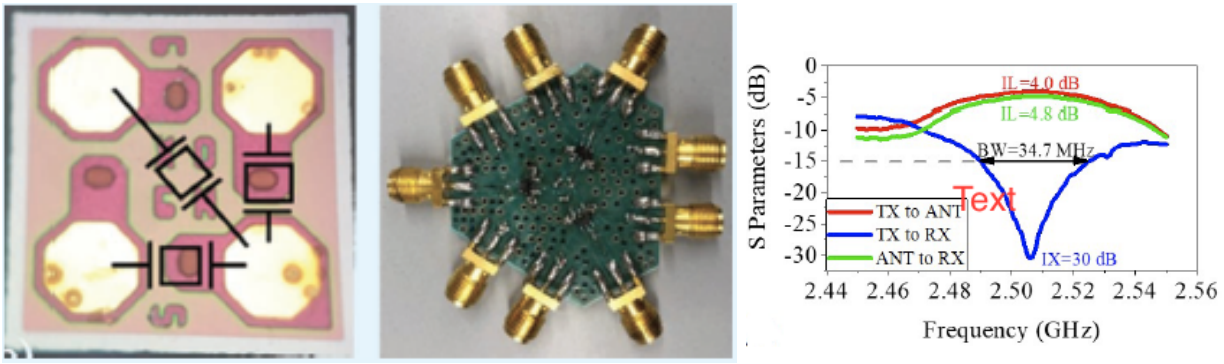



**Figure 2.30:** (**a**) Implementation of the switched capacitors in a modified wye topology where the inductors are transformed into a delta connection, (**b**) Photograph of the chip layout and the packaged chip mounted on a PCB. [48]




(a) (b)

**Figure 2.31:** (**a**) FBAR chip showing the schematic of connection and the designed PCB of the circulator. Three FBARs are monolithically integrated on one chip, (**b**) Measured insertion loss (IL) from TX to ANT and from ANT to RX and measured isolation (IX) from TX to RX. [49]

$$f_{n,\pm} = f_0 \pm \Delta f cos(2\pi f_m t + (n-1)2\pi/3)$$

where $f_{n,+}$ and $f_{n,-}$ are the modulation signals of the two-constituent single-ended circuits. A voltage-mode configuration was built and tested using two of the single-ended bandstop/delta circuits as shown in Fig. 2.29(a). A picture of the fabricated prototype is shown in the inset. The measured insertion loss, return loss, and isolation at the circulator's center frequency of 1 GHz were 1.78 , 23 , and 24 dB, respectively, and the fractional bandwidth was 2.3 % (23 MHz).

All the circuits mentioned above are based on printed circuit board (PCB) prototypes, which, despite outperforming previous works in many metrics, were still limited in size. To overcome this problem and to achieve significant miniaturization, an integrated circuit implementation is highly desirable. Toward this goal, Kord et. al. [48] modified the bandpass/wye topology to be compatible with CMOS technologies and experimentally validated the resulting circuit in a current-mode architecture using a 180 nm process. The modulated capacitors were implemented using switched capacitors as shown in Fig. 2.30(a), which resulted in a larger modulation index than varactors, alleviated the tradeoff between the index and the $Q$-factor, and permitted the use of digital clocks which can be easily integrated on chip. Fig. 2.30b) displays photos of the fabricated chip and the testing board. The measured

return loss, insertion loss, and isolation at the center frequency of 910 MHz were roughly 12 , 4.9 , and 60 dB, respectively.

Although a CMOS implementation of STM-AM circulators did significantly reduce the size compared to a PCB design, extreme miniaturization is still limited by the fact that on-chip inductors consume a large silicon area and exhibit low $Q$-factors. This problem can be overcome by using micromachined integrated devices, such as MEMS resonators. Such devices can exhibit a series resonance with a very high $Q$-factor, which mimics the response of a series LC tank while being much smaller in size. Yu et. al. [49] presented the first MEMS implementation of STM-AM circulators as shown in Fig. 3.10(a). If port 1, 2, and 3 are connected to receiver RX, transmitter TX, and antenna ANT, the insertion loss of signal transmission from ANT to RX and from TX to ANT and the isolation between TX and RX, which are the most important metrics in full-duplex operation are shown in Fig. 3.10(b). The measured return loss, insertion loss, and isolation at the center frequency of 2.5 GHz were roughly 15 , 4, and 30 dB, respectively with a bandwidth of 34.7 MHz.

# Chapter 3

# rf-SQUIDs and Cryogenic Microwave Phase Shifter

## 3.1 Introduction to Josephson Junctions and rf-SQUIDs

### 3.1.1 Flux Quantization in a Superconducting Loop

First predicted by F. London [50], flux quantization was observed experimentally by Deaver and Fairbank [51] and Doll and Näbauer [52] in 1961. They showed that the flux contained in a closed superconducting loop is quantized in units of the flux quantum

$$\Phi_0 = \mathrm{h}/2\mathrm{e} \qquad \approx 2.07 \times 10^{-15}\,\mathrm{Wb} \tag{3.1}$$

where, $\mathrm{h} \equiv 2\pi\hbar$ is the Planck's constant, and e is the electronic charge.

Flux quantization arises from the fact that the macroscopic wave function given by

$$\Psi(\vec{\mathbf{r}}, t) = \left|\Psi(\vec{\mathbf{r}}, t)\right| \exp\left[i\theta(\vec{\mathbf{r}}, t)\right] \tag{3.2}$$

must be single valued in going once around a superconducting loop. In the absence of the applied fields or currents, the phase $\theta(\vec{\mathbf{r}}, t)$ takes the same value throughout the superconductor for all Cooper pairs, which have charge 2e. In the case of a loop threaded by a magnetic flux, however, the phase around a loop changes by $2\pi n$, where n is the number of enclosed flux quanta.

### 3.1.2 Josephson Junctions

In 1962, B. Josephson provided a theoretical prediction of quantum mechanical tunneling of cooper pairs between two superconductors separated by a thin insulating layer [53] as shown in Fig. 3.1 a). Nine months after the publication of his theoretical paper, the effect was experimentally observed by Phil Anderson and John Rowell at the Bell labs [54]. They used tin-tin-oxide-lead (Sn-Sn$O_x$-Pb) junctions and observed zero-voltage currents whose maximum value before a voltage appeared was highly sensitive to magnetic fields as shown in Fig. 3.1 b). This Josephson coupled-superconductor effect is inherent in any superconductor-insulator-superconductor (SIS) tunnel junction if the insulating tunnel barrier is sufficiently thin to allow the coupling energy between superconducting pairs on the two sides to exceed thermal fluctuations.

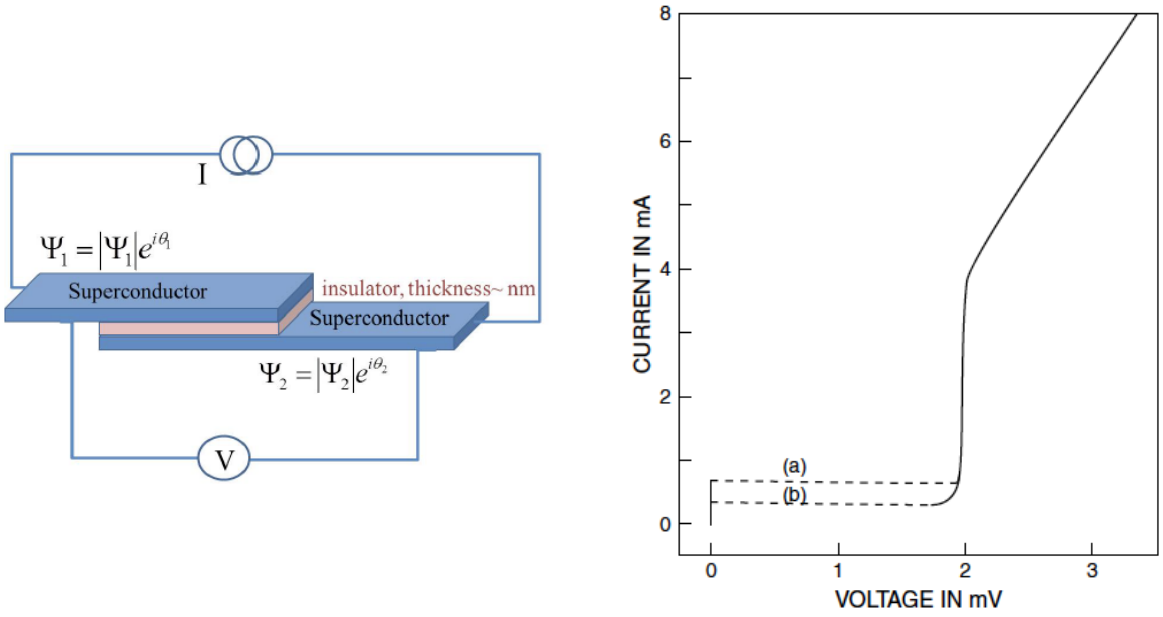



**Figure 3.1:** Left: The schematic of a Josephson junction, a thin layer of insulator sandwiched between two superconductors, Right: First time experimental verification of the Josephson effect. Current-voltage characteristics for a Sn-Sn$O_x$-Pb tunnel structure at ∼1.5 K, (a) for a field of $6 \times 10^{-7}$ T, and (b) for a field of $4 \times 10^{-5}$ T [53].

The Josephson effect provides a tunneling supercurrent given by [55]:

$$I = I_0 \sin \delta \tag{3.3}$$

at zero voltage, proportional to $\sin\delta$, where

$$\delta = \theta_1 - \theta_2 \tag{3.4}$$

is the difference between the phases of the pair states on each superconductor side, and $I_0$ is the critical current. In the presence of a voltage $V$ between the superconductors, $\delta$ evolves with time $t$ according to

$$\frac{\mathrm{d}\delta}{\mathrm{d}t} = \frac{2\mathrm{e}V}{\hbar} = \frac{2\pi V}{\phi_0} \tag{3.5}$$

Eq. 3.1 and 3.2 describe the static ("dc") and dynamic ("ac") properties of a Josephson junction. A high-quality Josephson tunnel junction has a hysteretic current-voltage (I-V) characteristic. As the current is increased from zero, the voltage switches abruptly to a nonzero value when $I$ exceeds $I_0$ but returns to zero only when $I$ is reduced to a value much less than $I_0$. This hysteresis can be eliminated by shunting the junction with an external shunt resistance.

Refractory Josephson Junctions are fabricated from thin, polycrystalline films of Nb, with Nb-$AlO_x$-Nb junctions fabricated in situ, i.e., by sequential deposition and Al oxidation without breaking vacuum. This process can yield spreads in critical current of only a few percent across the wafer. The trilayers are patterned with reactive ion etching, and their sides protected by anodization.

### 3.1.3 rf-SQUIDs

The Superconducting Quantum Interference Device (SQUID) combines the physical phenomenon of flux quantization and Josephson tunneling. SQUIDs; which are intrinsically flux-to-voltage transducers, are the most sensitive detectors of magnetic flux available [55]. They are amazingly versatile, being able to measure any physical quantity that can be converted to a flux, for example, magnetic field, magnetic field gradient, current, voltage, displacement, and magnetic susceptibility. As a result, the very first applications of SQUIDs were in the detection of tiny magnetic fields produced by the human brain and in the measurement of fluctuating geomagnetic fields in remote areas. There are two kinds of SQUIDs as shown in Fig. 3.2. The first, the dc-SQUID, consists of two Josephson junctions connected in parallel in a superconducting loop, and is so named because it can be operated with a steady

current bias. The second, the rf-SQUID, involves a single Josephson junction interrupting the current flow around a superconducting loop, and is operated with a radio frequency flux bias.

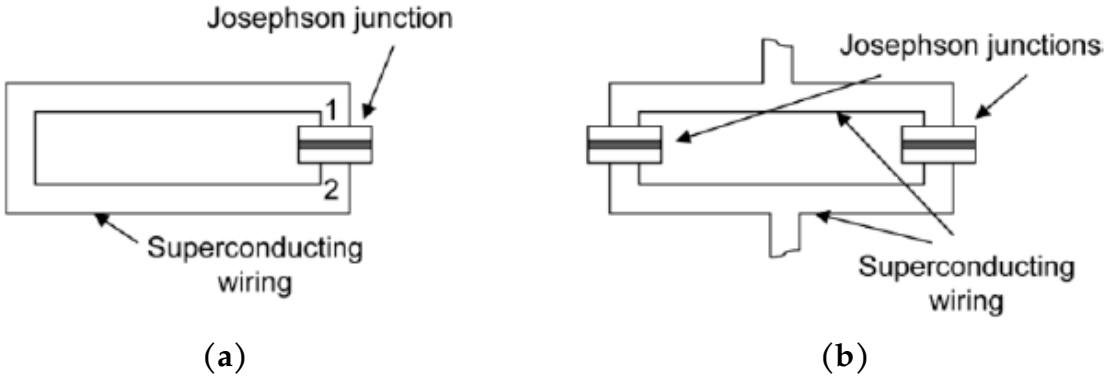



**Figure 3.2:** (**a**) One-junction rf-SQUID, (**b**) Two-junction dc-SQUID.

In both cases, the output from the SQUID is periodic with period $\phi_0$ in the magnetic flux applied to the loop. One generally is able to detect an output signal corresponding to a flux change of much less than one flux quantum. For building the microwave circuits as a part of my research, I will be dealing with only rf-SQUIDs.

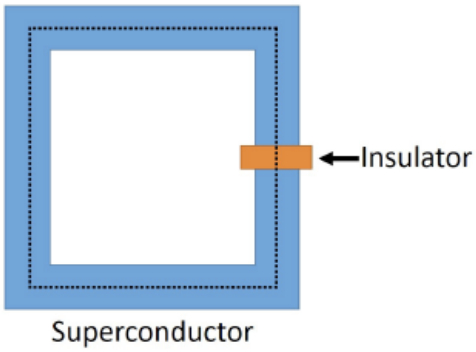



**Figure 3.3:** rf-SQUID consisting of a superconducting loop of inductance, $L$, interrupted by a single Josephson junction.

Flux quantization imposes the constraint

$$\delta + \frac{2\pi\phi_T}{\phi_0} = 2\pi n \tag{3.6}$$

On the total flux $\phi_T$ threading the loop. The phase difference $\delta$ across the junction determines the supercurrent

$$I_s = -I_0 \sin\left(\frac{2\pi\phi_T}{\phi_0}\right) \tag{3.7}$$

Flowing in the ring. This current flowing around the loop generates a flux given by:

$$\phi_L = -LI_0 \sin\left(\frac{2\pi\phi_T}{\phi_0}\right) \tag{3.8}$$

A quasistatic external flux phi thus gives rise to total flux given by

$$\phi_T = \phi - LI_0 \sin\left(\frac{2\pi\phi_T}{\phi_0}\right) \tag{3.9}$$

One of the important points to keep in mind when using RF SQUID as a flux-sensitive inductor is to operate it in the nonhysteretic regime (dispersive mode), which means $\beta = \left(\left(2\pi LI_0\right)/\phi_0\right) < 1$.

When the tunneling supercurrent flowing through the JJ is below a certain threshold, the "critical current", the JJ is electrically equivalent to a non-linear inductor. However, unlike varactors, the JJ is a lossless reactive element, its resistance in the superconducting state being lower than the resistance of a typical forward-biased semiconductor diode by orders of magnitude. SQUID inductance is a combination of the junction inductance and the inductance of the superconducting loop. This SQUID inductance is controlled by modulating the magnetic flux threading the junction loop.

## 3.2 rf-SQUIDs Coupled Microstrip TL

Phase shifters play a key role in the modern-day RF systems such as electronic scanning antenna arrays. Over the past years, both high temperature superconductor (HTS) and low temperature superconductor (LTS) phase shifters have been explored for incorporation into existing superconducting systems. In [56], ferroelectric materials were employed with HTS to develop phase shifters. Both HTS-based SQUIDs and LTS-based SQUIDs are proposed in [57, 58] to realize phase shifters. In [59], a magnetic-flux-tunable phase shifter utilizing three equidistant SQUIDs on a

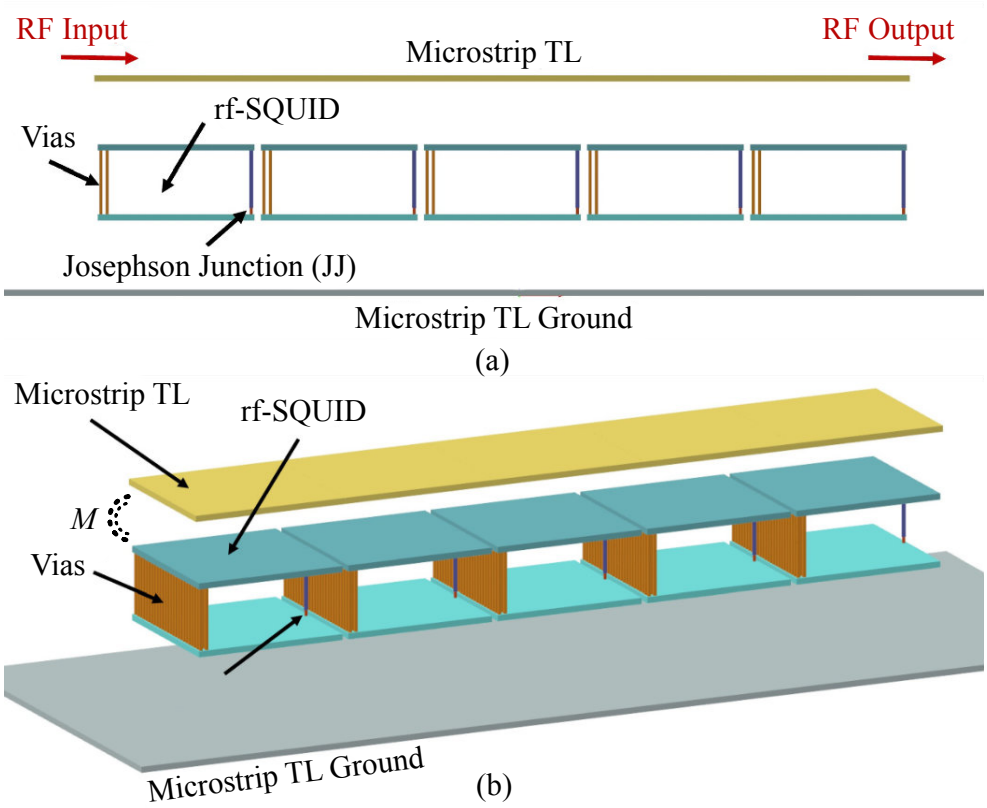



**Figure 3.4:** (a) Cross-section view, (b) 3D view of a microstrip transmission line coupled to an array of SQUIDs

transmission line (TL) was proposed. The phase shifter was employed to implement arbitrary single-qubit gates for qubits based on propagating microwave photons.

A Distributed Josephson Inductance (DJI) approach to building a superconducting phase shifter is presented here. In this approach, the RF signal passes through a fixed length of microstrip transmission line (TL) which is magnetically coupled to an array of superconducting quantum interference devices (SQUIDs) along its length as shown in Fig. 3.4.

In the absence of rf-SQUIDs, as shown in Fig. 3.5, the microstrip TL will have a fixed capacitance per unit length $C$ and a fixed inductance per unit length $L$. The small signal wave velocity of a transmission line is given by $v = 1/\sqrt{(L \cdot C)}$.
In the DJI approach, rf-SQUIDs are placed between the top conductor and the ground plane of the microstrip line. Each rf-SQUID consists of one Josephson junction shunted

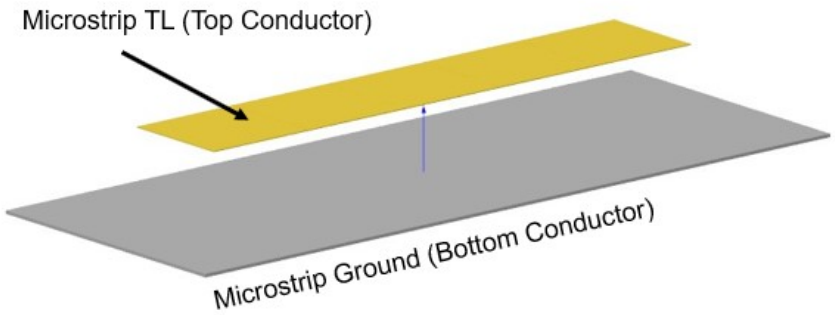



**Figure 3.5:** 3D view of the microstrip TL magnetically coupled to an array of rf-SQUIDs.

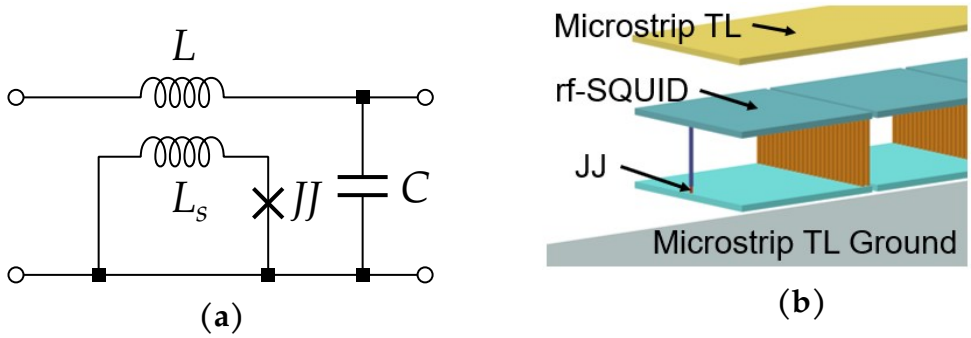



**Figure 3.6:** (**a**) Equivalent circuit of a TL unit cell containing a rf-SQUID, (**b**) 3D view of rf-SQUIDs placed between the top conductor and ground plane of TL.

by an inductive superconducting loop. The length of line containing one SQUID is much shorter than the RF wavelength. Each rf-SQUID is a superconducting loop extending on two metal layers shunted by vias on one end and JJ on the other end as shown in Fig. 3.6(b).

The equivalent circuit of a transmission line section coupled to a rf-SQUID is shown in Fig. 3.6(a). The magnetic coupling of the microstrip line to an array of rf-SQUIDs leads to a dynamic inductance per unit length ($L_{dyn}$) as shown in Fig. 3.7. Hence, coupling a large number of SQUIDs to a superconducting microstrip TL creates a variable magnetic medium in which wave velocity can be controlled electronically, $v = 1/\sqrt{(L_{dyn} \cdot C)}$.

When a dc control current $I_{dc}$ is passed through the microstrip TL, flux is linked to the SQUID loop since it is magnetically coupled to the TL. This linked flux results in a

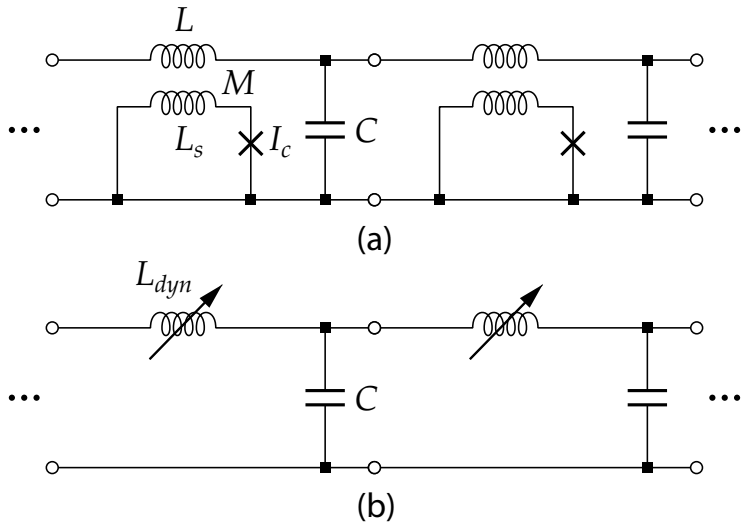



**Figure 3.7:** (a) The lumped element model of a distributed Josephson inductance (DJI) transmission line, (b) Small signal RF equivalent circuit of the DJI

change in the phase of the SQUID, thereby altering the dynamic inductance of the transmission line. The change in wave velocity and hence the phase delay in the TL can also be achieved by increasing the power of the RF signal which will provide an equivalent RF current $I_{RF}$ or by superimposing a dc control current on the RF signal current, $I = I_{dc} + I_{RF}\cos(\omega t)$, where $I$ is the total current along the upper conductor of the microstrip and $I_{RF}$ is the total RF current superimposed on the dc current $I_{dc}$. In other words, the output phase can be controlled using dc current or RF power or a combination of the two on the TL. The phase shift at the output can also be achieved through the application of an external magnetic field. The magnet is oriented so that its field passes through the SQUID loops. However, this work focuses on using either dc current or RF power for controlling the output signal phase.

The dynamic inductance in terms of the phase of the SQUIDs and the electrical parameters of the transmission line is presented. This derivation is inspired by the effective inductance expression for single rf-SQUID coupled to the RF tank circuit [60]. Each superconducting TL unit-cell consists of a series inductance, $L$, and a shunt capacitance, $C$. The series inductance of the transmission line cell is coupled to a single SQUID loop through a mutual inductance, $M$. The rf-SQUID loop consists of a superconducting loop with inductance, $L_s$, and a Josephson tunnel junction. The expression for the dynamic inductance of the rf-SQUID coupled TL can be analytically derived.

The flux through the inductor, $L$, and $L_s$ is given as $\Phi$, and $\Phi_s$, respectively. The flux through these inductors is related to the current through the two inductors by

$$\begin{bmatrix} \Phi \\ \Phi_s \end{bmatrix} = \begin{bmatrix} L & M \\ M & L_s \end{bmatrix} \begin{bmatrix} I \\ I_s \end{bmatrix}$$

$$\Phi = LI + MI_s \tag{3.10}$$

$$\Phi_s = MI + L_s I_s \tag{3.11}$$

where, $L$ is the self inductance per cell of the transmission line, $L_s$ is the self inductance of the SQUID and $M$ is the mutual inductance between the transmission line and one SQUID. $I$ is the current through the transmission line section and is controlled externally, while $I_s$ depends on the operating point of the SQUID.

According to the well known Josephson relation

$$I_s = I_c \sin\theta \tag{3.12}$$

where, $I_c$ is the critical current of the JJ and $\theta$ is the phase of the SQUID.

Phase of the SQUID, $\theta$ is expressed as

$$\theta = -\frac{2\pi\Phi_s}{\Phi_0} \tag{3.13}$$

where, $\Phi_0$ is the flux quantum $\left(\Phi_0 = 2.0679 \times 10^{-15}\,\text{Wb}\right)$. The negative sign reflects the fact that as $I$ is increased from zero, $\Phi_s$ initially opposes $\Phi$

Substituting Eq. (3.12) in (3.10)

$$\Phi = LI + MI_c \sin\theta \tag{3.14}$$

and substituting Eq. (3.12) in (3.11)

$$\Phi_s = MI + L_s I_c \sin\theta \tag{3.15}$$

Finding $\Phi_s$ from Eq. (3.13)

$$\Phi_s = -\frac{\theta\Phi_0}{2\pi}$$

Using value of $\Phi_s$ in Eq. (3.15)

$$-\frac{\theta\Phi_0}{2\pi} = MI + L_s I_c \sin\theta$$
$$-\theta = \frac{2\pi}{\Phi_0} MI + \frac{2\pi}{\Phi_0} L_s I_c \sin\theta$$

$$\frac{2\pi MI}{\Phi_0} = -\theta - \boxed{\frac{2\pi L_s I_c}{\Phi_0}} \sin\theta$$

The factor $(2\pi L_s I_c)\,/\Phi_0$ is the screening parameter (also called SQUID parameter), $\beta$.

$$\frac{2\pi MI}{\Phi_0} = -\theta - \beta \sin\theta$$
$$\theta = -2\pi\left(\frac{MI}{\Phi_0}\right) - \beta \sin\theta \tag{3.16}$$

The dynamic inductance is defined by

$$\boxed{L_{dyn} = \frac{\mathrm{d}\Phi}{\mathrm{d}I}} \tag{3.17}$$

Differentiating Eq. (3.14) w.r.t. $I$

$$\frac{\mathrm{d}\Phi}{\mathrm{d}I} = L + MI_c \cos\theta \left(\frac{\mathrm{d}\theta}{\mathrm{d}I}\right) \tag{3.18}$$

Differentiating Eq. (3.16) w.r.t. $I$

$$\begin{aligned} \frac{\mathrm{d}\theta}{\mathrm{d}I} &= -\frac{2\pi M}{\Phi_0} - \beta\cos\theta\left(\frac{\mathrm{d}\theta}{\mathrm{d}I}\right) \\ (1+\beta\cos\theta)\frac{\mathrm{d}\theta}{\mathrm{d}I} &= -\frac{2\pi M}{\Phi_0} \\ \frac{\mathrm{d}\theta}{\mathrm{d}I} &= -\frac{2\pi M}{\Phi_0\,(1+\beta\cos\theta)} \end{aligned} \tag{3.19}$$

Substituting Eq. (3.19) in (3.18)

$$\begin{aligned} L_{dyn} = \frac{\mathrm{d}\Phi}{\mathrm{d}I} &= L + MI_c\cos\theta\left(-\frac{2\pi M}{\Phi_0\,(1+\beta\cos\theta)}\right) \\ &= L - \frac{2\pi M^2 I_c\cos\theta}{\Phi_0\,(1+\beta\cos\theta)} \end{aligned} \tag{3.20}$$

The mutual coupling, $M$ between the two inductors $L$ and $L_s$ is related by the coupling coefficient, $k$

$$\boxed{k^2 = \frac{M^2}{LL_s}}$$

$$M^2 = k^2 LL_s \tag{3.21}$$

Substituting Eq. (3.21) in (3.20)

$$L_{dyn} = L - \frac{2\pi k^2 LL_s I_c\cos\theta}{\Phi_0\,(1+\beta\cos\theta)}$$

Substituting the SQUID Parameter, $\beta$

$$L_{dyn} = L - \frac{k^2\beta L\cos\theta}{(1+\beta\cos\theta)}$$

Hence, the dynamic inductance, $L_{dyn}$ of a transmission line cell coupled to a RF SQUID is

$$L_{dyn} = L\left(1 - \frac{k^2\beta\cos\theta}{(1+\beta\cos\theta)}\right) \tag{3.22}$$

Hence, the phase, $\Theta$ of the TL of length $l_{tot}$ coupled with an array of rf-SQUIDs is given by:

$$\Theta = \omega\sqrt{L_{dyn}C} \times l_{tot} \tag{3.23}$$

## 3.3 Simulations for Mutual Inductance and Coupling Coefficient

The values of the design parameters used for EM simulations are as follows:

Diameter of circular JJ, $d_{junc} = 3 \times 10^{-6}$ m

Critical current density of the JJ, $J_c = 1 \times 10^8$ A/m$^2$

Length of microstrip TL containing one SQUID, $l_{unit} = 50 \times 10^{-6}$ m

Total length of the microstrip TL, $l_{total} = 14.2 \times 10^{-2}$ m

Width of the microstrip TL, $w = 1.5 \times 10^{-6}$ m

Freq. of operation, $f_0 = 10 \times 10^9$ Hz

No. of rf-SQUIDs, $N_s = 2256$

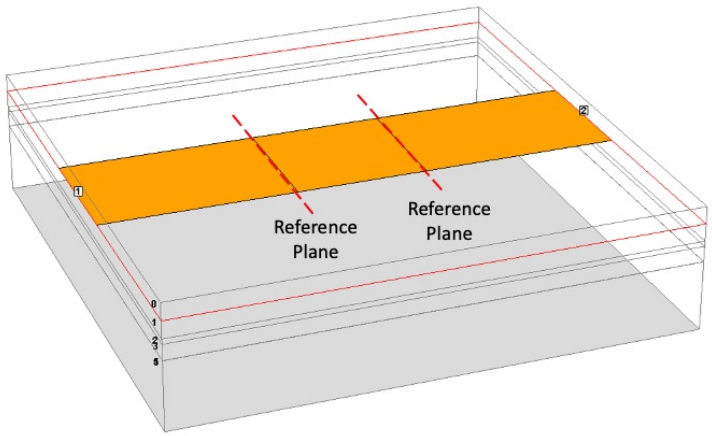



**Figure 3.8:** Microstrip TL unit-cell in Sonnet EM

We created a microstrip TL model in Sonnet EM as shown in Fig. 3.8. The length and width of the microstrip in the model are $w$ and $l_{unit}$, respectively, which represent the section of TL covering one SQUID. This is done in order to find the value of self inductance $L$ of the TL section when no SQUID is coupling to it. The simulated value for $L$ is given in table 3.1. Another 3D model is designed in Sonnet EM placing a rf-SQUID between the top conductor and ground plane of the microstrip TL as shown in Fig. 3.9. This is done in order to simulate the SQUID loop inductance, $L_s$, and then mutual inductance, $M$ and coupling coefficient, $k$. The vertical gap between the microstrip signal line and the rf-SQUID top conductor is selected to be 200 nm based on the fabrication process defined in section 3.4.1. The simulated values are given in table 3.1 and will be used in the analysis given in the following sections.

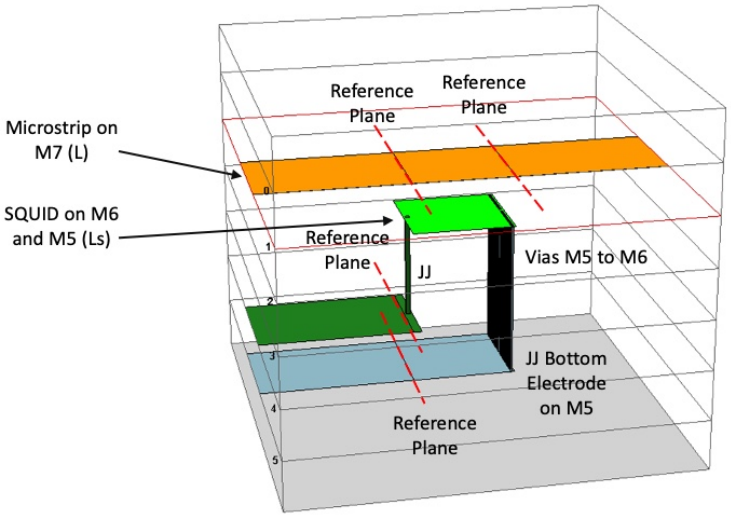



**Figure 3.9:** 3D model of an rf-SQUID in Sonnet EM

Critical current of the JJ, $I_c$, can be calculated from junction's area, $A_{junc}$ and critical current density, $J_c$:

$$I_c = J_c \times A_{junc} \tag{3.24}$$

$$I_c = (1 \times 10^8) \times (7.07 \times 10^{-12}) = 7.07 \times 10^{-4}\,\text{A}$$

Calculating SQUID Parameter, $\beta$ from SQUID inductance, $L_s$ and critical current, $I_c$:

**Table 3.1:** Simulated results for $L$, $L_s$, $M$ and $k$ using Sonnet EM

| TL Self Inductance $L$ (H) | rf-SQUID Self Inductance $L_s$ (H) | Mutual Inductance $M$ (H) | Coupling Coefficient $k$ |
|---|---|---|---|
| 16.5e-12 | 4.4e-13 | 2.24e-12 | 0.83 |

$$\beta = \frac{2\pi L_s I_c}{\Phi_0} \tag{3.25}$$

$$\beta = \frac{2\pi(4.4 \times 10^{-13})(1 \times 10^{8})}{2.0679 \times 10^{-15}} = 0.945 \tag{3.26}$$

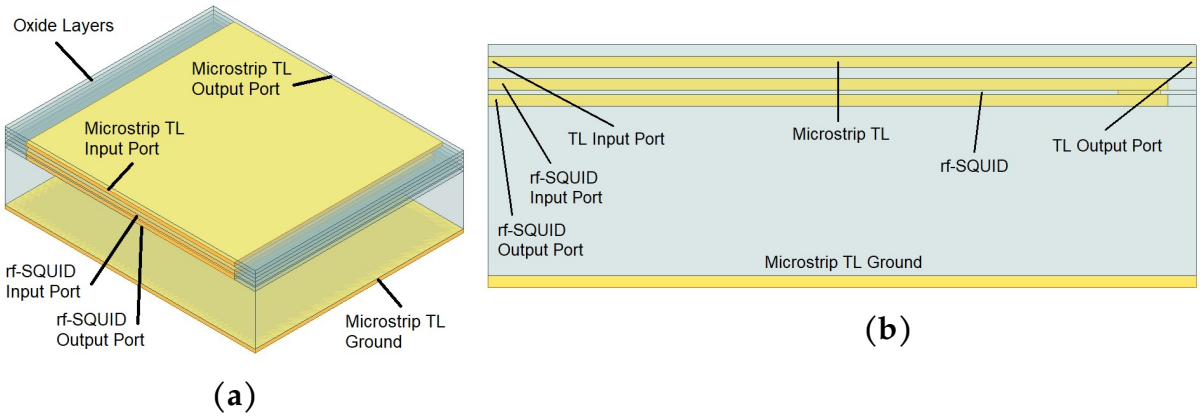



**Figure 3.10:** (**a**) rf-SQUID and TL model in Ansys Maxwell 3D, (**b**) Cross-section view of the model.

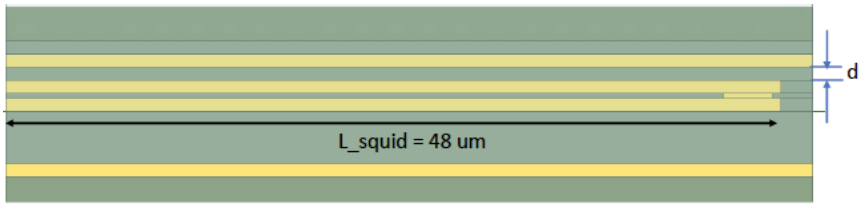



**Figure 3.11:** Simulation model of rf-SQUID coupling a microstrip TL in Ansys Maxwell 3D

**Table 3.2:** Simulated results for $L$, $L_s$, $M$ and $k$ using Ansys Maxwell 3D

| Gap $d$, (m) | TL Self Inductance $L$ (H) | rf-SQUID Self Inductance $L_s$ (H) | Mutual Inductance $M$ (H) | Coupling Coefficient $k$ |
|---|---|---|---|---|
| 5e-9 | 16.5e-12 | 4.4e-13 | 2.67e-12 | 0.991 |
| 10e-9 | 16.5e-12 | 4.4e-13 | 2.62e-12 | 0.972 |
| 20e-9 | 16.5e-12 | 4.4e-13 | 2.56e-12 | 0.950 |
| 50e-9 | 16.5e-12 | 4.4e-13 | 2.47e-12 | 0.917 |
| 80e-9 | 16.5e-12 | 4.4e-13 | 2.40e-12 | 0.891 |
| 100e-9 | 16.5e-12 | 4.4e-13 | 2.31e-12 | 0.857 |
| 200e-9 | 16.5e-12 | 4.4e-13 | 2.24e-12 | 0.831 |
| 300e-9 | 16.5e-12 | 4.4e-13 | 2.17e-12 | 0.805 |
| 500e-9 | 16.5e-12 | 4.4e-13 | 2.09e-12 | 0.776 |

For comparison, an rf-SQUID/TL 3D model was created in Ansys Maxwell 3D as shown in Fig. 3.10. Ansys Maxwell 3D is a simulation tool for studying the magnetic fields. Simulations are repeated for different values of the gap, $d$, between the microstrip TL and the top conductor of the rf-SQUID as shown in Fig. 3.11. The results of the mutual inductance $M$, and coupling coefficient $k$ are presented in Table 3.2. We observe that the mutual coupling increases as the gap between the rf-SQUID and top conductor of microstrip decreases. The magnetic flux density as shown in Fig. 3.12 can also be observed at various values of $d$.

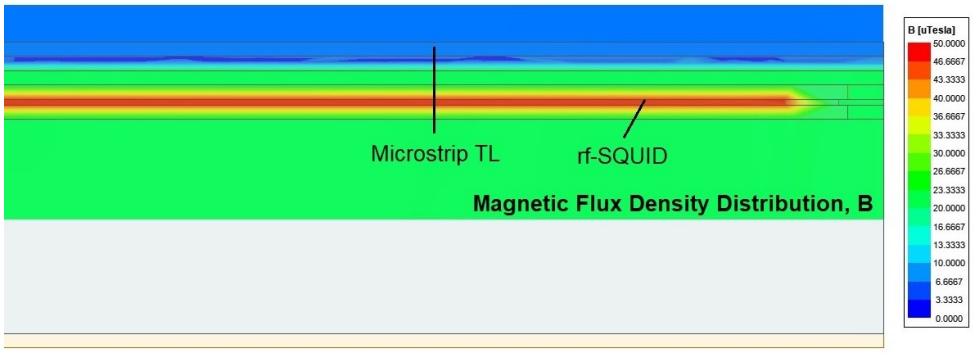



**Figure 3.12:** Magnetic flux density in rf-SQUID using Ansys Maxwell 3D

Knowing the values of $M$ and $k$, and other given parameters, the dynamic inductance and the total phase shift for DJI transmission line as a function of the dc current along the upper conductor is computed in Table 3.3. The computed values of dynamic inductance for the dc current ranging from 0 mA to 36 mA are plotted in Fig. 3.13(a). Relative phase shift with the input control current at 10 GHz is shown in Fig. 3.13(b). Hence, DJI transmission line introduces a phase delay which is adjustable using the control current,$I_{dc}$.

**Table 3.3:** Analysis of the dynamic inductance and phase shift as a function of current using the given and simulated parameters

| Current | | | | rf-SQUID Phase | | | | Phase Shift |
|---|---|---|---|---|---|---|---|---|
| $I$ | $M \times I$ | $L_s \times I_s$ | $\Phi_s$ | $\theta$ | $\cos\theta$ | $L_{dyn}$ | $\sqrt{(L_{dyn} \times C)}$ | $\Theta$ |
| (A) | (Wb) | (Wb) | (Wb) | (°) | | (H) | | (°) |
| Input | – | – | Eq. (3.11) | – | – | Eq. (3.22) | – | Eq. (3.23) |
| 0 | 0 | 0 | 0 | 0 | 0 | 0 | 0 | 0 |
| 1.5e-3 | 3.36e-12 | 3.11e-16 | 3.36e-12 | 7.5 | 0.99 | 10.98e-12 | 2.34e-13 | 0.05 |
| 3.0e-3 | 6.72e-12 | 3.11e-16 | 6.72e-12 | 15 | 0.97 | 11.06e-12 | 2.34e-13 | 0.19 |
| 4.5e-3 | 10.08e-12 | 3.11e-16 | 10.08e-12 | 22.5 | 0.92 | 11.18e-12 | 2.36e-13 | 0.43 |
| 6.0e-3 | 13.44e-12 | 3.11e-16 | 13.44e-12 | 30 | 0.87 | 11.37e-12 | 2.38e-13 | 0.77 |
| 7.5e-3 | 16.80e-12 | 3.11e-16 | 16.80e-12 | 37.5 | 0.79 | 11.61e-12 | 2.40e-13 | 1.23 |
| ⋮ | ⋮ | ⋮ | ⋮ | ⋮ | ⋮ | ⋮ | ⋮ | ⋮ |
| 34.5e-3 | 77.28e-12 | 3.11e-16 | 77.28e-12 | 172.5 | -0.99 | 18.59e-11 | 9.61e-13 | 130.07 |
| 36.0e-3 | 80.64e-12 | 3.11e-16 | 80.64e-12 | 180 | -1.00 | 21.25e-11 | 10.3e-13 | 141.94 |

Phase control can also be achieved using RF power instead of dc current. The dynamic inductance of the TL and the output phase shift achieved by varying the RF power from $-30$ dBm to 10 dBm is shown in Table 3.4.

RF current, $I_{rf}$ is computed from RF power, $P_{rf}$ using

$$I_{rf} = \sqrt{P_{rf}/Z_0} \tag{3.27}$$

A plot of the dynamic inductance for the RF power ranging from −30 dBm to 10 dBm is shown in Fig. 3.14(a) and the calculated phase shift at 10 GHz for various RF power levels is shown in Fig. 3.14(b).

## 3.4 Multi-layer Superconducting Fabrication Process

### 3.4.1 MIT Lincoln Laboratory (MIT-LL) SFQ5ee Process

All the proposed superconducting microwave devices are fabricated using MIT Lincoln Laboratory (MIT-LL) SFQ5ee fabrication process [61]. This mature and advanced integrated circuit fabrication process provides a solid technology platform for building the superconducting circuits. It is a niobium-based fabrication process using Nb/Al-$AlO_x$/Nb tri-layer technology with a current density, $J_c$ of 10 kA/cm$^2$. As shown in the cross section in Fig. 3.15, there are nine superconducting layers: eight niobium wiring layers M0–M7 and one layer of high kinetic inductance (HKI) material, L0. There is one normal metal layer, M8 (Pad), for chip contact metallization and chip packaging. Interconnects between all metal and resistor layers are formed by vias C0, C4, C5, and I0–I7. Most of the layer interconnects are etched vias filled with the

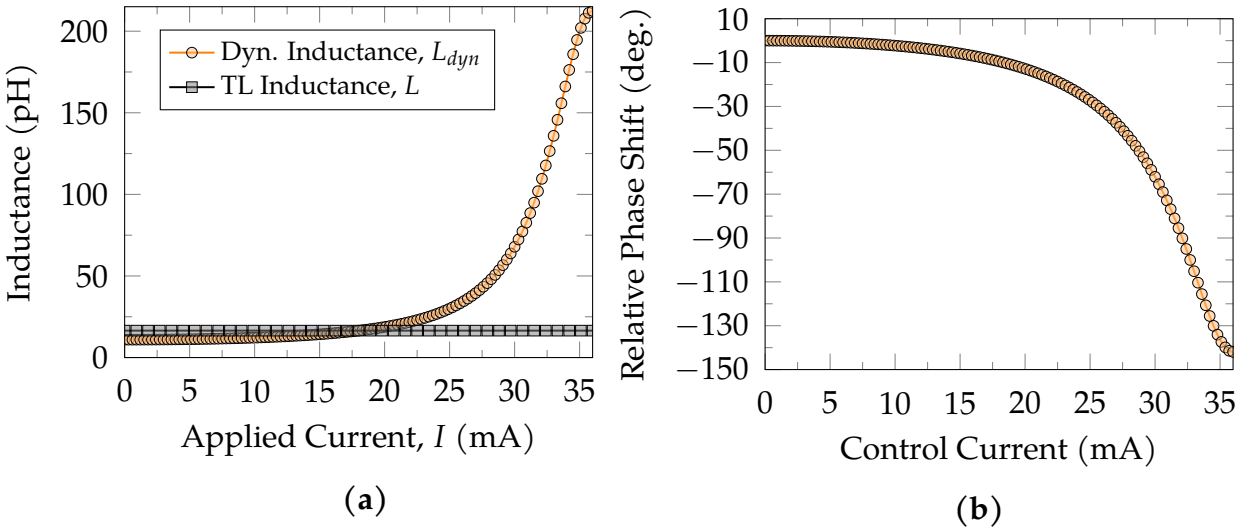



**Figure 3.13:** (**a**) Dynamic inductance, $L_{dyn}$ and transmission line inductance, $L$ of a unit-cell, (**b**) Calculated relative phase shift at 11.6 GHz as a function of dc current ranging from 0 mA to 8 mA

**Table 3.4:** Analysis of the dynamic inductance and phase shift as a function of RF power.

| RF Power $P_{rf}$ (dBm) | RF Power $P_{rf}$ (W) | RF Current $I_{rf}$ (A) | rf-SQUID Phase $\theta$ (°) | $\cos\theta$ | Dynamic Inductance $L_{dyn}$ (H) | $\sqrt{(L_{dyn} \times C)}$ | Relative Phase Shift $\Theta$ (°) |
|---|---|---|---|---|---|---|---|
| Input | Input | Eq. (3.27) | | | Eq. (3.22) | | Eq. (3.23) |
| -30 | 1.00e-6 | 1.32e-4 | 1.65 | 0.999 | 1.096e-11 | 2.332e-13 | 0.00 |
| -25 | 3.16e-6 | 2.34e-4 | 3.40 | 0.998 | 1.097e-11 | 2.333e-13 | 0.01 |
| -20 | 1.00e-5 | 4.16e-4 | 8.54 | 0.989 | 1.099e-11 | 2.336e-13 | 0.05 |
| -15 | 3.16e-5 | 7.41e-4 | 18.89 | 0.946 | 1.112e-11 | 2.349e-13 | 0.23 |
| -10 | 1.00e-4 | 1.32e-3 | 40.17 | 0.764 | 1.172e-11 | 2.412e-13 | 1.12 |
| -5 | 3.16e-4 | 2.34e-3 | 83.14 | 0.119 | 1.534e-11 | 2.760e-13 | 6.06 |
| 0 | 1.00e-3 | 4.16e-3 | 251.97 | -0.309 | 2.121e-11 | 3.245e-13 | 12.93 |
| 5 | 3.16e-3 | 7.41e-3 | 566.58 | -0.894 | 7.873e-11 | 6.252e-13 | 55.55 |
| 10 | 1.00e-2 | 1.32e-2 | 357.80 | -0.999 | 2.099e-10 | 1.021e-12 | 111.63 |

niobium metal of the subsequent superconducting layer.

Keeping in mind the Nb layers in the fabrication process, the DJI transmission line can be realized either by placing the rf-SQUIDs loop directly below the microstrip top conductor as shown in Fig. 3.17(a). In this case, the meandered microstrip top conductor will be designed on Nb layer M7 and rf-SQUID loop will spread on the Nb layers M5 and M6 shunted by a JJ using J5 and C5 on one end and vias I5 on the other end. The gap between the microstrip conductor and the rf-SQUID is dictated by the dielectric layer thickness given in the fabrication process. Another way to achieve the DJI phase shifter is by placing the rf-SQUIDs on both sides of the microstrip top conductor as shown in Fig. 3.17(b). In this design, both the microstrip signal line and the superconducting loop of the rf-SQUID are placed on the Nb layer M6. This design provides more control in terms of adjusting the amount of mutual coupling, as the distance of the SQUIDs from the signal line can be adjusted during design, however, the minimum gap between two is dictated by the fabrication process.

## 3.5 Cryogenic Test Setup for RF Measurements

### 3.5.1 Device Testing at Cryogenic Temperatures

All the superconducting microwave devices in this thesis report are measured using the cryogenic test setup shown in Fig. 3.18. The setup includes a Lakeshore cryogenic probe station, a Keysight performance network analyzer (PNA), a source measurement unit (SMU) or a power supply unit. The chips for testing are loaded in the cryogenic chamber along with the calibration substrate as shown in the enlarged section in Fig. 3.18. The chamber is pumped to very low pressure of $1 \times 10^{-6}$ mbar and the temperature is lowered down to 77 K using liquid nitrogen which is followed by liquid helium to lower it further down to 3.8 K. The temperature is maintained at 3.8 K for the entire duration for consistent and repeatable measurements. SOLT calibration is done at cryogenic temperatures. For on-wafer measurements, the chamber has two dc probes and two ground-signal-ground (GSG) RF probes which are connected to the two ports of Keysight PNA. The dc excitation (control current/control voltage) can be provided in precisely controlled steps using SMU.

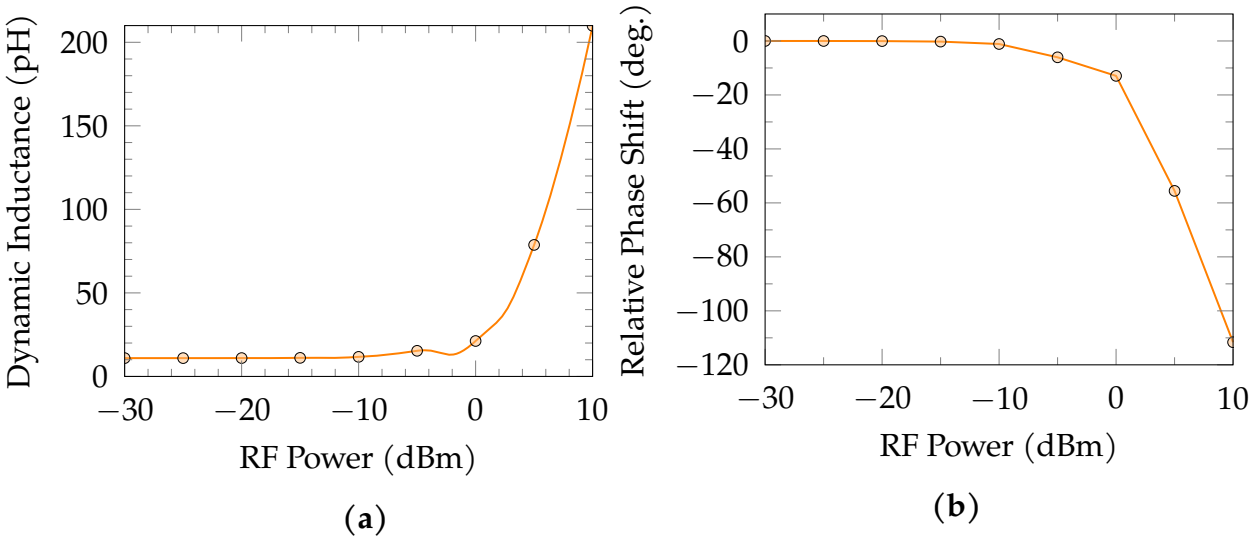



**Figure 3.14:** (**a**) Dynamic inductance, $L_{dyn}$ of a transmission line cell as a function of RF power ranging from −30 dBm to 10 dBm, (**b**) Calculated relative phase shift for the RF power range −30 dBm to 10 dBm

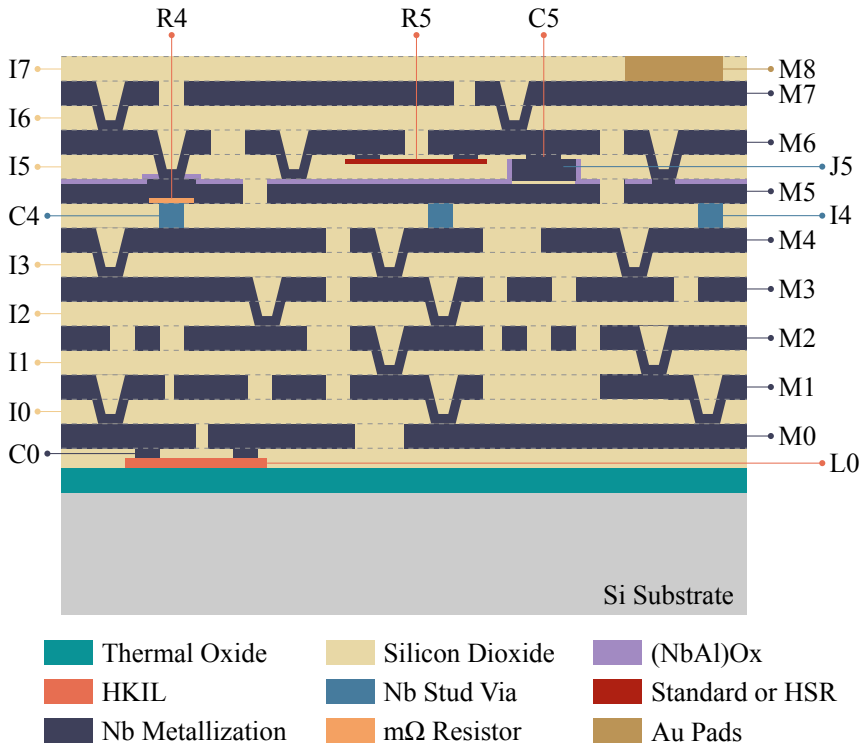



**Figure 3.15:** Cross section of the MIT-LL 10 kA/cm$^2$ SFQ5ee process.

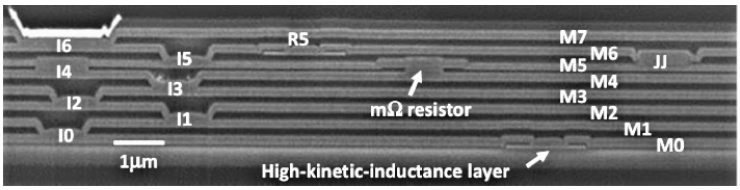
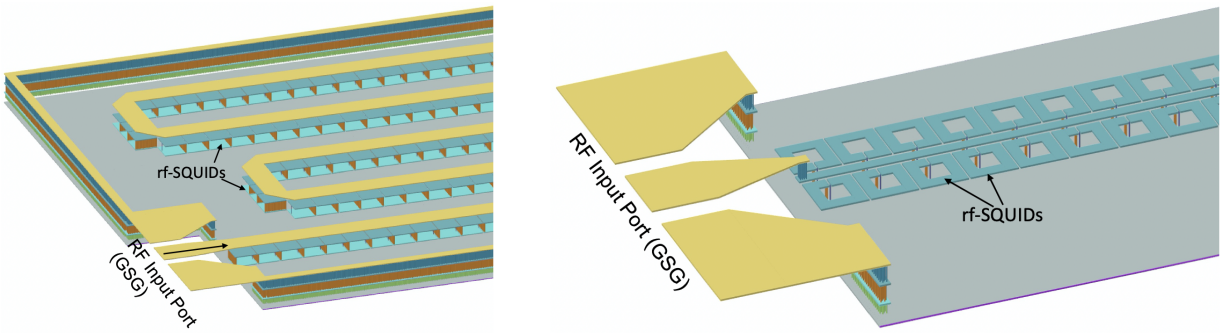



**Figure 3.16:** Scanning electron microscope (SEM) of the wafer cross section highlighting the MIT-LL SFQ5ee process node. Various Nb metal layers (M0-M7), vias (I0-I6), josephson junction (JJ), resistor layers (r5 and mΩ), and a high-kinetic inductance layer are indicated [61].

## 3.6 LTS Phase Shifter Using rf-SQUIDs

sec:phase-shifter1 After the simulations and theoretical analysis presented in the sections 3.2 and 3.3, a phase shifter is designed with a microstrip TL strongly coupled to an array of rf-SQUIDs placed between it's top conductor and the ground plane as shown in Fig. 3.19. The current that is flowing on the superconducting TL generates a magnetic flux that is coupled to the SQUID loop varying its inductance.

The array of rf-SQUIDs effectively represents an array of variable inductors coupled to the TL. Each rf-SQUID extends on two Nb layers shunted by vias on one end and a JJ on the other end. The device is realized using MIT-LL SFQ5ee Nb based fabrication process described in section 3.4.1. The optical micrograph of the design is shown in




(a) (b)

**Figure 3.17:** (**a**) rf-SQUIDs placed under the microstrip TL using two additional Nb layers, (**b**) rf-SQUIDs placed on both sides of the microstrip TL on the same Nb layer.

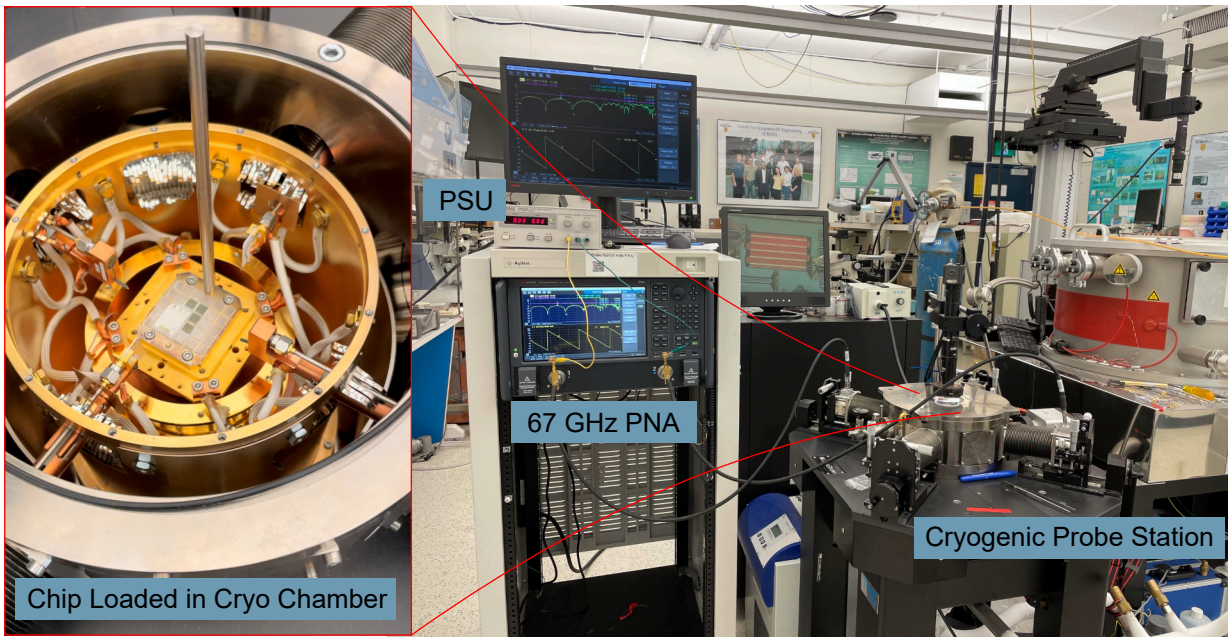



**Figure 3.18:** Cryogenic test setup at CIRFE showing the Lakeshore probe station, PNA and PSU. The enlarged image highlights the chips loaded in the cryo chamber.

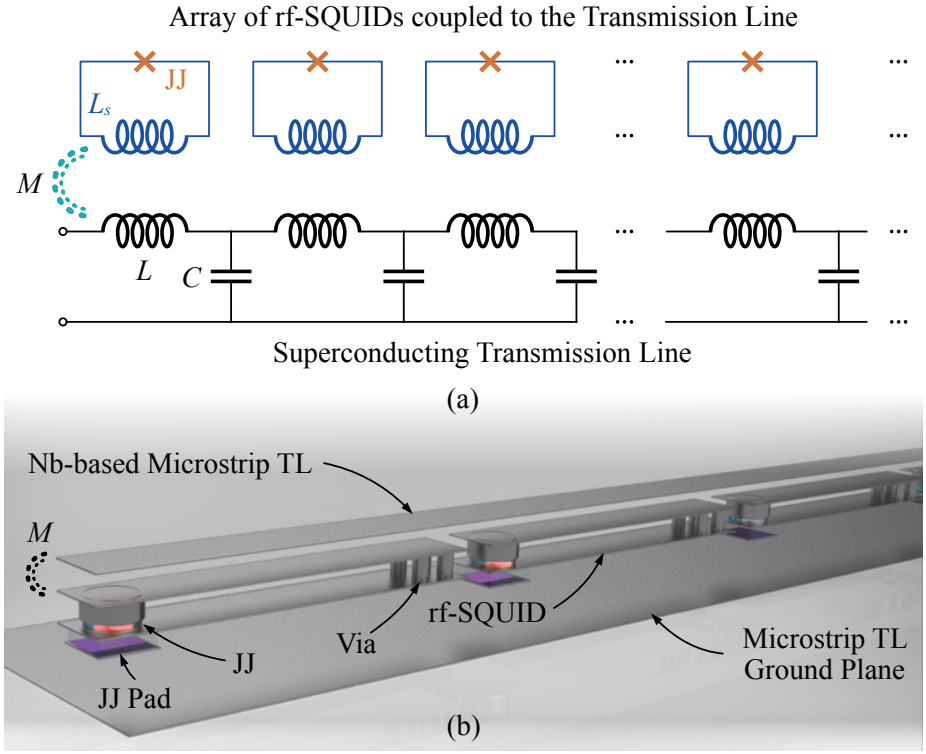



**Figure 3.19:** (a) Schematic of the phase shifter comprising of an array of rf-SQUIDS coupled to the superconducting transmission line (TL), (b) 3D rendered image showing rf-SQUIDs distributed underneath the superconducting TL.

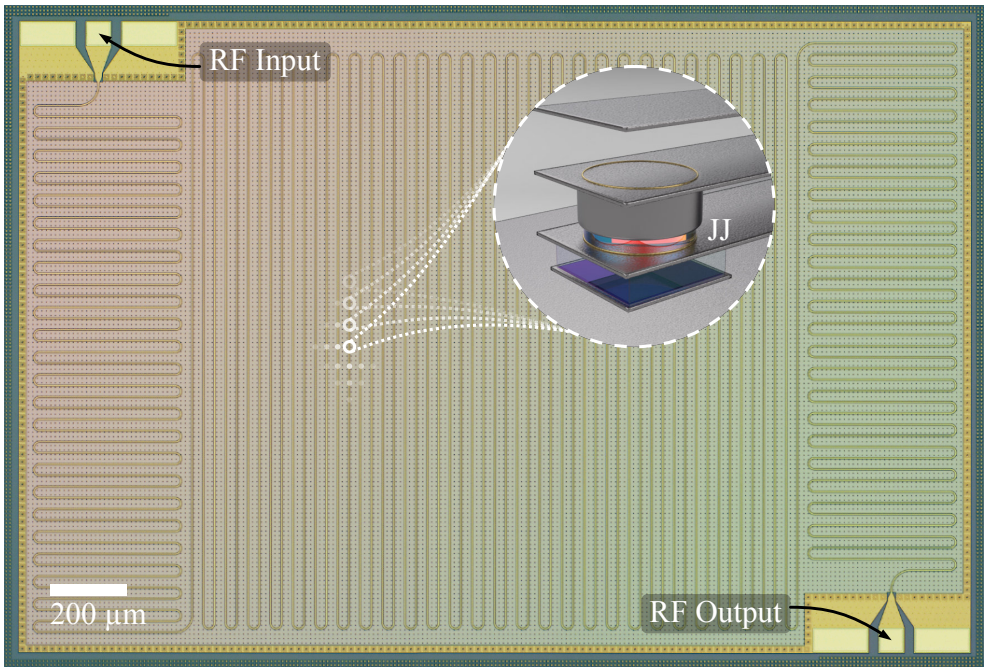



**Figure 3.20:** Optical micrograph of the fabricated phase shifter. The signal is given at the RF input, which connects to a meandered microstrip line coupled with rf-SQUIDs and a phase shift is observed in the signal at the RF output.

Fig. 3.20. This design of phase shifter has 2256 rf-SQUIDs placed directly below a meandered microstrip TL. The total device footprint is 2.5 mm x 1.6 mm.

By varying the analog control current injected on the RF line via a bias tee, it is possible to control the variable inductance resulting from the coupling between the rf-SQUIDs and the TL, subsequently affecting the phase of the transmitted signal. The device is tested at a temperature of 4 K in a cryogenic probe station shown in Fig. 3.18. A control current is provided on the superconductor TL, increasing linearly from 0 mA to 36 mA.

The measured RF performance including the phase shift, insertion loss, and return loss of the phase shifter over dc to 26.5 GHz is shown in Fig. 3.21. The measured phase shift is highlighted in *X*-band and *K*-band in Fig. 3.21(a) and (b), while the *S*-parameters are given in Fig. 3.21(c) for a minimum current $I_{\text{min}}$ of 0.1 mA and a maximum current $I_{\text{max}}$ of 36 mA . A total relative phase change of 130° is seen at 10 GHz and 328° at 22.25 GHz. The insertion loss variation of the phase shifter over the *X*-band and *K*-band is 0.46±0.23 dB and 2.5 ± 1 dB, respectively. The return loss is better than 20 dB over the *X*-band and better than 14 dB in the *K*-band.

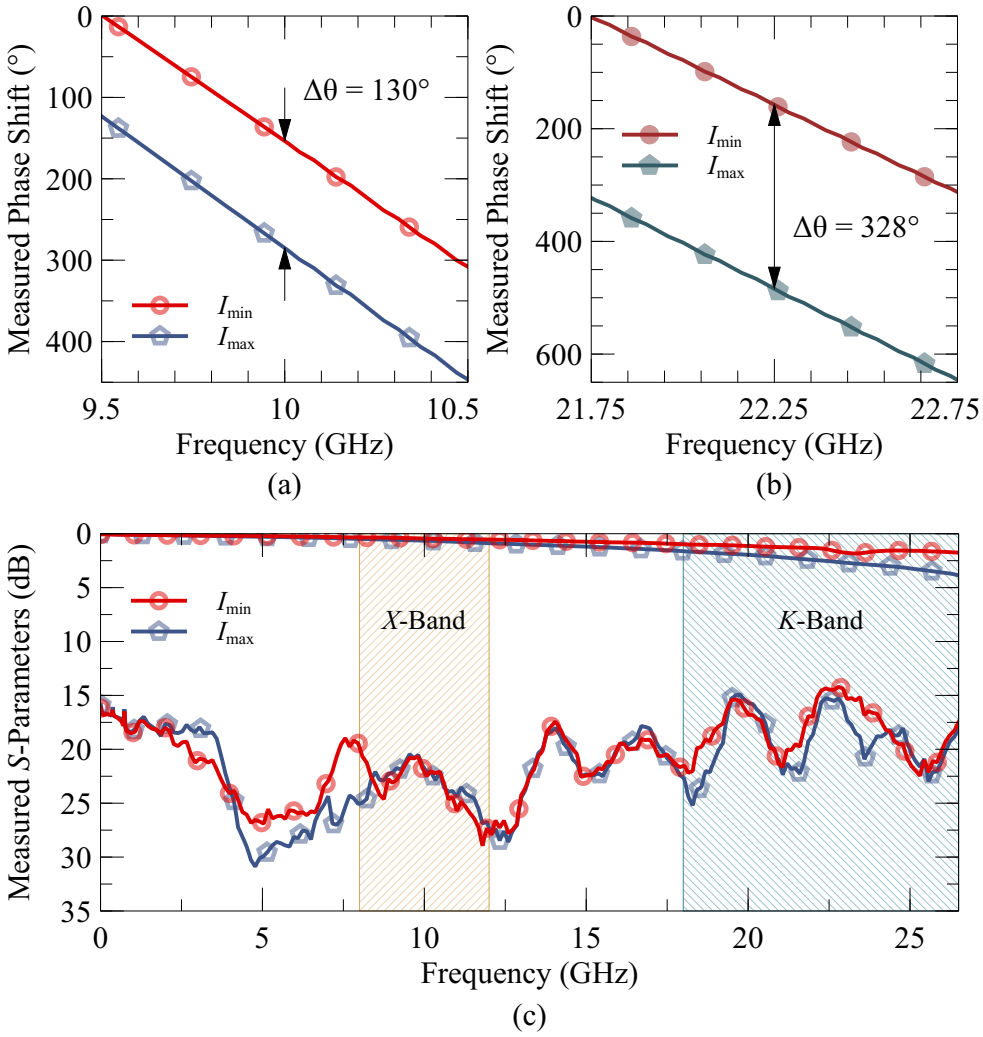



**Figure 3.21:** Measured relative phase shift and $S$-parameters of the phase shifter with control current of $I_{min} = 0\,\text{mA}$ and $I_{max} = 36\,\text{mA}$ over (a) 9.5 GHz to 10.5 GHz, (b) 21.75 GHz to 22.75 GHz, (c) insertion loss and return loss for the frequency range 0 GHz to 26.5 GHz.

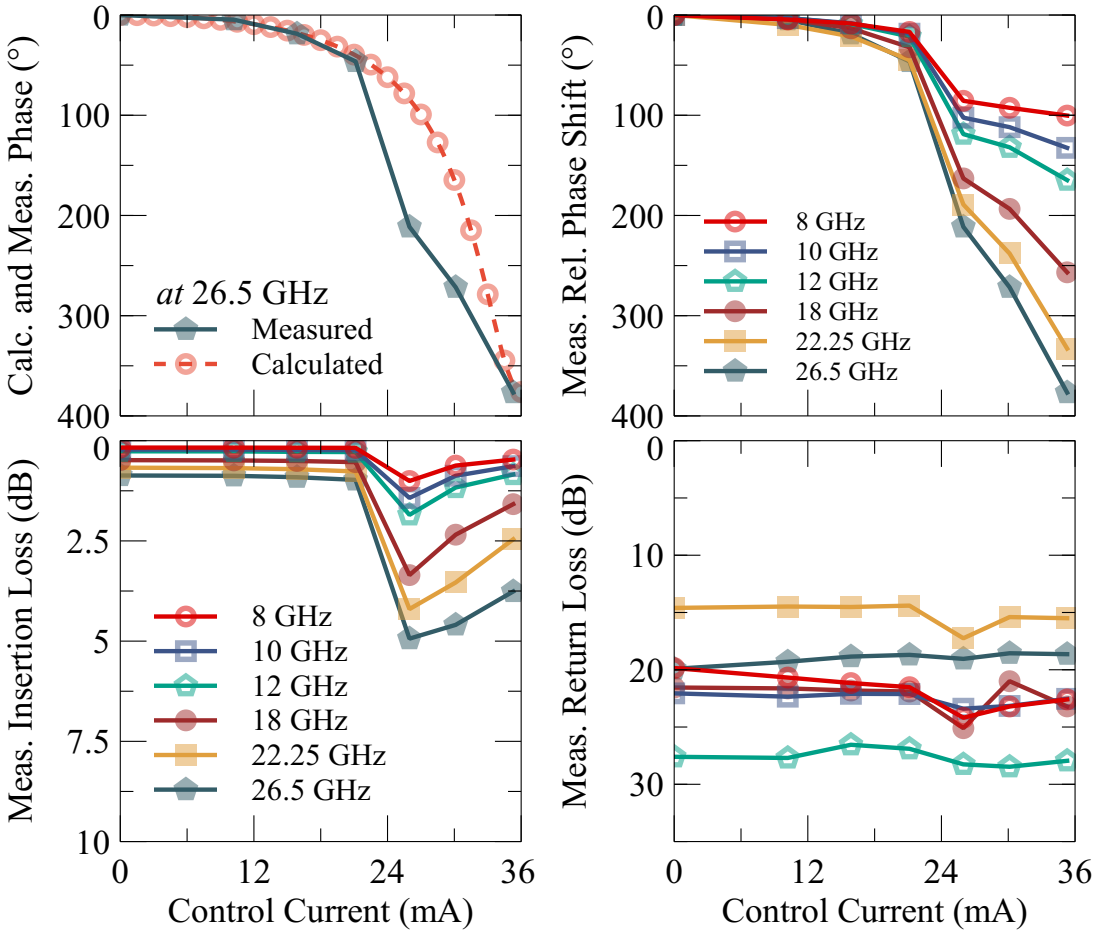



**Figure 3.22:** Measurement results of the phase shifter for a control current ranging from 0 mA to 36 mA. The phase shift, insertion loss and return loss for three different frequencies in the *X*-band and *K*-band are shown.

The theoretically calculated phase based on the expression given in section 3.2 at 26.5 GHz is shown along with the measured phase shift from the fabricated device in Fig. 3.22. The analytical solution does not include parasitic elements along the TL, thus a resonant behavior around 26 mA in the measured device can not be predicted with a theoretical model. The measured RF response of the device with respect to control current at the center and two extreme frequencies in the *X*-band (8 GHz, 10 GHz, 12 GHz) and *K*-band (18 GHz, 22.25 GHz, and 26.5 GHz) is also shown. In the *X*-band, the maximum relative phase shift of 100°, 132° and 165° is achieved at 8 GHz, 10 GHz

and 12 GHz, respectively. The corresponding insertion loss at the three frequencies stays at an almost constant level for lower current values and later shows an increase, with the maximum insertion loss being 1.85 dB at 12 GHz at a control current of 26 mA. The return loss at all three frequencies for the entire control current range is better than 20 dB. The phase shift of the device at the *K*-band frequencies follows a similar pattern, with maximum relative phase shift of 257°, 332° and 376° and insertion loss variation of $1.92\pm1.4$ dB, $2.44\pm1.7$ dB, and $2.9\pm2$ dB observed at 18 GHz, 22.25 GHz and 26.5 GHz, respectively. The return loss at 18 GHz is better than 14 dB for the three frequencies in *K*-band.

The phase tunability can be further optimized by tuning the junction diameters and also the total length of the rf-SQUID loops. The measured average resistance of the phase shifter remains stable at 0.83 Ω with varying control current, exhibiting a power consumption of less than 1 mW at maximum control current.

To conclude, the proposed LTS-based phase shifter demonstrates analog ultra-wideband response in the X- and K-bands. A maximum relative phase shift of 130° and 328° is obtained at 10 GHz and 22.25 GHz, respectively, with a control current of 36 mA.

# Chapter 4

# Superconducting Microwave Resonator and Reflective Type Phase Shifter

## 4.1 Superconducting Tunable Microwave Resonator

Superconducting tunable microwave resonators are popular for their applications in microwave tunable filters [62, 63], tunable couplers [64], tunable parametric amplifiers [65], SQUID multiplexers [66–68], astrophysical detectors [69], and scanning microwave microscopes [70]. With the booming interest in quantum computing, the superconducting resonators are highly in demand for the qubit readout, capture, storage, on-demand release, and routing of single microwave photons [71–73].

The most common approach for developing superconducting resonators primarily benefits from the current-dependence/magnetic-field dependence of nonlinear kinetic inductance (KI) in a superconducting transmission line [74, 75]. Coplanar waveguide (CPW) resonators have shown tunability through the application of a perpendicular magnetic field, but the tunability range is limited to only few MHz, or 0.05% for a 6 GHz resonator [76]. A tunability range of 6% and 15%, based on a change of kinetic inductance with dc current has been observed in ultra-thin Niobium (Nb) and Niobium Nitride (NbN) nanowires, respectively, with widths of approximately 100 nm [77]. A resonance frequency tunability of 180 MHz around 4.5 GHz is reported in a superconducting resonator made from niobium titanium nitride (NbTN) film [78]. Very recently, superconducting resonators have been implemented using Josephson Junctions (JJs) or rf-SQUIDs as tunable inductors. The tunability is achieved by

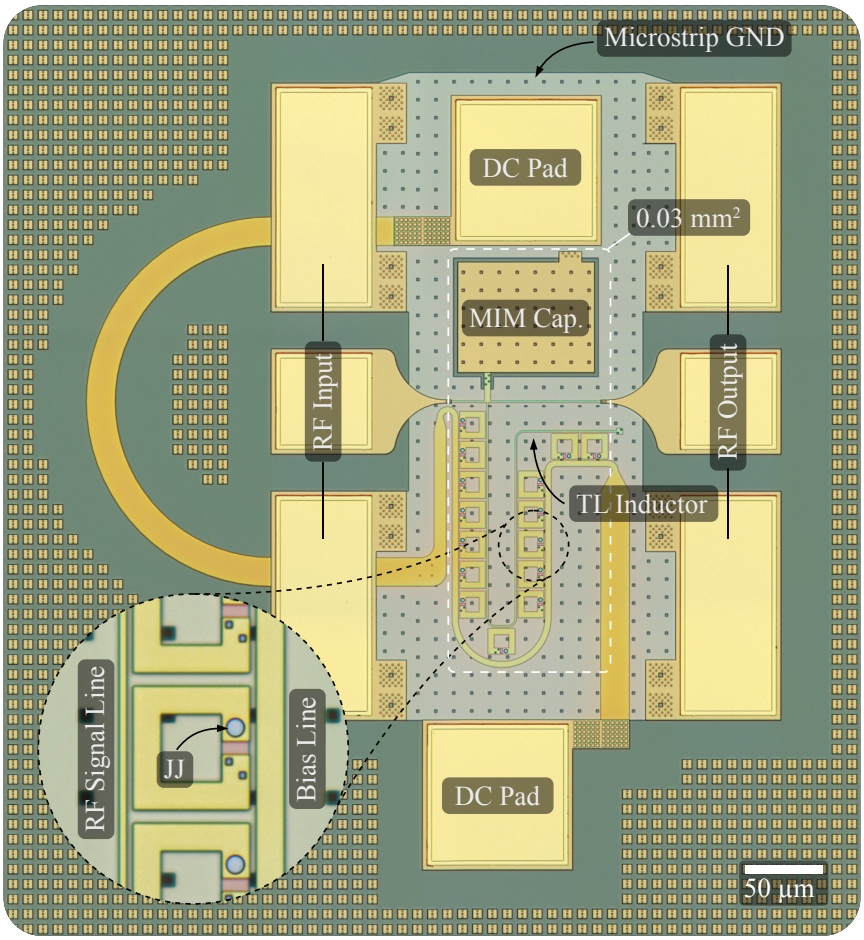



**Figure 4.1:** Optical micrograph of the LTS resonator highlighting the MIM capacitor and the microstrip TL inductor connected in shunt with the central microstrip connecting two RF ports. The control line runs parallel to the rf-SQUIDs array and terminates in a DC pad on each end. The inset highlights the rf-SQUID loop placed between the microstrip inductor (carrying the RF signal) and the dc control line.

applying an external magnetic field. Most of the reported superconducting resonators use a single rf-SQUID and provide a tuning range of typically about 500 MHz [79–82].

The design and experimental data of a tunable resonator using an array of rf-SQUIDs as the tunable element is presented in the following sections. This resonator is excellent for monolithic integration with other low-temperature superconducting (LTS) integrated circuits requiring a wide tunability range and high tuning speed.

### 4.1.1 Design and Operation Principle of the Tunable Resonator

An optical micrograph of the fabricated resonator is shown in Fig. 4.1. It consists of an RF input port and output port connected by a superconducting microstrip transmission line (TL). A multi-layer metal-insulator-metal (MIM) capacitor and a microstrip inductor are connected in shunt with the TL section. The MIM capacitor and the microstrip tunable inductor are sized to tune the resonance frequency within the frequency band 4 GHz to 8 GHz, which is one of the most popular for the quantum systems. The tunable inductor is implemented using a transmission line loaded with an array of rf-SQUIDs and is terminated in a short circuit. A second TL carrying a dc current is placed adjacent to the array of rf-SQUIDs to tune their inductance. Through mutual coupling, the tunable inductance of the SQUID tunes the effective inductance of the microstrip transmission line, thus making the resonance frequency of the resonator tunable. The SQUID inductance can be tuned by either one of the control mechanisms: externally applied magnetic field using the dc current carrying TL or by varying the input RF power. The design parameters of the presented resonator are given in Table 4.4. Another variation of the resonator design using a single RF port can also be made by placing both the inductor and capacitor elements in series instead of shunt as shown in Fig. 4.2.

The microstrip TL inductor is designed by placing the top conductor and the ground plane on two different Nb layers spaced with layers of $SiO_2$ to achieve a characteristic impedance $Z_0 = 50\,\Omega$. The rf-SQUID used in the design is a Nb-based superconducting loop shunted by a single Nb-$AlO_x$-Nb JJ. The superconducting loop can be designed either on the same microstrip signal Nb layer in the form a ring as shown in the inset of Fig. 4.1. Alternatively, the SQUIDs can be placed between the top conductor of the microstrip and the ground plane using two additional Nb layers [83]. The inductor TL is terminated in a short circuit and is folded in order to reduce the chip area. An array of fifteen rf-SQUIDs is laid out along the length of the microstrip inductor. The dc control current could also be potentially applied to the microstrip TL through bias tees directly on the RF input port [57, 83]. In that case, the control current cannot be exceeded beyond the threshold critical current of the superconductor or the material will switch to its non-superconducting state and the device performance suffers significantly.

In the proposed design, we have used a separate control TL which runs parallel to the rf-SQUIDs and is terminated by a dc pad on each end to provide the control current. Hence, the rf-SQUID loop lies between the RF microstrip signal line and the control line as shown in Fig. 4.1 and Fig. 4.2. The amount of dc current provided to the control

**Table 4.1:** Design specifications of Superconducting Resonator

| **Name of the Parameter** | **Value** |
|---|---|
| Width of microstrip inductor line | 1 μm |
| Area of each plate of MIM capacitor | 91 μm × 73 μm |
| Area of each SQUID loop | 18 μm × 17 μm |
| Number of SQUIDs | 15 |
| Diameter of circular JJs | 3 μm |
| Critical current of JJ | 0.707 mA |
| Gap between rf-SQUIDs and microstrip inductor | 1 μm |
| Gap between adjacent rf-SQUIDs | 2 μm |
| Width of dc control line | 4 μm |

line determines the flux coupled to the SQUID inductance loops which changes the dynamic inductance of the rf-SQUID. The SQUIDs act as variable inductors, and since they are magnetically coupled to the inductor microstrip TL section, change in SQUID inductance causes change in the resonator inductance and hence the resonance frequency.

When an external control current $I_{\text{ext}}$ is provided to the control line with inductance $L_c$, a magnetic field is generated, which produces an external magnetic flux $\phi_{\text{ext}}$ given by:

$$\phi_{\text{ext}} = L_c I_{\text{ext}} \tag{4.1}$$

When the SQUID loop with a self-inductance $L_s$ is threaded by the external flux $\phi_{\text{ext}}$, due to flux quantization condition, a circulating current $i_s$ is induced in order to screen this flux. The flux due to the circulating current also adds to the total flux $\phi_s$, which is expressed as:

$$\phi_s = \phi_{\text{ext}} + L_s i_s \tag{4.2}$$

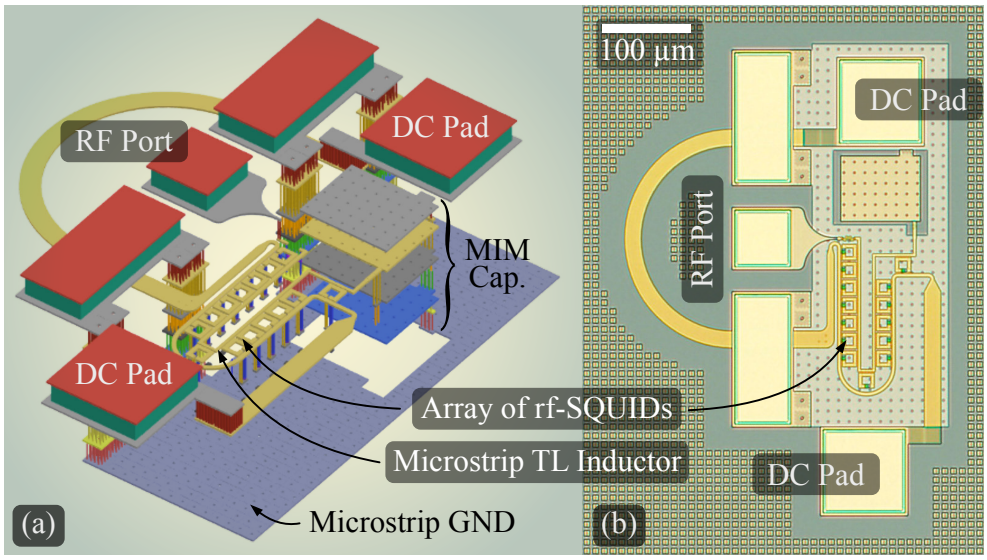



**Figure 4.2:** (a) 3D view of the proposed LTS resonator layout comprising a single RF port, a MIM capacitor, a microstrip TL inductor and an array of rf-SQUIDs, (b) Optical micrograph of the fabricated device.

The amount of circulating supercurrent is determined as:

$$i_s = -I_c \sin\left(\frac{2\pi\phi_s}{\phi_0}\right) \tag{4.3}$$

where, $I_c$ is the critical current of the JJ and $\phi_0 = 2.0679 \times 10^{-15}$ is the magnetic flux quantum.

The superconducting loop inductance $L_s$ is coupled to the TL inductor $L_r$ with mutual inductance $M$. The value of mutual inductance $M$ depends on the gap between the rf-SQUID and the microstrip TL. The coupling coefficient $K$ and the screening parameter $\beta$ of rf-SQUID are given by:

$$K^2 = \frac{M^2}{L_r L_s}, \qquad \beta = \frac{2\pi L_s I_c}{\phi_0} \tag{4.4}$$

The inductance is then varied by the magnetic field generated by the dc current carrying wire placed on the side. The effective inductance of the microstrip line is then

given as:

$$L_r' = L_r(1 - \Delta L) \tag{4.5}$$

where $\Delta L$ is given by:

$$\Delta L = \frac{K^2}{1 + 1/\beta \cos(2\pi\phi_s/\phi_0)} \tag{4.6}$$

If $C_r$ is the capacitance of the MIM capacitor, then in the absence of control current, the resonance frequency is given by $f_r = 1/2\pi\sqrt{L_r C_r}$. Providing a control current will change with the variable inductance of the TL and the resonance frequency changes by $f_r' = 1/2\pi\sqrt{L_r' C_r}$. Using an array of rf-SQUIDs and high critical current JJs allows us to obtain wider tunability range.

### 4.1.2 MIM Capacitor

Multi-layer stacked MIM capacitor is used as it offers higher capacitance density and higher self resonance compared to the interdigitated capacitor design. The entire MIM multi-layer stack shown in the 3D view in Fig. 4.2 consists of four Nb metal layers and three dielectric layers in between the metal layers, effectively realizing three capacitors connected in parallel. A higher capacitance using a smaller area is achieved, thanks to the extremely thin $SiO_2$ dielectric layer between the Nb layers allowed by the fabrication process. The design uses a stack of four Nb 91 µm × 73 µm rectangular sections separated by three ≈ 200 nm thick dielectric layers. The capacitance value offered by the stack can be closely estimated by means of Sonnet EM simulations. The simulated value of capacitance is 4.85 pF and the self resonance was >11 GHz. The overall capacitor area can be further reduced and the value of achieved capacitance can be increased by increasing the number of stacked metal layers as the fabrication process allows for 8 Nb layers.

### 4.1.3 Experimental Measurements of Superconducting Resonator

The frequency response of the fabricated resonator is measured using the Lakeshore probe station, Keysight performance network analyzer (PNA-X) and a source measurement unit (SMU). All measurements are performed at the cryogenic temperature of 3.8 K achieved using liquid nitrogen, followed by liquid helium. The

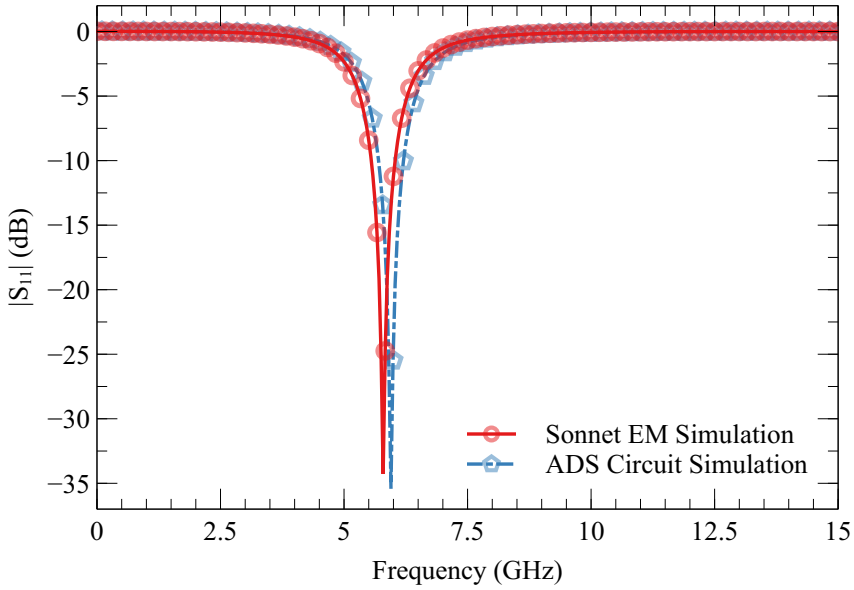



**Figure 4.3:** Simulated $S_{11}$ of the resonator using ADS circuit simulation and Sonnet EM simulation showing a close match.

device response is simulated starting from a circuit model in Keysight ADS followed by a Sonnet EM simulation as shown in Fig. 4.3. The $S$-parameters of the resonator are measured as a function of the applied control current to the dc control line. As shown in the measurements given in Fig. 4.4, with no dc current flowing in the control line, the device shows resonance peak at 5.63 GHz. For a control current sweep from 0 mA to 2 mA, a tunability of 1.24 GHz is observed. Fig. 4.5 shows the corresponding phase of $S_{11}$ for the tunable range.

We also measured the resonance response of the device by varying the RF power provided at the input port of the resonator as shown in Fig. 4.6. A few MHz frequency shift is observed for the initial increase in RF power, but rapid change can be seen after −10 dBm. In actual system applications, such resonators operate at a power level that is almost constant.

Table 4.5 compares the proposed resonator with the current state-of-the-art. Various superconducting resonators are compared on the basis of overall dimensions, tuning range, operation frequency, design topology and superconductor material used. Most of the superconducting resonators in literature utilize kinetic inductance based resonance frequency tuning. The disadvantage of such approach is the low tuning

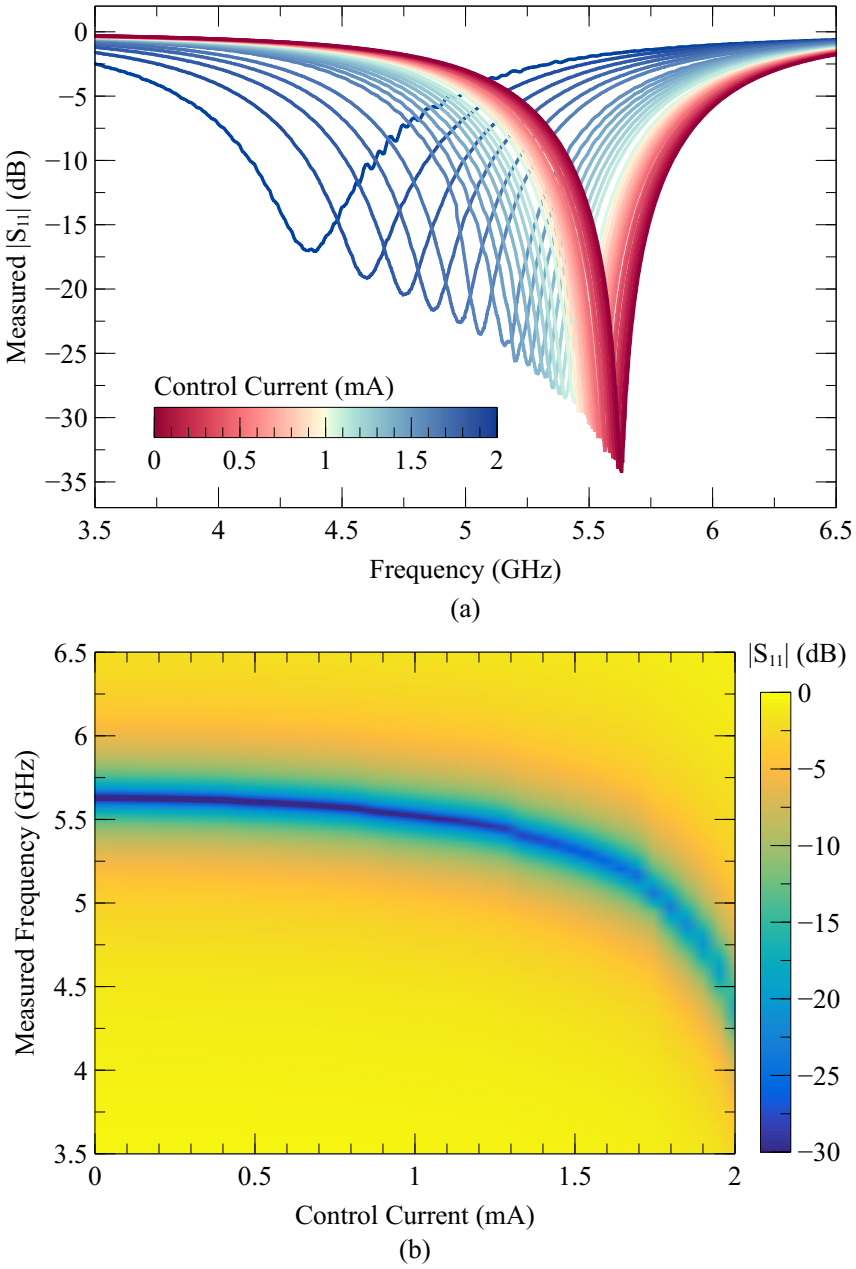



**Figure 4.4:** (a) Measured $S_{11}$ of the resonator for a control current sweep from 0 mA to 2 mA. (b) Resonance frequency shift as a function of control current.

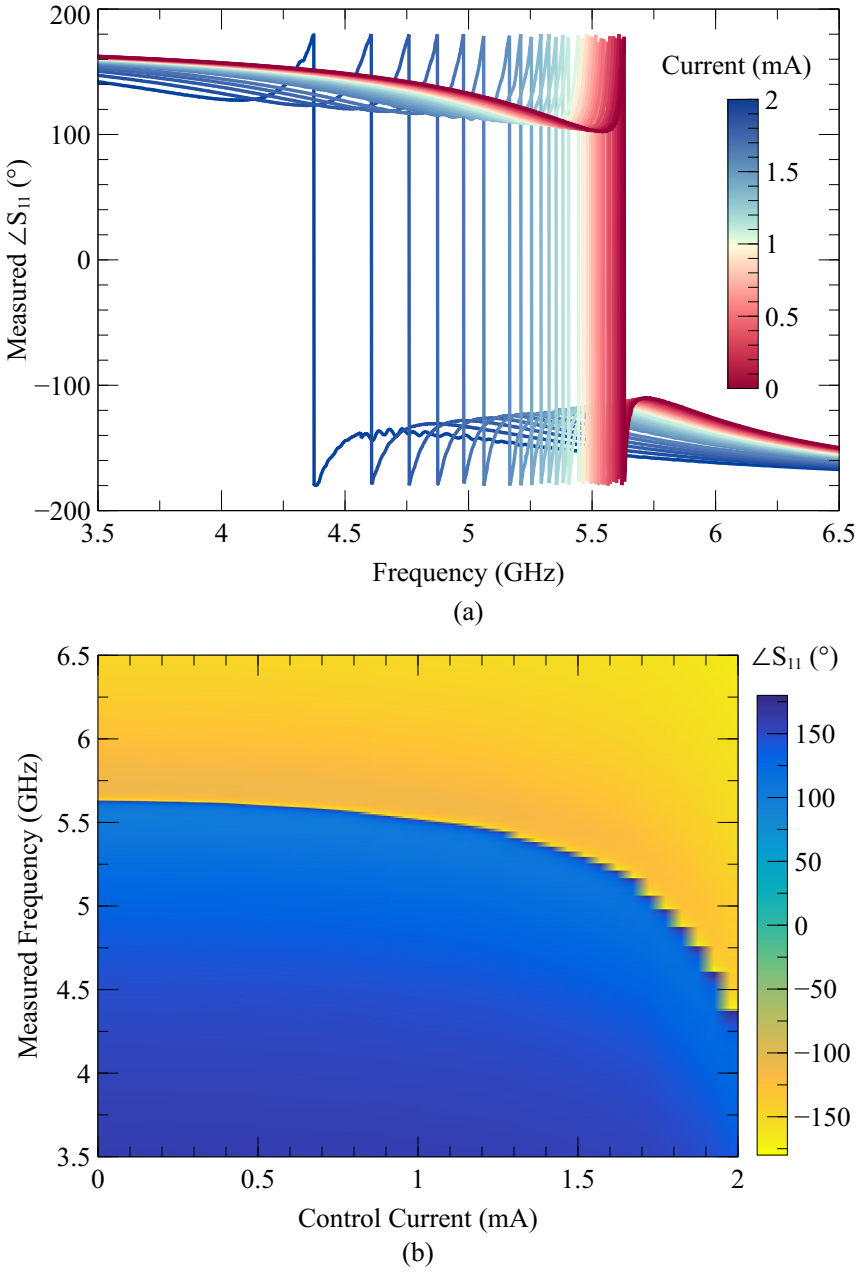



**Figure 4.5:** (a) Measured $S_{11}$ of the resonator for different values of RF power ranging from $-30$ dBm to 0 dBm. (b) Resonance frequency shift as a function of input RF power.

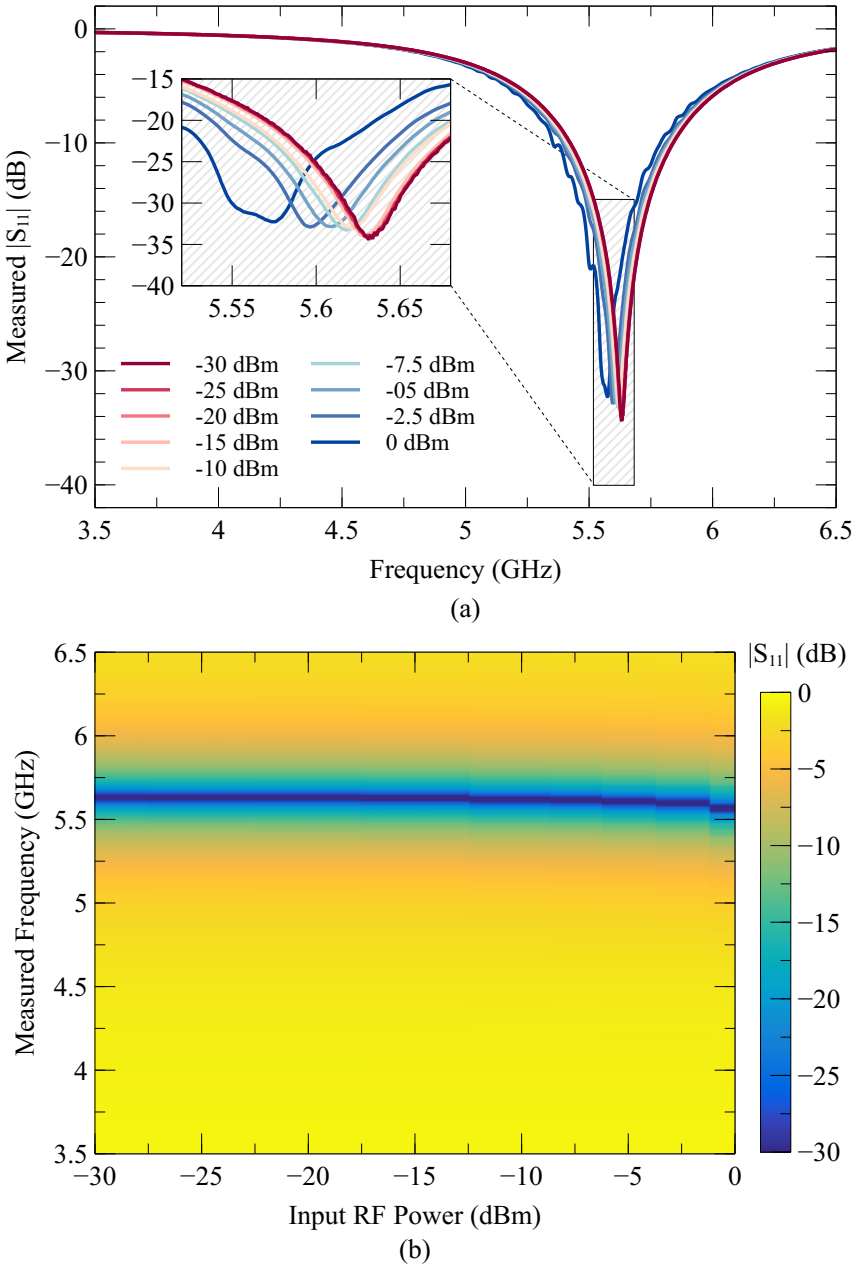



**Figure 4.6:** (a) Measured $S_{11}$ of the resonator for different values of RF power ranging from $-30$ dBm to 0 dBm. (b) Resonance frequency shift as a function of input RF power.

**Table 4.2:** Comparison of the proposed superconducting resonator with state-of-the-art

| | **Res. Freq. (GHz)** | **Design Topology** – | **LTS/ HTS** – | **Control Type (Magnetic field/current)** | **Overall Size (mm × mm)** | **Tuning Range (MHz)** | **No. of SQUIDs Used** |
|---|---|---|---|---|---|---|---|
| This | 5.63 | SQUIDs | Nb | DC current (0 mA to 2 mA) | 0.11 × 0.28 | 1240 | 15 |
| [76] | 6 | KI | Nb | Mag. Field (−0.2 mT to 0.2 mT) | 10 × 3 | 2 | NA |
| [74] | 2.4 | KI | NbN | DC current (0 mA to 3.5 mA) | 2.7 × 0.9 | 62 | NA |
| [75] | 7.6 | KI | NbTiN | DC current (0 mA to 5 mA) | 11.14 × 7.14 | 95 | NA |
| [78] | 4.5 | KI | NbTiN | DC current (0 mA to 0.25 mA) | 0.15 × 0.45 | 180 | NA |
| [79] | 4.54 | SQUIDs | Al | Mag. Flux($\phi/\phi_0$) (−0.5 to 0.5) | 0.16 × 0.22 | 580 | 6 |
| [80] | 6.9 | SQUIDs | Al | Mag. Flux($\phi/\phi_0$) (−0.5 to 0.5) | 2.59 × 1.36 | 670 | 1 |
| [81] | 7.41 | SQUIDs | Nb | Mag. Field (0 μT to 10 μT) | 1.15 × 1.55 | 100 | 1 |
| [82] | 5 | SQUIDs | Nb/Al | Mag. Flux($\phi/\phi_0$) (−0.5 to 0.5) | 5.4 × 5.4 | 700 | 2 |

range. Other designs using rf-SQUIDs for frequency tuning, however, use only one or a maximum of 6 rf-SQUIDs, which limits the tuning range. The proposed resonator not only provides a large tuning range with fine analog tuning response but also has the smallest device footprint compared to the state-of-the-art.

To conclude, a compact LTS microwave resonator with a large tuning range of 1.24 GHz at a fundamental resonance frequency of 5.6 GHz is presented. The tunability is achieved by coupling an array of rf-SQUIDs to a mirostrip TL by varying the control current via on-chip external dc control circuitry. The proposed resonator circuit is fabricated using a multi-layer Nb-based microfabrication process node. The presented device is compared with the current state-of-the-art highlighting largest tuning range and smallest device footprint. The tuning range of the resonator can be further enhanced by increasing the array size of the rf-SQUIDs, which makes this presented design scalable. Superconductor resonators have a potential use in various reconfigurable microwave devices.

## 4.2 LTS Wideband Quadrature Hybrid Couplers

Quadrature hybrid couplers are used to combine and split the microwave signal and serve as an important part of complex monolithically integrated circuits and systems [84–88]. Cryogenic test systems employ 90° hybrid couplers along with the active circuitry such as cryogenic mixers and balanced amplifiers [89, 90]. Recently, the superconducting hybrid couplers have been explored for applications in quantum information processing circuits [91][92]. While room temperature hybrid couplers are commercially available, they are bulky and cannot be easily integrated with cryogenic circuits. Very few papers are reported on wideband niobium-based hybrid couplers operating at 4 K [93].

There are different configurations for building hybrid coupler such as, branch line, Lange, tandem coupled line designs [94]. While the first two offer a narrowband coupling performance, the last one offers a wideband performance, however, it requires a very tight gap between the coupled lines to achieve the desired 3 dB coupling, which can be a design constraint in many fabrication processes. The MIT-LL superconducting process [61] offers the feasibility of realizing very tight gaps between narrow width transmission lines. In the previous attempts to design tandem couplers, air bridges/bond wires are used to provide crossovers for tandem connections which have significant effect on the coupler performance. This fabrication process makes it possible to realize low loss bridges using the second niobium layer leading to a highly

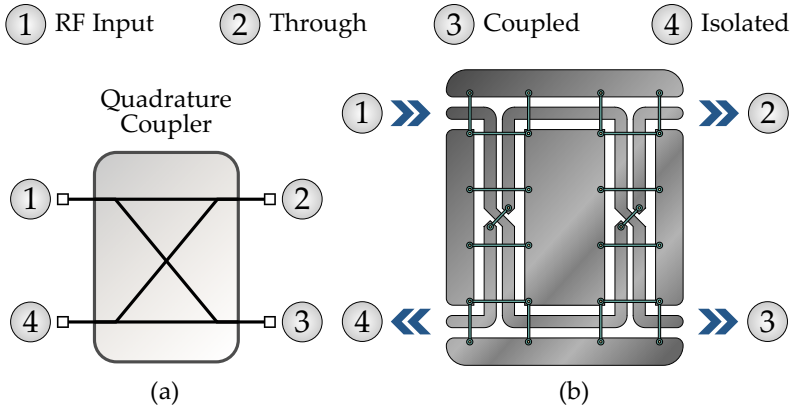



**Figure 4.7:** (a) Schematic of the quadrature hybrid coupler displaying all the four RF ports: Input, Through, Coupled and Isolated. (b) The design of CPW-based hybrid coupler using two tandem coupled lines and interconnections between signal lines and ground planes.

miniaturized design with relatively low insertion loss. In the section, design, simulations and measurements of quadrature hybrid couplers using a tandem coplanar waveguide (CPW) architecture from low temperature superconductor (LTS) Niobium (Nb) are presented. The design topology is well suited for monolithic integration with other superconducting components. The crossovers, which are essential for the tandem structure, are routed from a second niobium layer in a multi-layer fabrication process.

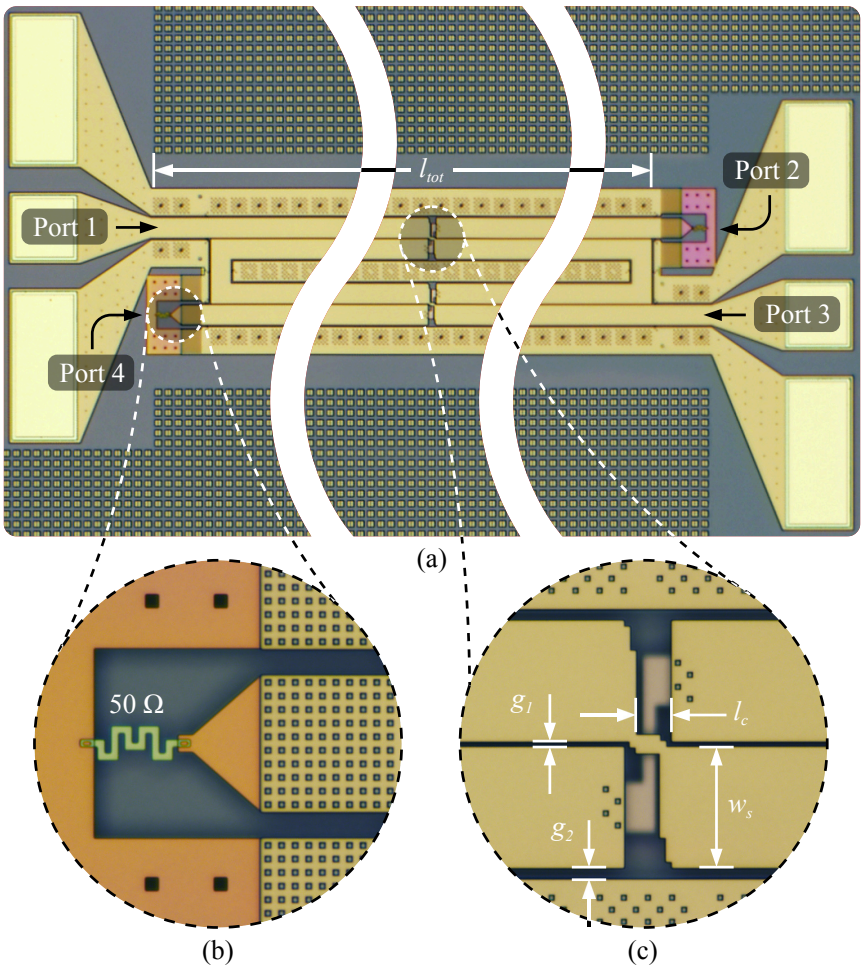



**Figure 4.8:** (a) Optical micrograph of the fabricated hybrid coupler. The length has been trimmed to include the ends and the center part of the design, (b) an enlarged image of the monolithically integrated 50 Ω micro resistor termination, (c) an enlarged image of the coupled lines crossover in the tandem design highlighting the dimensional parameters.

**Table 4.3:** Various parameters on device geometry

| Geometry Parameter | Hybrid Coupler design-A $f_0 = 30\,\text{GHz}$ | Hybrid Coupler design-B $f_0 = 10\,\text{GHz}$ |
|---|---|---|
| $l_{tot}$ | 864 µm | 2375 µm |
| $l_c$ | 6 µm | 6 µm |
| $w_s$ | 20 µm | 20 µm |
| $g_1$ | 1 µm | 1 µm |
| $g_2$ | 2 µm | 2 µm |

### 4.2.1 Design of CPW Based Hybrid Coupler

A CPW based tandem hybrid coupler design shown in Fig. 4.7 consists of two section CPW parallel-coupled lines. The hybrid coupler shown in Fig. 4.8 is a four-port device,

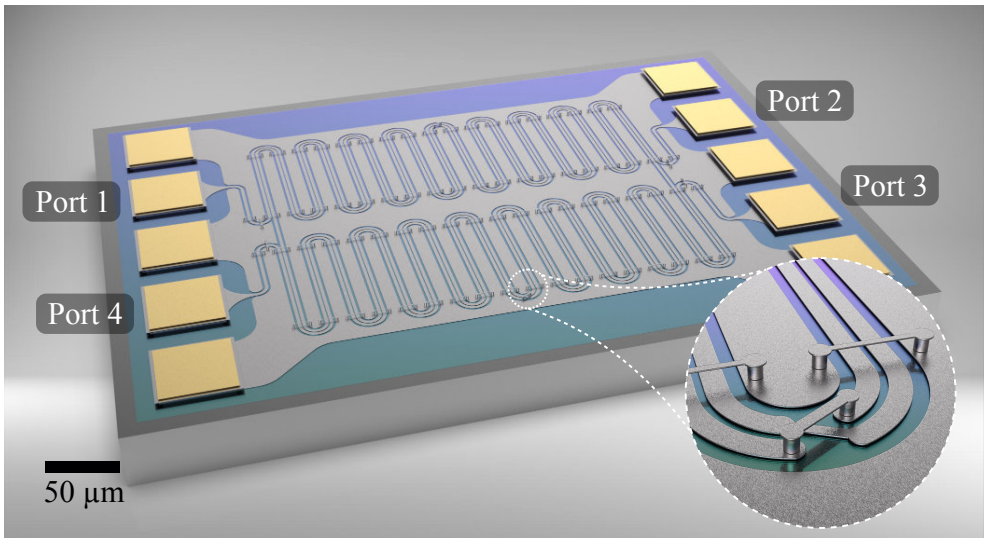



**Figure 4.9:** 3D rendered image of the meandered hybrid coupler design-C with a compact footprint of 0.45 mm×0.31 mm. The enlarged section shows the crossovers connecting the coupled lines and the ground planes.

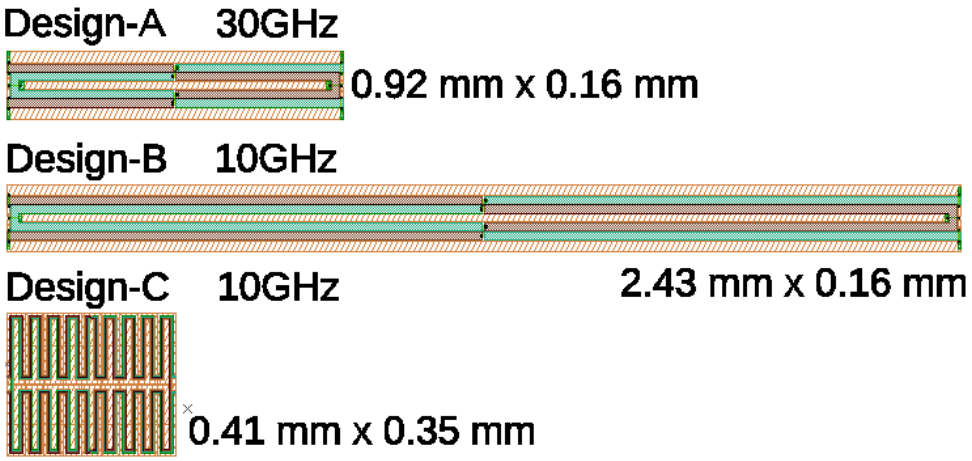



**Figure 4.10:** Size comparison of the hybrid couplers design-A, design-B, and design-C. The design-C has 64% smaller footprint compared to design-B while operating at the similar wide-band frequency range.

the input, through, coupled and isolated ports are referred to as ports 1,2,3 and 4, respectively. The signal provided at input port 1 is split equally between the direct port 2 and the coupling port 3, while port 4 acts as the isolation port. Tandem configuration, comprising the $n$-section parallel-coupled lines, can achieve a high coupling even with relatively low coupling values of the individual sections. The design has two center conductors placed side by side and the bridges, designed to connect the individual ground planes and the signal lines, are placed on the second niobium layer through vias. The 50 Ω micro resistor termination is shown in the enlarged section in Fig. 4.8(b), and (c) highlights the connection between the signal lines at the crossover, achieved through vias and a second metal layer at the bottom. Both the coupled and through lines in the design are selected to be quarter wavelength long ($\lambda/4$) at 10 GHz for the first hybrid design-A and at 30 GHz for the second hybrid design-B.

The design dimensions are then finely optimized in simulation using Sonnet EM to get the desired RF performance. The optimized dimensional parameters used in design-A and design-B are listed in Table 4.3 with the only difference between design-A and design-B being the length of the coupled lines.

Designing a hybrid coupler at lower frequencies requires longer length of the tandem coupled lines, hence, Fig. 4.9 shows a highly compact design for the hybrid coupler design-C. In this design, the coupled lines are carefully meandered such that they fit in an area 64% less than the hybrid coupler design-A with the same center frequency of

10 GHz as shown in Fig. 4.10. The crossovers in the rendered image (Fig. 4.9) are shown as air bridges for illustration and better understanding.

### 4.2.2 Simulations and Experimental measurement

The hybrid coupler designs are simulated using Sonnet EM and Fig. 4.13 shows the simulated S-parameter response of the hybrid coupler design-B. The lakeshore cryogenic probe station used for measurements has only two RF GSG probes, hence, the network analyzer is connected to two out of four ports of the hybrid coupler, while the other two ports are terminated in 50 Ω load. A standalone design of the micro resistor shown in Fig. 4.11 was tested, and the measurement results show good agreement with the simulated response over the 10 MHz to 50 GHz frequency range. The CPW pads and tapers were de-embedded during micro resistor measurement.

Measurement results of the hybrid coupler design-A at 4 K are shown in Fig 4.12, and are in agreement with the simulated response in Sonnet EM. The device shows excellent 3 dB coupling over the frequency range of 26 GHz to 44 GHz with less than 0.5 dB insertion loss at the coupling and through ports, and the return loss is better than 24 dB. The hybrid coupler design-B designed at the center frequency of 10 GHz demonstrates 3 dB coupling response from 8 GHz to 18 GHz with the measured insertion loss at the coupled port <1 dB and return loss >22 dB as shown in Fig. 4.13. The device measurements show excellent agreement with the simulation results. The

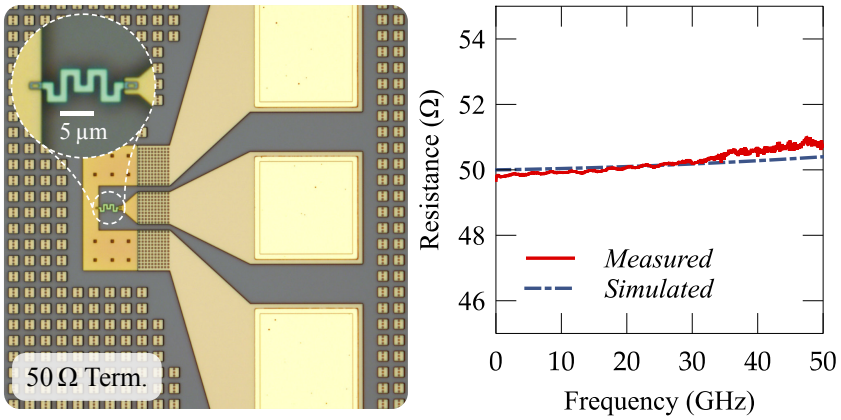



**Figure 4.11:** Left: Optical micrograph of a single port integrated 50 Ω termination used for verification, right: The simulated and measured response of the termination from dc to 50 GHz.

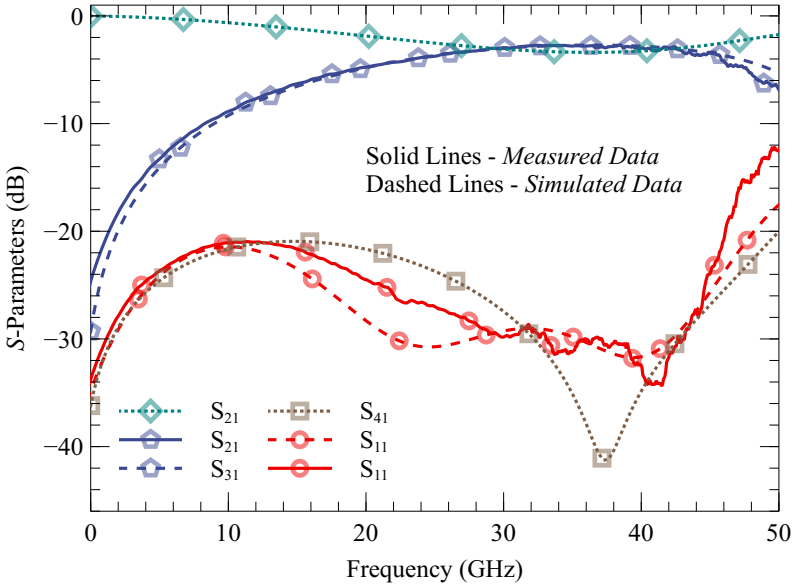



**Figure 4.12:** Simulation and measurement of the hybrid coupler design-A with the desired coupling performance observed over the 26 GHz to 44 GHz frequency range.

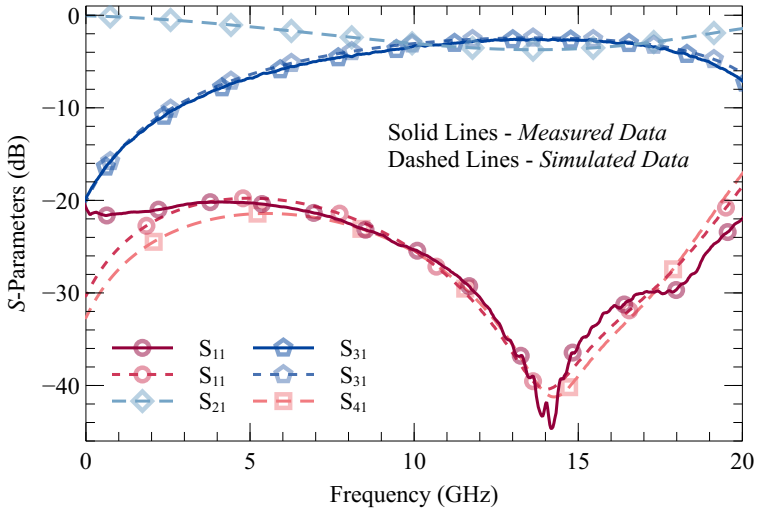



**Figure 4.13:** Simulated and measured S-parameters of the hybrid coupler design-B showing excellent coupling for the frequency range 8 GHz to 18 GHz. The simulation results are represented by dotted lines, and the solid lines demonstrate the measured response of the device.

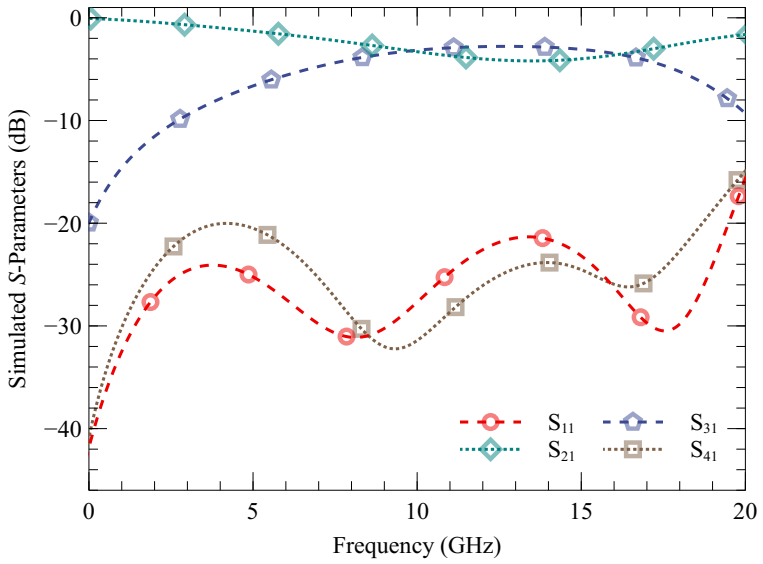



**Figure 4.14:** S-parameters simulation of the compact hybrid coupler design-C showing the 3 dB coupled response between 8 GHz and 18 GHz.

simulated S-parameter results for the proposed compact hybrid coupler design-C are displayed in Fig. 4.14. The coupler demonstrates an insertion loss less than 1 dB over the frequency range 8 GHz to 18 GHz and the return loss and isolation better than 20 dB.

To conclude, the design and measurement results of two fabricated wideband quadrature hybrid couplers using tandem coupled lines are discussed. A highly compact version of hybrid coupler using meandered coupled lines with 64% area reduction compared to the original design is also demonstrated. Hybrid couplers are important passive components used in various microwave circuits such as mixers, balanced amplifiers and phase shifters.

To conclude, the design and measurement results of two fabricated wideband quadrature hybrid couplers using tandem coupled lines are discussed. A highly compact version of hybrid coupler using meandered coupled lines with 64% area reduction compared to the original design is also demonstrated. Hybrid couplers are important passive components used in various microwave circuits such as mixers, balanced amplifiers and phase shifters.

## 4.3 Reflective Type Phase Shifter

The advances towards the use of microwaves in the quantum signal processing regime have inspired research on a suite of superconducting RF components such as circulators, isolators, Josephson parametric amplifiers, beam splitters, phase shifters, and kinetic inductance travelling wave amplifiers. Although many room-temperature phase shifters are available in the literature using CMOS, SiGe, Phase change material (PCM) and MEMS technologies [4–7], the most important factor when employing microwaves for quantum technologies is the requirement of cryogenics. Considering the challenges involved in the successful delivery of room-temperature generated microwave signals to the qubit chip, for the furtherance of large-scale quantum systems, tremendous efforts are being made to integrate the microwave photon generation, modulation, and routing in the cryogenic conditions adjacent to the qubits [95]. In order to tune the phase of on-chip coherent microwave sources [3], a compact, low-loss, fast tunable, wide-band phase shifter is needed. In the chip-to-chip quantum network communication with microwave photons [96], the phase shifter provides the freedom to precisely control the propagating microwave photons enabling the transfer of quantum states between distant spaced qubits [97]. Very recently, superconducting phase shifters have found applications in the future secure communication using far-field microwave quantum technologies [98, 99].

A combination of ferroelectric/ferrite materials with high temperature superconductors (HTS) has been successfully used to obtain phase shifts at microwave frequencies [100–102]. Initial experimentation on using single HTS SQUID to achieve phase shift in microwave signals began in 1991 [103] and soon after, long arrays of LTS/HTS superconducting quantum interference devices (SQUIDs) (>1500) coupled with a microwave transmission line (TL) demonstrated to provide a tunable wave velocity, and hence, a phase shift at the output [58, 104, 105]. A phase shifter employing 2256 rf-SQUIDs has been recently proposed [83]. When the SQUIDs are coupled to an external magnetic flux, they behave as variable inductors coupled to the transmission line. The issue with the design [83] is that the phase shift is achieved at the expense of changing characteristic impedance of the TL leading to reflections at the input port, which is undesirable in the single-photon quantum applications.

In this section, a reflective-type phase shifter (RTPS) topology in which an array of rf-SQUIDs is used to achieve the dynamic inductance in the tunable reflective loads is demonstrated. The design uses fewer number of SQUIDs in comparison to the 2256 rf-SQUIDs used in [83]. In the proposed design, only 56 rf-SQUIDs are used in each tunable load to achieve the desired phase shift over a wide frequency band with

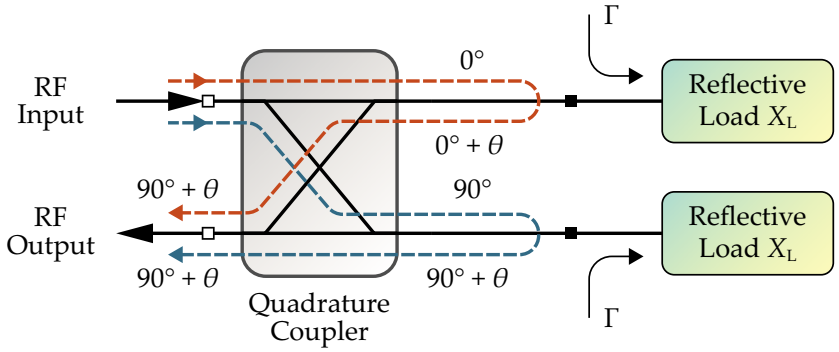



**Figure 4.15:** Schematic of the proposed reflection-type phase shifter (RTPS) consisting of a quadrature hybrid coupler terminated with two identical reflective loads. The input RF signal is split equally by the hybrid coupler, reflected off of the two reflective loads, and the phase shifted signal is obtained at the RF output. Γ is the reflection coefficient and $X_L$ is the tunable reactance of each reflective load.

minimum reflections.

### 4.3.1 RTPS Design and Operation Principle

The schematic of the proposed rf-SQUIDs-based RTPS is shown in Fig. 5.3 and the layout of the phase shifter is shown in Fig. 4.16. The total device area is 2.5 mm × 0.24 mm and the various dimensional parameters are given in Table 4.4. The RF signal is provided at the input port and the desired phase shifted signal is obtained at the output port. The output phase is controlled by the control current provided to the DC line, which tunes the flux threading each rf-SQUID loop, providing a phase shift between the signal at input and output port.

The proposed RTPS comprises of a 90° (quadrature) hybrid coupler and two identical reflective loads as shown in the circuit topology in Fig. 5.3. The designed quadrature hybrid coupler splits the signal provided at the input port equally between the through and coupled ports with 90° phase difference between them. The through and coupled ports of the hybrid coupler are terminated in identical tunable reflective loads. Hence, each half of the input signal reflects off of the reflective load and combines destructively (out-of-phase) at the input port, resulting in desired input matching, and constructively (in-phase) at the isolated port, giving the desired phase shift at output. Depending on the load type, the RF signal at input port will be transmitted to output port with its phase shifted by an angle $\theta_{out}$

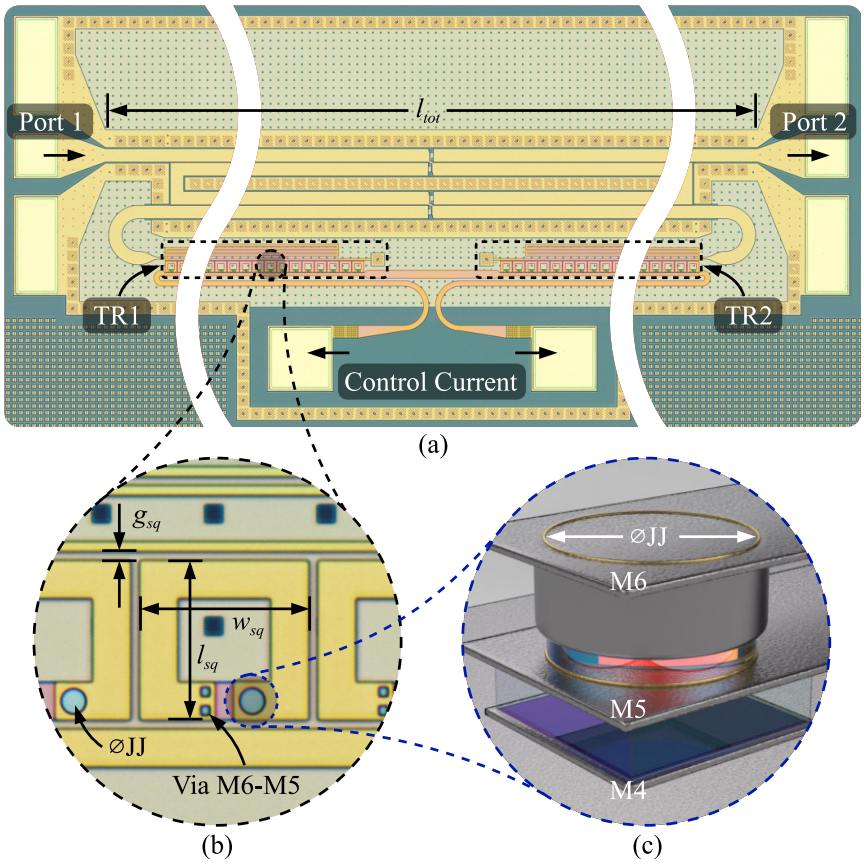



**Figure 4.16:** Layout of the proposed LTS based reflective-type phase shifter (RTPS) showing the monolithic integration of a hybrid coupler section with two identical reflective loads. An array of rf-SQUIDs is used to provide tunable inductance in each reflective load. Dimensional parameters of each rf-SQUID are highlighted along with the Nb/$AlO_x$/Nb JJ used in each SQUID loop.

If $Z_0$ is the characteristic impedance of the quadrature coupler and $Z_L$ is the impedance of the reflective load, the phase shift between input and output port will vary with the load impedance $Z_L$ as given by the relation:

$$\begin{aligned} \theta_{\text{out}} &= -\frac{\pi}{2} - 2\tan^{-1}\left(\frac{Z_L}{Z_0}\right) \\ &= \frac{\pi}{2} - \angle\Gamma_L \end{aligned} \tag{4.7}$$

**Table 4.4:** Design specifications of Superconducting Resonator

| **Name of the Parameter** | **Value** |
|---|---|
| Width of microstrip inductor line | 1 μm |
| Gap between rf-SQUIDs and microstrip inductor ($g_{sq}$) | 1 μm |
| Length of SQUID washer ($l_{sq}$) | 17 μm |
| Width of SQUID washer ($w_{sq}$) | 18 μm |
| Number of SQUIDs in each reflective load | 56 |
| Gap between adjacent rf-SQUIDs | 1 μm |
| Diameter of circular JJs | 3 μm |
| Critical current of JJ | 0.707 mA |
| Width of dc control line | 4 μm |

where $\angle\Gamma_L$ is the phase of the load reflection coefficient. $Z_L$ is the impedance of the reflective load, which is mainly reactive in superconducting circuits.

If $Z_{L\text{min}}$ and $Z_{L\text{max}}$ are the minimum and maximum impedance values of the tunable load, respectively, then the total phase shift range $\theta_{\text{range}}$ achieved can be described as:

$$\begin{aligned}\theta_{\text{range}} &= -2\left|\tan^{-1}\left(\frac{Z_{L\text{max}}}{Z_0}\right) - \left(\frac{Z_{L\text{min}}}{Z_0}\right)\right| \\ &= \angle\Gamma_{L\text{max}} - \angle\Gamma_{L\text{min}}\end{aligned} \tag{4.8}$$

where $\angle\Gamma_{L\text{max}}$ and $\angle\Gamma_{L\text{min}}$ are the maximum and minimum values of the phase of reflection coefficient. The device layout in Fig. 4.16 shows a hybrid coupler terminated by two monolithically integrated reflective loads. The impedance value of each reflective load is made tunable by using rf-SQUIDs.

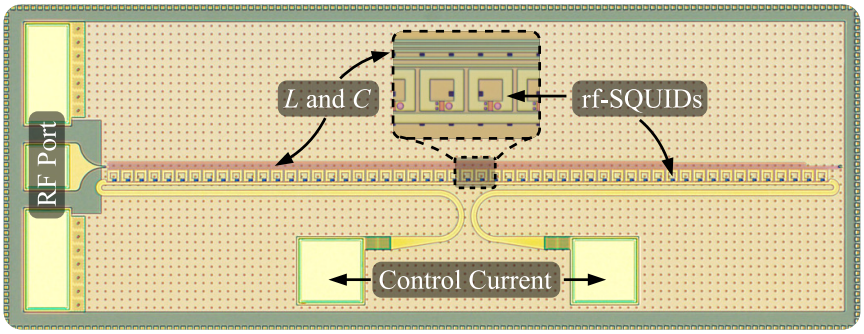



**Figure 4.17:** Fabricated micrograph of the standalone reflective load used in the proposed RTPS.

### 4.3.2 Tunable Reflective Load

The reflective load can be designed by using a combination of inductive and capacitive elements in many possible series and parallel configurations. The standalone reflective load section used in the proposed RTPS is shown in Fig. 4.17. The load design utilizes two shunt microstrip line sections, one of which ends in an open circuit (capacitive element) and the other microstrip section is terminated at the ground plane (inductive element). The dimensions of the microstrip sections are optimized using Sonnet EM simulator and meandered to achieve smaller footprint. We designed the resonant loads with the capacitive open-ended microstrip section 1 µm wide and 1000 µm long, and inductive short-ended microstrip section with width 1 µm and length 1076 µm. The vertical gap between the two Nb layers forming the microstrip signal line and ground plane is 0.615 µm. An rf-SQUID offers a variable inductance when coupled to an external magnetic flux. Adding an array of 56 rf-SQUIDs alongside the shorted microstrip section provides the tunability in load impedance and phase shift. The value of microstrip inductance changes with the change in inductance of the rf-SQUIDs. The change in inductance provided by each rf-SQUID can be studied analytically using the approach of Barone and Paterno [60].

In order to derive the expression for the change in inductance of the microstrip inductor when coupled to an array of rf-SQUIDs, we consider a unit-cell microstrip TL model shown in Fig. 4.18. The microstrip unit-cell consists of an equivalent shunt capacitance $C_m$ and series inductance $L_m$, which is coupled to one superconducting loop with inductance $L_s$ and JJ with inductance $L_j$. The coupling between the inductors $L_m$ and $L_s$ is defined in terms of mutual coupling $M_1$ and coupling coefficient $K_1$. In the proposed topology, an additional microstrip control TL is monolithically integrated on-chip, which runs parallel to the rf-SQUIDs. The unit inductance of the control

microstrip TL $L_c$ is coupled to the SQUID loop inductance $L_s$ with mutual inductance $M_2$ and coupling coefficient $K_2$.

$$K_1^2 = \frac{M_1^2}{L_m L_s}; \qquad K_2^2 = \frac{M_2^2}{L_s L_c} \tag{4.9}$$

When a control current $i_{dc}$ is provided to the control TL, a magnetic field is generated around the microstrip top conductor, which produces a geometrical flux $\phi_{ext}$ inside the SQUID loop given by:

$$\phi_{ext} = M_2 i_{dc} \tag{4.10}$$

A circulating current $i_s$ is induced in the SQUID loop to screen this flux, due to flux quantization condition. The flux due to the circulating current also adds to the total flux $\phi_s$, leading to the following expression:

$$\phi_s = \phi_{ext} + L_s i_s \tag{4.11}$$

The circulating supercurrent depends on two factors: the critical current $I_c$ of the JJ and the total flux in the SQUID loop:

$$i_s = -I_c \sin \frac{2\pi\phi_s}{\phi_0} \tag{4.12}$$

where $\phi_0$ is the flux quantum ($\phi_0 = 2.0679 \times 10^{-15}$Wb) and $I_c$ is determined by the area of the junction $A$ and the current density $J_c$ of the Nb-AlOx-Nb junctions ($I_c = J_c \times A = 0.707\,\text{mA}$). The behaviour of the SQUID is characterized by the screening parameter of rf-SQUID given by:

$$\beta = \frac{2\pi L_s I_c}{\phi_0} \tag{4.13}$$

For this application, the condition $\beta < 1$ is satisfied, the internal flux in the SQUID increases monotonically with the external flux $\phi_{ext}$.

SQUID inductance is a combination of the junction inductance and the inductance of the superconducting loop. The effective inductance controlled by modulating the magnetic flux threading the junction loop can be obtained as:

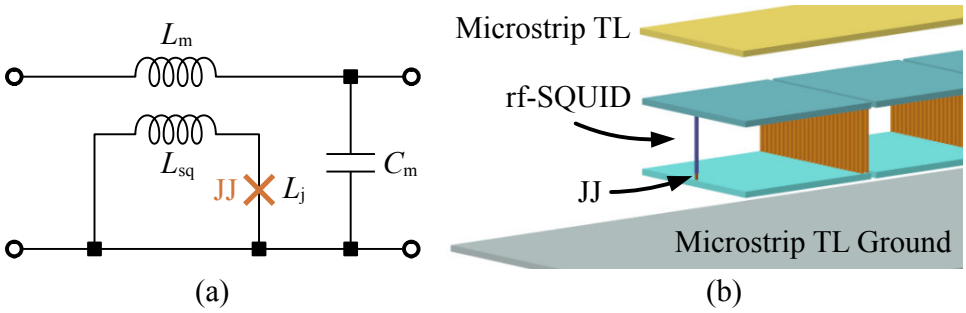



**Figure 4.18:** (a) Circuit model of a single rf-SQUID coupled to microstrip line section, (b) 3D realization of the circuit model.

$$L_{eff} = -\frac{d\phi_{ext}}{di_s} \tag{4.14}$$

Differentiating Eq. (4.11) w.r.t $i_s$

$$\frac{d\phi_{ext}}{di_s} = -L_s + \frac{1}{di_s/d\phi_s} \tag{4.15}$$

Differentiating Eq. (4.12) w.r.t $\phi_s$

$$\frac{di_s}{d\phi_s} = -\frac{2\pi I_c}{\phi_0}\cos\left(\frac{2\pi\phi_s}{\phi_0}\right) \tag{4.16}$$

Combining Eqs. (4.13, 4.14, 4.15, 4.16)

$$L_{eff} = L_s + \frac{L_s}{\beta\cos(2\pi\phi_s/\phi_0)} \tag{4.17}$$

$$L_{eff} = L_s + L_j$$

where $L_j$ is the junction equivalent inductance.

$$L_j = \frac{L_s}{\beta\cos(2\pi\phi_s/\phi_0)}$$

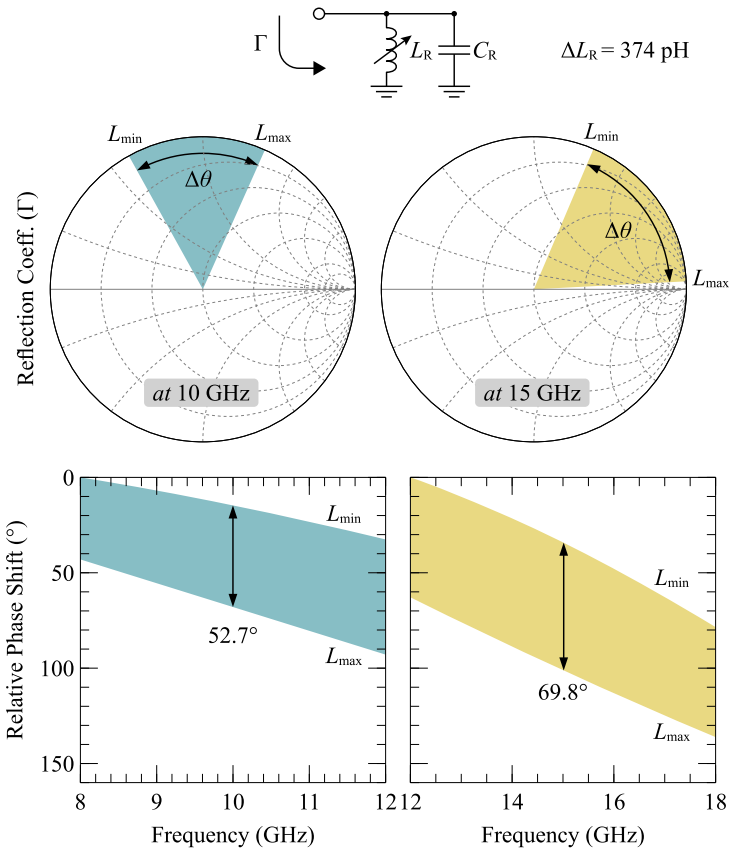



**Figure 4.19:** The lumped element equivalent circuit of the reflective load and the simulated load impedance range and phase shift range.

The effective inductance of the microstrip inductor $L'_m$ coupled to the SQUID is given as:

$$\begin{aligned} L'_m &= L_m \left[1 - K_1^2 \frac{L_s}{L_j + L_s}\right] \\ &= L_m \left[1 - \frac{K_1^2}{1 + (1/\beta \cos(2\pi\phi_s/\phi_0))}\right] \end{aligned} \tag{4.18}$$

The inductance of the microstrip inductor unit-cell is changed as:

$$L'_{\mathrm{m}} = L_{\mathrm{m}}(1 - \Delta L)$$

The change in inductance is expressed as:

$$\Delta L = \frac{K_1^2}{1 + 1/\beta \cos(2\pi\phi_{\mathrm{s}}/\phi_0)} \tag{4.19}$$

The inductance change resulting from a single SQUID is scaled when an array of rf-SQUIDs is coupled throughout the length of the microstrip inductor. As shown in Fig. 4.17, the equivalent circuit of the proposed reflective load topology consists of an inductor $L_{\mathrm{R}}$ connected in parallel with a capacitor $C_{\mathrm{R}}$ with individual reactances given by:

$$X_{L_{\mathrm{R}}} = \omega_0 L_{\mathrm{R}}; \qquad X_{C_{\mathrm{R}}} = \frac{-1}{\omega_0 C_{\mathrm{R}}} \tag{4.20}$$

An array of 56 SQUIDs leads to a total inductance change $\Delta L_{\mathrm{R}}$ of 374 pH. The change in inductance leads to a change in phase of the load reflection coefficient as shown on the smith chart in Fig. 4.19 at 10 GHz and 15 GHz. The phase shift $\theta$ from the reflective loads is obtained when the inductor is varied between minimum inductance ($L_{\mathrm{min}}$) and maximum inductance ($L_{\mathrm{max}}$) values in the *X*- and *Ku*- band frequencies. A method to increase the phase shift range is described in detail in section 4.3.3.

Using the dimensional parameters of the design given in Table 4.4, the theoretical phase prediction of the proposed RTPS at 10 GHz with the control current ranging from 0 mA to 6.25 mA is compared with the measured phase shift from the fabricated structure at 10 GHz and 15 GHz in the section 4.3.3.

### 4.3.3 Measurement Results

The fabricated phase shifter is tested using the experimental setup shown in Fig. 3.18. Calibration is done at cryogenic temperatures. The S-parameters of the phase shifter are measured using on-wafer probing with ground-signal-ground (GSG) RF probes on the input and output ports. A source measurement unit (SMU) is used to provide the control current in precisely controlled steps. The analog operation of the phase shifter is observed by providing control current at the DC pads. The measured S-parameters

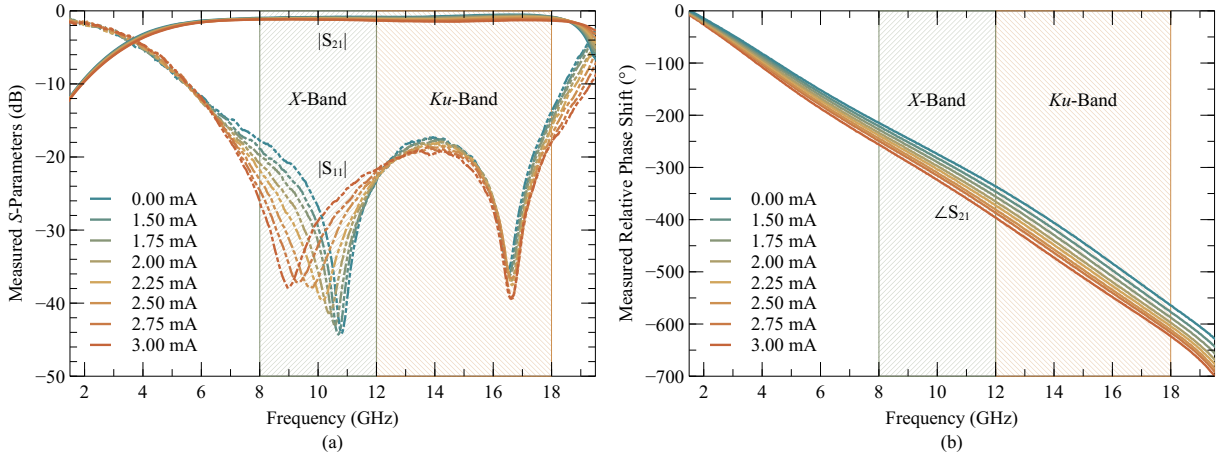



**Figure 4.20:** (a) Measured S-parameters of the analog phase shifter from 8 GHz to 18 GHz for the control current range 0 mA to 3 mA, and (b) Measured relative phase shift of the device in the *X*- and *Ku*- Band.

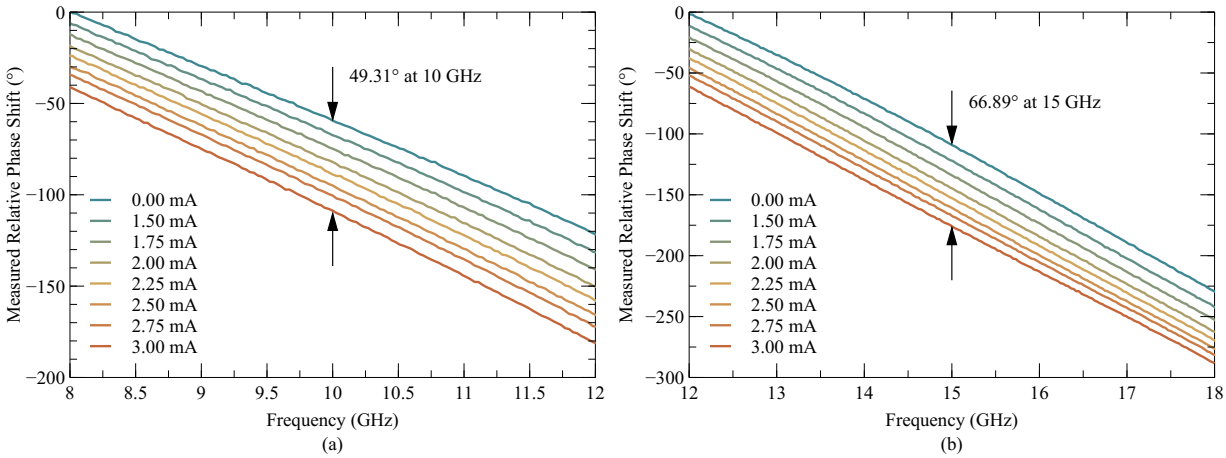



**Figure 4.21:** Measured relative phase shift for control current values 0 mA to 3 mA (a) in the frequency range 8 GHz to 12 GHz, and (b) in the frequency range 12 GHz to 18 GHz.

from the proposed device over the frequency range 8 GHz to 18 GHz are shown in Fig. 4.20(a), and the unwrapped relative phase shift over the operating range is shown in Fig. 4.20(b). The measured insertion loss is <1.5 dB for all values of control current from 0 mA to 3 mA over the frequency range 8 GHz to 18 GHz. The measured return loss of the phase shifter module is >17 dB for the entire bandwidth. The return loss is

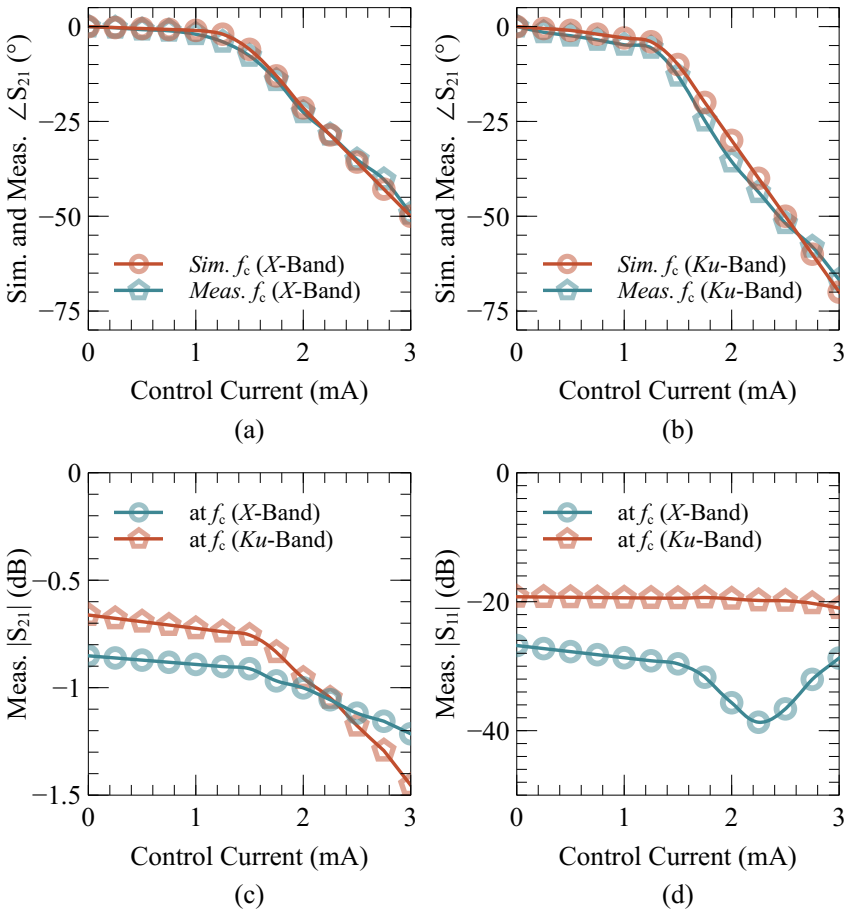



**Figure 4.22:** Simulated phase shift prediction with the change in control current from 0 mA to 3 mA and the measured phase shift from the fabricated device (a) at the centre frequency 10 GHz in the *X*- band, (b) at the centre frequency 15 GHz in the Ku- band, (c) measured insertion loss at 10 GHz and 15 GHz with the control current, (d) measured return loss with the control current at 10 GHz and 15 GHz.

greater than 26 dB at 10 GHz and greater than 35 dB at 16.5 GHz for the entire control current range of 0 mA to 3 mA.

The measured phase tuning range in the *X*- band and *Ku*- band is shown in Fig. 4.21(a) and (b), respectively. The maximum phase shift of 49.31° is observed at 10 GHz with continuous and dense tuning steps. Control current can be varied between 0 mA to 3 mA to get any desired phase value within 49.31° region. In the *Ku*- band, a phase shift

**Table 4.5:** Comparison of the proposed phase shifter with state-of-the-art

| | **Operating Frequency (GHz)** | **Active Element –** | **Superco. Material (LTS/HTS)** | **Overall Size ($mm^2$)** | **Control Type (Magnetic Field/ DC Current)** | **Phase Shift (°)** | **Ins. Loss (dB)** | **No. of squid/ JJs** |
|---|---|---|---|---|---|---|---|---|
| This | 8 – 18 | rf-SQUIDs | Nb (LTS) | 0.6 | DC Current | 49° at 10 GHz | 2 | 112 |
| [103] | 9.95 – 10.05 | rf-SQUIDs | YBCO (HTS) | 4.94 | Mag. Field | 10° at 10 GHz | 5 | 1 |
| [104] | 8 – 12 | rf-SQUIDs | YBCO (HTS) | 12 | Mag. Field/Current | 20° at 10 GHz | 2 | 2000 |
| [58] | 5 – 15 | rf-SQUIDs | Nb (LTS) | 20 | Mag. Field/Current | 60° at 11.6 GHz | 5 | 1600 |
| [105] | 8 – 12 | JJ array | YBCO (HTS) | 25 | DC Curr./RF Power | 8° at 10 GHz | 1.2 | 300 |
| [83] | 8 – 27 | rf-SQUIDs | Nb (LTS) | 4 | DC Current | 130° at 10 GHz | 0.69 | 2256 |

range of 66.89° is achieved at 15 GHz for the control current ranging from 0 mA to 3 mA. The measured change in phase with respect to control current at 10 GHz and 15 GHz is plotted along with the simulated phase shift prediction in Fig. 4.22(a) and (b), respectively. The measured values agree well with the simulated phase shift. The insertion loss variation with control current at the centre frequencies in *X*- and *Ku*-band is given in Fig. 4.22(c). The insertion loss at 10 GHz is less than 1.2 dB for the control current range 0 mA to 3 mA and less than 1.5 dB at the frequency 15 GHz. Fig. 4.22(d) highlights the change in return loss with the control current at 10 GHz and 15 GHz. The return loss is better than 27 dB for the entire control current range at 10 GHz and better than 19 dB at 15 GHz.

Table 4.5 compares the proposed phase shifter with other state-of-the-art superconducting phase shifters operating in the similar frequency range. Various rf-SQUID/JJ array based phase shifters are compared on the basis of type of superconductor material, overall size, control type, phase shift range, insertion loss performance, and the number of SQUIDs/JJs used. Most of the rf-SQUIDs based phase shifters in literature are implemented as a microstrip transmission line coupled to an array of rf-SQUIDs. The biggest drawback of this approach is that a large number of SQUIDs are required to achieve the phase shift, for instance, 2000 YBCO based rf-SQUIDs are used in [104] to attain a phase shift range of 20° at 10 GHz, and 1600 Nb based rf-SQUIDs used in [58] provide a maximum phase shift of 60° at 11.6 GHz. In our previous work utilizing a similar approach [83], we demonstrated a maximum relative phase shift of 130° at 10 GHz with 2256 rf-SQUIDs. Using YBCO based JJ arrays, [105] exhibited a phase shift of 8° at 10 GHz. Another major drawback of these

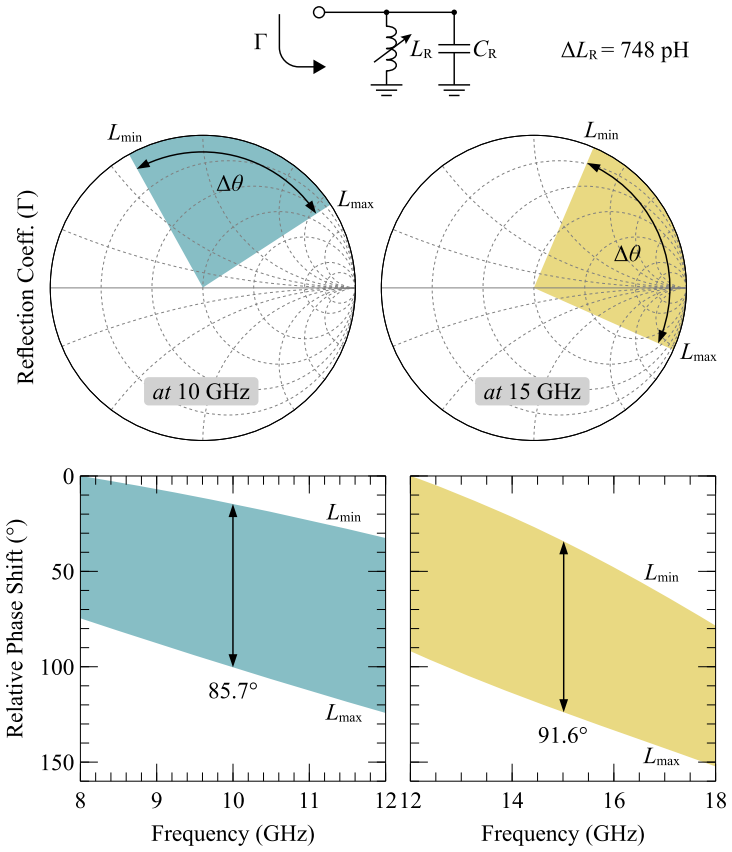



**Figure 4.23:** The lumped element equivalent circuit of the reflective load and the improved load impedance range and phase shift range.

designs is their large device footprint due to the use of a long microstrip line. Moreover, this approach is prone to exceeding the current density of the superconductor and self-heating. In [103], a phase shift of 10° is observed at 10 GHz with single rf-SQUID. However, the device reported in [103] is not a wideband phase shifter and has a very narrow operating range of 9.95 GHz to 10.05 GHz. The proposed analog phase shifter shows a relative phase shift of 49° at 10 GHz using lesser number of rf-SQUIDs and smaller chip area compared to all the others. The chip area can be further reduced by using the meandered type design of the hybrid coupler described in [106].

### 4.3.4 Maximizing the Phase Shift

In order to increase the phase shift, the difference between maximum and minimum impedance values of the tunable load in Eq. 2 needs to be increased. Simply increasing the number of rf-SQUIDs will increase the variable inductance range and hence the phase shift. We have simulated and predicted an increased phase shift of 85.7° at 10 GHz and 91.6° at 15 GHz if the number of rf-SQUIDs in each reflective load are doubled. Simulated unwrapped relative phase shift with 748 pH change in inductance in each reflective load is shown in Fig. 4.23. Other reflective load topologies can be used and optimized to achieve a higher phase shift. Another possible solution is to cascade two RTPS modules, and can be extended upto $n$ number of cascaded stages to achieve increased phase shift range [107]. However, in the cascaded RTPS approach, the insertion loss of the device also scales up with each added stage.

To summarize, an analog rf-SQUIDs-based reflective type phase shifter that provides a 49° and 67° continuous phase shift in the *X*- and *Ku*-bands, respectively is developed. The phase shifter offers low insertion loss for different phase states over the whole bandwidth. The proposed structure utilizes a tandem hybrid coupler that offers 3 dB coupling to the through and coupled ports. An array of rf-SQUIDs coupled to the microstrip acts as variable inductor in the reflective loads and provide a repeatable and precise operation of changing the signal phase with low control current. The effect of increasing the number of rf-SQUIDs in each reflective load is studied to optimize and increase the phase shift range. Since this design offers a dense analog tunable phase shift range, it can serve as a useful component for the quantum circuits tool box.

# Chapter 5

# Power Dependent Microwave Power Limiter and Variable Attenuator

## 5.1 Superconducting Microwave Power Limiter Using rf-SQUIDs

Cryogenic RF receivers utilize low-temperature superconductor (LTS) Josephson Junction (JJ) based analog-to-digital converter (ADC) to digitize the RF signal directly from the antenna without the need of an analog down-conversion circuit [108]. Such ADCs are based on rapid single-flux-quantum (RSFQ) technology, hence, they are at a high risk of getting damaged even by RF signals with very low power levels above $-15$ dBm [9, 10]. In addition to the ADCs, analog circuits like low-noise amplifiers (LNAs) also require high-performance input signal limiters. Most power limiters are not capable of limiting such low power levels. Our objective is to develop a LTS power limiter which can provide protection against power levels above -15 dBm and can be monolithically integrated with other components on the superconducting chip.

The most common configurations of a limiter circuit utilize semiconductor PIN diodes or Schottky diodes connected in single-stage, multi-stage, anti-parallel, or stacked fashion [24–26]. Such semiconductor diode-based limiters have a major limitation that the threshold power level is high and cannot be reduced below a certain power level. Various RF-MEMS based power limiters have also been reported utilizing the self-actuation phenomenon of the MEMS switches at high RF power levels [28, 31] or varactors to control the input signal [84]. The advantages of using MEMS for power

limiter applications include linearity, low power consumption, high isolation, and low insertion loss. However, reliability issues of the MEMS devices and the high threshold RF power level for limiting are the major drawbacks of this approach [88]. Another approach used to develop microwave power limiting devices is based on reversible semiconductor-to-metal transition of vanadium dioxide thin films, but they fail to offer low threshold power levels [33]. The magnetostatic wave (MSW) frequency selective limiters have significantly low threshold power levels ($< -25\,\text{dBm}$), but MSW are long wavelength spin waves that exist only over a limited frequency range (400 MHz to 4 GHz) [35].

The previous attempts to develop a superconducting power limiter as discussed in detail in chapter 2 utilize the switching of high temperature superconductor (HTS) transmission line from low-loss superconducting state to the high-loss normal state when the microwave currents in the device exceed the critical value at high RF power levels [16, 19]. A major drawback of such designs is that all of the energy is dissipated into the superconductor at its switching to the normal state, causing excessive heating of the superconductor and delayed recovery of the superconducting state after the operation. Moreover, all the above techniques [16, 19, 24–26, 28, 31, 33, 35, 84, 88] are not amenable to monolithic integration with superconducting receivers. In this paper, we use radio frequency superconducting quantum interference devices (rf-SQUIDs) as the active element to achieve the power limiting operation. The developed power limiter demonstrates a threshold limiting power of $-15\,\text{dBm}$ and can be monolithically integrated with other superconducting components. With the recently growing interest in quantum computers, this power limiter can also serve as a valuable addition to the quantum engineering library by limiting the RF power of the control signals provided to the sensitive qubits.

### 5.1.1 RF Power Dependent Phase Shift in DJI Transmission line

A microstrip transmission line (TL) tightly coupled to an array of rf-SQUIDs provides a phase shift at the output controlled by the dc current as demonstrated in chapter 4, section 3.2. This phase shifting response can also be achieved using RF power instead of dc current as shown in the theoretical analysis in section 3.2. The amount of RF power provided to the microstrip TL controls the flux through SQUID inductance loops. Individual SQUID acts as a flux sensitive variable inductor, and since it is magnetically coupled to the microstrip TL, change in SQUID inductance causes change in the effective inductance of the TL and hence the phase of the output signal [57, 58]. The response of a meandered microstrip with an array of 3196 rf-SQUIDs laid out in

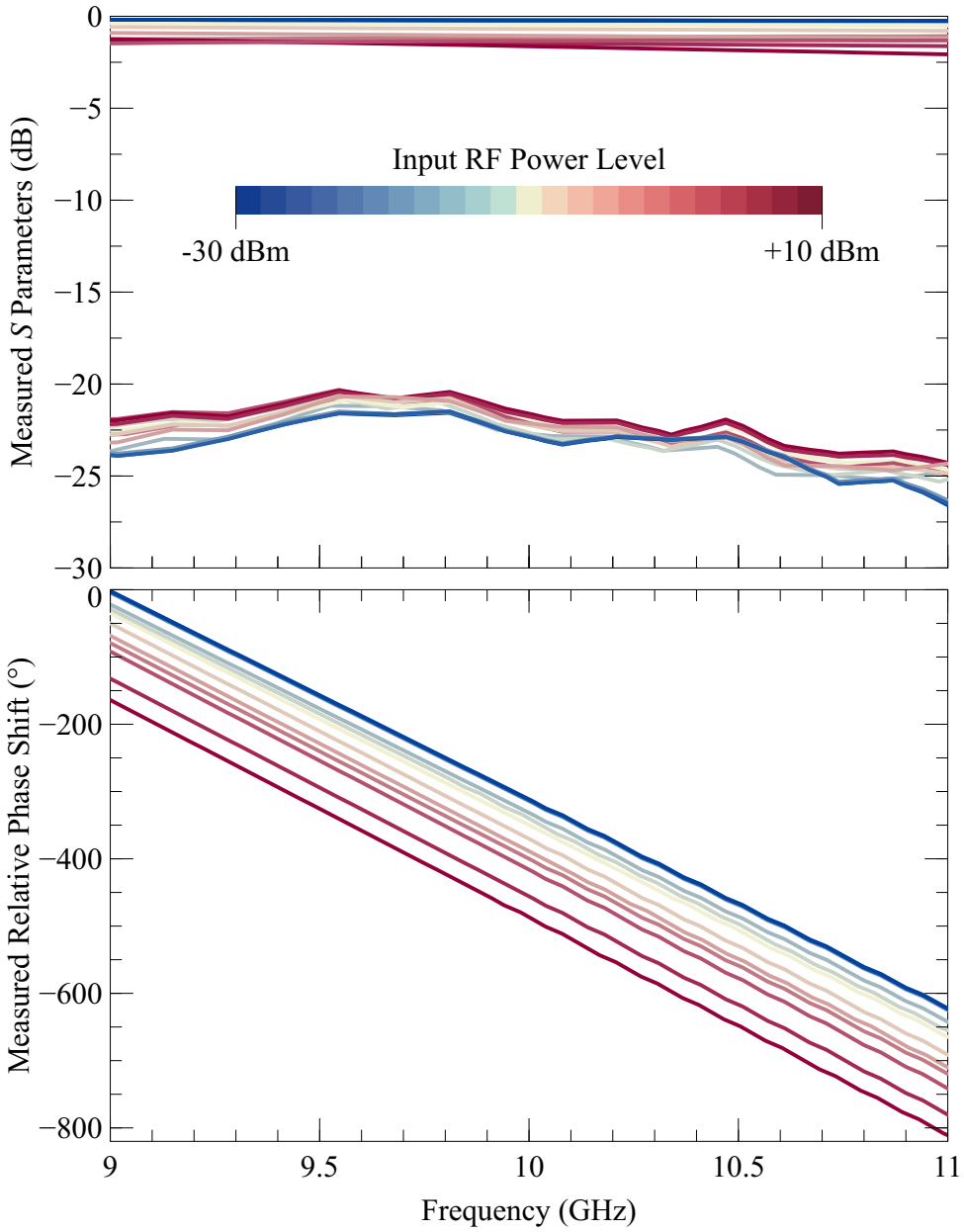



**Figure 5.1:** Measured S-parameters and relative phase shift of the microstrip line coupled with rf-SQUIDs over the RF power sweep from −30 dBm to 10 dBm.

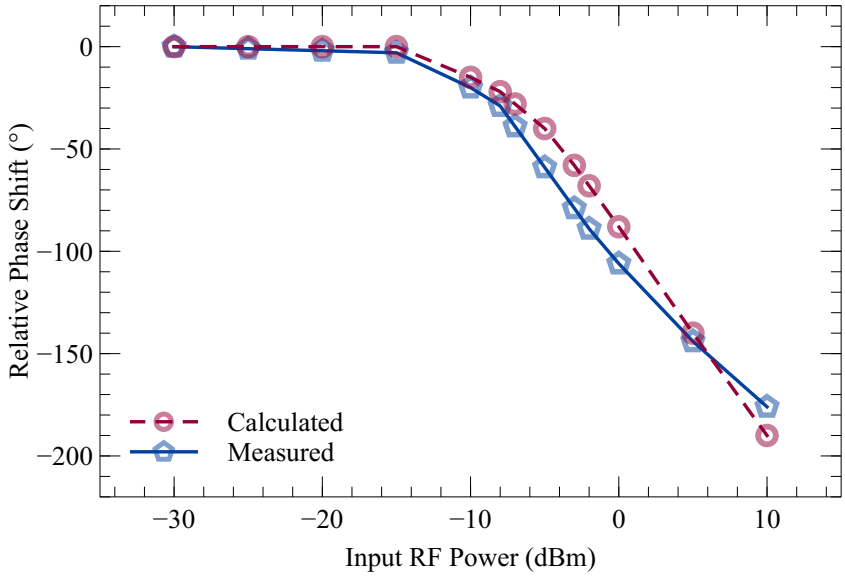



**Figure 5.2:** Calculated phase shift prediction with the change in RF power and the measured phase shift from the fabricated device.

series along the length of the microstrip top conductor is shown in Fig. 5.1. In the operating frequency range of 9 GHz to 11 GHz, a phase change of 176° is observed when the RF power is swept from −30 dBm to 10 dBm. The insertion loss stays below 1.6 dB for all input power levels, and the return loss is maintained at $>$ 20 dB as shown in Fig. 5.1. The theoretical prediction of phase shift with RF power at 10 GHz as described in section 3.2 is in close agreement with the measured relative phase shift from the fabricated device.

### 5.1.2 Power Limiter Design and Operation Principle

The schematic of the proposed LTS power limiter, as shown in Fig. 5.3, comprises of two 90° (quadrature) hybrid couplers. Each quadrature hybrid coupler consists of four ports namely: input port (1), through port (2), coupled port (3) and an isolated port (4). The through and coupled ports of the first hybrid coupler are terminated by two identical length microstrip transmission lines (TL). One of the microstrip TL is coupled to rf-SQUIDs throughout its length, hence offers a variable phase as explained in detail in chapter 4. The other ends of the two microstrip TLs are connected to port 1 and port 4 of the second hybrid coupler. The output RF powers at the two remaining ports are

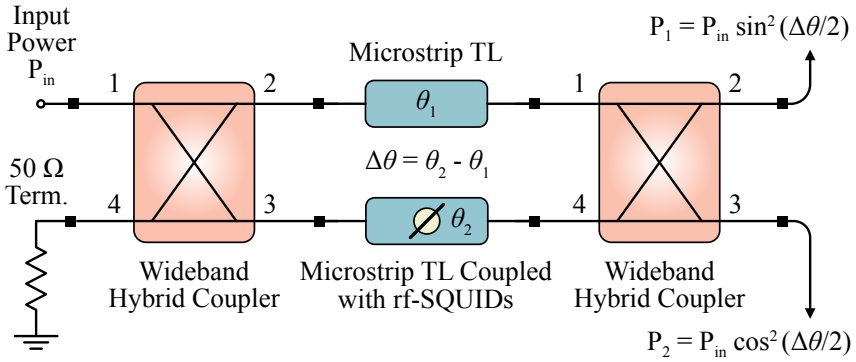



**Figure 5.3:** Schematic of the proposed power limiter consisting of two quadrature hybrid couplers and two microstrip TLs. One of the microstrip TL is coupled to an array of rf-SQUIDs and provides a variable phase $\theta_2$, while the other microstrip TL offers a fixed phase angle $\theta_1$. The output powers $P_1$ and $P_2$ are a function of the phase difference $\Delta\theta$ between the two microstrip TLs.

$P_1 = P_{in} \sin^2(\Delta\theta/2)$ and $P_2 = P_{in} \cos^2(\Delta\theta/2)$. Hence, the output power is controlled by the phase difference $\Delta\theta$ between the two microstrip TLs, which in turn depends on the RF power. An optical micrograph of the fabricated device is presented in Fig. 5.4. The two microstrip meandered conductors are designed on two different Nb layers with ground plane between them to make the design compact as shown in Fig. 5.5. The SQUIDs are placed between the top microstrip and the ground plane, using two additional Nb layers shorted by a JJ. An array of rf-SQUIDs is placed throughout the length of the top microstrip with 2 μm gap between two consecutive SQUIDs.

A power limiter is designed using the design topology shown in Fig. 5.4. Two hybrid couplers are used in the design with two phase shifters offering different phases at same RF power level. A complete layout of the power limiter designed for operation at 10 GHz is shown in Fig. 5.4. The input RF signal is given at the port 1 of hybrid coupler 1 and its port 2 is connected to the microstrip line on M1 with no rf-SQUIDS (acting as first phase shifter). Port 3 of the hybrid coupler 1 is connected to the microstrip line on M7 with an array of rf-SQUIDS below it. The ground plane for both microstrip TLs lies on M4. A 3D view of the microstrip lines on different superconducting layers is shown in Fig. 5.5. Port 4 is terminated in a matched 50 ohm load. A zoomed view of the 50 Ω resistor is shown in the inset in Fig. 5.4. Using symmetry of the hybrid coupler design, port 1 of hybrid 2 is connected to M1 microstrip line and port 4 is connected to M7 microstrip containing rf-SQUIDs. Port 2 is terminated in 50 Ω load and the output RF signal is measured at port 3.

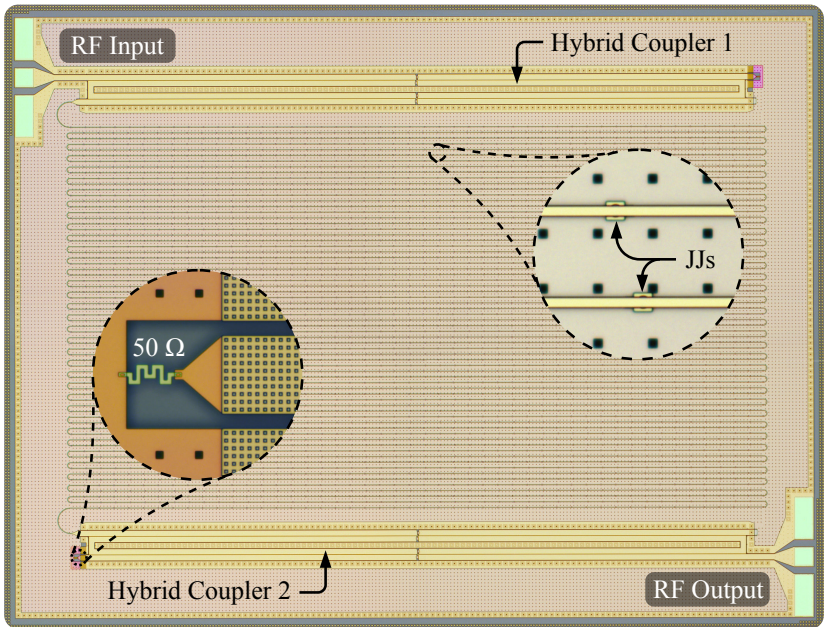



**Figure 5.4:** Optical micrograph of the developed power limiter showing the monolithic integration of two quadrature hybrid coupler sections with two meandered microstrip TLs. The JJs underneath the top microstrip TL and the 50 Ω load termination are highlighted.

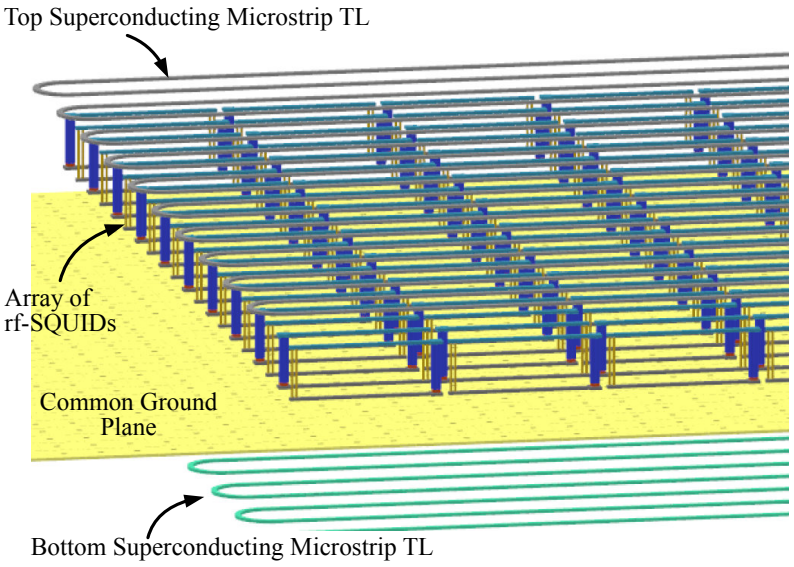



**Figure 5.5:** Layout of the meandered microstrip TLs used in the power limiter. The top microstrip is coupled to rf-SQUIDs. The two microstrip lines share a common ground plane.

**Table 5.1:** Design specifications of LTS Power Limiter

| Name of the Parameter | Value |
|---|---|
| Length of microstrip line | 16.8 cm |
| Diameter of circular JJs | 3 μm |
| Critical current of JJ | 0.707 mA |
| Length of each rf-SQUID | 50 μm |
| Length of Hybrid coupler | 2.33 mm |
| Coupling gaps in Hybrid coupler | 1 μm |

### 5.1.3 Measurement Results of Power Limiter

The RF performance of the fabricated power limiter is measured using Lakeshore cryogenic probe station and Keysight performance network analyzer (PNA-X). The chips are loaded in the4 K temperature stage as shown in Fig. 5.6. Our measurement test chamber is fully shielded to ensure no interference from external magnetic fields.

The fabricated power limiter is tested at different RF power levels ranging from −30 dBm to 10 dBm and the measured insertion loss and return loss over the frequency range 9 GHz to 11 GHz are indicated in Fig. 5.7. At the centre frequency of 10 GHz, the insertion loss increases from 0.3 dB to 24 dB for the input RF power sweeping from −15 dBm to 10 dBm while no change in the insertion loss is observed up to −15 dBm and the insertion loss curved overlap at 0.3 dB. The measured return loss at the input port is maintained at better than 20 dB for all power levels. The limiter offers minimum attenuation when a low-power signal is incident on it, but as the signal crosses the threshold level, the attenuation starts increasing with increasing power as shown in Fig. 5.8. The incident RF power is transmitted through the circuit with minimum insertion loss at low power levels until the threshold value of −15 dBm is reached. When the input RF power increases above the threshold value, the signal is attenuated and the output signal level is limited at −15 dBm.

Two tone intermodulation testing is performed at 10 GHz, with a frequency separation of 100 MHz between the two signals. The measurements results shown in Fig. 5.9 reveal that no nonlinear harmonics are present at the power limiter output spectra at

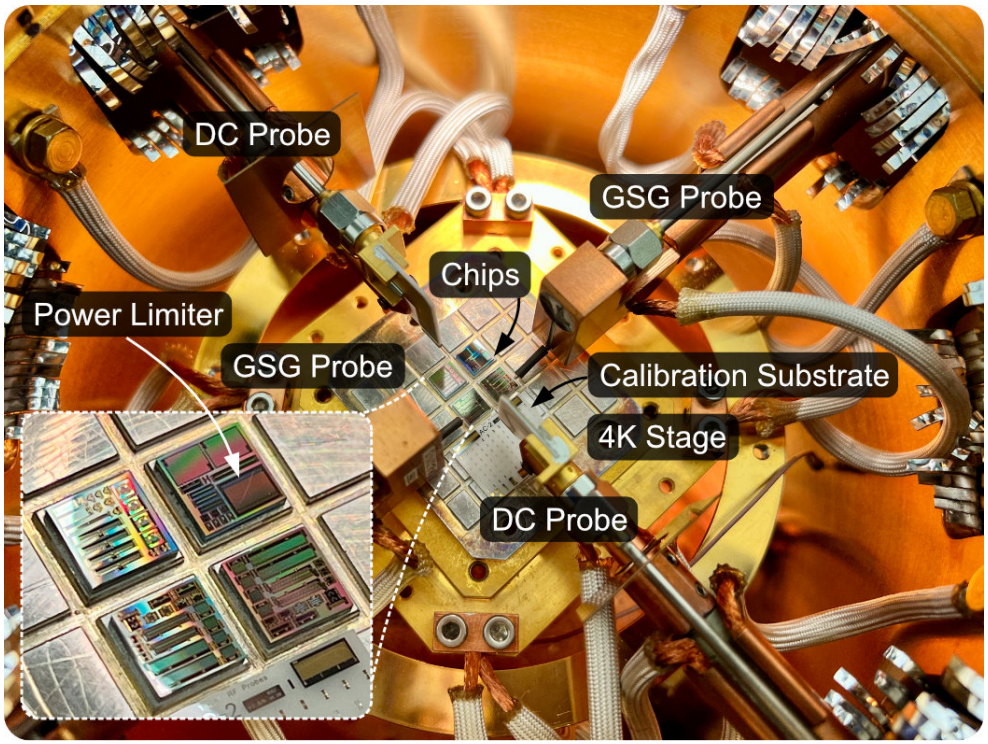



**Figure 5.6:** The chips loaded inside the cryogenic chamber of Lakeshore probe station for testing. The chamber has two RF GSG probes, two dc probes and the chip holder is loaded on the 4 K temperature stage.

the levels of input signal up to at least $-20$ dBm. The intermodulation products start appearing in the spectrum at power levels $\geq -15$ dBm.

It is worth highlighting that the phase of the rf-SQUID loaded microstrip TL can be controlled using various methods such as dc current, external magnetic field, RF power, or dc superimposed with RF power. The objective of the presented power limiter is to demonstrate the RF power dependency on the limiting operation without providing any additional bias or excitation signals. While majority of the power limiters behave like a circuit breaker which cuts off the output power instead of truly limiting it while the proposed power limiter limits the output power at a designed threshold power level. To the best of our knowledge, this is the first ever demonstration of an RF power dependent power limiter for cryogenic systems.

In conclusion, a novel design of a microwave power limiter for applications in superconductor based receivers is presented. A pair of wideband hybrid couplers is

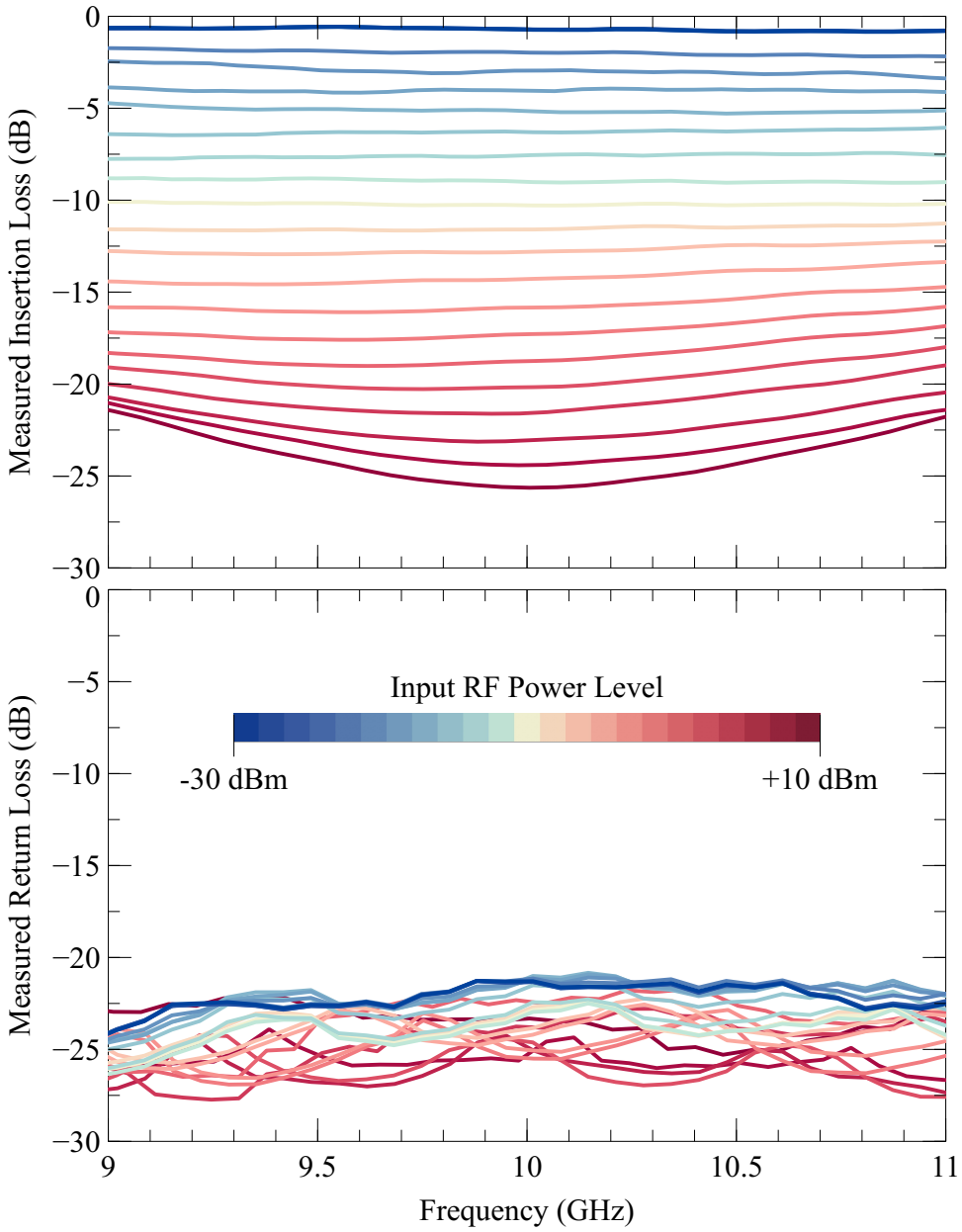



**Figure 5.7:** Measured insertion loss and return loss response of the power limiter over the frequency range 9 GHz to 11 GHz with the input RF power level sweeping from −30 dBm to 10 dBm.

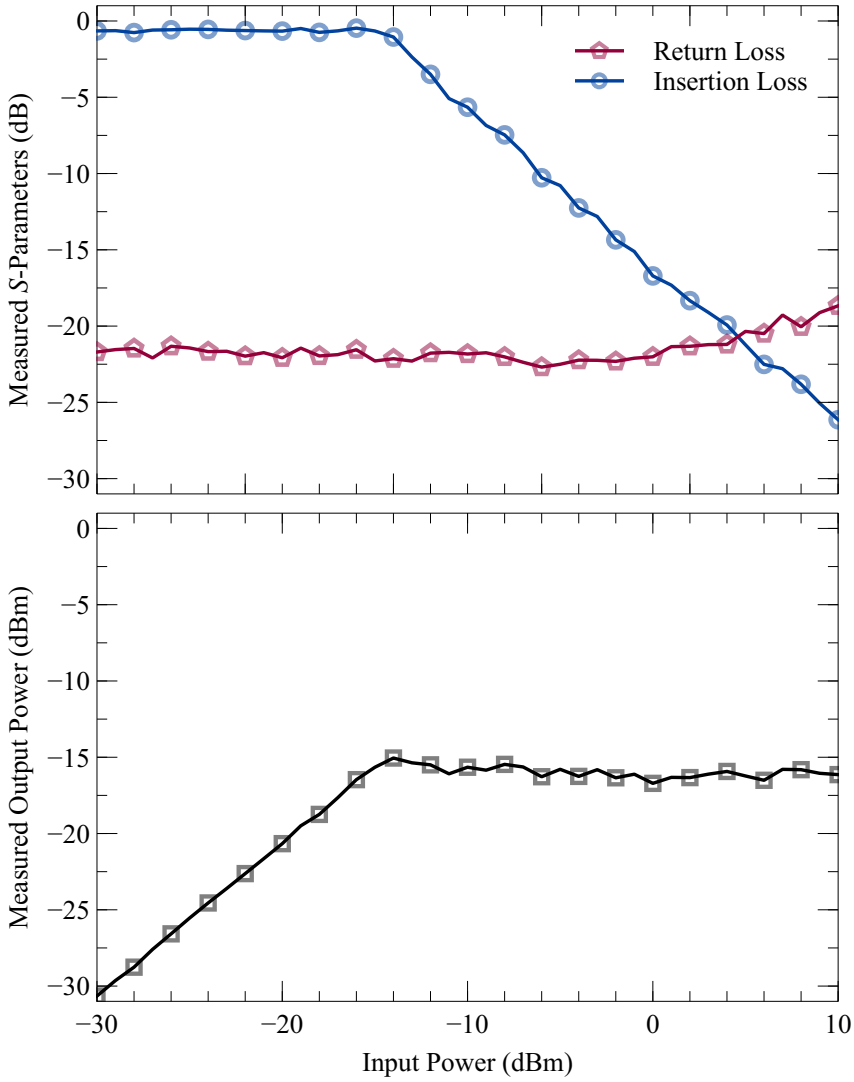



**Figure 5.8:** (a) Measured insertion loss and return loss of the power limiter for the input RF power range of −30 dBm to 10 dBm, (b) Measured output RF power as the input RF power is increased from −30 dBm to 10 dBm.

used in the design along with two microstrip transmission lines, one of which is magnetically coupled to an array of rf-SQUIDs. Measured *S*-parameters and non-linear performance of the power limiter were investigated over power levels ranging from −30 dBm to 10 dBm. The power limiter begins to limit the RF signal when the

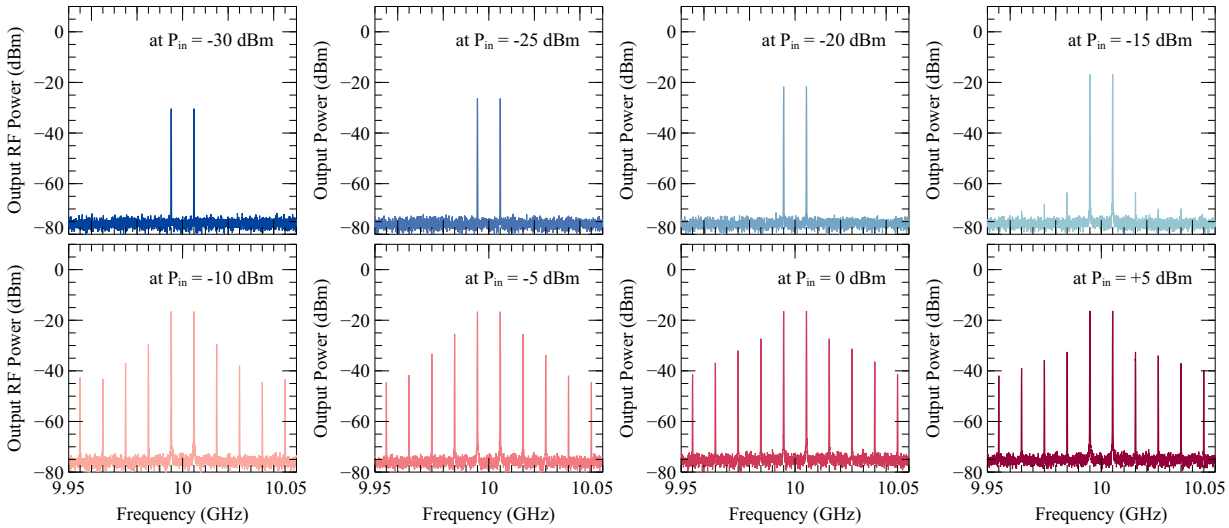



**Figure 5.9:** Two tone intermodulation response of the power limiter at different input RF power levels ranging from −30 dBm to 5 dBm.

threshold power level of −15 dBm is exceeded. A detailed analysis of the inductance variation of the microstrip TL due to magnetic flux coupling with rf-SQUIDs is presented, from which the change in output phase with the applied RF power is theoretically analyzed. The simulation results of mutual coupling between rf-SQUIDs and microstrip TL are presented. The phase shift obtained from the rf-SQUID coupled transmission line can be adjusted by increasing the number of coupled rf-SQUIDs.

## 5.2 Variable Attenuator

In the physical implementation of modern superconducting quantum computing systems, radio frequency (RF) attenuators play a significant role in the measurement and control setup for qubits. The quantum state of a qubit is read out by probing with heavily attenuated microwave signal (typically <-60dBm) [1] The input microwave signal travels through a chain of attenuators mounted at different temperature stages. Ideally, the attenuators and directional couplers used on the input line need to be well thermalized and should have minimal self-heating to avoid the dephasing of qubits. Excess thermal photons generated by the microwave components limit the coherence times of superconducting qubit.

The commercial off-the-shelf microwave attenuators have a downside that the stainless-steel package along with the insulator material inside have low thermal conductivities at low temperatures. Such attenuators, not designed for operation at millikelvin temperatures, raise the noise temperature on the input line. Recent research efforts involve using materials with better thermal and electrical properties and using improved circuit topologies. A fixed level of attenuation is achieved using a lumped-element thin-film resistive network made from nichrome (NiCr) [109]. The fundamental limitation is that even with proper choice of materials and circuit layout, the temperature difference inside the resistive network cannot be reduced below a certain level at millikelvin temperatures [110]. Microwave cavity attenuators made from low-temperature compatible normal metals such as brass, oxygen-free-high-thermal-conductivity (OFHC) copper have been explored, but they offer extremely narrowband performance [111]. Not only in the quantum measurement systems, but the demand for on-chip precise microwave attenuators for integrated mm-wave superconducting receivers is long standing [108, 112]. Previously, the performance of a Josephson junction (JJ) itself as a variable attenuator has been explored based on its change in the microwave impedance when dc biased at different points in the current-voltage characteristics [113], but it fails to offer a wide dynamic range and is limited to a few micro-watts saturation level. This welcomes other microwave techniques to achieve the desired attenuation.

In this section, an experimental demonstration of a dc current controlled LTS microwave attenuator is presented which provides variable and flat attenuation over a wide frequency range without depending on the dissipative properties of the material and can be monolithically integrated with other superconducting components to provide a single-chip solution.

The proposed design consists of two quadrature couplers and two microstrip transmission line (TL) sections as shown in the optical image in Fig. 5.10. One of the TL is coupled to an array of 230 rf-SQUIDs which represents electromagnetically coupled variable inductors, providing a variable phase $\theta_1$ controlled by low dc control current. The other microstrip TL offers a fixed phase $\theta_2$. The output attenuation is a function of the phase difference $\Delta\theta$ between the two TLs. The dc control current is provided using a separate microstrip line running parallel to the rf-SQUID loops. The unused ports of the hybrid couplers are terminated in matched load using 50 ■ monolithically integrated microresistors as shown in the first callout in Fig. 5.10 using the high-sheet-resistance layer R5 in the fabrication process. The second callout in the image shows the interconnections in the hybrid coupler design routed from a second Nb layer using vias. The gap $g_1 = 1\,\mu$m, gap $g_2 = 2\,\mu$m, $l_c = 8\,\mu$m and $w_s = 20\,\mu$m. The

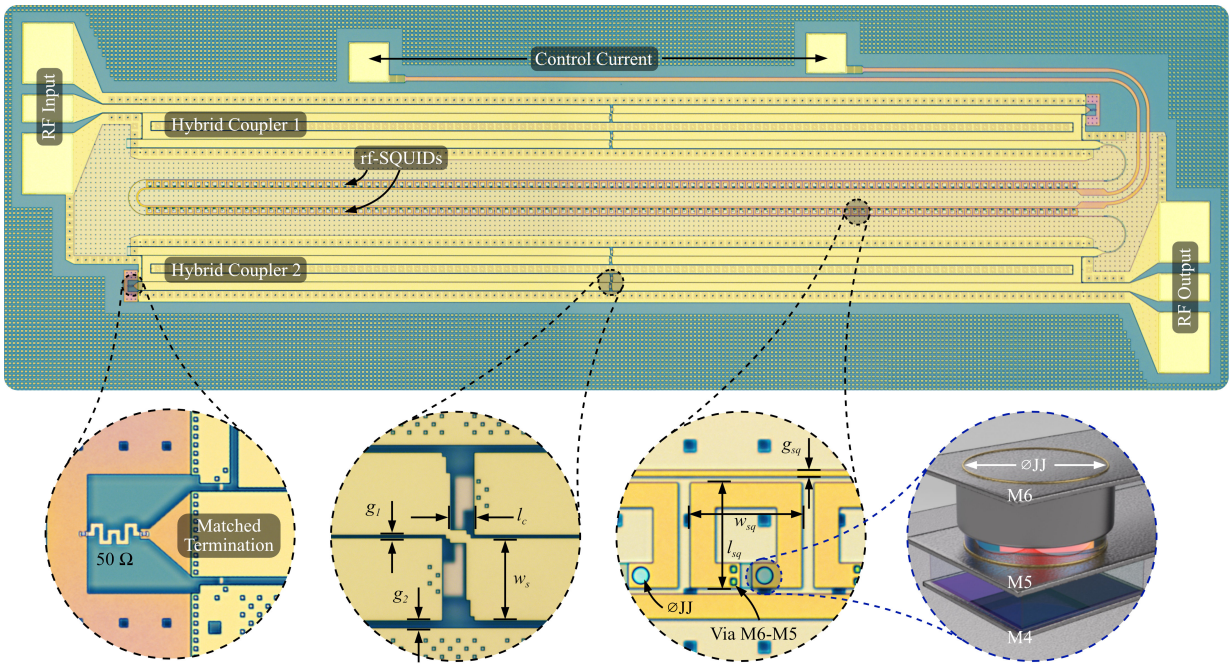



**Figure 5.10:** Design layout of a superconducting microwave variable attenuator consisting of two microstrip TLs disposed between two hybrid couplers. One of the microstrip TL is loaded with 230 rf-SQUIDs. The unused hybrid coupler's ports are terminated with 50 Ω micro-resistors.

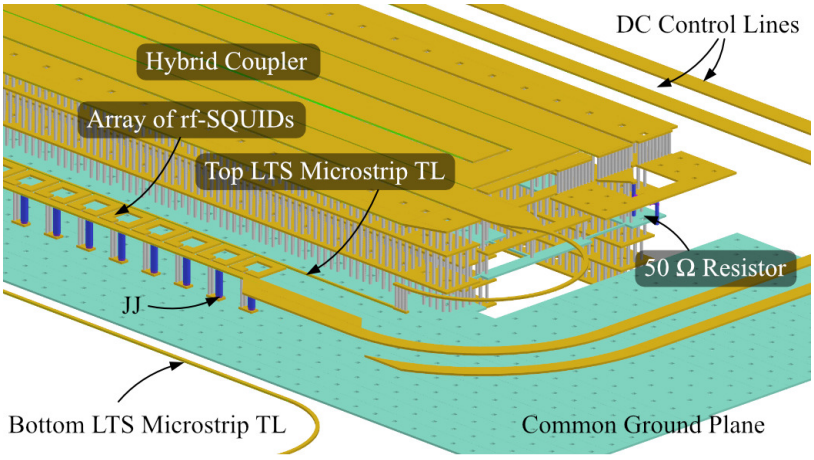



**Figure 5.11:** Layout of the folded microstrip TLs used in the variable attenuator. The top microstrip is coupled to an array of rf-SQUIDs. The top an bottom microstrip line share a common ground plane.

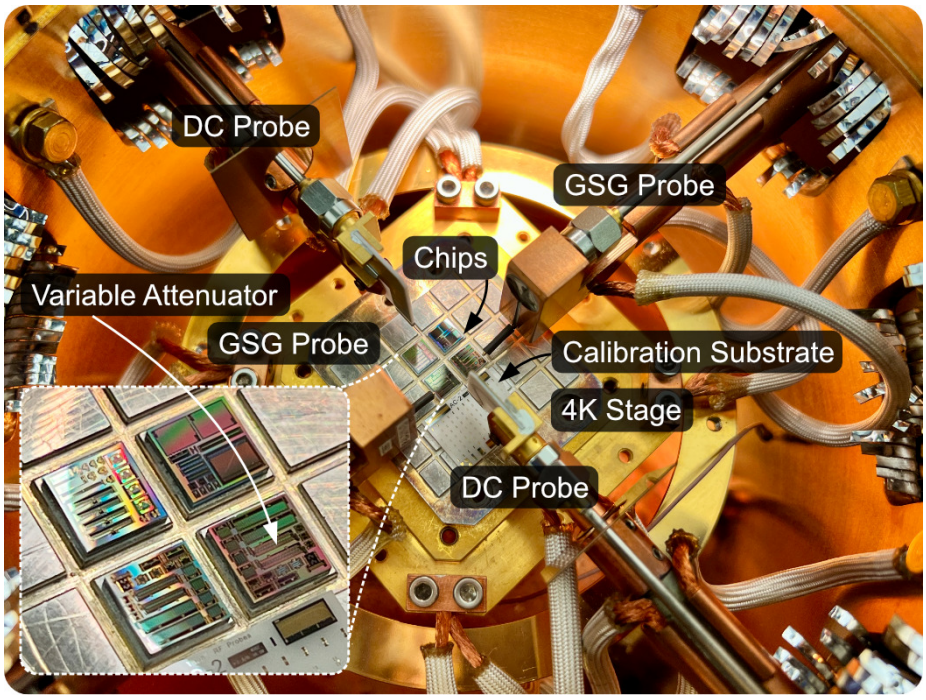



**Figure 5.12:** The chips loaded inside the cryogenic chamber of Lakeshore probe station for testing. The chamber has two RF GSG probes, two dc probes and the chip holder is loaded on the 4 K temperature stage.

rf-SQUID design is highlighted in the third callout where $g_{sq} = 1\,\mu$m, $w_{sq} = 18\,\mu$m and $l_{sq} = 17\,\mu$m. The JJ $\oslash$ used in the design is 3 µm, which is a tri-layer juntion as shown in the rendered image in the fourth callout of Fig. 5.10. The overall device dimensions are 2.6 mm $\times$ 0.5 mm. The two microstrip lines are arranged on different Nb layers (M6 and M1) with a common ground plane between them (M4) as shown in Fig. 5.11. The rf-SQUIDs are placed along the top microstrip.

The variable attenuator is fabricated using MIT-LL SFQ5ee process and tested in Lakeshore Cryogenic Probe station on 4 K stage as shown in Fig. 5.12. The measurement results of the S-parameters are shown in Fig. 5.13. Looking at the measured magnitude of $S_{21}$, the device displays more than 30 dB of precise analog flat attenuation tuning range over 8 GHz to 12 GHz with a dc control current ranging from 0 mA to 4.5 mA. The device exhibits a very wideband operation with impressive variable attenuation seen not only in the $X-$ band but also in $Ku-$ band. The return loss at the input port for most states is less than 17 dB from 8 GHz to 18 GHz. To the

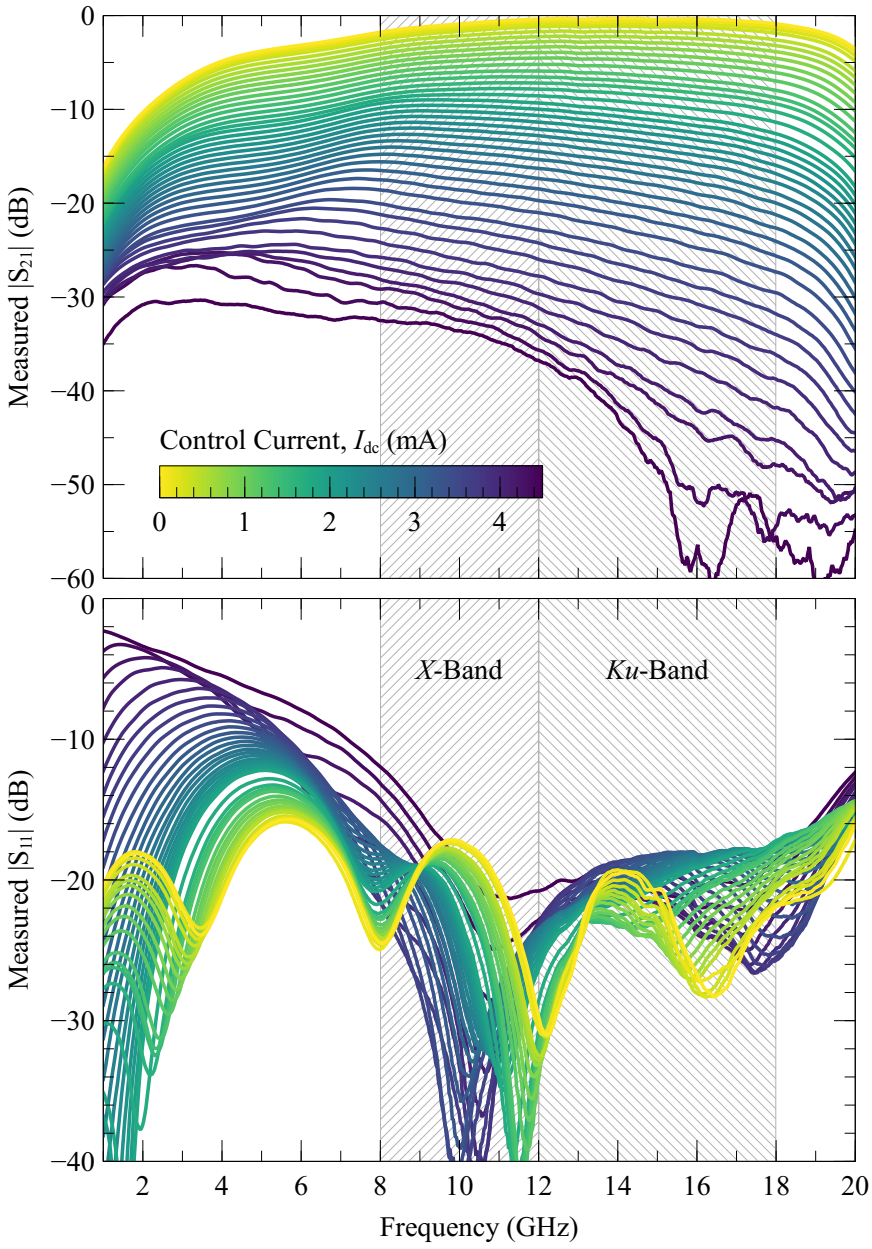



**Figure 5.13:** Measured S parameters of the variable attenuator showing the insertion loss $S_{21}$ and return loss $S_{11}$ for the control current sweep from 0 mA to 4.5 mA.

best of our knowledge, this is the first implementation of a variable attenuator using distributed rf-SQUIDs.

### 5.2.1 Phase Shifter Using rf-SQUIDs

Since the variable attenuation mentioned above is a result of the phase difference between the two TLS, it is interesting to individually know the phase shift offered by the microstrip TL coupled to 230 rf-SQUIDs with control current. A standalone device is designed as shown in the optical image of the fabricated device in Fig. 5.14 with two RF ports connected by a meandered microstrip TL. The microstrip TL is coupled to 230 rf-SQUIDs (same as used in variable attenuator). The rf-SQUID loops lay along the length of the microstrip and a second microstrip line running parallel to the SQUID loops is used to provide DC flux. The dc control current is provided on the two DC pads. The overall footprint of the phase shifter is 0.64 mm $\times$ 0.55 mm.

The phase shifter is tested at 4K, for a dc current sweep from 0 mA to 4.5 mA, a signal phase shift of 130° is measured at 10 GHz in $X-$band and 184° at 15 GHz in $Ku-$band as shown in Fig. 5.15. For the entire control current sweep from 0 mA to 4.5 mA, the measured insertion loss ($S_{21}$) is less than 1 dB in the $X-$band and less than 2 dB for entire frequency range 1 GHz to 20 GHz. The return loss at the input port is better than 18 dB in both $X-$ and $Ku-$ bands.

To verify the concept and study any coupling effects between the microstrip RF line and the dc control current microstrip line, another clone of the device is fabricated as shown in the optical image in Fig. 5.16 with rf-SQUIDs removed from the layout. The measurement results shown in Fig. 5.17 show no phase shift with the dc current sweep and the insertion loss and return loss remain consistent. This proves that the phase shift is a result of the variable inductance of rf-SQUIDs with the dc flux.

To summarize, a LTS analog microwave variable attenuator is developed which can be monolithically integrated with other components on the superconducting chip. The variable attenuator design uses two wideband hybrid couplers and a phase shifter. The phase shifter realized using a superconducting microstrip transmission line coupled to an array of rf-SQUIDs provides a phase shift of 130° at 10 GHz and 184° at 15 GHz. The variable phase shift is controlled by using dc current, which effectively controls the level of attenuation at the output. The variable attenuator exhibits more than 30 dB of precise analog flat attenuation tuning range in the *X*-band with more than 45 dB of dc current controlled attenuation in *Ku*-band. The device is fabricated using a multilayer advanced superconducting process by MIT Lincoln laboratory. The large variable

attenuation range demonstrated by the device and its potential for monolithic integration with other Nb-based circuits makes it a desirable candidate for quantum circuit measurements.

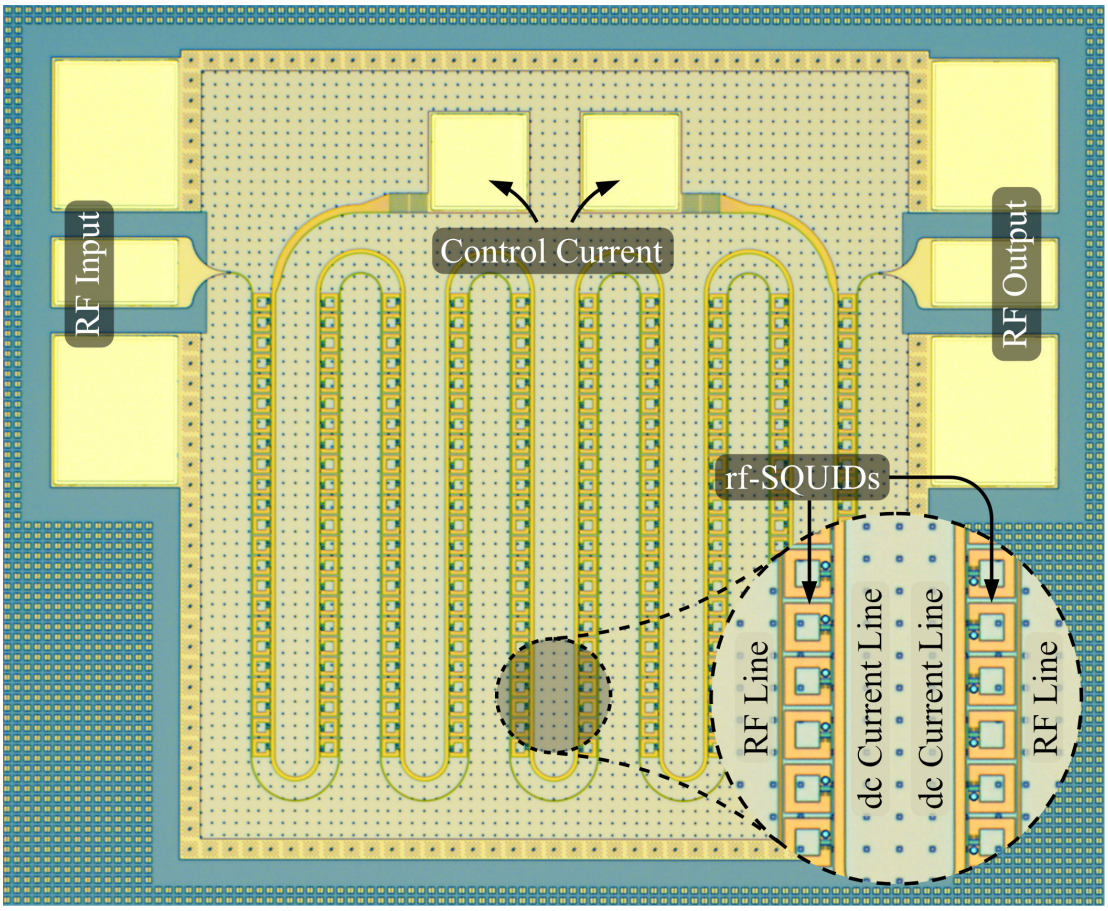



**Figure 5.14:** Optical micrograph of the fabricated phase shifter consisting of an array of rf-SQUIDs placed along a meandered microstrip TL connecting the two RF ports. The control current is provided to a separate microstrip running parallel to the rf-SQUIDs. The enlarged section highlights the rf-SQUID loop placed between the RF signal carrying microstrip line and the dc current line.

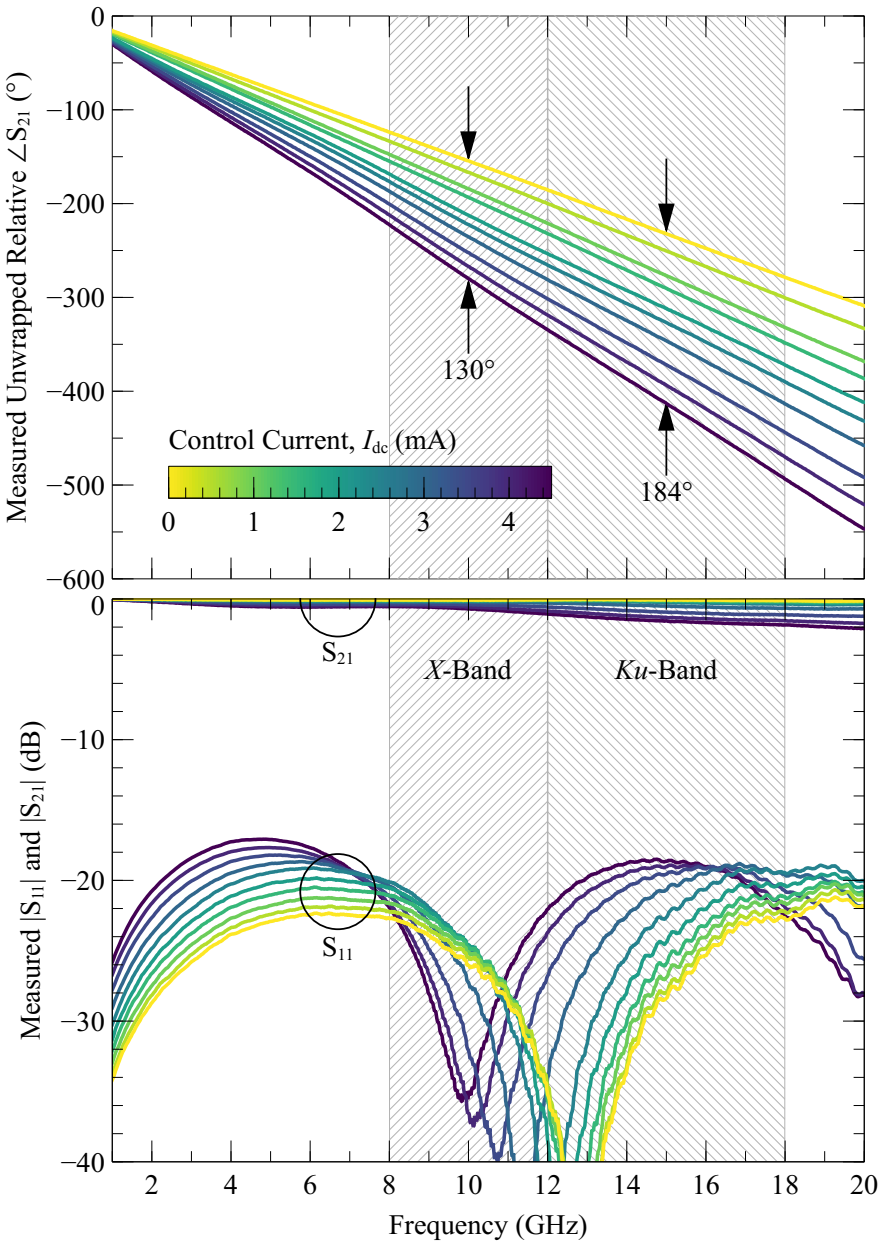



**Figure 5.15:** Measured S-parameters of the phase shifter from 1 GHz to 20 GHz with a dc current sweep from 0 mA to 4.5 mA. The relative phase shift ($\angle S_{21}$), insertion loss ($|S_{21}|$), return loss ($|S_{11}|$) in the *X*-band and *Ku*-band are highlighted.

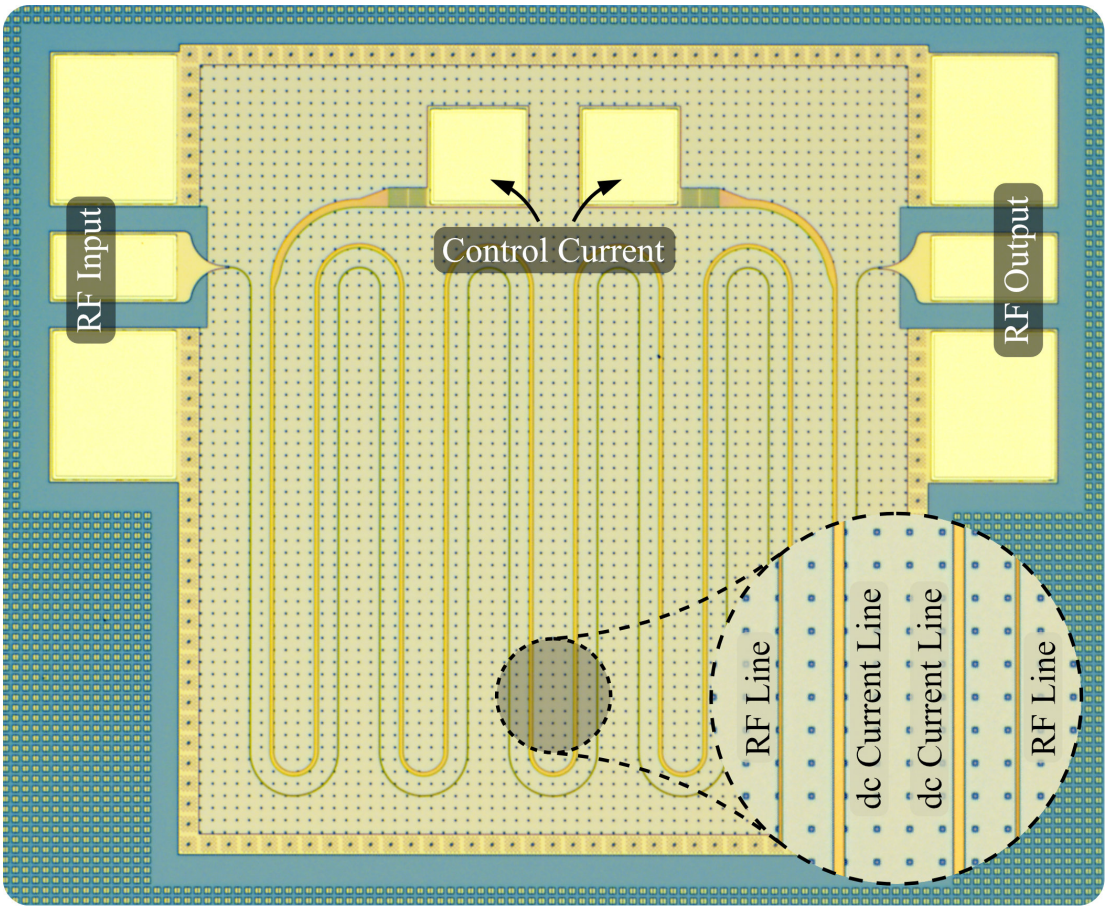



**Figure 5.16:** Optical micrograph of the phase shifter design similar to Fig. 5.14 with the rf-SQUIDs removed. Two parallel running microstrip lines can be seen in the highlighted section.

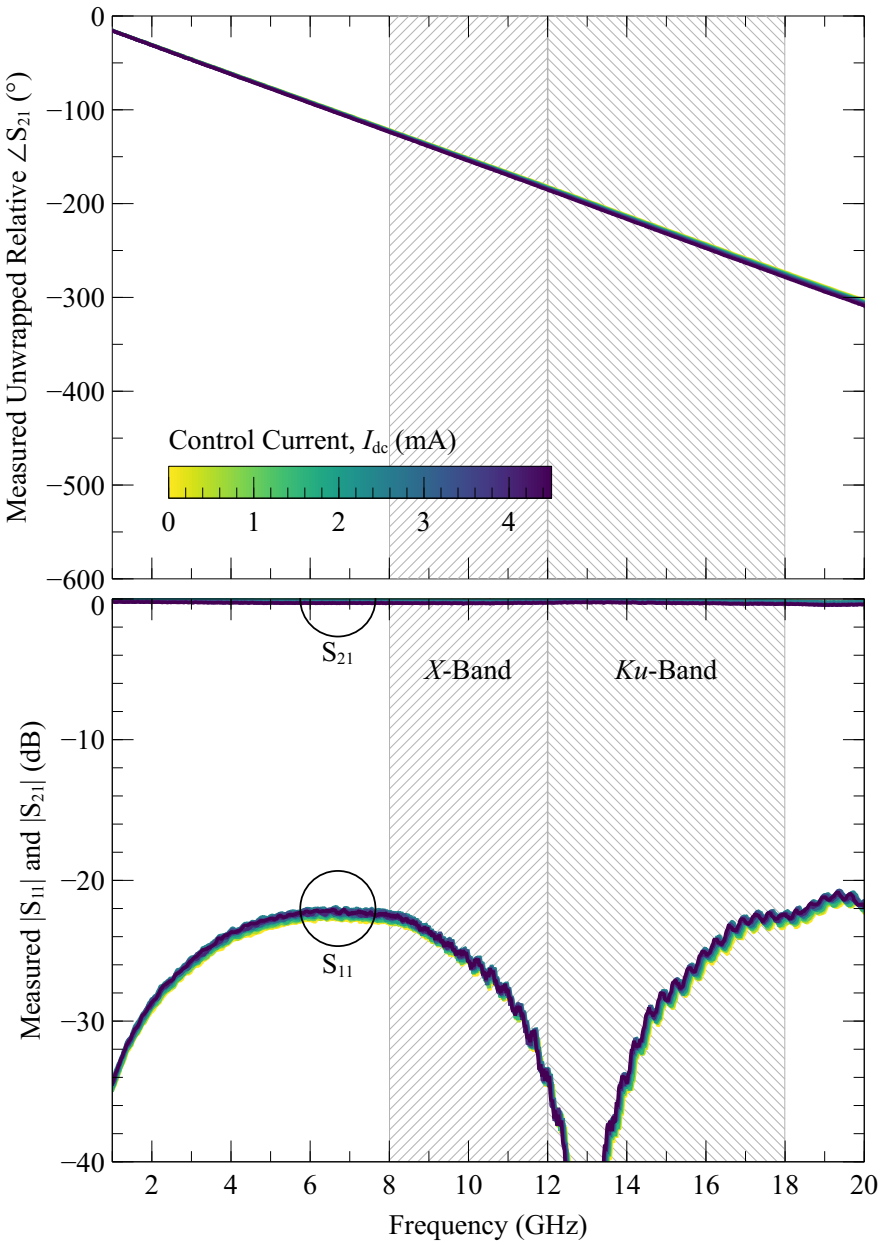



**Figure 5.17:** Measured S-parameters of the phase shifter from 1 GHz to 20 GHz with a dc current sweep from 0 mA to 4.5 mA. No change in signal phase ($\angle S_{21}$), insertion loss ($|S_{21}|$), return loss ($|S_{11}|$) is observed.

# Chapter 6

# Magnetless Superconducting Circulator

## 6.1 LTS Microwave Magnetless Circulator

RF cryogenic circulators play a prominent role in the readout of quantum bits (qubits). Readout signals require significant amplification (typically 70 dB to 80 dB) for room temperature demodulation circuitry. This is achieved by using a Josephson parametric amplifier which is implemented as a single-port device that amplifies in reflection. RF circulator is a three-port non-reciprocal device that allows the signals to flow in one direction while inhibiting propagation in the reverse direction. Hence, circulators play a very important role of separating the incoming signals from the reflected amplified output from the Josephson parametric amplifier while maintaining a 50 Ω impedance at the quantum circuit.

For a very long time, nonreciprocity has been almost exclusively achieved through magnetic biasing of ferrite materials. While conventional ferrite type circulators can be designed to operate at cryogenic temperatures [114, 115], such circulators are incompatible with other superconducting components. There are a number of reasons that ferrite circulators are inconvenient for quantum computing research. First, they are bulky, occupying valuable space in a dilution refrigerator. Second, they require a large magnetic bias field that is incompatible with the superconducting microwave circuit-based qubits are built on. Third, they introduce loss that is inherent to microwave propagation in ferrite materials. This loss on top of other losses from cables and connectors, impacts the overall system noise or measurement efficiency. With that being the case, in the last few years, a number of researchers are working on the development of such nonreciprocal devices that emphasize compactness, freedom

from large magnetic bias fields, very low loss, and have the potential to be monolithically integrated with other components on a single superconducting chip. Such cryogenic circulators also find application in the front-end of integrated superconductor receiver systems.

In our approach to building a superconducting magnet-less circulator, we will use the principle of spatiotemporal modulation angular-momentum (STM-AM). The concept of STM-AM was initially introduced by Andrea Alu et. al. in 2014 who presented a magnetless circulator for airborne sound by synthesizing an effective angular-momentum bias in the form of the mechanical rotation of air inside a circularly symmetric resonant acoustic cavity [116]. Some notable works extending these concepts to realize various nonreciprocal components for electromagnetic signals, including gyrators, isolators and circulators have been reported. However, all of the above-mentioned implementations are at room temperature either on a PCB using varactors [47], monolithic CMOS integration [48], or using MEMS [49]. However, development of cryogenic circulators using STM-AM remains unexplored and an absolute need. Instead of achieving nonreciprocity through the use of magnetic materials, time-dependent reactive elements can be used to provide nonreciprocal operation. A standard superconducting circuit element, the Josephson junction, can be operated as a time-variable reactance.

## 6.2 Operation Principle

The technique used here to accomplish magnetic-free non-reciprocity is founded on angular momentum biasing of a resonant ring. In case of acoustic waves, mechanically spinning a fluid generates the angular momentum required to achieve non-reciprocity [116]. In case of electromagnetic waves, an effective electronic spin can be realized by spatiotemporal modulation using a travelling wave [45].

The primary circuit topology is shown in Fig. 6.1(c). The scheme is based on the parametric modulation of three identical, strongly and symmetrically coupled resonators arranged in a loop. We propose connecting three bandstop LC resonators in a delta topology. This circuit does not allow transmission to any port without modulation, however, when angular momentum is imparted, the degenerate modes of the loop split, allowing nonreciprocal transmission. Each resonator consists of a fixed value capacitor connected across an rf-SQUID (or an array of rf-SQUIDs), which acts as a flux-tunable inductor. The flux modulation is achieved by coupling the SQUID to a fixed coil which provides the modulated rf signal. The rf-SQUIDs inductively coupled

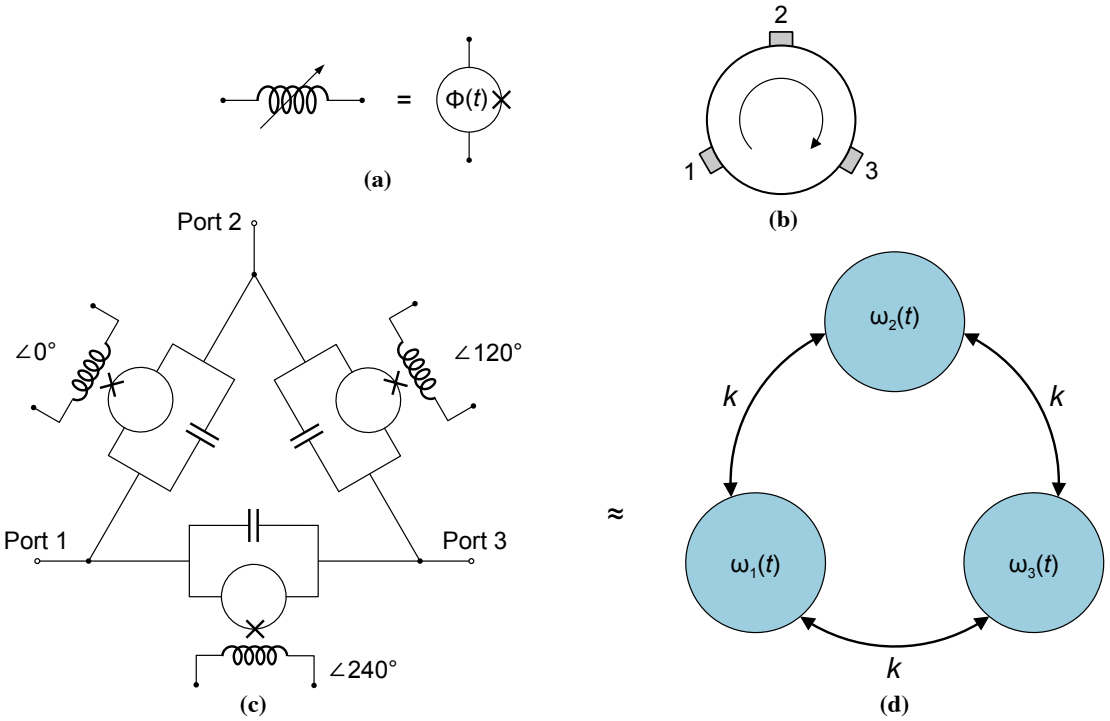



**Figure 6.1:** (**a**) rf SQUID is used as a tunable inductor, (**b**) Three port circulator showing the direction of signal circulation, (**c**) The proposed schematic of a superconducting circulator based on synthetic rotation. Three rf SQUIDs are modulated by RF signal 120° out of phase from each other. The phase progression between the three modulating signals establishes the direction of circulation, (**d**) The SQUIDs act as tunable inductors and modulate the coupling coefficient between the three resonators with resonance frequencies $\omega_1(t)$, $\omega_2(t)$, $\omega_3(t)$

to external bias are used as the non-linear element. The resonant frequencies of the individual tanks are modulated by external signals with the same amplitude and a relative phase difference of 120°, imparting an effective electronic angular momentum to the system. Three oscillatory microwave tones are required to modulate the inductance and, therefore, the frequency of three resonant circuits in a cyclic manner.

The circuit can be represented as three resonators with resonance frequencies of $\omega_1$, $\omega_2$, and $\omega_3$ coupled to each other with a coupling coefficient $k$, as shown in Fig. 6.1(d). Without modulation, all the three LC tanks resonate at the same frequency of

$$\omega_1 = \omega_2 = \omega_3 = \omega_0 = 1/\sqrt{L_0 C}$$

with temporal modulation

$$\omega_1(t) = \omega_0 + a_m cos(\omega_m t)$$
$$\omega_2(t) = \omega_0 + a_m cos(\omega_m t + 2\pi/3)$$
$$\omega_3(t) = \omega_0 + a_m cos(\omega_m t + 4\pi/3)$$

where $\omega_0$ is the static value of the resonant frequency, $a_m$ is the modulation amplitude and $\omega_m$ is the modulation frequency. The currents flowing through the three resonators can be intepreted as a superposition of two counter-rotating modes. Without modulation, these two counter-rotating modes are degenerate, consequently, if a signal is applied from one port, transmission to the other ports is equal and the network is reciprocal. When modulation applied, it synthesizes an effective angular-momentum bias in the clockwise direction because the phases of the modulation signals increase by 120°in that direction, thus lifting the degeneracy of the rotating modes and enabling them to oscillate at different frequencies, achieving a nonreciprocal routing of the signals between the ports. It can be seen that by choosing proper modulation amplitude and frequency, the two modes interfere destructively at one port and constructively at the other port, thus fulfilling the operation of a circulator. This theory is validated with simulations in the following section.

## 6.3 Simulations

A Matlab simulink model is developed based on the proposed circuit topology. Three resonators, each consisting of a variable inductor connected across a fixed capacitor, are connected in delta topology. The modulation signal is applied in a clockwise manner with 120° phase increment between the successive ports. Ideally, the signal applied at port 1 should be routed entirely to port 2 (with minimal insertion loss), with no signal at port 3 (maximum isolation). In order to find the values of frequency and amplitude of the modulation signal that will lead to the desired circulation operation, the input signal transmission to all the three ports is noted for a sweep of frequency values and amplitude. Fig. 6.2 shows the S-parameters versus the normalized modulation frequency $f_m/f_0$ and normalized modulation amplitude $\Delta L/L_0$ for $f_0 = 10\,\text{GHz}$, $C = 0.76\,\text{pF}$, and $L_0 = 0.37\,\text{nH}$. For a signal applied at port 1, Fig. 6.2(a) shows the surface plot of transmitted signal (in dB) to port 3 (isolation), while Fig. 6.2(b) shows the signal (in dB) received at port 2 (insertion loss). Fig. 6.2(c) shows the reflected signal (in dB) back to port 1 (return loss). Fig. 6.3(a-c) shows the 3D plots of isolation ($S_{31}$),

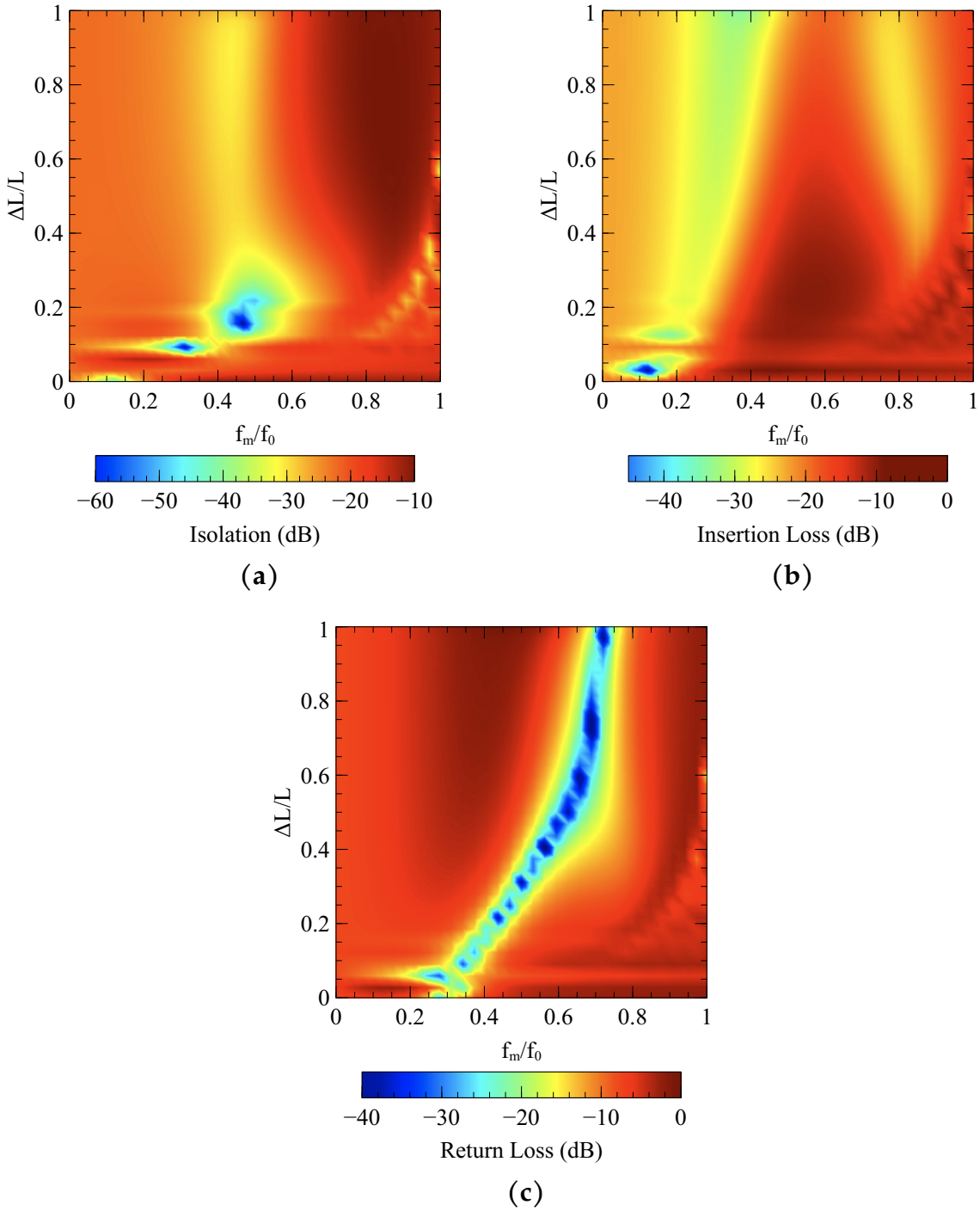



**Figure 6.2:** Surface plots of S-parameters versus the normalized modulation frequency and normalized modulation amplitude (**a**) Isolation, (**b**) Insertion Loss, (**c**) Return Loss.

insertion loss ($S_{21}$) and return loss ($S_{11}$). Fig. 6.2(a-c) and Fig. 6.3(a-c) allow us to find the modulation parameters for which the S-parameters become optimum, ideally, with minimum return loss, minimum insertion loss, and maximum insertion loss.

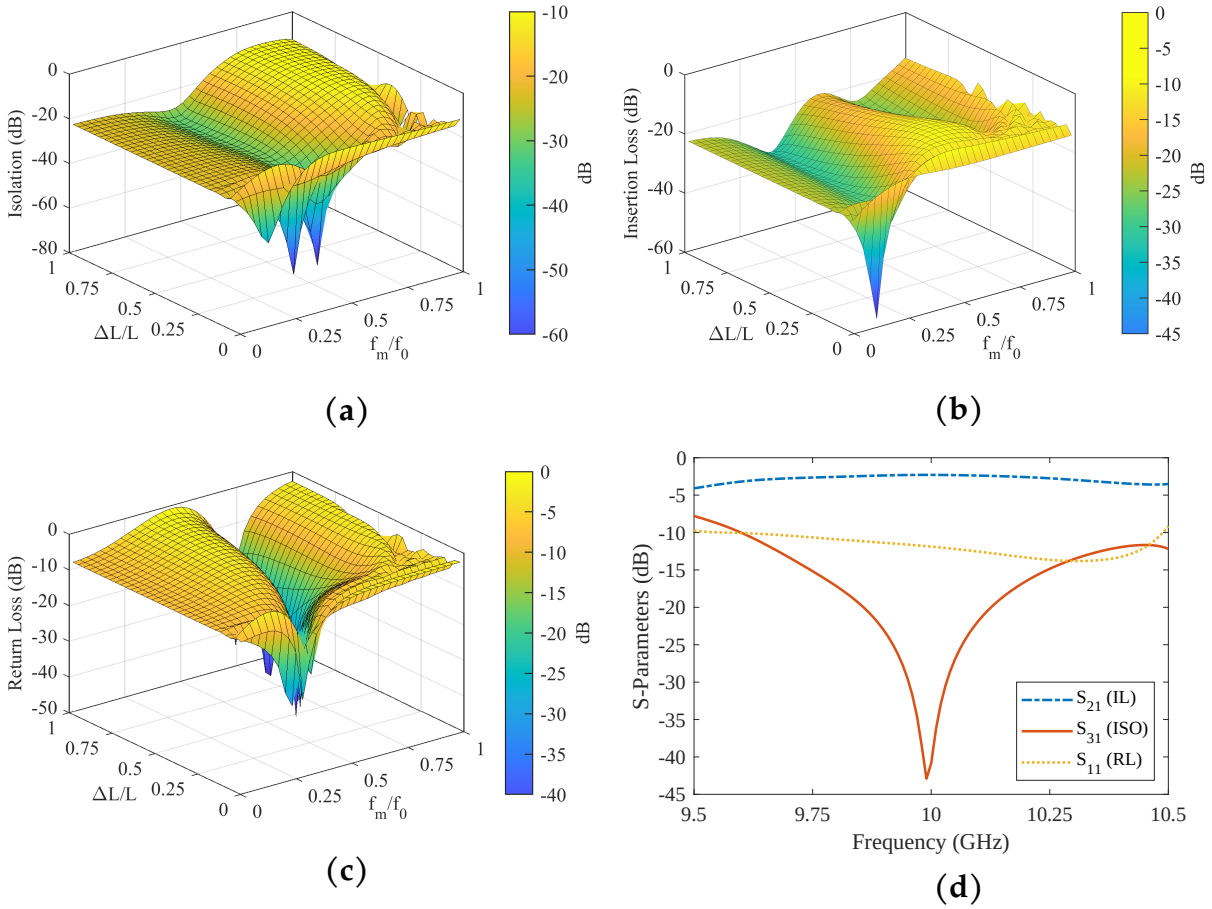



**Figure 6.3:** 3D plots of S-parameters versus the normalized modulation frequency and normalized modulation amplitude (**a**) Isolation, (**b**) Insertion Loss, (**c**) Return Loss, (**d**) Simulated S-parameters showing non-reciprocal operation.

These quantities do not necessarily become optimum under the same modulation parameters, showing that we may need to tradeoff one or several of them when selecting the best possible modulation parameters. In this case the selected modulation frequency is 1.63 GHz and the amplitude is 0.47 times the inductance $L_0$. Using these selected values, the S-parameters of the circulator are shown in Fig. 6.3(d). The values for isolation, IL, and RL at 10 GHz are 43 dB, 12 dB and 2 dB, respectively.

## 6.4 Circulator Design

In the design implementation, each resonator consists of a metal-insulator-metal (MIM) capacitor, $C$, connected in parallel with a meandered microstrip inductor, $L$, as shown in Fig. 6.4. The resonator design is simulated using Sonnet EM and the resonance is observed at 10 GHz. In order to make the inductor tunable, an array of 34 rf-SQUIDs is placed along the length of the inductor. The circulator design has three branches arranged in a delta fashion, where each branch connects two consecutive RF ports. A resonator is placed in each of these branches.

Modulation is applied using a delay TL placed alongside the rf-SQUIDs. The length of

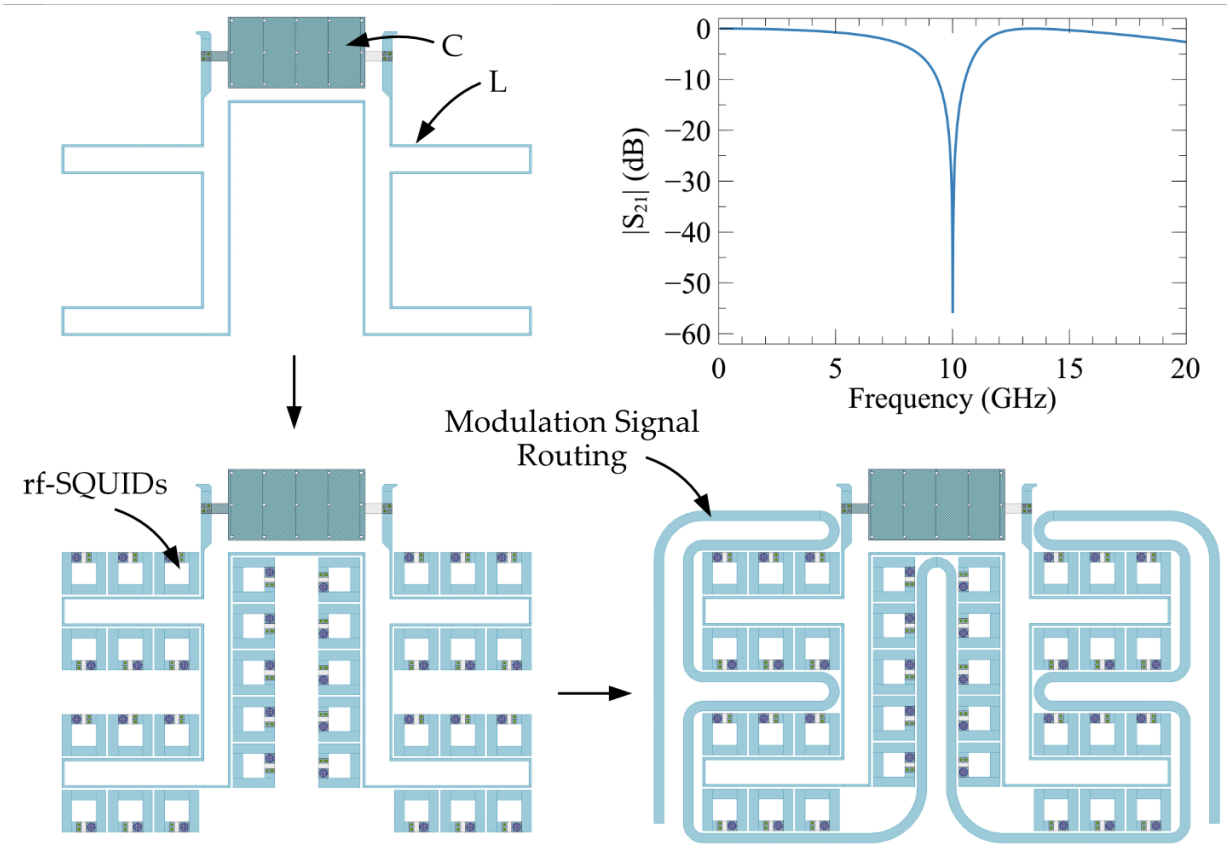



**Figure 6.4:** The resonator design steps: (1) a MIM capacitor and microstrip inductor, the Sonnet EM simulation for the resonator, (2) rf-SQUIDs coupled to the inductor, (3) modulation signal routed alongside the rf-SQUIDs.

the delay TL between two consecutive resonators is adjusted such that it provides a phase delay of 120° at the modulation frequency of 1.63 GHz. Fig. 6.5 shows the meandered microstrip TL model simulated in Sonnet EM and the $\angle S_{21}$ of 120°. Another meandered microstrip section is shown in Fig. 6.6, displaying a $\angle S_{21}$ of 240°.

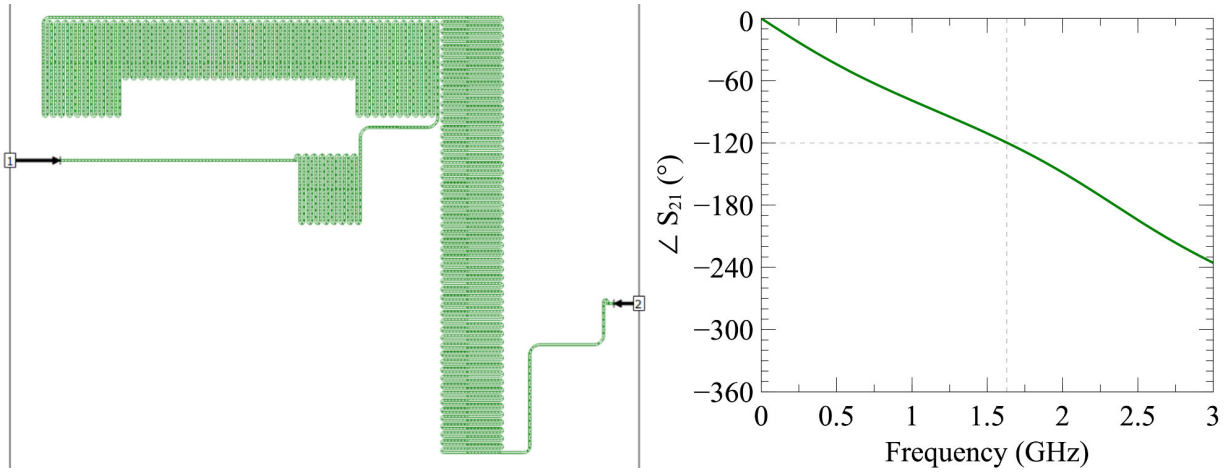



**Figure 6.5:** Sonnet EM model of a meandered microstrip line, simulated phase of 120° at 1.63 GHz.

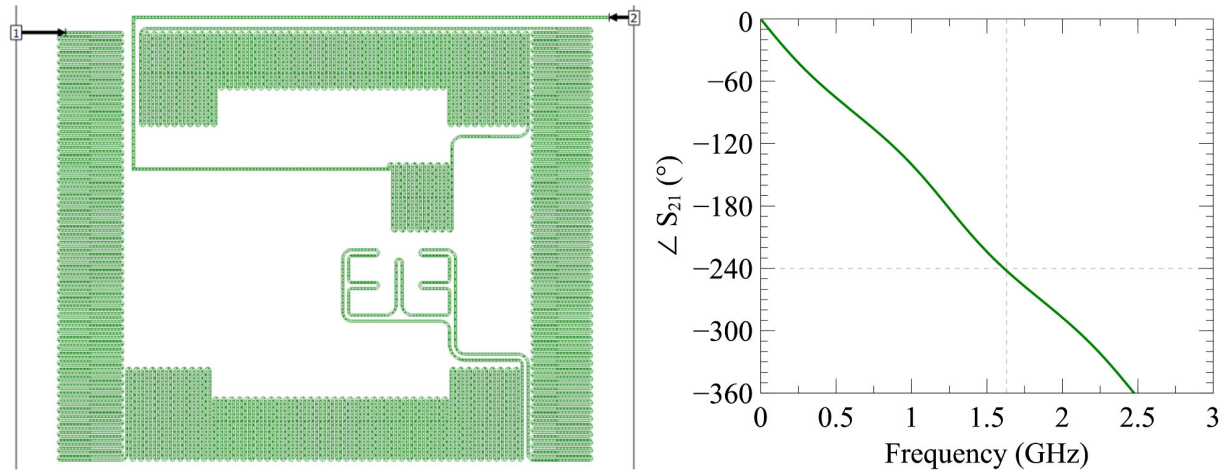



**Figure 6.6:** Sonnet EM model of a meandered microstrip line, simulated phase of 240° at 1.63 GHz.

The complete circulator layout is shown in Fig. 6.7, consisting of three identical resonators connected in delta topology. The signal is provided from the three RF ports

and an additional port for providing the modulation signal. The modulation signal from the port is provided to first resonator, which after meandering is provided to second resonator with a phase delay of 120°. The signal is provided to the third resonator after an additional meandered length providing a phase of 240°. Due to circulator's threefold rotational symmetry, the non-reciprocal operation can be seen even by rotating the indices as $(1,2,3) \rightarrow (2,3,1) \rightarrow (3,1,2)$.

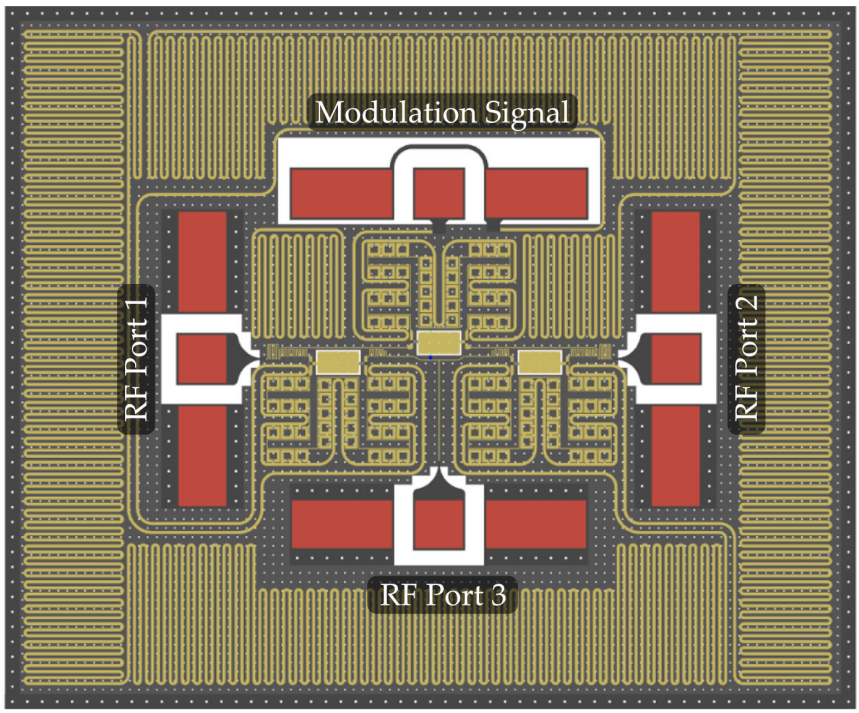



**Figure 6.7:** 2D layout of the superconducting magnetless circulator consisting of three resonators and the meandered delay lines.

Fig. 6.8 shows the 3D view of the circulator layout. It highlights the multi-layer design of the circulator. The highlighted sections show the resonator and the rf-SQUIDs. The rf-SQUID loop is designed on the same layer as the microstrip inductor and is shunted by a JJ. A stack of three metal layers separated by dielectric are used in MIM capacitor keeping the footprint small. This monolithic implementation allows for a compact circulator design compared to the state-of-the-art and also the potential to integrate it with other superconducting components one a single chip.

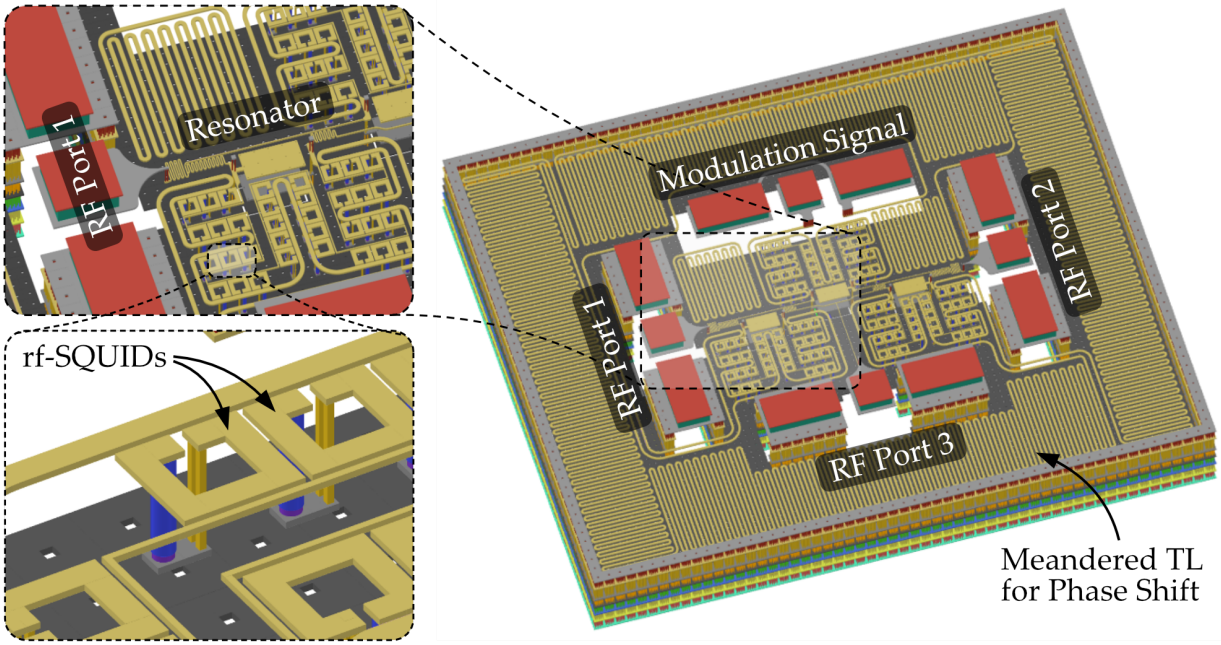



**Figure 6.8:** 3D layout image of the superconducting magnetless circulator consisting of three resonators and the meandered delay lines.

## 6.5 Fabrication and Future Improvement

The cryogenic circulator is fabricated using superconducting Nb 8-layer fabrication process. The RF pads are on layer M8 and the meandered microstrip delay line on layer M6. For the resonators, the inductor line is designed on layer M6 with the ground plane lying on layer M4. The MIM capacitor is made from three Nb-layers M6-M4 separated by two $SiO_2$ dielectric layers. The optical image of the fabricated circulator is shown in Fig. 6.9. The overall device footprint is 0.88 mm $\times$ 1.08 mm, however each resonator is 0.15 mm $\times$ 0.21 mm. The enlarged sections highlight the resonator and the rf-SQUID design used in the resonator. If one of the ports of the proposed device is terminated in matched load, it functions as an isolator which is another useful component in the quantum readout circuitry.

This circulator design provides a lot of scope for further improvement. Using multiple-pole filters instead of a single pole LC resonator arranged in the wye/delta topology to achieve the desired circulator operation with wider bandwidth can be investigated. The reconfigurability in the circulator operation using analog modulation

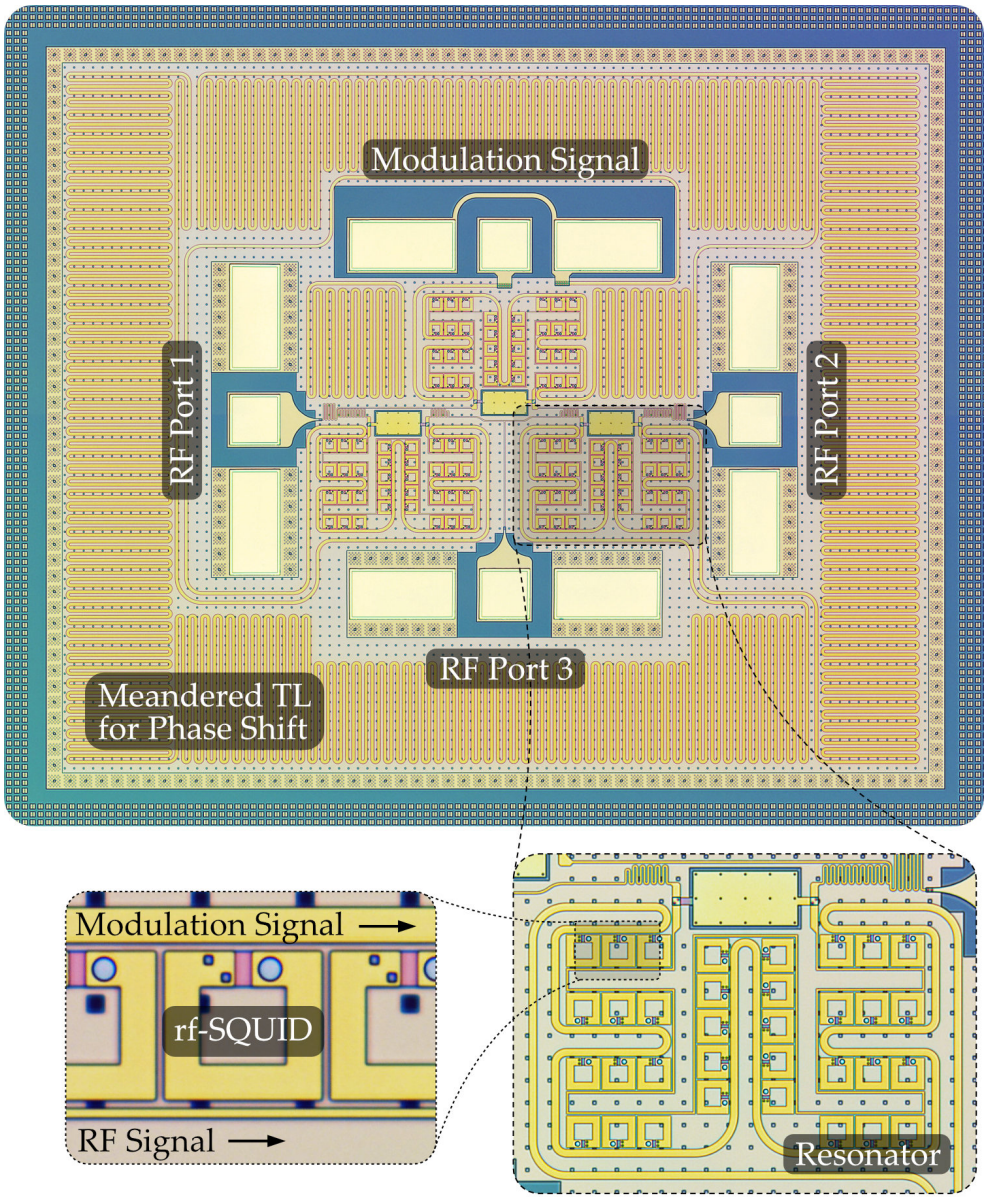



**Figure 6.9:** Optical micrograph of the LTS magnetless circulator. The enlarged sections show a single resonator and rf-SQUID. The overall chip footprint is 0.88 mm $\times$ 1.08 mm.

can be explored.

# Chapter 7

# Conclusion

The main focus of this doctoral thesis is on the development of high performance and reliable superconducting microwave devices such as phase shifters, tunable resonator, power limiter, variable attenuator and magnetless circulator. The proposed devices offer a reconfigurable operation using arrays of rf-SQUIDs and are fabricated using MIT-LL SFQ5ee multi-layer Nb-based fabrication process. The major contributions of this research are summarized below:

## Contributions

The major contributions of this thesis are outlined as follows:

- A Nb-based analog ultra-wideband phase shifter for X- and K- band is presented. The device is realized by coupling an array of rf-SQUIDs to a meandered microwave TL, and the resulting dynamic inductance of the TL is theoretically analyzed. The mutual coupling between rf-SQUIDs and microstrip TL is simulated using Sonnet EM and Ansys Maxwell 3D. The phase of the output signal is tuned by using dc control current and the experimental results are discussed. The phase shift by changing RF power is also experimentally tested and reported.
- A superconducting resonator design using an array of rf-SQUIDs as the tunable inductors is presented. The design comprises of a multi-layer MIM capacitor and a microstrip inductor line loaded by an array of rf-SQUIDs. With applied dc

current, the device offers an ultra-wide tuning range with which surpasses the tunability offered by other state-of-the-art superconducting resonators. The presented resonator is excellent for monolithic integration with other LTS integrated circuits requiring a wide tunability range and high tuning speed.

- Quadrature hybrid couplers serve as an important part of many complex monolithically integrated circuits and systems. While room temperature hybrid couplers are commercially available, they cannot be easily integrated with cryogenic circuits. The design and experimental measurements of Nb-based quadrature hybrid couplers using tandem coplanar waveguide architecture are presented. The design is well suited for monolithic integration with other superconducting circuits. In this report, the hybrid coupler is successfully integrated with two rf-SQUID tunable reflective loads to build a reflective-type phase shifter. The phase tuning with dc current is achieved by using on-chip external dc control circuitry.

- A novel design of a microwave power dependent power limiter is presented for applications in superconductor-based receivers. The topology uses a pair of wideband hybrid couplers along with two microstrip TLs, one of which is magnetically coupled to an array of rf-SQUIDs and offers a variable phase while the other microstrip TL provides a fixed phase. Measured S-parameters and non-linear performance of the power limiter are investigated for a range of RF power levels. A design of variable attenuator based on this topology is also presented, in which the variable levels of attenuation are achieved using dc current. To the best of our knowledge, these are the first implementations of a microwave power limiter and a variable attenuator using rf-SQUIDs.

- The principle of spatiotemporal modulation angular-momentum (STM-AM) is explored for developing a superconducting magnetless circulator. The device consists of three strongly and symmetrically coupled resonators. The proposed design uses rf-SQUIDs, which act as flux-tunable inductors to achieve the desired spatiotemporal modulation. The challenges with the proposed implementation and device measurement are reported and possible resolutions are mentioned for future work.

In summary, the focus of this research has been on the development of monolithically integrated, reconfigurable superconducting microwave devices suitable for quantum applications.

# Thesis List of Publications
## (*as of November 2022*)

## Conference Papers

1 **N. K. Khaira**, T. Singh and R. R. Mansour, "Cryogenic Wideband Quadrature Hybrid Couplers Implemented in a Low Temperature Superconductor Multilayer Process," in *IEEE MTT-S International Microwave Symposium Digest* (*IMS*), Denver, CO, USA, Jun 19–24, 2022. pp. 160–163.

2 **N. K. Khaira**, T. Singh and R. R. Mansour, "Josephson Junctions-Based Low-Temperature Superconducting Phase Shifter for X- and K- Bands Using MIT-LL SFQ5ee Process," in *IEEE MTT-S International Microwave Symposium Digest* (*IMS*), Denver, CO, USA, Jun 19–24, 2022. pp. 1–3. (**Top 10 Student Paper Finalist, and among the top papers selected for publication in IEEE MWCL.**)

3 **N. K. Khaira**, T. Singh and R. R. Mansour, "Low Temperature Superconductor rf-SQUIDs-Based Analog Microwave Variable Attenuator," in *2022 Applied Superconductivity Conference* (*ASC 2022*), Honolulu, HI, USA, Oct 23–28, 2022. pp. 1–2 (Invited Talk).

## Journal Articles

4 **N. K. Khaira**, T. Singh and R. R. Mansour, "Josephson Junctions-Based Low-Temperature Superconducting Phase Shifter for X- and K- Bands Using MIT-LL SFQ5ee Process," in *IEEE Microwave and Wireless Components Letters*, vol. 32, no. 6, pp. 692-695, Jun. 2022. doi: 10.1109/LMWC.2022.3163351.

5 **N. K. Khaira**, T. Singh and R. R. Mansour, "Wideband Power Dependent Power Limiter Based on Distributed Low Temperature Superconductor rf-SQUIDs for Cryogenic RF Receivers," in *IEEE Transactions on Microwave Theory and Techniques*, pp. 1–9, 2022. doi: 10.1109/TMTT.2022.3223873 (*in press*)

6 **N. K. Khaira**, T. Singh and R. R. Mansour, "Low Temperature Superconductor rf-SQUIDs-Based Fully Integrated Reflective-Type Analog Phase Shifter for Quantum Applications," *IEEE Transactions on Microwave Theory and Techniques*, pp. 1–9, 2022. doi: 10.1109/TMTT.2022.3219892 (*in press*)

7 **N. K. Khaira**, T. Singh and R. R. Mansour, "Low Temperature Superconducting Microwave Resonator with Ultra-wide Tuning Range Using an Array of rf-SQUIDs," in *IEEE Transactions on Applied Superconductivity*, pp. 1–5, 2022. (*under review*)

8 **N. K. Khaira**, T. Singh and R. R. Mansour, "Cryogenic Microwave Variable Attenuator Based on rf-SQUIDs for Application in Quantum Systems," in *IEEE Transactions on Applied Superconductivity*, pp. 1-7, 2022. (*under review*).

## Patents

9 **N. K. Khaira**, T. Singh and R. R. Mansour, "Monolithic Low Temperature Superconductor rf-SQUIDs Based Wideband Power Dependent Power Limiter," US Patent Application No. 63/315,440. Filed. March 01,2022.

10 **N. K. Khaira**, T. Singh, M. Golcheshmeh and R. R. Mansour, "Magnet-less Superconducting Microwave Circulator Using rf-SQUIDs," US Patent Application No. 63/400,027. Filed. August 22,2022.

# References


[1] S. Krinner, S. Storz, P. Kurpiers, P. Magnard, J. Heinsoo, R. Keller, J. Luetolf, C. Eichler, and A. Wallraff, "Engineering cryogenic setups for 100-qubit scale superconducting circuit systems," *EPJ Quantum Technology*, vol. 6, no. 1, p. 2, 2019.

[2] L. Ranzani and J. Aumentado, "Circulators at the quantum limit: Recent realizations of quantum-limited superconducting circulators and related approaches," *IEEE Microwave Magazine*, vol. 20, no. 4, pp. 112–122, Apr. 2019.

[3] C. Yan, J. Hassel, V. Vesterinen, J. Zhang, J. Ikonen, L. Grönberg, J. Goetz, and M. Möttönen, "A low-noise on-chip coherent microwave source," *Nature Electronics*, vol. 4, no. 12, pp. 885–892, 2021.

[4] Y. Yu, P. G. Baltus, A. de Graauw, E. van der Heijden, C. S. Vaucher, and A. H. van Roermund, "A 60 GHz phase shifter integrated with LNA and PA in 65 nm CMOS for phased array systems," *IEEE Journal of Solid-State Circuits*, vol. 45, no. 9, pp. 1697–1709, 2010.

[5] T. M. Hancock and G. M. Rebeiz, "A 12-GHz SiGe phase shifter with integrated LNA," *IEEE Trans. Microw. Theory Techn.*, vol. 53, no. 3, pp. 977–983, 2005.

[6] T. Singh and R. R. Mansour, "Loss compensated PCM GeTe-based latching wideband 3-bit switched true-time-delay phase shifters for mmWave phased arrays," *IEEE Trans. Microw. Theory Techn.*, vol. 68, no. 9, pp. 3745–3755, 2020.

[7] T. Singh, N. K. Khaira, and R. R. Mansour, "Thermally actuated SOI RF MEMS-based fully integrated passive reflective-type analog phase shifter for mmWave applications," *IEEE Trans. Microw. Theory Techn.*, vol. 69, no. 1, pp. 119–131, Jan. 2020.

[8] C. Lim, "Limiters protect ADCs without adding harmonics," Microwave & RF (MWRF.com), vol. 54, pp. 56–60, Jan. 2015.

[9] O. A. Mukhanov, V. K. Semenov, W. Li, T. V. Filippov, D. Gupta, A. M. Kadin, D. K. Brock, A. F. Kirichenko, Y. A. Polyakov, and I. V. Vernik, "A superconductor high-resolution ADC," *IEEE Transactions on Applied Superconductivity*, vol. 11, no. 1, pp. 601–606, Mar. 2001.

[10] S. Rylov, L. Bunz, D. Gaidarenko, M. Fisher, R. Robertazzi, and O. Mukhanov, "High resolution ADC system," *IEEE Transactions on Applied Superconductivity*, vol. 7, no. 2, pp. 2649–2652, Jun. 1997.

[11] O. Vendik, "Microwave components and devices based on high temperature superconductors," in *Proceedings of the Third International Kharkov Symposium 'Physics and Engineering of Millimeter and Submillimeter Waves'* (*MSMW*), Kharkov, Ukraine, Sep. 1998, pp. 50–52.

[12] M. Bielski, O. Vendik, M. Gaĭdukov, E. Gol'Man, S. Karmanenko, A. Kozyrev, S. Kolesov, and T. Samoĭlova, "Surface resistance of Y-Ba-Cu-O ceramics in the region between RF and microwave frequencies," *Soviet Journal of Experimental and Theoretical Physics Letters*, vol. 46, p. S145, Aug. 1987.

[13] T. VanDuzer and W. V. Hassenzahl, "Scanning the issue - Special issue on applications of superconductivity," *Proceedings of the IEEE*, vol. 92, no. 10, pp. 1511–1516, Oct. 2004.

[14] M. Lindmayer and H. Mosebach, "Current limiting properties of YBCO-films on sapphire substrates," *IEEE Transactions on Applied Superconductivity*, vol. 9, no. 2, pp. 1369–1372, Jun. 1999.

[15] A. Heinrich, R. Semerad, H. Kinder, H. Mosebach, and M. Lindmayer, "Fault current limiting properties of YBCO-films on sapphire substrates," *IEEE Transactions on Applied Superconductivity*, vol. 9, no. 2, pp. 660–663, Jun. 1999.

[16] J. C. Booth, D. A. Rudman, and R. H. Ono, "A self-attenuating superconducting transmission line for use as a microwave power limiter," *IEEE Transactions on Applied Superconductivity*, vol. 13, no. 2, pp. 305–310, Jun. 2003.

[17] J. C. Booth, K. Leong, and S. A. Schima, "A superconducting microwave power limiter for high-performance receiver protection," in *Proceedings of the IEEE MTT-S International Microwave Symposium Digest*. Fort Worth, TX, USA: IEEE, Jun. 2004, pp. 139–142.

[18] B. Belyaev, I. Govorun, A. Leksikov, and A. Serzhantov, "Receiver protecting device based on microstrip structure with high-temperature superconductor film," *Technical Physics Letters*, vol. 38, no. 3, pp. 211–214, 2012.

[19] B. Belyaev, I. Govorun, A. Leksikov, A. Serzhantov, and A. A. Leksikov, "Reflective power limiter for x-band with htsc switching element," *IEEE Transactions on Applied Superconductivity*, vol. 26, no. 6, pp. 1–6, 2016.

[20] E. Rocas, C. Collado, J. Mateu, N. Orloff, and J. C. Booth, "Modeling of self-heating mechanism in the design of superconducting limiters," *IEEE Transactions on Applied Superconductivity*, vol. 21, no. 3, pp. 547–550, Sep. 2010.

[21] D. M. Sheen, S. M. Ali, D. E. Oates, R. S. Withers, and J. Kong, "Current distribution, resistance, and inductance for superconducting strip transmission lines," *IEEE Transactions on Applied Superconductivity*, vol. 1, no. 2, pp. 108–115, Jun. 1991.

[22] W. Weeks, L.-H. Wu, M. McAllister, and A. Singh, "Resistive and inductive skin effect in rectangular conductors," *IBM Journal of Research and Development*, vol. 23, no. 6, pp. 652–660, 1979.

[23] Skyworks Solutions, Inc., "PIN limiter diodes in receiver protectors," Application Note, Aug. 2008.

[24] Z. R. Szczepaniak, A. Arvaniti, K. Sawicka-Szczepaniak, and E. Sedek, "Nonlinear resonant circuits for microwave low power limiters," *IEEE Microwave and Wireless Components Letters*, vol. 17, no. 12, pp. 870–872, Dec. 2007.

[25] D. G. Smith, D. D. Heston, and D. L. Allen, "Designing high-power limiter circuits with gaas pin diodes," in *1999 IEEE MTT-S International Microwave Symposium Digest (Cat. No. 99CH36282)*, vol. 1. IEEE, 1999, pp. 329–332.

[26] S. Deng, C. Gao, S. Chen, J. Sun, and K. Wu, "Research on linearity improvement of silicon-based PIN diode limiters," *IEEE Microwave and Wireless Components Letters*, vol. 30, no. 1, pp. 62–65, Jan. 2019.

[27] D. G. Smith, D. D. Heston, J. Heston, B. Heimer, and K. Decker, "Designing reliable high-power limiter circuits with GaAs PIN diodes," in *Proceedings of the IEEE MTT-S International Microwave Symposium Digest*, vol. 2. Seattle, WA, USA: IEEE, Jun. 2002, pp. 1245–1247.

[28] J. Gauvin, O. Vendier, J.-L. Cazaux, and P. Blondy, "Microwave power limiters based on RF-MEMS," in *Proceedings of the 26th IEEE International Conference on Micro Electro Mechanical Systems (MEMS)*, Taipei, Taiwan, Jan. 2013, pp. 769–772.

[29] R. Malmqvist, R. Jonsson, C. Samuelsson, S. Reyaz, P. Rantakari, A. Ouacha, T. Vähä-Heikkilä, J. Varis, and A. Rydberg, "Self-actuation tests of ohmic contact and capacitive RF MEMS switches for wideband RF power limiter circuits," in *International Semiconductor Conference (CAS)*, Sinaia, Romania, Oct. 2012, pp. 217–220.

[30] J. R. Reid, L. A. Starman, and R. T. Webster, "RF actuation of capacitive MEMS switches," in *Proceedings of the IEEE MTT-S International Microwave Symposium Digest*, vol. 3, Philadelphia, PA, USA, Jun. 2003, pp. 1919–1922.

[31] D. Shojaei-Asanjan, M. Bakri-Kassem, and R. R. Mansour, "Analysis of thermally actuated RF-MEMS switches for power limiter applications," *Journal of Microelectromechanical Systems*, vol. 28, no. 1, pp. 107–113, Jan. 2019.

[32] J. Givernaud, A. Crunteanu, A. Pothier, C. Champeaux, A. Catherinot, and P. Blondy, "CPW self-resetting power limiting devices based on microwave power induced semiconductor-metal transition in vanadium dioxide," in *Proceedings of the IEEE MTT-S International Microwave Symposium Digest*, Boston, MA, USA, Jun. 2009, pp. 109–112.

[33] J. Givernaud, A. Crunteanu, J.-C. Orlianges, A. Pothier, C. Champeaux, A. Catherinot, and P. Blondy, "Microwave power limiting devices based on the semiconductor–metal transition in vanadium–dioxide thin films," *IEEE Transactions on Microwave Theory and Techniques*, vol. 58, no. 9, pp. 2352–2361, Sep. 2010.

[34] S. Stitzer, "Frequency selective microwave power limiting in thin YIG films," *IEEE Transactions on Magnetics*, vol. 19, no. 5, pp. 1874–1876, Sep. 1983.

[35] J. D. Adam and S. N. Stitzer, "MSW frequency selective limiters at UHF," *IEEE Transactions on Magnetics*, vol. 40, no. 4, pp. 2844–2846, 2004.

[36] H. Suhl, "The theory of ferromagnetic resonance at high signal powers," *Journal of Physics and Chemistry of Solids*, vol. 1, no. 4, pp. 209–227, 1957.

[37] S. M. Gillette, M. Geiler, J. D. Adam, and A. L. Geiler, "Ferrite-based reflective-type frequency selective limiters," in *Proceedings of the IEEE MTT-S International Microwave Workshop Series on Advanced Materials and Processes for RF and THz Applications (IMWS-AMP)*, Ann Arbor, MI, USA, Jul. 2018, pp. 1–3.

[38] D. Shojaei-Asanjan, S. Attar, and R. R. Mansour, "Tunable RF MEMS-based frequency dependent power limiter," in *Proceedings of the IEEE MTT-S International Microwave Symposium Digest*, San Francisco, CA, USA, Jun. 2016, pp. 1–3.

[39] J. Wang, A. Yang, Y. Chen, Z. Chen, A. Geiler, S. M. Gillette, V. G. Harris, and C. Vittoria, "Self biased y-junction circulator at *Ku* bandband," *IEEE Microwave and Wireless Components Letters*, vol. 21, no. 6, pp. 292–294, 2011.

[40] V. Laur, G. Vérissimo, P. Quéffélec, L. A. Farhat, H. Alaaeddine, E. Laroche, G. Martin, R. Lebourgeois, and J. Ganne, "Self-biased y-junction circulators using lanthanum-and cobalt-substituted strontium hexaferrites," *IEEE Transactions on Microwave Theory and Techniques*, vol. 63, no. 12, pp. 4376–4381, 2015.

[41] A. Saib, M. Darques, L. Piraux, D. Vanhoenacker-Janvier, and I. Huynen, "Unbiased microwave circulator based on ferromagnetic nanowires arrays of tunable magnetization state," *Journal of Physics D: Applied Physics*, vol. 38, no. 16, p. 2759, 2005.

[42] S. Tanaka, N. Shimomura, and K. Ohtake, "Active circulators—the realization of circulators using transistors," *Proceedings of the IEEE*, vol. 53, no. 3, pp. 260–267, 1965.

[43] T. Kodera, D. L. Sounas, and C. Caloz, "Magnetless nonreciprocal metamaterial (mnm) technology: Application to microwave components," *IEEE Transactions on Microwave Theory and Techniques*, vol. 61, no. 3, pp. 1030–1042, 2013.

[44] S. Wang, C.-H. Lee, and Y.-B. Wu, "Fully integrated 10-ghz active circulator and quasi-circulator using bridged-t networks in standard cmos," *IEEE Transactions on Very Large Scale Integration (VLSI) Systems*, vol. 24, no. 10, pp. 3184–3192, 2016.

[45] N. A. Estep, D. L. Sounas, J. Soric, and A. Alù, "Magnetic-free non-reciprocity and isolation based on parametrically modulated coupled-resonator loops," *Nature Physics*, vol. 10, no. 12, pp. 923–927, 2014.

[46] A. Kord, D. L. Sounas, and A. Alù, "Magnet-less circulators based on spatiotemporal modulation of bandstop filters in a delta topology," *IEEE Transactions on Microwave Theory and Techniques*, vol. 66, no. 2, pp. 911–926, 2017.

[47] A. Kord, D. L. Sounas, and A. Alu, "Pseudo-linear time-invariant magnetless circulators based on differential spatiotemporal modulation of resonant junctions," *IEEE Transactions on Microwave Theory and Techniques*, vol. 66, no. 6, pp. 2731–2745, 2018.

[48] A. Kord, M. Tymchenko, D. L. Sounas, H. Krishnaswamy, and A. Alù, "Cmos integrated magnetless circulators based on spatiotemporal modulation angular-momentum biasing," *IEEE Transactions on Microwave Theory and Techniques*, vol. 67, no. 7, pp. 2649–2662, 2019.

[49] Y. Yu, G. Michetti, A. Kord, M. Pirro, D. L. Sounas, Z. Xiao, C. Cassella, A. Alù, and M. Rinaldi, "Highly-linear magnet-free microelectromechanical circulators," *Journal of Microelectromechanical Systems*, vol. 28, no. 6, pp. 933–940, 2019.

[50] F. London, *Superfluids*. New York: Wiley, 1950.

[51] B. S. Deaver Jr and W. M. Fairbank, "Experimental evidence for quantized flux in superconducting cylinders," *Physical Review Letters*, vol. 7, no. 2, p. 43, 1961.

[52] R. Doll and M. Näbauer, "Experimental proof of magnetic flux quantization in a superconducting ring," *Physical Review Letters*, vol. 7, no. 2, p. 51, 1961.

[53] B. D. Josephson, "Possible new effects in superconductive tunnelling," *Physics letters*, vol. 1, no. 7, pp. 251–253, 1962.

[54] P. W. Anderson and J. M. Rowell, "Probable observation of the josephson superconducting tunneling effect," *Physical Review Letters*, vol. 10, no. 6, p. 230, 1963.

[55] J. Clarke and A. I. Braginski, *The SQUID Handbook: Fundamentals and Technology of SQUIDs and SQUID Systems, Volume I*. New York: Wiley-Vch, 2006.

[56] G. F. Dionne, D. E. Oates, and D. H. Temme, "Low-loss microwave ferrite phase shifters with superconducting circuits," in *IEEE MTT-S Intl. Microw. Symp. Dig. (IMS)*, San Diego, CA, USA, May 1994, pp. 101–103.

[57] C. M. Jackson, J. H. Kobayashi, E. B. Guillory, C. Pettiette-Hall, and J. F. Burch, "Monolithic HTS microwave phase shifter and other devices," *J. Supercond.*, vol. 5, no. 4, pp. 417–422, 1992.

[58] D. J. Durand, J. Carpenter, E. Ladizinsky, L. Lee, C. M. Jackson, A. Silver, and A. D. Smith, "The distributed Josephson inductance phase shifter," *IEEE Trans. Appl. Supercond.*, vol. 2, no. 1, pp. 33–38, Mar. 1992.

[59] J. Zhang, T. Li, R. Kokkoniemi, C. Yan, W. Liu, M. Partanen, K. Y. Tan, M. He, L. Ji, L. Grönberg *et al.*, "Broadband tunable phase shifter for microwaves," *AIP Adv.*, vol. 10, no. 6, p. 065128, 2020.

[60] A. Barone and G. Paterno, *Physics and applications of the Josephson effect*. Wiley Online Library, 1982, vol. 1.

[61] S. K. Tolpygo, V. Bolkhovsky, T. J. Weir, A. Wynn, D. E. Oates, L. M. Johnson, and M. A. Gouker, "Advanced fabrication processes for superconducting very large-scale integrated circuits," *IEEE Trans. Appl. Supercond.*, vol. 26, no. 3, pp. 1–10, Apr. 2016.

[62] R. Rafique, T. Ohki, P. Linner, and A. Y. Herr, "Niobium tunable microwave filter," *IEEE Trans. Microw. Theory Techn.*, vol. 57, no. 5, pp. 1173–1179, 2009.

[63] T. Zhou, L. Fang, S. Li, L. Ji, F. Song, M. He, X. Zhang, and S. Yan, "Nonlinear inductance of intrinsic Josephson junction arrays and its application to tunable filters," *IEEE Trans. Appl. Supercond.*, vol. 17, no. 2, pp. 586–589, 2007.

[64] F. Wulschner, J. Goetz, F. R. Koessel, E. Hoffmann, A. Baust, P. Eder, M. Fischer, M. Haeberlein, M. J. Schwarz, M. Pernpeintner *et al.*, "Tunable coupling of transmission-line microwave resonators mediated by an rf-SQUID," *EPJ Quantum Techn.*, vol. 3, no. 1, pp. 1–10, 2016.

[65] M. Castellanos-Beltran and K. Lehnert, "Widely tunable parametric amplifier based on a superconducting quantum interference device array resonator," *Appl. Phys. Lett.*, vol. 91, no. 8, p. 083509, 2007.

[66] K. Lehnert, K. Irwin, M. Castellanos-Beltran, J. Mates, and L. Vale, "Evaluation of a microwave SQUID multiplexer prototype," *IEEE Trans. Appl. Supercond.*, vol. 17, no. 2, pp. 705–709, 2007.

[67] J. Mates, G. C. Hilton, K. D. Irwin, L. R. Vale, and K. Lehnert, "Demonstration of a multiplexer of dissipationless superconducting quantum interference devices," *Appl. Phys. Lett.*, vol. 92, no. 2, p. 023514, 2008.

[68] E. M. Vavagiakis, Z. Ahmed, A. Ali, K. Arnold, J. Austermann, S. M. Bruno, S. K. Choi, J. Connors, N. Cothard, S. Dicker *et al.*, "The Simons Observatory: Magnetic sensitivity measurements of microwave SQUID multiplexers," *IEEE Trans. Appl. Supercond.*, vol. 31, no. 5, pp. 1–5, 2021.

[69] G. Vardulakis, S. Withington, D. Goldie, and D. Glowacka, "Superconducting kinetic inductance detectors for astrophysics," *Meas. Sci. Techn.*, vol. 19, no. 1, p. 015509, 2007.

[70] S. E. de Graaf, A. Danilov, A. Adamyan, and S. Kubatkin, "A near-field scanning microwave microscope based on a superconducting resonator for low power measurements," *Rev. Sci. Instr.*, vol. 84, no. 2, p. 023706, 2013.

[71] K. Osborn, J. Strong, A. J. Sirois, and R. W. Simmonds, "Frequency-tunable Josephson junction resonator for quantum computing," *IEEE Trans. Appl. Supercond.*, vol. 17, no. 2, pp. 166–168, 2007.

[72] M. Pierre, I.-M. Svensson, S. Raman Sathyamoorthy, G. Johansson, and P. Delsing, "Storage and on-demand release of microwaves using superconducting resonators with tunable coupling," *Appl. Phys. Lett.*, vol. 104, no. 23, p. 232604, 2014.

[73] Y. Zhu and W. Jia, "Single-photon quantum router in the microwave regime utilizing double superconducting resonators with tunable coupling," *Physical Rev. A*, vol. 99, no. 6, p. 063815, 2019.

[74] A. Adamyan, S. Kubatkin, and A. Danilov, "Tunable superconducting microstrip resonators," *Appl. Phys. Lett.*, vol. 108, no. 17, p. 172601, 2016.

[75] A. Asfaw, A. Sigillito, A. Tyryshkin, T. Schenkel, and S. A. Lyon, "Multi-frequency spin manipulation using rapidly tunable superconducting coplanar waveguide microresonators," *Appl. Phys. Lett.*, vol. 111, no. 3, p. 032601, 2017.

[76] J. Healey, T. Lindström, M. Colclough, C. Muirhead, and A. Y. Tzalenchuk, "Magnetic field tuning of coplanar waveguide resonators," *Appl. Phys. Lett.*, vol. 93, no. 4, p. 043513, 2008.

[77] A. J. Annunziata, D. F. Santavicca, L. Frunzio, G. Catelani, M. J. Rooks, A. Frydman, and D. E. Prober, "Tunable superconducting nanoinductors," *Nanotechn.*, vol. 21, no. 44, p. 445202, 2010.

[78] M. R. Vissers, J. Hubmayr, M. Sandberg, S. Chaudhuri, C. Bockstiegel, and J. Gao, "Frequency-tunable superconducting resonators via nonlinear kinetic inductance," *Appl. Phys. Lett.*, vol. 107, no. 6, p. 062601, 2015.

[79] M. Sandberg, C. Wilson, F. Persson, T. Bauch, G. Johansson, V. Shumeiko, T. Duty, and P. Delsing, "Tuning the field in a microwave resonator faster than the photon lifetime," *Appl. Phys. Lett.*, vol. 92, no. 20, p. 203501, 2008.

[80] Z. Wang, Y. Zhong, L. He, H. Wang, J. M. Martinis, A. Cleland, and Q. Xie, "Quantum state characterization of a fast tunable superconducting resonator," *Appl. Phys. Lett.*, vol. 102, no. 16, p. 163503, 2013.

[81] O. Kennedy, J. Burnett, J. Fenton, N. Constantino, P. Warburton, J. Morton, and E. Dupont-Ferrier, "Tunable Nb superconducting resonator based on a constriction nano-SQUID fabricated with a Ne focused ion beam," *Physical Rev. Appl.*, vol. 11, no. 1, p. 014006, 2019.

[82] I.-M. Svensson, M. Pierre, M. Simoen, W. Wustmann, P. Krantz, A. Bengtsson, G. Johansson, J. Bylander, V. Shumeiko, and P. Delsing, "Microwave photon generation in a doubly tunable superconducting resonator," in *Journal of Physics: Conference Series*, vol. 969, no. 1. IOP Publishing, 2018, p. 012146.

[83] N. K. Khaira, T. Singh, and R. R. Mansour, "Josephson junctions-based low-temperature superconducting phase shifter for *X*-and *K*-Bands using MIT-LL SFQ5ee process," *IEEE Microw. Wireless Compon. Lett.*, vol. 32, no. 6, pp. 692–695, Jun. 2022, doi:10.1109/LMWC.2022.3163351.

[84] N. K. Khaira, T. Singh, and R. R. Mansour, "Monolithically integrated RF MEMS-based variable attenuator for millimeter-wave applications," *IEEE Trans. Microw. Theory Techn.*, vol. 67, no. 8, pp. 3251–3259, Aug. 2019.

[85] N. K. Khaira, T. Singh, and R. R. Mansour, "RF MEMS based 60 GHz variable attenuator," in *Proc. IEEE MTT-S Int. Microw. Workshop Ser. Adv. Mater. Processes for RF and THz Appl.* (*IMWS-AMP*), Ann Arbor, MI, USA, Jul. 2018, pp. 1–3.

[86] N. K. Khaira, "SOI RF-MEMS based variable attenuator for millimeter-wave applications," Ph.D. dissertation, Dept. Elect. Comput. Eng., Univ. of Waterloo, Waterloo, ON, Canada, May 2019.

[87] T. Singh, "Monolithically integrated phase change material GeTe-based RF components for millimeter wave applications," Ph.D. dissertation, Dept. Elect. Comput. Eng., Univ. of Waterloo, Waterloo, ON, Canada, Apr. 2020.

[88] T. Singh, N. K. Khaira, and R. R. Mansour, "Thermally actuated SOI RF MEMS-based fully integrated passive reflective-type analog phase shifter for mmWave applications," *IEEE Trans. Microw. Theory Techn.*, vol. 69, no. 1, pp. 119–131, Jan. 2021.

[89] I. Malo-Gomez, J. D. Gallego-Puyol, C. Diez-Gonzalez, I. Lopez-Fernandez, and C. Briso-Rodriguez, "Cryogenic hybrid coupler for ultra-low-noise radio astronomy balanced amplifiers," *IEEE Trans. Microw. Theory Techn.*, vol. 57, no. 12, pp. 3239–3245, 2009.

[90] R. Gawande, R. Reeves, L. Samoska, K. Cleary, A. C. Readhead, T. Gaier, P. Kangaslahti, M. Varonen, S. Church, K. Devaraj *et al.*, "W-band IQ sub-harmonic mixers with low LO power for cryogenic operation in large arrays," in *Proc. 9th Eur. Microw. Integr. Circuits Conf. (EUMIC)*, Rome, Italy, Oct. 2014, pp. 301–304.

[91] H. Ku, F. Mallet, L. Vale, K. Irwin, S. Russek, G. Hilton, and K. Lehnert, "Design and testing of superconducting microwave passive components for quantum information processing," *IEEE Trans. Appl. Supercond.*, vol. 21, no. 3, pp. 452–455, 2010.

[92] E. Hoffmann, F. Deppe, T. Niemczyk, T. Wirth, E. Menzel, G. Wild, H. Huebl, M. Mariantoni, T. Weißl, A. Lukashenko *et al.*, "A superconducting 180 hybrid ring coupler for circuit quantum electrodynamics," *Appl. Phys*, vol. 97, no. 22, p. 222508, 2010.

[93] P. D. Laforge, R. R. Mansour, and M. Yu, "Diplexer design implementing highly miniaturized multilayer superconducting hybrids and filters," *IEEE Trans. Appl. Supercond.*, vol. 19, no. 2, pp. 47–54, 2009.

[94] T.-Y. Chang, C.-L. Liao, and C. H. Chen, "Novel uniplanar tandem couplers," in *Proc. 32nd Eur. Microw. Conf. (EUMC)*, Milan, Italy, Sept. 2002, pp. 1–4.

[95] J. Hornibrook, J. Colless, I. C. Lamb, S. Pauka, H. Lu, A. Gossard, J. Watson, G. Gardner, S. Fallahi, M. Manfra *et al.*, "Cryogenic control architecture for large-scale quantum computing," *Physical Review Applied*, vol. 3, no. 2, p. 024010, 2015.

[96] P. Magnard, S. Storz, P. Kurpiers, J. Schär, F. Marxer, J. Lütolf, T. Walter, J.-C. Besse, M. Gabureac, K. Reuer *et al.*, "Microwave quantum link between superconducting

circuits housed in spatially separated cryogenic systems," *Physical Review Letters*, vol. 125, no. 26, p. 260502, 2020.

[97] C. J. Axline, L. D. Burkhart, W. Pfaff, M. Zhang, K. Chou, P. Campagne-Ibarcq, P. Reinhold, L. Frunzio, S. Girvin, L. Jiang *et al.*, "On-demand quantum state transfer and entanglement between remote microwave cavity memories," *Nature Physics*, vol. 14, no. 7, pp. 705–710, 2018.

[98] Z.-L. Xiang, M. Zhang, L. Jiang, and P. Rabl, "Intracity quantum communication via thermal microwave networks," *Physical Review X*, vol. 7, no. 1, p. 011035, 2017.

[99] R. Di Candia, H. Yiğitler, G. Paraoanu, and R. Jäntti, "Two-way covert quantum communication in the microwave regime," *PRX Quantum*, vol. 2, no. 2, p. 020316, 2021.

[100] C. M. Jackson, J. H. Kobayashi, A. Lee, C. Pettiette-Hall, J. F. Burch, R. Hu, R. Hilton, and J. McDade, "Novel monolithic phase shifter combining ferroelectrics and high temperature superconductors," *Microw. Optical Techn. Lett.*, vol. 5, no. 14, pp. 722–726, 1992.

[101] P. Wang, C. Tan, Y. Ma, W. Cheng, and C. Ong, "Planar tunable high-temperature superconductor microwave broadband phase shifter with patterned ferroelectric thin film," *Superconductor Science and Technology*, vol. 20, no. 1, p. 77, 2006.

[102] G. F. Dionne, D. E. Oates, and D. H. Temme, "YBCO/ferrite low-loss microwave phase shifter," *IEEE Trans. Appl. Supercond.*, vol. 5, no. 2, pp. 2083–2086, 1995.

[103] C. Jackson and D. Durand, "10 GHz high temperature superconductor phase shifter," in *IEEE MTT-S Intl. Microw. Symp. Dig. (IMS)*. Boston, MA, USA: IEEE, Jul. 1991, pp. 165–168.

[104] J. H. Takemoto-Kobayashi, C. M. Jackson, E. B. Guillory, C. Pettiette-Hall, and J. F. Burch, "Monolithic high-T/sub c/superconducting phase shifter at 10 GHz," *IEEE Trans. Microw. Theory Techn.*, vol. 40, no. 12, pp. 2339–2344, 1992.

[105] S. Berkowitz, C. Shih, W. Mallison, D. Zhang, and A. Hirahara, "Demonstration of a 20 GHz phase shifter using high-temperature superconducting SNS junctions," *IEEE Trans. Appl. Supercond.*, vol. 7, no. 2, pp. 3056–3059, 1997.

[106] N. K. Khaira, T. Singh, and R. R. Mansour, "Cryogenic wideband quadrature hybrid couplers implemented in a low temperature superconductor multilayer process," in *2022 IEEE/MTT-S International Microwave Symposium-IMS 2022*. IEEE, 2022, pp. 160–163.

[107] M. Tabesh, A. Arbabian, and A. Niknejad, "60GHz low-loss compact phase shifters using a transformer-based hybrid in 65nm CMOS," in *IEEE Custom Integrated Circuits Conference (CICC)*, 2011, pp. 1–4.

[108] E. B. Wikborg, V. K. Semenov, and K. K. Likharev, "RSFQ front-end for a software radio receiver," *IEEE Trans. Appl. Supercond.*, vol. 9, no. 2, pp. 3615–3618, Jun. 1999.

[109] J.-H. Yeh, J. LeFebvre, S. Premaratne, F. Wellstood, and B. Palmer, "Microwave attenuators for use with quantum devices below 100 mK," *Journal of Applied Physics*, vol. 121, no. 22, p. 224501, 2017.

[110] M. L. Roukes, M. Freeman, R. Germain, R. Richardson, and M. Ketchen, "Hot electrons and energy transport in metals at millikelvin temperatures," *Physical review letters*, vol. 55, no. 4, p. 422, 1985.

[111] Z. Wang, S. Shankar, Z. Minev, P. Campagne-Ibarcq, A. Narla, and M. H. Devoret, "Cavity attenuators for superconducting qubits," *Physical Review Applied*, vol. 11, no. 1, p. 014031, 2019.

[112] V. Koshelets and S. Shitov, "Integrated superconducting receivers," *Superconductor Science and Technology*, vol. 13, no. 5, p. R53, 2000.

[113] V. Koshelets, S. Shitov, A. Shchukin, A. Baryshev, L. Filippenko, G. M. Fischer, and J. Mygind, "Josephson tunnel junction microwave attenuator," *Applied physics letters*, vol. 63, no. 23, pp. 3218–3220, 1993.

[114] E. Denlinger, R. Paglione, D. Kalokitis, E. Belohoubek, A. Pique, X. Wu, T. Venkatesan, A. Fathy, V. Pendrick, S. Green *et al.*, "Superconducting nonreciprocal devices for microwave systems," *IEEE Microwave and Guided wave letters*, vol. 2, no. 11, pp. 449–451, 1992.

[115] R. R. Mansour, S. Ye, V. Dokas, B. Jolley, G. Thomson, W.-C. Tang, and C. M. Kudsia, "Design considerations of superconductive input multiplexers for satellite applications," *IEEE Transactions on Microwave Theory and Techniques*, vol. 44, no. 7, pp. 1213–1228, 1996.

[116] R. Fleury, D. L. Sounas, C. F. Sieck, M. R. Haberman, and A. Alù, "Sound isolation and giant linear nonreciprocity in a compact acoustic circulator," *Science*, vol. 343, no. 6170, pp. 516–519, 2014.

# Appendices

# Appendix A

# Complete Microfabrication Chip Layouts

## 5mm $\times$ 5mm Chip Layouts for MIT-LL

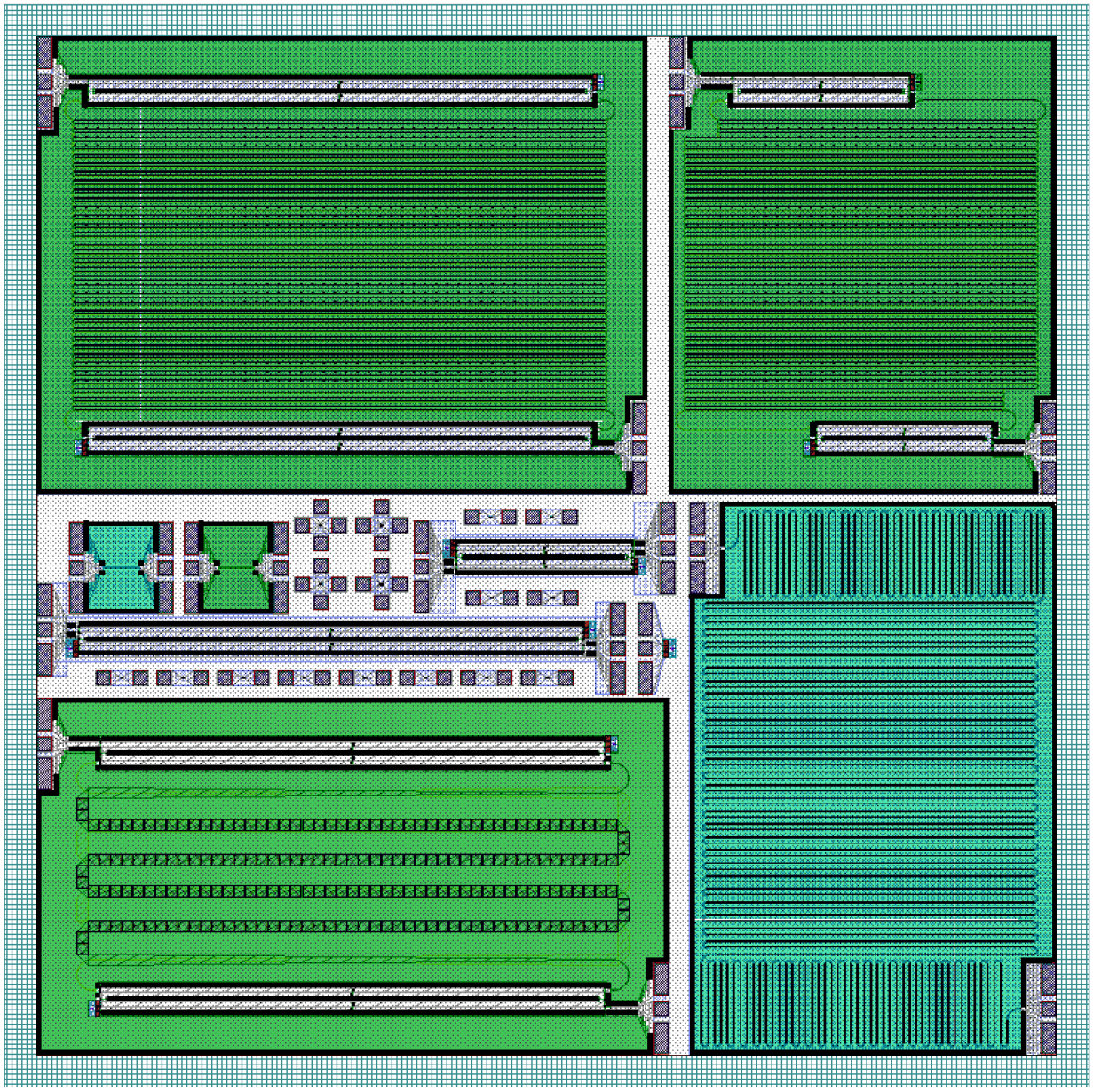


**Figure A.1:** 5mm x 5mm chip layout submitted to MIT-LL.

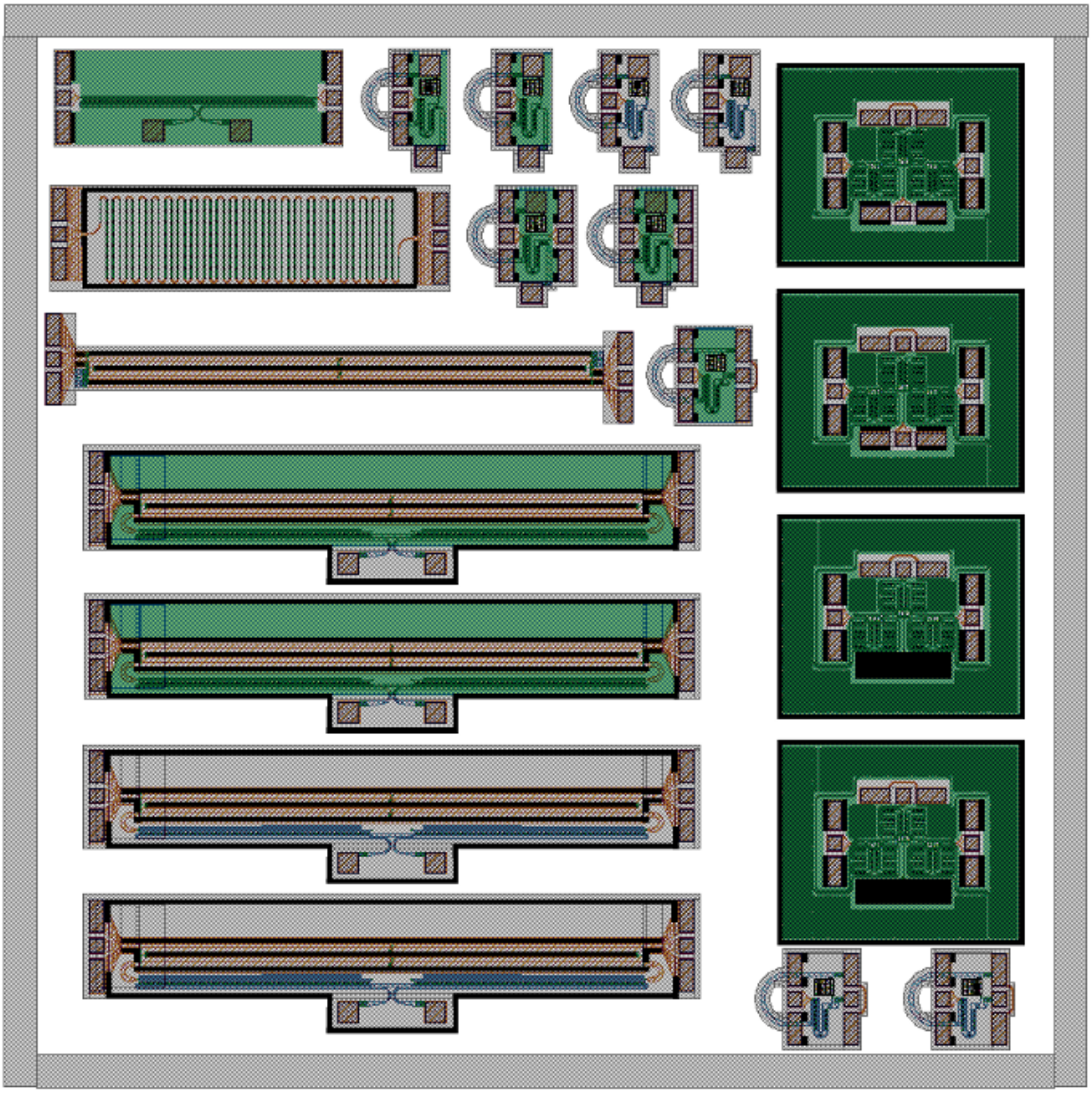


**Figure A.2:** 5mm x 5mm chip layout submitted to MIT-LL.

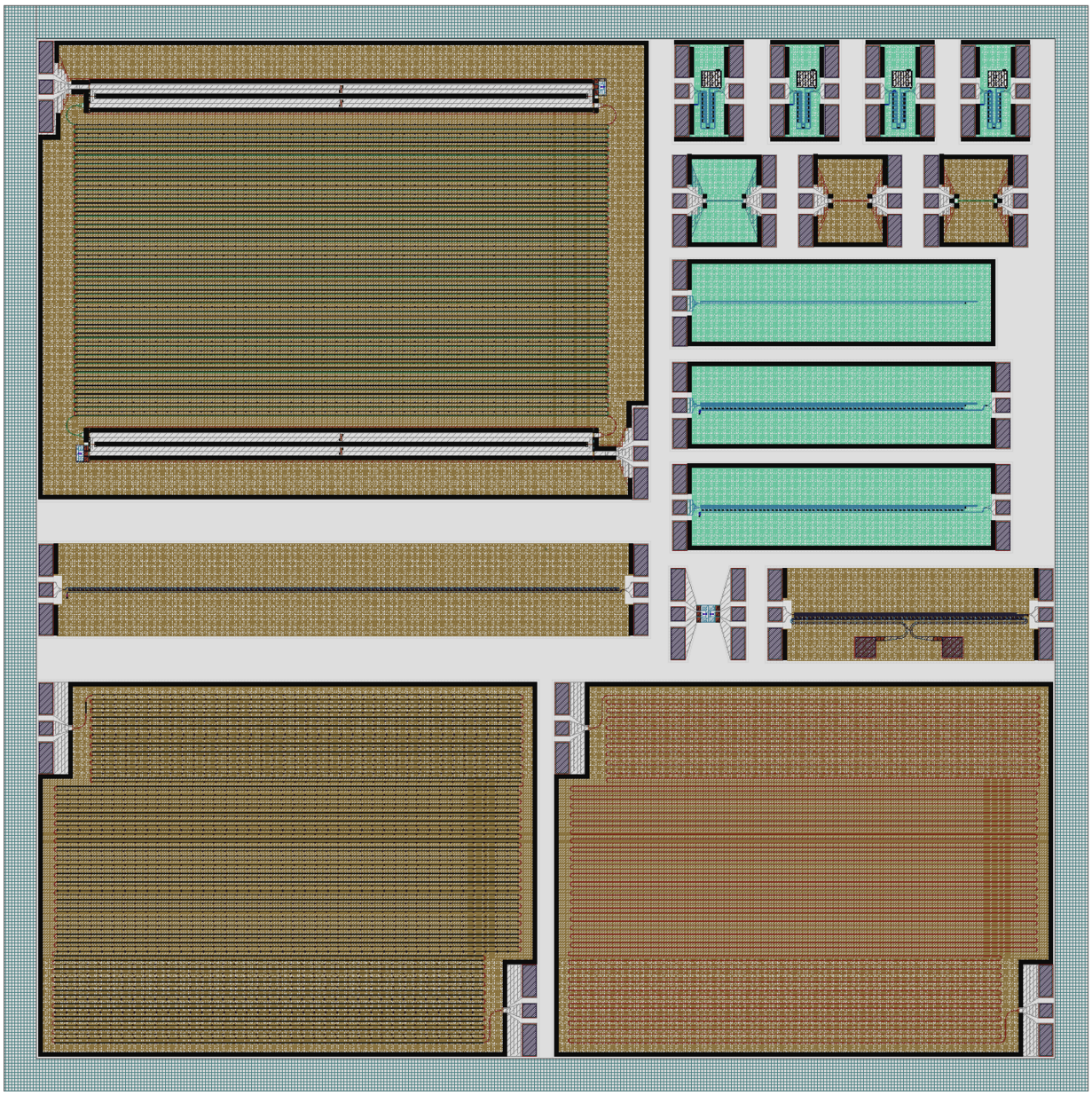


**Figure A.3:** 5mm x 5mm chip layout submitted to MIT-LL.

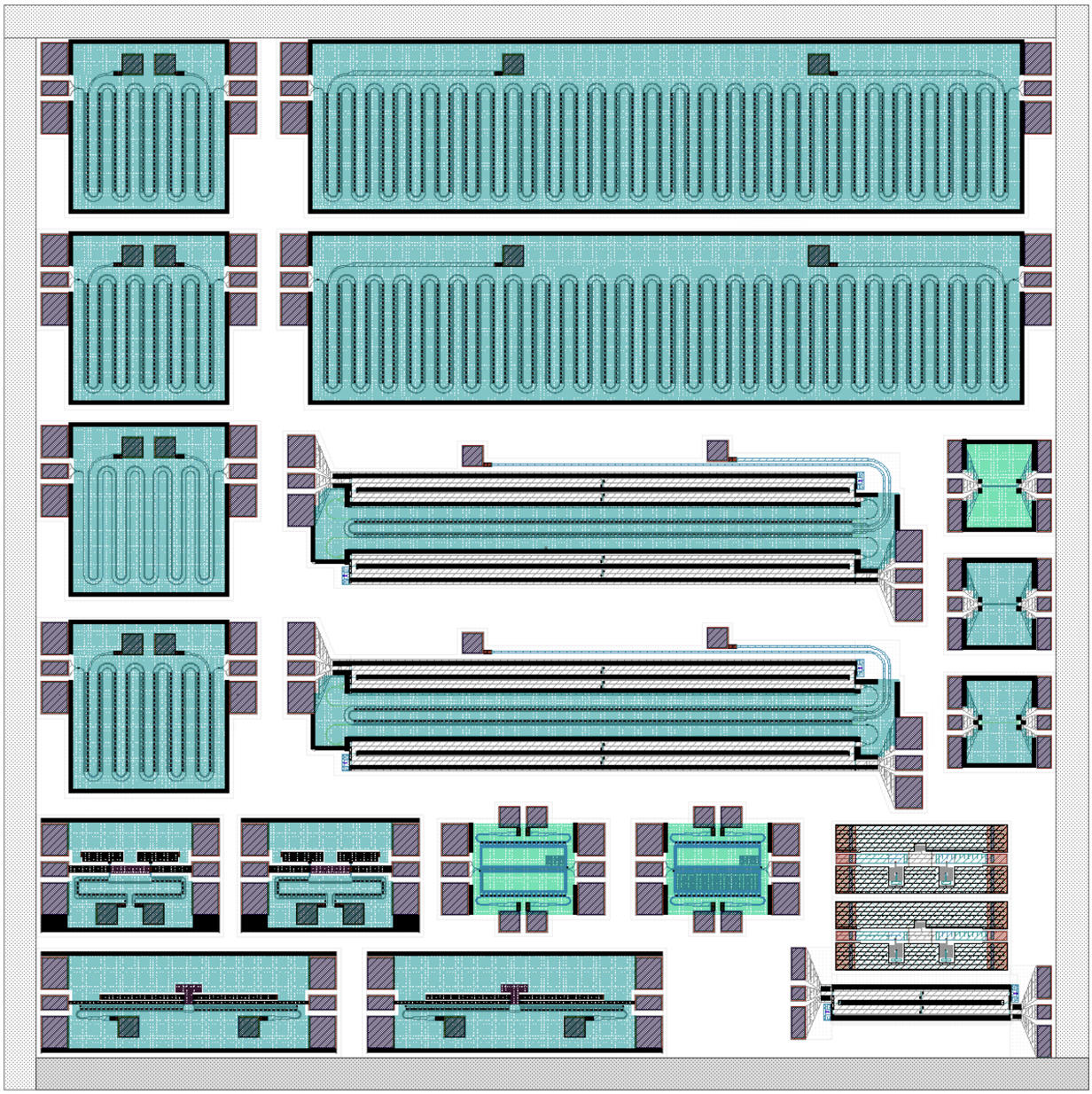


**Figure A.4:** 5mm x 5mm chip layout submitted to MIT-LL.

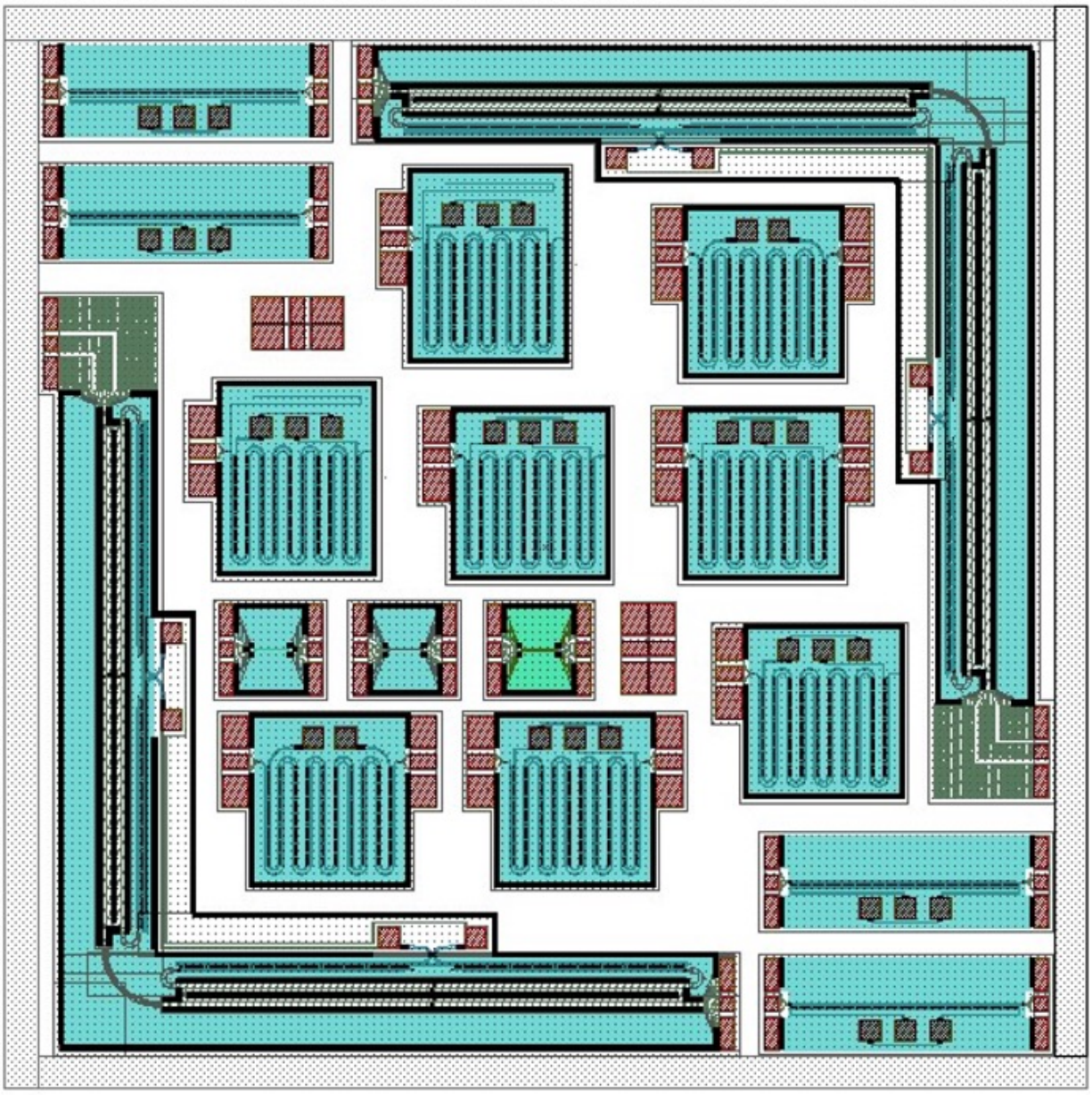


**Figure A.5:** 5mm x 5mm chip layout submitted to MIT-LL.

# Glossary

**Active RF Components** rely on an external power source to perform their functions. Some of the most commonly used active RF components are: power amplifiers, low-noise amplifiers, diodes, limiters, switches, transistors, mixers, phase-locked loops, data converters etc.

**Bandwidth (BW)** is the range of frequencies for which the RF performance falls within specific limits.

**Bias Tee** is used to supply DC currents or voltages to bias RF circuits. A Bias tee is a three-port device consisting a capacitor and an inductor. A Bias Tee can be thought of as a diplexer with an ideal capacitor that allows AC through but blocks the DC bias and an ideal inductor that blocks AC but allows DC.

**Characteristic Impedance ($Z_0$)** is the characteristic property of a transmission line describing the ratio between electric and magnetic fields.

**Circulator** is a passive, non-reciprocal three- or four-port device, in which a microwave or radio-frequency signal entering any port is transmitted to the next port in rotation (only).

**Coaxial Cable** is a type of transmission line consisting of two concentric conductors insulated from each other. In its flexible form it consists of either a solid or stranded center conductor surrounded by a dielectric. A braid is then woven over the dielectric to form an outer conductor. A protective plastic covering is placed on top of the braid.

**Coplanar Waveguide (CPW)** is a type of electrical planar transmission line which can be fabricated using printed circuit board technology, and is used to convey RF and microwave-frequency signals. On a smaller scale, coplanar waveguide transmission lines are also built into monolithic microwave integrated circuits.

**dBm** is unit of level used to indicate that a power ratio (expressed in dB) with reference to one milli-watt (mW). It is a relative measure of signal power where the reference 0 dBm = 1 mW

**De-Embedding** is mathematically removing the measurements affected by the fixture leaving only the behavior of the device under test. This is commonly used when there are non-coaxial connection from the VNA to the DUT, and it is used on circuit board traces, backplane channels, semiconductor packages, connectors or other discrete components.

**Decibel (dB)** is a relative unit without dimensions calculated as ten times the logarithm to the base 10 of a power ratio or as twenty times the logarithm to the base 10 of a voltage ratio.

**Dielectric Constant ($\epsilon_r$)** is the electrical property of a material that describes its behavior in an electric field. The dielectric constant of the dielectric material is the most important design parameter for transmission lines and MIM capacitors, and determines dimensions, losses and propagation characteristics.

**Dynamic Range** in terms of signal analyzer dynamic range is the maximum power ratio (in dB) between a high power signal and low power signal that are present at the input of the signal analyzer – such that both signals can be discerned and measured at the same time or in the same display.

**GSG Probe** is a type of contact probe with ground-signal-ground (GSG) contact geometry in coplanar waveguide (CPW) configuration with specified pitch (spacing). GSG probes are most commonly used to perform on-wafer/die RF measurements.

**Heterogeneous Integration** refers to the assembly and packaging of multiple separately manufactured components onto a single chip in order to improve functionality and enhance operating characteristics.

**Impedance Match** is a condition in which the impedance of a component or circuit is equal to the internal impedance of a transmission line. This gives maximum transfer of energy from the source to the load, as well as minimum reflection and distortion.

**Insertion loss (IL)** is the amount of signal attenuation (expressed in dB) between the input and output ports of the RF device when the switch is in the ON-state. Insertion loss should be as low as possible for maximum power transfer.

**Intermodulation Distortion (IMD)** is a phenomenon that occurs when two or more fundamental frequencies are present in an electronic circuit.

**Isolation (ISo)** is the amount of signal attenuation (expressed in dB) between the input and output ports of the RF device when the switch is in the OFF-state. Isolation should as high as possible.

**Matched Load (ML)** is a device used to terminate a transmission line or waveguide so that all the energy from the signal source will be absorbed.

**Microfabrication** is the process of fabricating miniature structures of micrometer scales and smaller. Historically, the earliest microfabrication processes were used for integrated circuit fabrication, also known as "semiconductor device fabrication".

**Microstrip** is a type of transmission line configuration which consists of a conductor over a parallel ground plane, and separately by a dielectric substrate.

**Millimeter Wave (mmWave)** communication systems have attracted significant interest regarding meeting the capacity requirements of the future 5G network. Millimeter waves are electromagnetic (radio) waves typically defined to lie within the frequency range of 30 GHz to 300 GHz. The microwave band is just below the millimeter-wave band and is typically defined to cover the 3 GHz to 30 GHz range.

**Monolithic Integration** is a process of manufacturing a complete functional circuit or group of circuits in a single piece of substrate. Monolithic integration provides the flexibility of miniaturization, performance enhancements and packaging ready devices.

**Niobium (Nb)** a chemical element with atomic number 41. Niobium becomes a superconductor at cryogenic temperatures. At atmospheric pressure, it has the highest critical temperature of the elemental superconductors at 9.2 K. It also has the greatest magnetic penetration depth of any element.

**Passive RF Components** does not require a power source to perform their functions. Some of the most commonly used passive RF components are: capacitors, inductors, resistors, baluns, filters, attenuators, antennas, switches, phase shifters, hybrids, power dividers, power combiners, matching networks etc.

**Phase Shifter** is used to change the transmission phase angle of an input signal. Ideally phase shifters provide an output signal with an equal amplitude to the input signal, any loss here will be accounted to the insertion loss of the component. The input signal is shifted in phase at the output based on the configuration of the phase shifter selected.

**PIN Diode** a diode with a wide, undoped intrinsic semiconductor region between a p-type semiconductor and an n-type semiconductor region. The p-type and n-type regions are typically heavily doped because they are used for ohmic contacts.

**Probe Station** is used to physically acquire signals from the internal nodes of a semiconductor device. The probe station utilizes manipulators and probe heads which allow precise positioning of fragile probes (DC/RF) on the surface of a DUT. Probe station allows on-wafer testing flexibility, and is often faster and more flexible to test a new electronic device than to wire bond and package.

**Return Loss (RL)** is the magnitude of the reflection coefficient (expressed in dB), and the amount of reflected signal relative to the incident signal.

**RF Front End** is a device or module that incorporates all the circuitry between the antenna and at least one mixing stage of a receiver and possibly the power amplifier of the transmitter. They are used in a wide variety of RF products and applications. Examples include wireless systems and FM radio systems.

**RF Power Rating** is the maximum level of RF power that passes through the RF device without degradation to the switch lifetime when it is in the ON-state.

**S-Parameters** are used to describe the relationship between different ports, when it becomes especially important to describe a network in terms of amplitude and phase versus frequencies, rather than voltages and currents.

**Source Measure Unit (SMU)** is an instrument that can precisely source voltage or current and simultaneously measure voltage and/or current. It combines the useful features of a digital multimeter (DMM), power supply, true current

source, electronic load and pulse generator, all into a single, tightly synchronized instrument.

**Spectrum Analyzer** measures the magnitude of an input signal versus frequency within the full frequency range of the instrument. The primary use is to measure the power of the spectrum of known and unknown signals.

**Superconducting Quantum Interference Device (SQUID)** a device based on superconducting loops containing Josephson junctions. It is a very sensitive magnetometer used to measure extremely subtle magnetic fields as low as $5 \times 10^{-14}$ T

**Superconductor** a material that achieves superconductivity, which is a state of matter that has no electrical resistance and does not allow magnetic fields to penetrate. An electric current in a superconductor can persist indefinitely. Superconductivity can only be typically achieved at very cold temperatures.

**Transmission Line** is a tri-layer junction made by sandwiching a thin layer of a nonsuperconducting material between two layers of superconducting material. Below the critical temperature, pairs of superconducting electrons can "tunnel" right through the nonsuperconducting barrier from one superconductor to another, causing a supercurrent to flow.

**Transmission Line** is a specialized cable or other structure designed to conduct alternating current of radio frequency, that is, currents with a frequency high enough that their wave nature must be taken into account.

**Variable Attenuator** is a tunable passive electronic device that reduces the power of a signal without appreciably distorting its waveform. An attenuator is effectively the opposite of an amplifier, though the two work by different methods. While an amplifier provides gain, an attenuator provides loss, or gain less than 1.

**Vector Network Analyzer (VNA)** is a device used to measure S-parameters of the circuit of interest for various frequencies. VNA is a test instrument that measures the response of a network as vector: real and imaginary parameters so that its performance can be characterized.

**Wavelength ($\lambda$)** is the distance, measured in the direction of propagation, of a repetitive electrical pulse or waveform between two successive points that are characterized by the same phase of vibration.

**Yttrium Barium Copper Oxide (YBCO)** a family of crystalline chemical compounds that displays high-temperature superconductivity. It includes the first material ever discovered to become superconducting above the boiling point of liquid nitrogen (77 K) at about 92 K. Many YBCO compounds have the general formula $YBa_2Cu_3O_{7-x}$.